SEPTEMBER 1955

A.I.Ch.E. JOURNAL

UNIVERSITY OF MICHIGAN
JAN 21 1956
EAST ENGINEERING LIBRARY

Published by the American Institute of Chemical Engineers

CONTENTS

Studies of Thermal Conductivity of Liquids
BYRON C. SAKIADIS AND JESSE COATES

Fundamentals of the Hydrodynamic Mechanism of Splitting in Dispersion Processes
J. O. HINZE

Efficiency and Capacity Factors in Lube Extraction
J. R. FELIX AND C. H. HOLDER

Thermodynamic Properties of Air
E. M. LANDSBAUM, W. S. DODDS, W. F. STEVENS, B. J. SOLLAMI, AND L. F. STUTZMAN

Diffusional Film Characteristics in Turbulent Flow: Dynamic Response Method
JOHN J. KEYES, JR.

Total Pressure Method for Vapor-liquid Equilibria at Low Absolute Pressures: Aniline-nitrobenzene System
G. W. HOLTZLANDER AND J. W. RIGGLE

Low-temperature Oxidation of Ammonia in Fixed and Fluidized Beds
H. F. JOHNSTONE, J. D. BATCHELOR, AND C. Y. SHEN

Liquid-liquid Extraction in Continuous-flow Agitated Extractors
A. W. FLYNN AND R. E. TREYBAL

Effect of Drying Conditions on Drying Rate and Physical Properties of a Porous Solid
E. H. LEBEIS AND T. A. BURTIS

Extraction of Petroleum Fractions by Ammonia Solvents
M. R. FENSKE, R. H. MCCORMICK, H. LAWROSKI, AND R. G. GEIER

Effect of Void Volume and Prandtl Modulus on Heat Transfer in Tube Banks and Packed Beds
JOEL WEISMAN

Gas-solid Contact in Fluidized Beds
C. Y. SHEN AND H. F. JOHNSTONE

Prediction of Ternary Vapor-liquid Equilibria from Boiling-point Data
MITSUHO HIRATA

Analysis of Gas-fluidized Solid Systems by X-ray Absorption
E. W. GROHSE

Rate of Fall of Single Liquid Droplets
WILLIAM LICHT AND G. S. R. NARASIMHAMURTY

Mechanism of Heat Transfer to Fluidized Beds
H. S. MICKLEY AND D. F. FAIRBANKS

Diffusion Coefficients in Hydrocarbon Systems: *n*-Hexane in the Gas Phase of the Methane–, Ethane–, and Propane–*n*-Hexane Systems
L. T. CARMICHAEL, B. H. SAGE, AND W. N. LACEY

Chemical Factors in Propellant Ignition
MELVIN A. COOK AND FERRON A. OLSON

Estimation of Ternary Vapor-liquid Equilibrium: Acetone-methanol-chloroform, Acetone-methanol-carbon tetrachioride, and Acetone-methanol-methyl acetate
W. H. SEVERNS, JR., ALEXANDER SESONSKE, R. H. PERRY, AND R. L. PIGFORD

Foote
LITHIUM HYDROXIDE

The basic lithium salt for industrial use, Foote lithium hydroxide provides chemically unique properties which are being applied to a host of products ranging from ceramic formulations to multi-purpose grease manufacture and welding rod coatings. Many other industrial uses of lithium are in the development stage.

Foote's integrated lithium facilities—raw material, production, research—are your assurance of an abundant supply of lithium for you and all industry.

We invite you to investigate and apply the unusual properties of lithium hydroxide and its derivatives in your products or processes.

Write for technical data sheets.

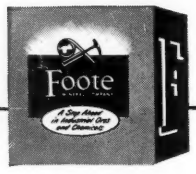

LITHIUM HYDROXIDE
FOR INDUSTRY

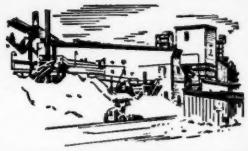

Kings Mountain, N.C. . . . where Foote is mining large deposits of spodumene.

Sunbright, Va. . . . the world's largest lithium chemical plant.

FOOTE MINERAL COMPANY
448 Eighteen West Chelten Building, Philadelphia 44, Pa.
RESEARCH LABORATORIES: Berwyn, Pa. • PLANTS: Exton, Pa.; Kings Mountain, N.C.; Sunbright, Va.

SEPTEMBER 1955

A.I.Ch.E. JOURNAL

Vol. 1 No. 3

ADVISORY BOARD

C. M. Cooper, O. E. Dwyer, W. C. Edmister, E. R. Gilliland, A. N. Hixson, W. R. Marshall, Jr., R. H. Newton, R. L. Pigford, J. M. Smith, Theodore Vermeulen, R. R. White, R. H. Wilhelm

PUBLISHER

F. J. Van Antwerpen

EDITOR

Harding Bliss

The A.I.Ch. E. Journal, an official publication of the American Institute of Chemical Engineers, is devoted in the main to theoretical developments and research in chemical engineering and allied branches of engineering and science. Manuscripts should be submitted to the New York office.

September Song 273

Studies of Thermal Conductivity of Liquids ..... Byron C. Sakiadis and Jesse Coates 275

Fundamentals of the Hydrodynamic Mechanism of Splitting in Dispersion Processes ..... J. O. Hinze 289

Efficiency and Capacity Factors in Lube Extraction ..... J. R. Felix and C. H. Holder 296

Thermodynamic Properties of Air ..... E. M. Landsbaum, W. S. Dodds, W. F. Stevens, B. J. Sollami, and L. F. Stutzman 302

Diffusional Film Characteristics in Turbulent Flow: Dynamic Response Method ..... John J. Keyes, Jr. 305

Total Pressure Method for Vapor-liquid Equilibria at Low Absolute Pressures: Aniline-nitrobenzene System ..... G. W. Holtzlander and J. W. Riggle 312

Low-temperature Oxidation of Ammonia in Fixed and Fluidized Beds ..... H. F. Johnstone, J. D. Batchelor, and C. Y. Shen 318

Liquid-liquid Extraction in Continuous-flow Agitated Extractors ..... A. W. Flynn and R. E. Treybal 324

Effect of Drying Conditions on Drying Rate and Physical Properties of a Porous Solid ..... E. H. Lebeis and T. A. Burtis 329

Extraction of Petroleum Fractions by Ammonia Solvents ..... M. R. Fenske, R. H. McCormick, H. Lawroski, and R. G. Geier 335

Effect of Void Volume and Prandtl Modulus on Heat Transfer in Tube Banks and Packed Beds ..... Joel Weisman 342

Gas-solid Contact in Fluidized Beds ..... C. Y. Shen and H. F. Johnstone 349

Prediction of Ternary Vapor-liquid Equilibria from Boiling-point Data ..... Mitsuho Hirata 354

Analyis of Gas-fluidized Solid Systems by X-ray Absorption ..... E. W. Grohse 358

Rate of Fall of Single Liquid Droplets ..... William Licht and G.S.R. Narasimhamurty 366

Mechanism of Heat Transfer to Fluidized Beds ..... H. S. Mickley and D. F. Fairbanks 374

Diffusion Coefficients in Hydrocarbon Systems: *n*-Hexane in the Gas Phase of the Methane–, Ethane–, and Propane–*n*-Hexane Systems ..... L. T. Carmichael, B. H. Sage, and W. N. Lacey 385

Chemical Factors in Propellant Ignition ..... Melvin A. Cook and Ferron A. Olson 391

Estimation of Ternary Vapor-liquid Equilibrium: Acetone-methanol-chloroform, Acetone-methanol-carbon tetrachloride, and Acetone-methanol-methyl acetate ..... W. H. Severns, Jr., Alexander Sesonske, R. H. Perry, and R. L. Pigford 401

Communications to the Editor 410

Publication Office, Orange, Connecticut. Published quarterly in March, June, September, and December by the American Institute of Chemical Engineers, 25 West 45 Street, New York 36 New York. Manuscripts and other communications should be sent to the New York office. Correspondence with the editor may be addressed to him at Yale University, 225 Prospect Street, New Haven 11, Connecticut. Statements and opinions in the *A.I.Ch.E. Journal* are those of the contributors, and the American Institute of Chemical Engineers assumes no responsibility for them. Subscriptions: one year, member $4.50, nonmember $9.00; two years, member $7.50, nonmember $16.00; additional yearly postage, Canada 50 cents, Pan American Union $1.50, other foreign $2.00 (foreign subscriptions payable in advance). Single copies: $3.00. Second-class mail privileges authorized at Orange, Connecticut. Copyright 1955 by the American Institute of Chemical Engineers.

NEW...

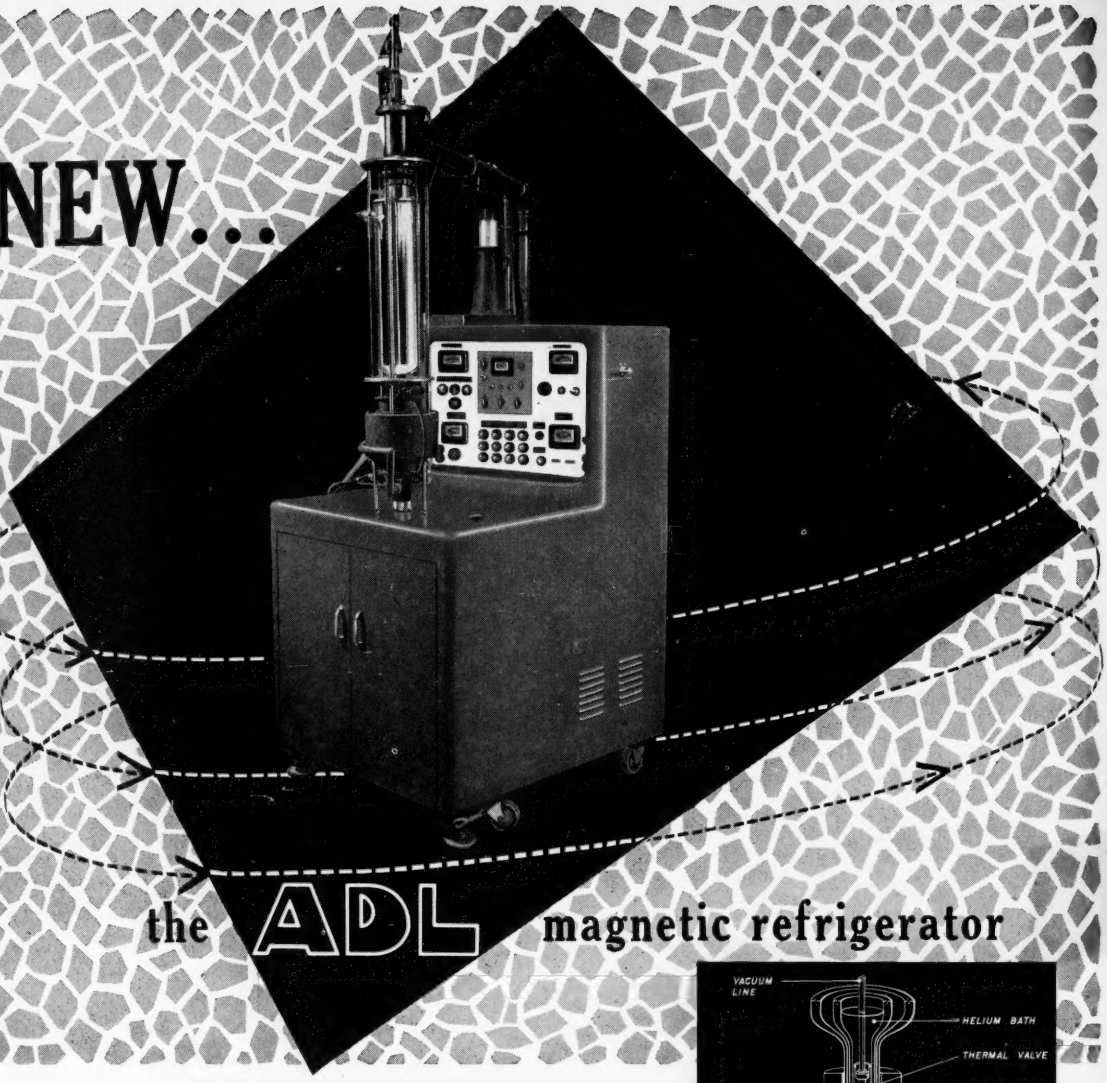

the ADL magnetic refrigerator

continuous refrigeration below 1°K

Now, it is possible and practical, to carry on research at temperatures as low as 0.25°K. Arthur D. Little, Inc., has translated the cyclic technique of magnetic cooling, developed by J. G. Daunt and C. V. Heer, into a practical laboratory apparatus — the ADL Magnetic Refrigerator. It will maintain any temperature in the 1°K to 0.25°K range.

simplifies cryogenic research in a new region of lower temperature:

- Allows many exothermic experiments requiring a large continuous heat input to be performed which previously have not been possible.
- Permits isothermal magnetic measurements of paramagnetic substances at or near their ferromagnetic or antiferromagnetic transition points so that complete phase diagrams can be established for this transformation.
- Establishes a lower isothermal temperature reservoir to act as the initial temperature for paramagnetic cooling in nuclear orientation studies.
- Allows accurate calorimetry in a region important for electronic specific heat measurements.
- Provides a constant-temperature, liquid helium bath down to 0.25°K for study of the anomalous properties of both helium 4 and 3.

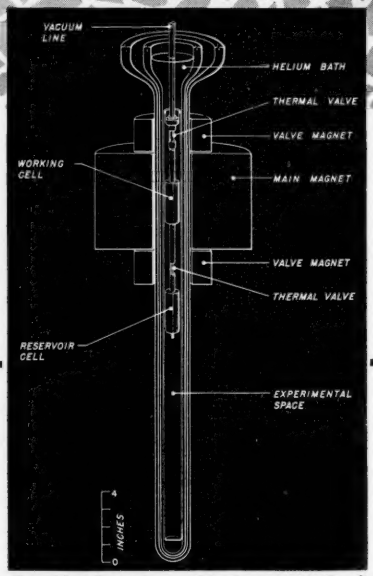

The refrigerating system consists of a paramagnetic salt and the reservoir to be cooled, suspended in an evacuated chamber which is immersed in a liquid helium bath. In operation, the salt is magnetized, with the superconducting thermal valve connecting it to the bath opened to pass the heat of magnetization to the liquid. After this valve is closed, the salt is demagnetized, and thus cools itself. The salt then, in turn, cools the reservoir by the opening of a similar thermal valve connecting them. This cycle repeats automatically.

Write, for more information on the ADL Magnetic Refrigerator,

Arthur D. Little, Inc.

30 Memorial Drive, Cambridge 42, Mass.

SEPTEMBER SONG

Many greetings are ordinarily extended to the graduating chemical engineers in June, but one may well wonder whether September is not a better time. It is in September that the full implications of graduation become apparent. Examinations, term papers, dissertations are behind one, but in their places come many new challenges of even more consequence. It is in September that the summer letdown is forgotten and the neophyte engineer must come to grips with his new job. His performance at such a time is of great importance to him and to the organization which employs him, and it is entirely proper that his job should occupy his best and fullest efforts.

Many adjustments must be made, since the change from academic to industrial environment is not a small one. There are a great many things to be learned in industry which are quite different from those stressed in a university and, indeed, which cannot properly be taught there. First, of course, the details and techniques of the industry itself must be mastered. Second, the necessity for team work and the great importance of getting along with people will soon become apparent. Third, certain routines and channels of information must be learned so that work may be accomplished expeditiously. Thus the one-time college senior or new Ph.D. becomes a freshman again and a very busy one at that.

In this transition period one bridge between academic and industrial life is our professional literature. Some of each man's particular interests, originating in college days, will certainly be covered in *Chemical Engineering Progress* and in the *A.I.Ch.E. Journal*, and no editorial encouragement to read such articles is needed. Furthermore, of course, many new topics will assume interest and importance, as they will have bearing on the new job. Such articles will be of direct and immediate benefit in solving the problems at hand. The editor remembers very well how the solution to a particularly difficult problem which he met on his first job was made possible because of the timely appearance of a fine communication in the *Transactions of the American Institute of Chemical Engineers.*

However it is not the pursuit of particular interests with which we are concerned here. It is rather with the general reading of our professional literature. In industry it is all too easy to become so specialized that one may forget the broader aspects of chemical engineering. It is distressingly easy to lose sight of the fundamentals and the theory of our field, on which all the rest depends. One can be so carried away by practice and by details that the foundation is lost in the process. It is here that we hope that the *A.I.Ch.E. Journal,* with its array of distinguished authors, may be of particular value. Keeping up with the literature, with its constant reexamination and extension of basic theory, is an essential for the young man. We shall be publishing about one hundred papers each year, and at least half of these we expect to be concerned with subjects of general interest to the young graduate. Certainly, also, these papers should represent extensions of ideas and subjects with which the young engineer presumably once had some familiarity. The editor's plea to these men is to read the Journal carefully. A program of one paper read each week would be a reasonable one, and such a plan would bring great satisfaction in keeping fresh and active the inquisitive, scientific attitude.

From personal experience in industry the editor knows how easy it is to become wrapped up in the thrill of industrial enterprise and accomplishment and to forget the foundations on which the whole was built. Whether a new graduate hopes to remain an engineer, and to become a very fine one, or whether he wants to go ahead in the field of management and sales, keeping up with the literature is one of the best ways to assure the intellectual keenness and alertness on which any advancement depends.

H. B.

CEC increases the scope of

industrial mass spectrometry

through two great instruments for process monitoring and control

Consolidated's Model 21-610 mass-spectrometer and its companion, the new Model 21-620, far excel all other instruments of comparable price in performance capabilities and reliability in industrial environment. The extreme sensitivity of the 21-610—accurate to a few parts per million—qualify it for highly critical purity studies as well as process monitoring and control applications. Fitted with an accessory hand-held probe, either model serves as a leak detector for any gas within its mass-range. The 21-620's resolving power up to mass 150 further extends the applicability of an industrial mass-spectrometer to research laboratories and medical centers, as well as to plants of chemical, petro-chemical, petroleum and gas industries. Nearly identical in appearance, the 21-610 features the Diatron ion analyzer and the 21-620, a new cycloidal focusing analyzer.

21-620 Except for slightly less sensitivity, the 21-620 has all the capabilities of the 21-610 plus many others. Where the task is to analyze "heavy" gases or liquids, either in plant locations or in the laboratory, the 21-620 process monitor mass-spectrometer is the ideal control instrument.

21-610 The 21-610 is completely self-contained, needing only 110 volts and a small quantity of cooling water for operation. Moderately priced, easily movable, and economical to operate, the 21-610 is industry's ideal instrument for chemical research, process control and leak detection.

CEC Service Engineers quick change of ion analyzers (right) adds flexibility to Consolidated's two process monitoring mass-spectrometers. A cycloidal focusing analyzer assembly of the 21-620 type is being mounted in the vacuum rack in place of the Diatron analyzer of the 21-610.

The basic instrument can be augmented by many available accessories, thus broadening its application scope. At the far right, are a gas or light-liquid sample inlet system and chart recorder.

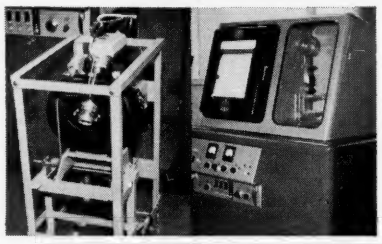

Consolidated Engineering
CORPORATION
300 North Sierra Madre Villa, Pasadena 15, California

Sales and Service through **CEC INSTRUMENTS, INC.,** *a subsidiary with offices in: Pasadena, Atlanta, Chicago, Dallas, Detroit, New York, Philadelphia, Washington, D. C.*

ANALYTICAL INSTRUMENTS FOR SCIENCE AND INDUSTRY

Investigate the application of industrial mass-spectrometry to your business. For full details about CEC's two companion process monitoring mass-spectrometers, send for Bulletin CEC 1824A-X23.

Studies of Thermal Conductivity of Liquids

BYRON C. SAKIADIS and JESSE COATES
Louisiana State University, Baton Rouge, Louisiana

Part I

Values of thermal conductivity and temperature coefficients for fifty-three pure organic liquids, obtained with newly designed, extensively tested apparatus, are presented. For thirty-one of these liquids values of thermal conductivity or temperature coefficients have not been previously reported. The statistically determined maximum error in the presented values of thermal conductivity of liquids is ±1.50%.

A method of correlating the thermal conductivity of liquids based on a modified statement of the theory of corresponding states is presented. Group contributions to the thermal conductivity were calculated. The thermal conductivity of liquids was predicted by this method and the average deviation of the calculated from the observed values for forty-seven liquids is ±1.50%. The proposed method of correlation permits the calculation of the thermal conductivity of a series of liquids at any temperature from a single known value.

The thermal conductivity of liquids is an important physical property, the value of which is required in the solution of most heat transfer correlations. The accuracy of the various correlations predicting these heat transfer coefficients cannot be better than the accuracy with which the thermal conductivity is known. Until recently, nevertheless, the available data were scanty and of doubtful accuracy. During recent years considerable effort has been expended in the experimental determination of the thermal conductivity of various liquids, but little progress has been made toward developing an apparatus that yields dependable results.

This paper presents experimental results on fifty-three pure organic liquids obtained with a newly designed, extensively tested apparatus. The results are correlated on a semitheoretical basis from a modified statement of the theory of corresponding states. An alternative theoretical equation for predicting the thermal conductivity of liquids is given in Part II. The two methods of correlation are mutually supporting.

APPARATUS

The thermoconductimetric apparatus was described in detail in an earlier publication (*5*), where the results of a number of tests were also presented. The design features were decided upon as a result of previous experimental and theoretical studies (*4, 5*) on the various features of previously used apparatus.

The apparatus (Figure 1) is of the steady state type. In it the liquid layer is enclosed between two, 6-in.-diam. horizontal parallel steel bars and heated downward to eliminate convection currents. To establish isothermal surfaces, the top and bottom bars are heated and cooled respectively by large amounts of water drawn from and returned to constant-temperature baths. The water rate is great enough to eliminate much temperature change after the water circulates through the apparatus. Heat flows in series through the liquid layer and a 4-in.-thick steel bar. To improve the accuracy of measuring the heat flow, eighteen thermocouples were embedded in the steel bars in four layers at different positions from the center of the bars, and the heat flow was measured by means of the thermal conductivity of steel and the dimensions of the bar. The thermal conductivity of the piece of steel used in the apparatus was determined in a separate, specially constructed apparatus (*5*). Heat losses were minimized by enclosing the bars in a glass cylinder and providing thermal guarding. This feature also permitted visual observation of the liquid layer, the thickness of which can be varied and is measured by means of three micrometers. This makes it possible to study the presence and effects of heat transfer by radiation across the liquid layer. The steel bars were nickel and chrome plated, the metal surfaces in contact with the liquid layer being highly polished.

Method of Calculation. In this apparatus the thermal conductivity of the liquid may be calculated by two independent methods, an extrapolation method and an over-all-resis-

tance-to-heat-flow method. The extrapolation method, used by most investigators, is based on the equation for heat conduction involving the temperature drop across the liquid layer which is obtained by extrapolation of the thermocouple readings to the metal-liquid boundaries. The equation for heat conduction is

$$k = \frac{q\, x_L}{A\, \Delta\, t_L} \qquad (1)$$

This equation assumes that the surfaces are perfectly plane and that there are no surface effects of any kind. In practice this condition is simply not met. Even after careful plating and polishing, surface irregularities of about 0.0005 in. are common. They introduce a considerable error in thin-liquid-layer apparatus.

The over-all resistance to heat-flow method is based on calculating the resistance to heat flow due to the steel bars and the enclosed liquid layer. Hence

$$R_T = \frac{\Sigma\, (\Delta t)}{q} \qquad (2)$$

where

$\Sigma(\Delta t)$ = over-all temperature drop due to liquid layer and a known thickness of steel bars
q = heat flow across liquid layer and bars
R_T = total resistance to heat flow (including effects due to surface irregularities and films)

$$R_T = R_S + R_L \qquad (3)$$

and

$$R_S = \frac{x_S}{k_S\, A} \qquad (4)$$

$$R_L = \frac{x_L}{k_L\, A} \qquad (5)$$

where

R_S = resistance to heat flow due to steel bars alone (including effects due to surface irregularities and films)
R_L = resistance to heat flow due to liquid layer

The resistance to heat flow due to the steel bars alone, R_S, is determined by making a run with the bars in direct contact. Subtracting this resistance from the resistance determined for a given liquid thickness, R_T, gives the resistance due to the liquid layer alone, R_L, and the thermal conductivity of the liquid is calculated from Equation (5).

The over-all resistance method is considered more correct because it takes into account the effect of surface irregularities and films. It also makes it possible to study the presence and effects of any convection currents or other extraneous factors.

Precision of Measurements. The described apparatus was submitted to a number of tests to establish its accuracy and dependability. It was shown that, within the range of experimental conditions, heat transfer by radiation across the liquid layer is negligible with no absorption taking place. Evidence was also given to show the absence of convection currents in downward heating.

The described thermoconductimetric apparatus is used as a primary device. The experimentally determined maximum error in the value of thermal conductivity of liquids is $\pm 1.50\%$, of which $\pm 1.0\%$ is a statistically calculated maximum uncertainty in the determined value of thermal conductivity of steel.

RESULTS

The experimental results are presented in Table 1. The thermal conductivity of most liquids was determined at three temperatures equally spaced over the indicated temperature range, and the temperature coefficient was calculated from the results.

COMPARISON WITH LITERATURE VALUES

An extensive literature survey has been made (*3, 6*) and values of thermal conductivity for numerous liquids have been collected, classified, and evaluated. The more dependable results fall mainly into two groups differing consistently by about 5%. The first group comprises the results of L. Riedel and H. L. Mason, determined with a similar type of thin-film apparatus in the period 1940 to 1954. They found low values of thermal conductivity and temperature coefficients. The second group comprises the results of O. K. Bates et al. and T. K. Slawecki, determined with a thick- and thin-film type of apparatus respectively in the period 1933 to 1953. Their values of thermal conductivity are somewhat higher than those of the first group.

A comparison of some values of thermal conductivity determined by the authors with values published by these two groups of investiga-

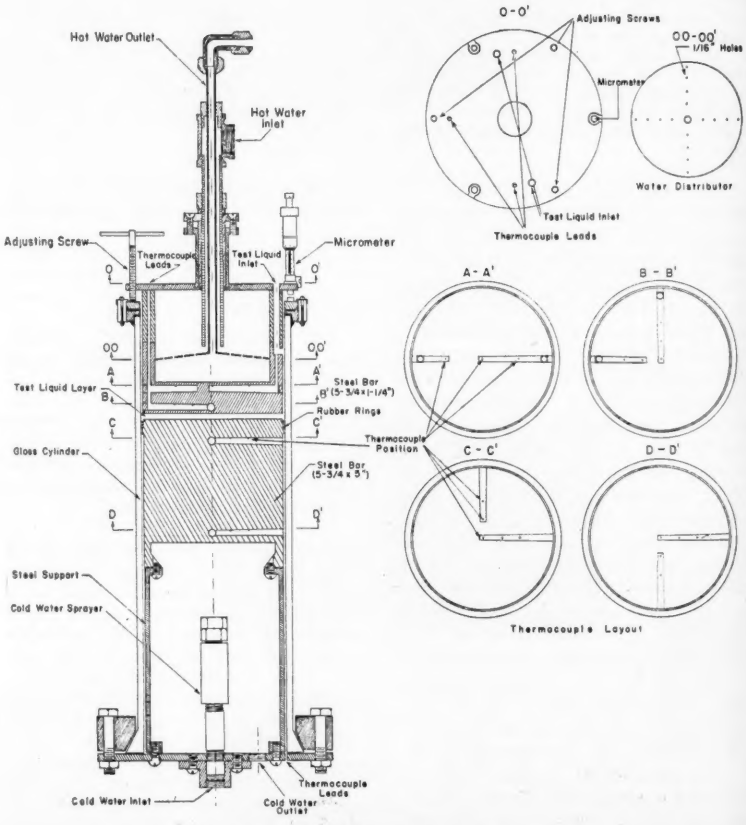

Fig. 1. Thermoconductimetric apparatus.

tors was made, and it was noted that the values of thermal conductivity of other investigators calculated by the extrapolation method (group 1) agree in general with the present authors' values calculated by the same method but are about 5% lower consistently than the values calculated by the correct over-all-resistance-to-heat-flow method. The difference is due to surface irregularities and films (*5*). This effect may be evaluated also from the over-all resistance of the bars when in direct contact. The presence of surface irregularities and films would increase the resistance to heat flow of the bars. Hence, it was found that if all the surface effects are due to surface irregularities, they are of the order of 0.0008 in. Since the metal surfaces were carefully machined, plated, and highly polished, at least to the same extent as in apparatus of other investigators, it is concluded that some of the best literature values of thermal conductivity are about 4 to 5% lower than the correct values.

The apparatus used by Bates et al. is a thick-film apparatus. The liquid-layer thickness was about 2 in., and the temperature drop across a given liquid-film thickness was determined by thermocouples placed within the liquid layer with their hot junctions located approximately 1/4 in. apart. The values obtained by Bates et al. agree well with the results of this investigation calculated by the correct over-all resistance method, which was to be expected as the liquid-film thickness is determined directly within the liquid layer and therefore is free of surface irregularities and films.

Although the results of T. K. Slawecki were calculated by the extrapolation method they agree with the authors' results calculated by the over-all-resistance-to-heat-flow method, probably because the liquid-layer thickness, in the apparatus used by Slawecki, was determined by electrical capacitance methods, which should give a true average value.

A comparison of the temperature coefficients of thermal conductivity for some liquids with literature values was made, and it was noted that the temperature coefficients of thermal conductivity determined in all thin-film types of apparatus are consistently lower than the values observed in this investigation; the values of Bates et al. are consistently higher.

TABLE 1.—OBSERVED VALUES OF THERMAL CONDUCTIVITY

Liquid	k at 100° F., B.t.u./(hr.) (sq. ft.) (°F./ft.)	$dk/dt \times 10^{-4}$ B.t.u./(hr.) (sq. ft.) (°F./ft.)/°F.	Temp. range, °F.	Source, purity*
n-Hexane	0.0714	−1.40	91–135	9a
n-Heptane	0.0725	−1.30	91–170	7b
n-Octane	0.0751	−1.15	93–170	9a
n-Nonane	0.0777	−1.30	92–171	9a
n-Decane	0.0770	−1.40	106–169	7b
n-Hexene-2	0.0715	−1.60	100–131	9c
n-Heptene-2	0.0747	−1.30	91–170	9a
n-Octene-2	0.0769	−1.40	92–171	9c
n-Octene-1	0.0740	−1.40	103–172	9c
2-Methyl pentane	0.0617	−1.00	87–121	9a
3-Methyl pentane	0.0628	−1.00	89–128	9a
2, 2-Dimethyl butane	0.0560	−0.93	85–110	9a
2, 3-Dimethyl butane	0.0592	−0.80	86–122	9a
2, 2, 4-Trimethyl pentane	0.0560	−1.05	101–171	9a
2, 2, 5-Trimethyl hexane	0.0623	−1.40	94–171	9a
Methyl alcohol	0.1187	−1.77	95–138	1b
Ethyl alcohol	0.0981	−1.20	95–167	10b
n-Propyl alcohol	0.0912	−0.95	95–168	6b
n-Butyl alcohol	0.0885	−1.02	94–170	1b
n-Amyl alcohol	0.0863	−0.91	94–170	5d
n-Hexyl alcohol	0.0878	−0.93	94–170	5d
n-Heptyl alcohol	0.0903	−0.81	95–169	5b
n-Octyl alcohol	0.0927	−1.00	95–170	7d
n-Decyl alcohol	0.0947	−1.18	95–170	5d
i-Propyl alcohol	0.0814	−0.95	94–171	8b
i-Butyl alcohol	0.0803	−0.81	94–170	5b
tert-Butyl alcohol	0.0670	−0.75	93–171	5b
Ethylene glycol	0.1510	+0.36	97–169	7b
Propylene glycol	0.1215	−0.35	96–169	4b
Glycerol	0.1789	+0.53	96–171	7b
Depropylene glycol	0.1007	−1.08	96–169	3c
Methyl acetate	0.0931	−1.92	96–120	7d
Ethyl acetate	0.0826	−1.62	106–145	6b
Propyl acetate (*n*-)	0.0796	−1.40	99–169	5b
Butyl acetate (*n*-)	0.0795	−1.26	98–170	7b
Amyl acetate (*n*-)	0.0782	−1.25	96–170	5b
Octyl acetate (*n*-)	0.0815	−1.45	104–170	2b
Methyl propionate	0.0849	−1.55	108–145	7b
Ethyl propionate	0.0800	−1.55	107–168	7b
Propyl propionate (*n*-)	0.0795	−1.34	108–170	5b
Amyl propionate (*n*-)	0.0790	−1.39	106–169	7b
Ethyl butyrate (*n*-)	0.0781	−1.38	107–169	5b
n-Amyl chloride	0.0676	−0.85	108–169	7b
1-Chlorodecane	0.0754	−1.23	106–169	5b
n-Propyl bromide	0.0571	−1.19	96–136	5b
n-Butyl bromide	0.0581	−1.13	103–170	5b
n-Amyl bromide	0.0599	−1.06	102–170	5b
n-Hexyl bromide	0.0614	−1.02	96–169	5b
n-Propyl iodide	0.0503	−0.90	105–170	5b
n-Heptyl iodide	0.0573	−0.98	102–169	5b
Nitromethane	0.1170	−1.97	110–168	5b
Nitroethane	0.0962	−1.55	108–168	5b
1-Nitropropane	0.0873	−1.44	110–169	5d

*

1 Allied Chemical & Dye
2. Brothers Chemical
3. Carbide & Carbon
4. City Chemical
5. Eastman Kodak
6. Fisher Scientific
7. Matheson, Coleman & Bell
8. Merck
9. Phillips Petroleum
10. U.S. Industrial

a. Pure, 99 mole % min.
b. Reagent, research, Eastman-highest purity.
c. Technical, 95 mole % min.
d. Practical, 95–98%

The difference between the values observed in this investigation and those of Bates et al. is due to the effect of heat transfer by radiation across the liquid layer in the apparatus used by Bates, which amounted to about 7% of the heat flow by conduction. Bates did not

correct for this heat transfer by radiation. Since for a given liquid-film thickness the heat transfer by radiation is greater for the higher or hotter section of the liquid layer than for the colder section, the calculated coefficient of thermal conductivity will be higher than the correct value, as noted. If the results obtained by Bates are corrected for the heat flow by radiation across the liquid layer, it will be found that the published values of thermal conductivity are about 0.8% high. The corrected values of the temperature coefficient agree in general with the values observed by the authors.

The low values of the temperature coefficient obtained with all thin-film apparatus are most probably due to the thermal expansion of the copper cylinders.

The accuracy of the results of this investigation, presented in Table 1, can also be shown indirectly by a comparison of the temperature coefficients for the homologue members of the alcohol series, which were fairly pure liquids. It will be noted that the temperature coefficients vary regularly from member to member, as expected. A plot of the temperature coefficients as a function of the number of carbon atoms was made, and a smooth curve drawn through the experimental points. The maximum deviation of any point from the curve was noted to be $\pm 0.08 \times 10^{-4}$ B.t.u./(hr.) (sq.ft.) (°F./ft.)/°F. For a temperature range of 74°F. covered in this investigation this corresponds to a maximum deviation of ±0.65% in the values of thermal conductivity, including the deviation due to any impurities in the liquids. The temperature coefficients for the same liquids determined by other investigators vary irregularly from liquid to liquid.

CORRELATION OF RESULTS

The basic conditions underlying the theory of corresponding states have been clearly stated (*2*). If all the conditions are met, it can be shown (*2*) that two systems should exhibit corresponding behavior if they are at the same reduced temperature and pressure or volume. Most liquids actually do not meet all the conditions; however, a corresponding-states behavior could arise under some other circumstances than those given, although the detailed behavior would be different.

Such a situation would arise when homologous members of the same series are considered. Hence the condition that all molecules should be spherically symmetrical could be changed to mean a group of nonspherical molecules having the same shape factor. This changes also the condition that the potential energy is a function only of intermolecular distance to a condition in which the potential energy has the same proportional dependence of potential on angular orientation. This permits the inclusion of polar substances. Finally the potential function may have a different shape, but it will be expected to vary uniformly.

The theory of corresponding states may then be stated on a broad basis in a different form. The same members of two different series will exhibit corresponding behavior to the same other members of their respective series, provided they are at the same reduced temperature and pressure. Since the effect of pressure on thermal conductivity is relatively small (*1*), the reduced pressure may be omitted from the correlation. Hence a plot of thermal conductivity as a function of number of carbon atoms, for the chain compounds, at the same reduced temperature should result in a family of curves of similar shape. Such a plot is shown in Figure 2. As predicted, the curves are parallel and have the same shape. The contribution to the thermal conductivity of a given functional group or atom in the molecule was determined by taking the hydrocarbon series as a basis and obtaining the difference between it and other series. These contributions are presented in Table 2.

TABLE 2.—STRUCTURAL CONTRIBUTION TO THE THERMAL CONDUCTIVITY OF LIQUIDS AT $T_r = 0.6$

		dk, B.t.u./(hr.) (sq.ft.) (°F./ft.)
Aliphatic alcohols	—OH	—0.0070
Esters	$-C(=O)-O-$	+0.0070*
Alkyl halides	—Cl	—0.0168
	—Br	—0.0248
	—I	—0.0310
Nitrated alkanes	$-NO_2$	0*
Isomerization		
	For 1 $-CH_3$ group	—0.0060
	For 2 $-CH_3$ groups	—0.0104
	For 3 $-CH_3$ groups	—0.0142
Bonding		
	One double bond=	+0.0010
Effective Number of Carbon Atoms, x		
Aliphatic hydrocarbons	C_nH_{2n+2}	$x = n$
Aliphatic alcohols	$C_nH_{2n+1}OH$	$x = n$
Esters	$C_nH_{2n}O_2$	$x = n-2$
Alkyl halides	$C_nH_{2n+1}Cl$	$x = n$
	$C_nH_{2n+1}Br$	$x = n+1$
	$C_nH_{2n+1}I$	$x = n+2$
Nitrated alkanes	$C_nH_{2n+1}NO_2$	$x = n$

*The first members of associated series such as alcohols and nitrated alkanes, have an abnormally high thermal conductivity; however, their relative values are consistent with the contributions given in Table 2. Hence any member of the alcohol series will differ from a corresponding member of the nitrate alkane series by 0.0070 B.t.u./(hr.) (sq.ft.) (°F/ft.), including methyl alcohol and nitromethane. However methyl alcohol will differ by more than 0.0070 from the first member of the hydrocarbon series or methane.

It will be noted that the effective number of carbon atoms, x, is not the same for all series. It is clear that the size of the substituted atoms or functional groups, and the polarity of the molecule, which affect the shape factor and intermolecular forces, determine the value of x.

A theoretical equation for predicting the thermal conductivity of liquids will be derived in Part II. According to the theoretical equation

$$k = C_p U_s \rho L \qquad (6)$$

Substituting an empirical equation for the velocity of sound in Equation (6) (Part II) results in

$$k = \frac{C_p R^3 \rho^4 L}{M^3} \qquad (7)$$

Values of the variables involved at 68°F. for members of the hydrocarbon and alcohol series are tabulated (Table 3) for purposes of comparison.

It will be noted that the specific heat and the critical density are approximately constant for members of the same series; whereas the intermolecular distance, L, varies somewhat from member to member. At the critical temperature Equation (7) may be expressed as follows,

$$k = C\,Y \qquad (8)$$

where

$C = C_p\ \rho_c^4$, group constant for a given series

$Y = R^3\ L/M^3$, group consisting of additive factors

If the small variations observed are neglected, the function Y may also be taken as a constant for a given series. Hence it may be predicted as a good approximation that at the critical temperature the thermal conductivity of a homologous series will be a constant and the same for all the members of the series. A plot of thermal conductivity of a given series as a function of reduced temperature, with the number of carbon atoms as a parameter, will result in a family of curves converging to a point at $T_r = 1.0$. Such a plot for the hydrocarbon series is shown in Figure 3. Only the last five members of the series were studied, the remaining members being used as a reference for the other series. It will be noted that, as expected, the convergence points for both the normal and associated liquids are arranged in the order of their relative critical densities. The method of calculation may be shown by an example.

Illustration. Calculate the thermal conductivity of *i*-butyl alcohol at 100.0°F.

Data: $T_c = 995.0$°R.

Effective carbon atom number $x = n = 4$

Structural contribution —OH	
	+0.0070
1 Isomerization	—0.0060
net	+0.0010

In Figure 3 locate the reference point for butane, at $T_r = 0.6$, 0.0775. Add 0.0010 and locate new point, 0.0785. Connect the new point with the convergence point for alcohols by a straight line. Read the value of thermal conductivity at $T_r = 0.563$ (100.0°F.), $k = 0.0818$ B.t.u./(hr.)(sq.ft.)(°F./ft.). The observed value at the same temperature is 0.0803 B.t.u./(hr.)(sq.ft.)(°F./ft.).

This method of correlation was used to predict the thermal conductivity of the liquids tested in this investigation. Representative results are presented in Table 4.

TABLE 3

Liquid	C_p, B.t.u./(lb.)(°F.)	$L \times 10^{-9}$, ft.	ρ_c lb./cu.ft.
n-Hexane	0.534	0.268	14.49
n-Heptane	0.526	0.251	14.59
n-Octane	0.522	0.245	14.59
n-Nonane	0.521	0.230	14.59
Ethyl alcohol	0.575	0.259	17.20
n-Propyl alcohol	0.563	0.230	17.02
n-Butyl alcohol	0.563	0.217	16.95
n-Amyl alcohol	0.560	0.206	16.90

The ratio R/M has been calculated also for a few liquids:

Liquid	R/M
n-Hexane	0.369
n-Heptane	0.362
n-Octane	0.358
Ethyl alcohol	0.318
n-Propyl alcohol	0.318
n-Butyl alcohol	0.319
Methyl acetate	0.273
Ethyl acetate	0.280
n-Propyl acetate	0.285

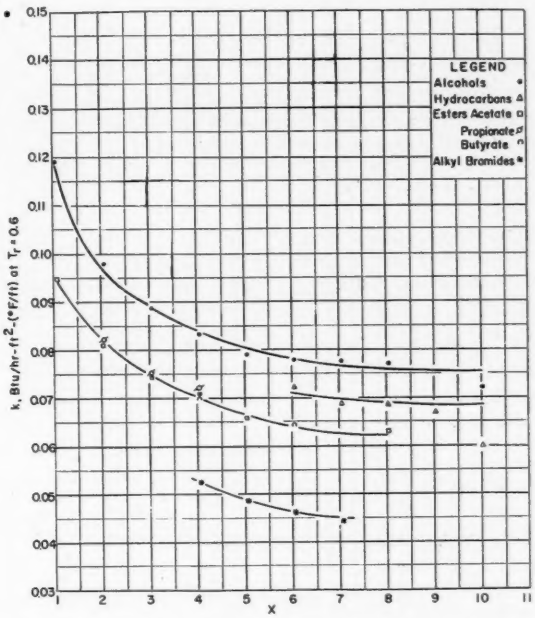

Fig. 2. Thermal conductivity vs. effective number of carbon atoms.

The average deviation of the calculated from the observed values of thermal conductivity for the forty-seven liquids is ±1.50%. The maximum deviation is about ±6.0%. Considering the purity of the liquids involved, the observed average deviation is satisfactory. It will be noted that the method of correlation was tested with respect both to the thermal conductivity and its temperature coefficient.

At any one temperature the thermal conductivity appears both to increase and to decrease with increasing molecular weight, as in the case of the hydrocarbons and aliphatic alcohols respectively. At the same reduced temperature, however, the thermal conductivity for all liquids decreases with molecular weight.

This method of correlation permits the calculation of the thermal conductivity of a series of liquids at any temperature from a single known value for one member. The convergence point may be established readily from its critical density. A straight line connecting the known experimental value with the convergence point will pass through the $T_r = 0.6$ point, the effective value of x being determined from the structure of the

molecule. The value read at $0.6T_c$ and the effective value of x will establish the structural contribution of the functional group in the series. The thermal conductivity at any temperature, for any member of the series, is then readily determined. The required single value may be calculated from the theoretical equation presented in Part II, in which case no experimental data are needed.

SUMMARY

Observed values of thermal conductivity and temperature coefficients are presented for fifty-three pure organic liquids. Values of thermal conductivity or temperature coefficients for thirty-one of these liquids have not been previously reported. It is indicated that the best literature values of thermal conductivity are most probably low, on account of surface effects that were not considered in most investigations.

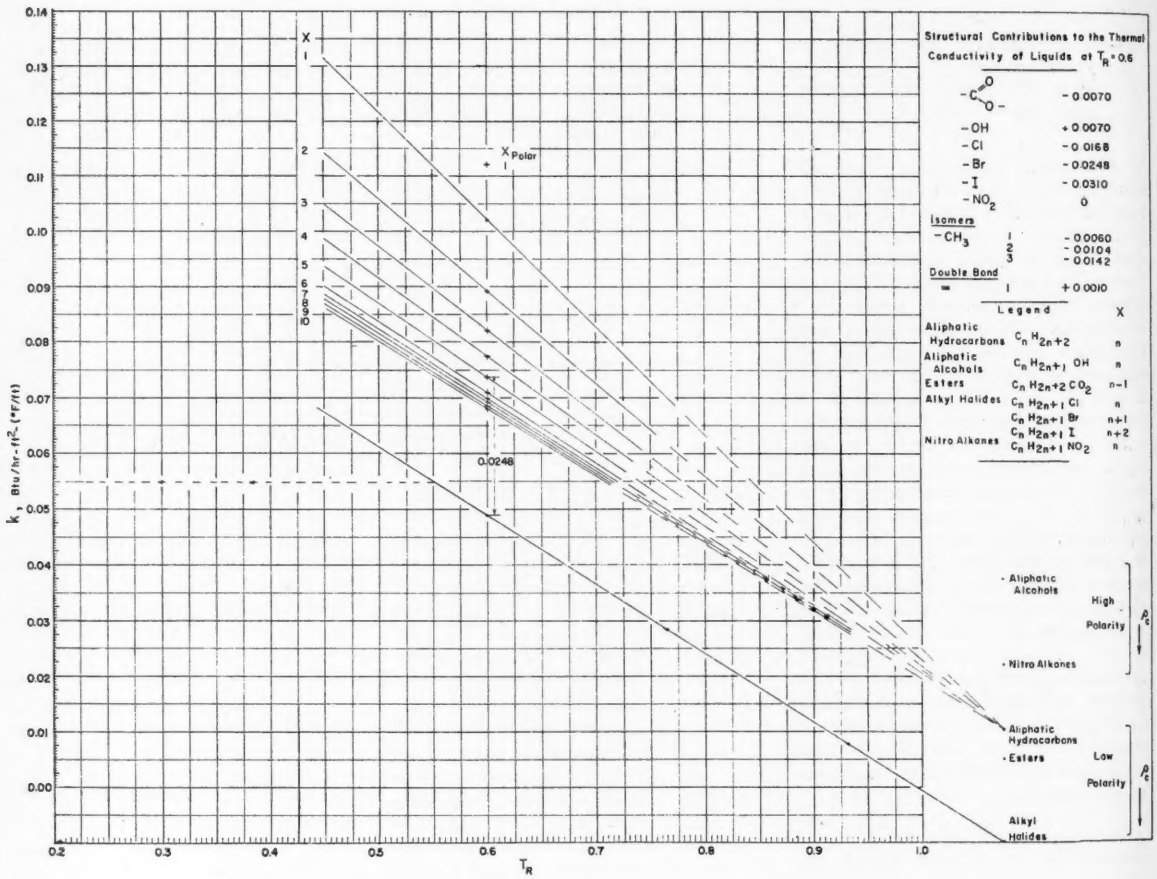

Fig. 3. Thermal conductivity of liquids vs. reduced temperature.

TABLE 4.—COMPARISON OF SOME EXPERIMENTAL VALUES OF THERMAL CONDUCTIVITY WITH VALUES CALCULATED BY CORRELATION BASED ON THE THEORY OF CORRESPONDING STATES

Liquid	T_c, °R.	T_r	$k_{calc.}$†	$k_{obs.}$†	% Dev.‡	T_r	$k_{calc.}$†	$k_{obs.}$†	% Dev.‡
n-Heptane	972.0	0.567	0.0738	0.0737	+0.14	0.648	0.0637	0.0634	+0.47
n-Nonane	1060.0*	0.520	0.0785	0.0787	+0.25	0.595	0.0691	0.0685	+0.87
Heptene-2	975.0*	0.565	0.0755	0.0759	−0.53	0.646	0.0651	0.0656	−0.61
n-Propyl alcohol	966.0	0.574	0.0922	0.0917	+0.54	0.650	0.0840	0.0847	−0.83
n-Hexyl alcohol	1102.0*	0.502	0.0867	0.0884	−1.92	0.571	0.0807	0.0813	−0.74
Methyl acetate	912.0	0.610	0.0935	0.0939	−0.43	0.635	0.0887	0.0893	−0.67
Amyl acetate (*n*-)	1090.0*	0.510	0.0782	0.0788	−0.76	0.578	0.0695	0.0695	0
Ethyl propionate	984.0	0.565	0.0807	0.0808	−0.12	0.635	0.0703	0.0699	+0.57
Ethyl butyrate (*n*-)	1020.0	0.555	0.0768	0.0771	−0.39	0.616	0.0683	0.0686	−0.44
1-Chlorodecane	1340.0*	0.422	0.0745	0.0747	−0.27	0.469	0.0683	0.0669	+2.10
n-Hexyl bromide	1210.0*	0.460	0.0613	0.0618	−0.81	0.520	0.0544	0.0544	0
n-Propyl iodide	1074.0*	0.526	0.0510	0.0498	+2.41	0.586	0.0445	0.0440	+1.13
Nitroethane	1004.0*	0.566	0.0945	0.0950	−0.52	0.625	0.0860	0.0857	+0.35
2-Methyl pentane	895.0	0.610	0.0637	0.0630	+1.11	0.650	0.0591	0.0596	−0.84
2, 2-Dimethyl butane	885.0	0.616	0.0590	0.0574	+2.78	0.644	0.0560	0.0551	+1.63
2, 2, 4-Trimethyl pentane	980.0	0.573	0.0575	0.0559	+2.86	0.644	0.0507	0.0486	+4.31
i-Butyl alcohol	995.0	0.555	0.0825	0.0808	+2.10	0.632	0.0757	0.0746	+1.47

*Estimated values. †k = B.t.u./(hr.)(sq. ft.)(°F./ft.) ‡Percentage deviation of calculated from observed values.

A method of correlating the thermal conductivity of liquids based on the theory of corresponding states has been developed and has been tested on a large number of liquids. The thermal conductivity of a series of liquids may be determined from one known value, at any one temperature, of one of its members.

ACKNOWLEDGMENT

The authors wish to acknowledge the assistance of N. Y. Chen, who performed part of the experimental work. This research was conducted under National Science Foundation Grants G-221 and 558. The Department of Chemical Engineering and the Engineering Experiment Station of Louisiana State University provided additional funds and facilities.

NOTATION

A = heat transfer area, normal to heat flow, sq.ft.
C_p = specific heat at constant pressure, B.t.u./(lb.) (°F.)
C = group of constants
k = thermal conductivity, B.t.u./(hr.) (sq.ft.) (°F./ft.)
L = mean available intermolecular distance, surface to surface, ft.
M = molecular weight, lb.
n = number of carbon atoms
q = rate of heat flow, B.t.u./hr.
R = resistance to heat flow, (°F.) (hr.)/B.t.u.
R = additive constant
T = absolute temperature, °R.
t = temperature, °F.
U_s = velocity of sound, ft./sec.
x = effective number of carbon atoms
x = thickness, ft.
Y = group of additive factors
ρ = density, lb./cu.ft.
Δt = temperature drop, °F.
$\Sigma(\Delta t)$ = over-all temperature drop, °F.

Subscripts

c = critical
L = liquid
r = reduced
S = steel
T = total

LITERATURE CITED

1. Bridgman, P. W., *Am. Acad. Arts and Sci.*, **49**, 141 (1923).
2. Pitzer, K. S., "Quantum Chemistry," Prentice-Hall, New York (1953).
3. Sakiadis, B. C., and J. Coates, *Louisiana State Univ. Eng. Expt. Sta. Bull.* No. 34 (1952).
4. *Ibid.*, No. 35 (1953).
5. *Ibid.*, No. 45 (1954).
6. *Ibid.*, No. 48 (1954).

Part II

An equation for predicting the thermal conductivity and its temperature coefficient of pure organic liquids has been derived on the basis of a particular molecular arrangement in the liquid. The equation is applicable to both normal and associated liquids. Detailed methods and tables are given in the Appendix for predicting the variables involved where no data are available. The equation has been tested on forty-two liquids, and the average deviation of the calculated from the observed values of thermal conductivity is ± 2.6%.

In Part I the values of thermal conductivity observed in this investigation were correlated on the basis of a modified statement of the theory of corresponding states. This method requires at least one experimental value. This part of the series presents the results of an attempt to derive without experimental information a simple theoretical equation for the prediction of thermal conductivity and its temperature coefficient.

The equation is derived on the basis of a particular molecular arrangement in the liquid, consistent with the results of X-ray diffraction studies in liquids. It has been tested on a large number of liquids (*see* Part I). The success of the equation in predicting the thermal conductivity of liquids, both normal and associated, justifies indirectly the assumptions made in its derivation and throws light on the mechanism of heat conduction in liquids.

PREVIOUS WORK

A number of equations, mostly empirical, for predicting the thermal conductivity of liquids have been presented. None of the theoretical equations appear to be satisfactory, as the predicted values of thermal conductivity vary widely from experimental data, and the empirical equations relating the thermal conductivity to other liquid properties are little better. The theory of the liquid state has not been developed to the point where a satisfactory equation for thermal conductivity may be arrived at without vitiating assumptions. An equation with as simplified a theoretical background as possible is therefore desirable.

One such equation was developed in 1923 by P. W. Bridgman(*1*), who assumed that the liquid molecules were arranged in a cubical lattice, at a distance d ft. apart, vibrating about centers,

$$d = \left(\frac{M}{N\rho}\right)^{1/3}$$

The total energy of a molecule was taken as $3RT/N$ ($3/2RT/N$ kinetic energy and $3/2RT/N$ potential energy), or $1/2RT/N$ for each degree of freedom. This was assumed to be propagated along a row of molecules with the velocity of sound U_s ft./sec. in the liquid. Bridgman obtained the equation

$$k = 3\frac{RU_s}{Nd^2}$$

B.t.u./(hr.) (sq. ft.) (°F./ft.)

Kardos(*8*) in 1934 modified Bridgman's equation to avoid specifying the amount of molecular energy. He considered an energy drop between adjacent molecular surfaces and substituted the distance L between the surfaces of adjacent molecules, instead of the distance d of their centers. He arrived by a reasoning similar to that of Bridgman at the following relation:

$$k = LU_s\rho C_p$$

The difficulty in using this equation lies in the finding of suitable values for the variables involved. Kardos suggested that as a first approximation L be assumed constant and equal to 3.12×10^{-10} ft.

The thermal conductivity of twenty-eight liquids was calculated by use of Bridgman's and Kardos' equations. The average deviation of the calculated from the observed values of thermal conductivity was found to be ±15 and ±23% respectively. The maximum deviation is ±40% and ±104% respectively; hence it would appear that the assumption of a constant L in Kardos' equation is not tenable if reasonably accurate values are required.

The theoretical equation proposed by Kardos will be interpreted on the basis of recent developments, and methods for determining the variables involved given. It will be shown that when the variables involved are properly evaluated the predicted values of thermal conductivity agree well with the values of thermal conductivity observed in this investigation.

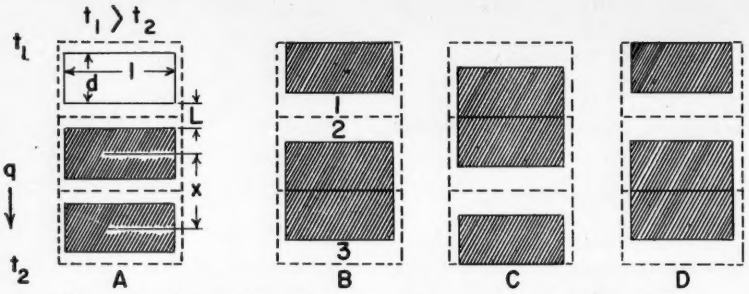

Fig. 1. Heat transfer mechanism with assumed molecular model.

The derivation of an equation for thermal conductivity requires the use of a model of the liquid state and the assumption of a mechanism of heat conduction. The model of liquid state considered here originates from the results of X-ray–diffraction studies of liquids.

BASIC CONCEPTS

The liquid state differs from the gas state in that the individual molecules are affected considerably by the presence of their neighboring molecules. It differs from the solid state in that the molecules have a certain degree of freedom on the macroscopic scale. The setting of a temperature gradient across a liquid layer should result in the formation of isothermal planes of liquid molecules having the same mean energy. This arrangement will cause the molecules to move in the direction of heat flow only. Owing to the large intermolecular forces existing in the liquid state, only a small fraction of the total energy is transferred by individual molecules over relatively long distances. The greater part of energy transfer takes place by the distant action of neighboring molecules, much in the same way that mechanical motion is transferred from point to point along a vibrating network of spheres connected by springs. Further, as a good approximation it can be assumed that on the average the energy transferred in a given time by a molecule moving freely in the direction of heat flow is equal to that transferred by a molecule vibrating about a mean position during the same time. This simplified model is substantially in agreement with the "cybotactic state" proposed by G. W. Stewart and coworkers (*17*) (*see also 14*) for isothermal conditions. G. W. Stewart attributes a "microcrystalline" structure to a liquid by assuming the presence of a large number of "cybotactic groups." These groups are not permanent and do not have sharp boundaries as in a crystal. Rather, over any appreciable time there are a greater number of these groups than of groups having completely disordered arrangement. The more elongated the molecule, as in a chain, the better the arrangement within the groups. The existence of a temperature gradient in a liquid layer should favor such an internal molecular arrangement.

In the case of a long-chain-hydrocarbon liquid, such as *n*-heptane (similar considerations apply to different-shaped molecules), the molecules in the liquid layer are oriented end to end on long chains in a two-dimensional pattern. The chains or layers repeat themselves throughout most of the liquid layer, some chains occasionally being disordered by molecules assuming different orientation; some groups may be broken up and new ones formed.

The process of heat conduction may be visualized as shown in Figure 1. In step *A* the molecules, represented by shaded rectangles, are in an assumed starting position. In step *B* molecule 1 moves toward a hotter molecule and molecules 2 and 3 move toward each other to collide. Molecule 1 on reaching the hotter molecule collides with it, picks up excess energy, and starts back. In step *C* molecule 1 collides with molecule 2, gives up its excess energy, and bounces back toward the hotter molecule again. In step *D* molecule 2 collides with molecule 3, giving up its newly gained excess energy. Steps *B* and *C* are repeated indefinitely. There is little or no lateral motion as adjacent molecules have the same mean absolute energy and the container walls are well insulated.

In Figure 1 the cross-sectional area of the molecules is represented as a rectangle, but no molecule has such sharp-edged boundaries. X-ray diffraction studies of the internal structure of molecules show that the carbon atoms in the molecule are arranged in a zigzag pattern at definite angles and distances apart, with the hydrogen atoms attached at definite positions in the chain. If each atom is visualized not as a point mass, but as distribution of charges in space, the molecule will appear like a rod with rough edges. The space occupied by this rod cannot be penetrated by any other molecule and represents the minimum volume or molecular volume at absolute zero v_o. For purposes of calculation it is easier to represent the minimum volume by a parallelopiped with height and width d equal to the diameter of the rod. The cross section of the molecule then may be represented by a rectangle, as in Figure 1.

At absolute zero the molar volume V_o is simply the sum of the minimum molecular volumes, or

$$V_o = \sum_1^N v_o \qquad (1)$$

As the temperature increases, the molecules begin to vibrate and the molar volume increases. The difference between the molar volume V at a given temperature and that at absolute zero is simply empty space within which the molecules move. As a consequence of the foregoing assumption that the molecules vibrate about fixed equilibrium positions, the available volume $V_a = V - V_o$ will be distributed around the minimum molecular volume, as shown in Figure 1 by dotted lines. It is clear therefore that according to the suggested mechanism of heat conduction, the significant intermolecular distance is the available distance between the molecular surfaces L and not the molecular diameter d.

DERIVATION OF EQUATION

An energy drop of

$$Q = -\left(\frac{dQ/N}{dx}\right)L = -L\left(\frac{dQ/N}{dT}\right)\frac{dT}{dx} \qquad (2)$$

per molecule along a row of molecules in the direction of heat flow, where $x = d + L$, may be considered. If it is assumed that heat is transmitted through the liquid with a velocity equal to the velocity of sound in the liquid U_s, the total energy, passing a fixed point in a row of molecules per unit time, is the product of the energy difference and the number of steps contained in a row U_s ft. long, or

TABLE 1.—COMPARISON OF SOME EXPERIMENTAL VALUES OF THERMAL CONDUCTIVITY WITH VALUES CALCULATED BY THEORETICAL EQUATION (8) AT 68°F.

Liquid	k_{obs}, B.t.u./(hr.)(sq. ft.)/(°F./ft.)	C_p, B.t.u./(lb.)(°F.)	U_s, ft./sec.	ρ, lb./cu. ft.	$L\times10^{-9}$, ft.	k_{calc}, B.t.u./(hr.)(sq. ft.)/(°F./ft.)	% Dev.*
n-Heptane	0.0767	0.526	3786	42.60	0.253	0.0773	+0.8
n-Amyl alcohol†	0.0892	0.560	4111	50.70	0.218	0.0916	+2.7
Octene-2	0.0814	0.503‡	3973‡	45.00	0.249	0.0806	−1.0
n-Octyl acetate	0.0861	0.485‡	4240	54.20	0.207	0.0831	−3.6
Ethyl propionate	0.0850	0.457	3940‡	55.50	0.239	0.0860	+1.2
Ethylene glycol	0.1498	0.575	5490	69.40	0.181	0.1428	−4.9
Glycerol	0.1772	0.570	6249	78.60	0.172	0.1734	−2.2
2, 2-Dimethyl butane	0.0590	0.518	3320‡	40.45	0.231	0.0579	−1.9
i-Propyl alcohol	0.0844	0.596	3900	49.00	0.214	0.0877	+3.9
n-Amyl bromide	0.0633	0.295‡	3720‡	75.90	0.207	0.0621	−1.9
n-Propyl iodide	0.0532	0.205‡	3190‡	109.00	0.210	0.0539	+1.3
n-Amyl chloride	0.0703	0.440‡	3885‡	55.00	0.216	0.0731	+4.0

*Percentage of deviation of calculated from observed values of thermal conductivity.
†For methyl and ethyl alcohol, nitromethane and nitroethane, the molecular length is much smaller than the diameter, and a different molecular arrangement becomes necessary.
‡Estimated values.

$$-L\left(\frac{dQ/N}{dT}\right)\left(\frac{dT}{dx}\right)\left(\frac{U_s}{x}\right)$$

The total energy transfer across unit area is the product of the energy transfer across a single row and the number of rows in unit cross section, or

$$\frac{q}{A} = -L\left(\frac{dQ/N}{dT}\right)\left(\frac{U_s}{x}\right)\left(\frac{dT}{dx}\right)\frac{1}{(yz)} \qquad (3)$$

where yz = cross-sectional area corresponding to the dimension x.

The equation for heat conduction per unit area is stated as

$$\frac{q}{A} = -k\frac{dT}{dx} \qquad (4)$$

Substituting Equation (3) in (4) and solving for thermal conductivity results in

$$k = \left(\frac{dQ/N}{dT}\right)\left(\frac{L}{x}\right)\frac{1}{(yz)}U_s \qquad (5)$$

as by definition

$$\left(\frac{dQ/N}{dT}\right)_p = \frac{MC_p}{N} \qquad (6)$$

where M = molecular weight, lb.
C_p = specific heat at constant pressure. B.t.u./(lb.)(°F.)

Also the molecular volume v is

$$yzx = \frac{M}{\rho N} \qquad (7)$$

where ρ = liquid density, lb./cu.ft. Substituting Equations (6) and (7) in (5) and canceling terms results in

$$k = C_p U_s \rho L \qquad (8)$$

where C_p = specific heat at constant pressure, B.t.u./(lb.)(°F.)
U_s = velocity of sound in the liquid, ft./hr.
ρ = liquid density, lb./cu.ft.
L = available intermolecular distance, ft.
k = thermal conductivity of liquid, B.t.u./(hr.)(sq.ft.)(°F./ft.)

The significance of the intermolecular distance L will be shown by consideration of *n*-heptane.

n-Heptane at 68°F.

Data. $k = 0.0767$ B.t.u./(hr.)(sq. ft.)(°F./ft.), value observed in this investigation
$C_p = 0.526$ B.t.u./(lb.)(°F.)
$\rho = 42.60$ lb./cu.ft.
$U_s = 1.364 \times 10^7$ ft./hr.

Substituting the given data in Equation (8) and solving for L results in

$$L = 0.251 \times 10^{-9} \text{ ft.}$$

X-ray–diffraction studies by G. W. Stewart and coworkers have shown that the diameter of the heptane molecule at about 68°F. is 1.77×10^{-9} ft. (5.40 Å.) This diameter actually corresponds to the dimension x shown in Figure 1, or

$$d + L = 1.77 \times 10^{-9} \text{ ft.}$$

It was stated above that the molecular volume for heptane may be taken as a parallelopiped, or

$$V = \sum_1^N v \qquad (9)$$

and

$$v = \frac{M}{\rho N} = (d + L)\,yz \qquad (7a)$$

where, as

$$z = x = d + L$$

$$v = (d + L)^2 y \qquad (7b)$$

Substituting values in Equation (7a) results in

$$v = \frac{100.20}{42.6\times2.73\times10^{26}} = 8.61 \times 10^{-27} \text{ cu. ft.}$$

and

$$y = \frac{8.61\times10^{-27}}{(1.77\times10^{-9})^2} = 2.752 \times 10^{-9} \text{ ft.}$$

It will be shown in the Appendix that the dimension y is actually equal to the molecular length l, or in other words there is no available volume between the ends of the molecules in a given layer, as if the molecules were arranged in a long continuous chain. If the intermolecular distance L is the only available distance, it should be possible to calculate the minimum molecular volume at absolute zero as follows:

$$v_o = d^2\,l \qquad (10)$$

Hence

$$d = 1.77 \times 10^{-9} - 0.251 \times 10^{-9} = 1.519 \times 10^{-9} \text{ ft.}$$

$$v_o = \left(1.519\times10^{-9}\right)^2\left(2.752\times10^{-9}\right) = 6.35 \times 10^{-27} \text{ cu. ft.}$$

If the density at absolute zero is available, the obtained answer can be checked; however, the results can be checked by a different method if the critical density is known. For n-heptane, $\rho_c = 14.58$ lb./cu.ft. The critical volume is next calculated by Equation (7), or

$$v_c = \frac{100.20}{14.58 \times 2.73 \times 10^{26}} = 25.2 \times 10^{-27} \text{ cu. ft.}$$

The ratio of the critical volume to the volume at absolute zero is

$$m = v_c/v_0 = \frac{25.2 \times 10^{-27}}{6.35 \times 10^{-27}} = 3.965$$

It is important to note that according to van der Waals' equation

$$v_c = 3v_0$$

Further it is found experimentally that v_c is more nearly equal to $4v_0$ than $3v_0$, in agreement with the value calculated above.
Berthelot's equation gives

$$v_c = 4v_0.$$

It is clear then that, if the ratio of the critical volume to the volume at the absolute zero is known, the thermal conductivity of a liquid can be calculated by reversing the illustrated procedure. For the case of n-heptane the ratio m was calculated by a method given in the Appendix and found to be equal to 3.98. By use of this value of m, the thermal conductivity of n-heptane was found to be 0.0773 B.t.u./(hr.)(sq.ft.)(°F./ft.), or 0.8% higher than the observed value.

It should be emphasized that the value of L will vary from liquid to liquid and is a function of temperature, becoming zero at the absolute zero. Kardos erroneously assigned a constant value to it.

Methods of calculating the variables involved in Equation (8) are given in the Appendix.

COMPARISON WITH EXPERIMENTAL VALUES

Equation (8) was used to predict the thermal conductivity of the liquids used in this investigation (*16*). The variables involved were calculated by the methods outlined in the Appendix. Representative results are shown in Table 1.

In the calculation of the thermal conductivity of isomers it was noted that a systematic deviation occurred. This was corrected as follows.

For isomers where $n = 1$, $v_c/v_o = v_c/v_o$ [Equation (20)]—0.23. (*See* Appendix, Table 4.)

For higher values of n the correction is probably $0.23n$, but there are no substantiating data available. The average deviation of the calculated from the observed values of thermal conductivity for forty-two liquids was found to be ±2.6%. The maximum deviation was about ±6%. Considering the errors introduced by the necessity for estimating two or more variables for some liquids, and the purity of the liquids involved, the observed average deviation is satisfactory. The method of calculation is shown by an example:

ILLUSTRATION 1. Calculate the thermal conductivity of propyl acetate at 68°F.

Data $C_p = 0.459$ B.t.u./(lb.)(°F.)
$\rho = 55.40$ lb./cu.ft.
$T_c = 988.5$°R.
$M = 102.13$
$U_s = 3912$ ft./sec.
$\rho_c = 18.42$ lb./cu.ft.
$T_f = 321.0$°R.

Calculation of ratio of critical to minimum molecular volume, v_c/v_o

$$\rho_o/\rho_c = 2\left\{1+\left(\frac{\rho_f/2-\rho_c}{\rho}\right)\left(\frac{T_c}{T_c-T_f}\right)\right\} \quad (20)$$

$$\rho_f = \frac{\omega_f}{\omega_{68°F.}}\rho_{68°F.}$$

$\omega_f = 0.1473$ [Eq. (22)]

$\omega_{68°F.} = 0.1298$ [Eq. 22)]

$\rho_c = 62.95$ lb./cu. ft.

$$\rho_o/\rho_c = 2\left\{1+\left(\frac{62.95/2-18.42}{18.42}\right)\left(\frac{988.5}{988.5-321.0}\right)\right\} \quad \rho_o/\rho_c = 4.09$$

No correction for isomerization.
Calculation of minimum molecular volume, v_0

$$v_o = v_c/4.09$$

$$v_c = \frac{M}{\rho_c N} = \frac{102.13}{2.73\times10^{26}\times18.42} = 20.3\times10^{-27} \text{ cu. ft.}$$

$$v_o = 20.3\times10^{-27}/4.09 = 4.952\times10^{-27} \text{ cu. ft.}$$

Calculation of intermolecular length, L

$$v = x^2 1 = \frac{M}{\rho N}$$

$x = 5.03$Å. $= 1.650 \times 10^{-9}$ ft.

(Table 4)

$$1 = \frac{M}{\rho N x^2} = 2.480 \times 10^{-9} \text{ ft.}$$

$$d = \left(\frac{v_o}{1}\right)^{\frac{1}{2}} = \left(\frac{4.952\times10^{-27}}{2.480\times10^{-9}}\right)^{\frac{1}{2}} = 1.415 \times 10^{-9} \text{ ft.}$$

$$L = x - d$$

$$L = (1.650 - 1.415) \times 10^{-9} = 0.235 \times 10^{-9} \text{ ft.}$$

Calculation of thermal conductivity, k

$$k = C_p U_s \rho L \quad (8)$$

$$k = (0.235 \times 10^{-9})\ (0.459)\ (55.40)\ (3912 \times 3600)$$

$k = 0.0841$ B.t.u./(hr.) (sq.ft.) (°F./ft.)

The observed value is 0.0841 B.t.u./(hr.)(sq.ft.)(°F./ft.)

TEMPERATURE COEFFICIENT OF THERMAL CONDUCTIVITY

The thermal conductivity of a liquid at a temperature other than 68°F. can be predicted by substituting the appropriate values for the specific heat, velocity of sound, and density. The intermolecular distance increases somewhat with increasing temperature, but not so much as would be expected from corresponding density changes. Since the coefficient of thermal expansion for many liquids is about the same, the effect of temperature on the intermolecular distance was determined for a few liquids from the known thermal conductivity, and the result applied to other liquids. It was found that

$$\frac{dL}{dt} = 0.0055 \times 10^{-11} \text{ ft./°F.} \quad (11)$$

Calculated and observed temperature coefficients of thermal conductivity for a few liquids, for which reliable values of the properties involved are available, are presented in Table 2.

TABLE 2.—CALCULATED AND OBSERVED TEMPERATURE COEFFICIENTS OF THERMAL CONDUCTIVITY $dk/dt \times 10^{-4}$, B.t.u. / (hr.) (sq.ft.) (°F./ft.) / °F.

Liquid	Calculated*	Observed
n-Hexane	—1.39	—1.40
n-Heptane	—1.44	—1.30
n-Octane	—1.22	—1.15
n-Propyl alcohol	—0.78	—0.95
n-Amyl alcohol.	—0.78	—0.91
Ethyl acetate...	—1.22	—1.62
2-Methyl pentane	—1.05	—1.00
2, 2, 4-Trimethyl hexane	—1.17	—1.05
Glycerol	+1.00	+0.53
Ethylene glycol.	+0.27	+0.36

*The effect of temperature on the intermolecular distance was estimated by Equation (11).

The calculated and observed temperature coefficients agree fairly well. The coefficients for ethylene glycol and glycerol are positive owing to the small negative temperature coefficient of the velocity of sound.

Since the density, velocity of sound, and specific heat vary linearly with temperature at temperatures sufficiently removed from the melting point, it will be expected that in this region the thermal conductivity will also vary linearly with temperature.

SUMMARY

An equation for predicting the thermal conductivity of pure organic liquids and its temperature coefficient has been derived and has been tested on a large number of liquids. Methods are given for predicting the variables involved where no data are available. The equation is applicable to both normal and associated liquids. The only assumption involved in its derivation is a particular molecular arrangement in the liquid. In the calculation of the intermolecular distance for chain compounds the assumption is made that the molecules are aligned, like rods in a bundle, perpendicular to the direction of heat flow. This arrangement is a good approximation for long-chain molecules. For shorter molecules the disorder increases and the molecular arrangement changes. The method is applicable also to other-shaped molecules. [For ring compounds *see* Part III (*16a*)] Although no data are given at this time, the intermolecular distance for ring compounds is calculated on the assumption that the rings are stacked like coins with their thickness perpendicular to the direction of heat flow. This arrangement is verified by X-ray–diffraction data of liquids and solids. For very small molecules, such as carbon tetrachloride, methyl chloride, and chloroform, the molecular volume is considered as a cube. In this case no X-ray–diffraction data are necessary.

ACKNOWLEDGMENT

This research was conducted under National Science Foundation grants G-221 and 558. The Department of Chemical Engineering and the Engineering Experiment Station of Louisiana State University provided additional funds and facilities.

NOTATION

A = heat transfer area, normal to heat flow, sq.ft.
a = a constant
b = a constant
C_p = specific heat at constant pressure, B.t.u./(lb.) (°F.)
d = mean intermolecular distance, center to center, ft.
d = molecular diameter, ft.
dt = temperature drop, °F.
k = thermal conductivity, B.t.u./(hr.) (sq.ft.) (°F.)
L = mean intermolecular distance, surface to surface, ft.
l = molecular length, ft.
M = molecular weight, lb.
m = ratio of critical to minimum molecular volume
N = Avogadro's number, 2.73×10^{26} molecules/lb.mole
n = effective branching contribution
n = integer representing the order of diffraction
Q = thermal energy, B.t.u.
q = rate of heat flow, B.t.u./hr.
R = gas constant, 1.987B.t.u./(lb. mole) (°R.)
R = additive constant
s = intermolecular distance, Å.
T = absolute temperature, °R.
t = temperature, °F.
t = molecular thickness, ring molecules only, ft.
U_s = velocity of sound, ft./sec.
V = molar volume at a given temperature, cu.ft./lb.mole
v = molecular volume at a given temperature, cu.ft./molecule
x = distance along X axis parallel to the direction of heat flow, ft.
x = sum of molecular diameter and mean intermolecular distance, $d + L$, ft.
x = thickness, ft.
y = distance along Y axis, parallel to the molecular length, perpendicular to the direction of heat flow, ft.
z = distance along Z axis, perpendicular to the molecular length, perpendicular to the direction of heat flow, ft.

Greek Letters

ρ = density, lb./cu.ft.
λ = wavelength of incident radiation, Å.
ϕ = scattering angle at maximum scattering intensity, degrees
ω = expansion factor

Subscripts

a = available
c = critical
f = freezing point
G = gas or vapor
L = liquid
0 = absolute zero
p = pressure
r = reduced

Conversion Factor

$1 Å = 3.28 \times 10^{-10}$ ft.

LITERATURE CITED

1. Bridgman, P. W., *Am. Acad. Arts Sci.*, **49**, 141 (1923).
2. Chow, W. M., and J. A. Bright, Jr., *Chem. Eng. Progr.* **49**, 175 (1953).
3. Compton, A. H., and S. K. Allison, "X-Rays," 2 ed., D. Van Nostrand, New York (1951).
4. Debye, P., and H. Menke, *Forts chr. Röntgenforchung*, 2, 1 (1931).
5. Freyer, E. B., J. C. Hubbard, and D. H. Andrews, *J. Am. Chem. Soc.*, **51**, 759 (1929).
6. Herz, *Z anorg. Chem.*, **153**, 269 (1926).
7. Hougen, O. A., and K. M. Watson, "Chemical Process Principles," Part II, John Wiley and Sons, New York (1948).
8. Kardos, A., *Forsch. Gebiete Ingenieurw.* **5**, 14 (1934).
9. Lagemann, R. T., D. R. McMillan, Jr., and W. E. Woolf, *J. Chem. Phys.*, **17**, 369 (1949).
10. LeBas, *J. Phys. Chem.*, **46**, 380 (1942).
11. Meissner, H. P., and E. M. Redding, *Ind. Eng. Chem.*, **34**, 521 (1942).
12. Michael, G. V., and George Thodos, *Chem. Eng. Progr. Symposium Ser.* No. 7, **49**, 131 (1953).
13. Perry, J. H., ed., "Chemical Engineer's Handbook," 3 ed., McGraw-Hill Book Company, Inc., New York (1950).
14. *Phys. Rev.*, pp. 28-31, **34**, 39 (1927).
15. Rao, R., *Current Sci.* (*India*) **9**, 534 (1940); *Indian J. Phys.*, **14**, 109 (1940) *J. Chem. Phys.*, **9**, 682 (1941).
16. Sakiadis, B. C., and Jesse Coates, *Eng. Expt. Station* Bul. No. 46, Louisiana State University, Baton Rouge (1954).
16*a*. Sakiadis, B. C., and Jesse Coates, "Studies of Thermal Conductivity of Liquid," Part III, to be published.
17. Stewart, G. W., and R. M. Morrow, *Phys. Rev.*, **30**, 232 (1927).
18. Sugden, S., *J. Chem. Soc.*, pp. 1780, 1786 (1927).
19. Telang, *Current Sci.* (*India*), 11, 461 (1942).
20. Timmermans, J., "Physico-Chemical Constants of Pure Organic Compounds," Elsevier Book Co., New York (1950).
21. Tsien, H. S., *J. Am. Rocket Soc.*, **23**, 17, 35 (1953).
22. Watson, K. M., *Ind. Eng. Chem.*, **23**, 360 (1931).
23. *Ibid.* **35**, 398 (1943).
24. Zernicke, F., and J. A. Prins, *Z. Physik.* **41**, 184 (1927).

APPENDIX

Calculation of Variables in Equation (8)

The use of Equation (8) requires reliable values of the variables involved. As few values of the velocity of sound in liquids have been published, it was necessary to survey the literature to develop a satisfactory method for predicting it where no values are available. The calculation of the available intermolecular distance requires X-ray–diffraction data. These data are available but require interpretation for use with Equation (8). Finally a satisfactory method for calculating the ratio of the critical to the minimum molecular volume had to be developed. In all instances it is important to note that the methods of evaluating the variables involved have a theoretical basis.

Specific heat. Reliable values of the specific heat of liquids are difficult to obtain. The most dependable values for a number of liquids have been collected by J. Timmermans (*20*). For other liquids the specific heat may be calculated from the specific heat of the ideal gas by the method proposed by Hougen and Watson (*7*). Chow and Bright (*2*) proposed an empirical method for predicting the specific heat of homologous series of liquids. A new method for calculating the specific heat of liquids at constant volume and at constant pressure has been developed by the authors and will be published later.

Density. Values of the liquid density at 68°F. are readily available. For values at other temperatures reference *20* may be consulted. Where no data are available, the method of generalized liquid densities proposed by Watson (*23*) is recommended.

Velocity of sound. Few values of the velocity of sound in liquids have been published in handbooks. However a literature survey was made by the authors (*16*), and data on a large number of liquids were collected and classified and a number of methods proposed by various investigators for predicting the velocity of sound in liquids are also given.

One of the simplest relations was proposed by Rao (*15*), who pointed out that

$$U_s = \left(\frac{R\rho}{M}\right)^3 \qquad (12)$$

TABLE 3.—STRUCTURAL CONTRIBUTIONS TO THE VELOCITY OF SOUND

Basic Radicals	R
CH_4	9.50
Benzene	23.25
Cyclohexane	27.50
Naphthalene	33.67
Additional Radicals or Atoms	
$-\overset{|}{\underset{|}{C}}-$, $-CH-$, $-CH_2-$, $-CH_3$	4.47
$-C(=O)-O-$	6.25
$-C(=O)-H$	2.30
$-C(=O)-$	4.47
$-NH-$	3.27
$-NH_2$	2.45
$-CO_2H$	4.83
$-C \vdots N$	4.20
$-O-$	1.40
$-OH$	0.70
$-Cl$	3.13
$-Br$	3.55
$-I$, $-NO_2$	4.58
$-S-$, $=S$	2.82
Bonding	
=	−1.30
≡	−2.60
Position	
o—	0
m—	0.30
p—	0.60

He indicated that R is substantially independent of temperature and that it is an additive function of the molecular structure, as in the case of the parachor.

Calculations on a large number of liquids made by the authors indicated that the structural contributions to the velocity of sound as given by Rao had to be modified if the relation was to hold at all. As a result, modified structural contributions were proposed (*16*). Additional work has resulted in a different set of structural contributions to the velocity of sound (*see* Table 3) that appears to correlate the data more satisfactorily. Each compound is considered as composed of a basic group which is modified by the substitution of other groups for atoms comprising it. Hence all liquids having a chain structure are considered as derived from methane. Similarly any compound having a ring is considered as derived from benzene, cylohexane, or naphthalene as the case may be. The contributions of the four basic groups are given in Table 3. The method of calculation will be shown by an illustration.

ILLUSTRATION 1. Calculate the velocity of sound in *m*-chlorotoluene at 68°F.

Formula = m-$CH_3C_6H_4Cl$
Mol. wt. = 126.58
ρ = 66.75 lb./cu.ft.

Base group		
(benzene) ..		23.25
—CH_3	1 × 4.47	4.47
—Cl	1 × 3.13	3.13
m-position		0.30
	R =	31.15

$$U_s = \left(\frac{R\rho}{M}\right)^3 = \left(\frac{31.15 \times 66.75}{126.58}\right)^3 =$$

4,410 ft./sec

The value observed by Lagemann, McMillan, and Woolf (*9*) is 4,324 ft./sec.

The independence of the constant R with temperature will be shown for the case of *n*-heptane

Temp., °F.	$R_{obs.}$*
68	36.70
86	36.70
104	36.70
122	36.72
140	36.75

*Calculated from the data of Freyer, Hubbard, and Andrews (*5*).

The velocity of sound for 135 pure organic liquids of all chemical types was calculated by the authors, using the structural contributions given in Table 3, and it was found that the average deviation from the experimental values was ±2.6%. The maximum observed deviation was ±8.0%. Comparison of experimental values showed that the most reliable values may vary by about 1 to 2%, extreme values vary by about 6%. It must be noted that Equation (12) is applicable to both normal and associated liquids. A semiempirical equation for predicting the velocity of sound for normal liquids only has been proposed by Tsien (*21*).

Intermolecular distance. In order to calculate the available intermolecular distance L, the following variables must be known accurately: x, equal to $d + L$; v_c, critical volume; and v_c/v_0, ratio of critical to minimum molecular volume.

DIMENSION x. The dimension x is determined by X-ray–diffraction measurements. One method of analyzing the results is by using the simple Bragg's law

$$n\lambda = 2s \sin 1/2\phi \qquad (13)$$

The primary normal alcohols exhibit two scattering peaks. One of these has been identified as corresponding to the molecular length l and the other as the molecular diameter x, or distance from center to center of adjacent molecules. Thus for n-amyl alcohol $s_1 = 4.48$ Å.; $s_2 = 13.10$ Å.

The dimension s_1 corresponds to the molecular diameter x and is observed to remain constant from member to member of the series, as expected. The dimension s_2 corresponds to the molecular length and is observed to increase regularly as the number of carbon atoms increases. Actually the dimension s_2 represents two molecular lengths, where the alcohol molecules appear to be arranged in pairs head to head.

Strictly speaking, Bragg's law is applicable only when interference occurs over a large number of regularly spaced layers, as in a crystal. In the case of liquids the number of such layers that may be considered as regularly spaced is probably not large. In the extreme case of only two diffracting centers it has been shown(*3*) that the diffraction maxima occur at

$$\left(\frac{n+1}{n}\right)\lambda = 2s \sin 1/2\phi \qquad (14)$$

This differs from Bragg's law by the factor $(n+1)/n$ and indicates that for a real liquid the correct formula will be intermediate between Equations (13) and (14).

An alternative method, applicable strictly to liquids which consist of spherical molecules, has been developed by Zernicke and Prins (*24*) and Debye and Menke(*4*). This method consists of determining the radial distribution of molecules based upon the observed scattering intensity; however, unless the data have been obtained with high precision over a large range of s values, it may be questioned whether a more reliable value of the spacing is obtained by the radial distribution method than by Bragg's law(*3*). In any case the values found by the two methods differ by only a few per cent.

Since for the calculation of the thermal conductivity it is important to know the molecular diameter x, a survey of literature on scattering of X rays by liquids was made by the authors. The publishing data were recalculated on the basis of the equation

TABLE 4.—MOLECULAR DIAMETER x, Å., OF PURE ORGANIC LIQUIDS FROM X-RAY-DIFFRACTION MEASUREMENTS

at 68° F.

I. Straight-chain molecules

	C_1*	C_2	C_3	C_4	C_5	C_6†
Acids	4.10	4.70	5.00	5.20	→	→
Alcohols	4.30	4.60	5.09	→	→	→
Aldehydes		4.45	5.01	5.20	→	→
Amides	4.13	4.80	5.10			
Amines (mono, di)			5.03	5.20	→	→
Esters			4.91	5.03	→	→
Ethers				5.29		
Halogenated hydrocarbons		4.70‡				
Hydrocarbons						5.40 →
Ketones			5.10	→	→	→
Mercaptans			4.96	5.01		
Nitrated alkanes		4.60**	5.01			
Nitriles		4.43	4.84			

*The subscript indicates the number of carbon atoms in the molecule.
†The arrows indicate that the molecular diameter remains the same for all longer molecules.
‡Methyl iodide.
**Nitromethane.

II. Cyclic compounds (t dimension)*

	t, Å
Benzene, pyridine	5.30
Naphthalene	5.81
Cyclopentane	5.50
Cyclohexane, piperidine	5.73
Cycloheptane	5.86

*The rings are presumed to have disk shapes and to be arranged in stacks. The t dimension refers to the thickness of the disk

III. Branched contributions, straight-chain and cyclic compounds (Substitution of $-CH_3$ group for hydrogen $\Delta x = 0.42n$†)

1. Chain compounds*

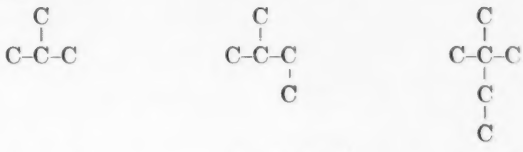

$n = 1$ $n = 1$ $n = 2$

2. Cyclic compounds*‡

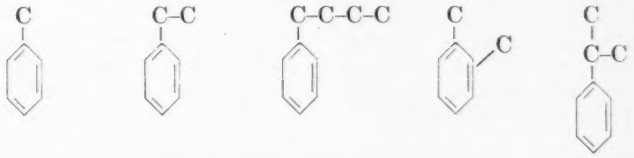

$n = 1$ $n = 1$ $n = 1$ $n = 2$ $n = 2$

*The position of substitution is immaterial, 1- 2, 3, or 0, *m*-, *p*-, etc.
†The letter n refers to the number of substituent $-CH_3$ groups as shown in the illustrations. For example, if two $-CH_3$ groups are substituted in 2, 4- positions as in 2, 4-dimethyl pentane, the effective n is 1, since the molecule is presumed to be rotating, and the swept volume is the same whether one or two $-CH_3$ groups have been substituted. The same applies to the case of 2, 2, 4- dimethyl pentane.
‡The branched contribution should be added to the t dimension.

IV. Substitutions*

Substitution of hydrogen atom by	Δx, Å†	Δx, Å‡
1. NH_2, CHO	0.10	0.80
2. F, I	0.10	
3. OH	0	0.20
4. CN, O (ketone)	0	
5. NO_2	0.50	0.75

*For ring compounds the contributions should be added to the t dimension.
†Single substitution. Substitution in combination with Cl, Br, the position of substitution is immaterial. Substitution in combination with —CHO, $—NH_2$ in *p*-position.
‡Substitution in *o*, and *m*-positions in combination with —CHO, $—NH_2$, —OH.

$$1.14\,\lambda = 2s \sin 1/2\phi \qquad (15)$$

which is intermediate between Equations (13) and (14) for $n = 1$.

Only the molecular diameter x was considered, since the remaining dimensions can be calculated from the geometry of the molecule and the liquid density. Actually many liquids, notably the hydrocarbons, show one diffraction peak only, corresponding to the x dimension.

It may be noted that these dimensions, determined from scattering data, can be used to calculate the liquid density on the basis of the proposed molecular arrangement. For alcohols

$$v = (s_2/2)\, s_1^2 \qquad (7c)$$

and from Equation (7*a*)

$$\rho = \frac{M}{Nv} = \frac{M}{N(s_2/2)s_1^2}$$

For *n*-amyl alcohol

$$\rho = \frac{88.15}{2.73\times10^{26}\ (6.55\times1.14\times3.28\times10^{-10})(4.48\times1.14\times3.28\times10^{-10})^2}$$

$$\rho = 47.0 \text{ lb./cu. ft.}$$

The observed liquid density at 68°F. is 50.7 lb./cu.ft.

The bulk of the literature data is summarized in Table. 4

The intermolecular distances determined from X-ray–diffraction measurements in pure liquids agree well with measurements on monomolecular liquid films and with studies on the structure of micelles formed in soap solutions. They approximate also values obtained from measurements on materials in the solid state. For example

	Liquid x, Å.	Solid x, Å.
Capric acid	5.21	4.79
Lauric acid	5.56	5.04
Palmitic acid	5.50	5.03
Erucic acid	5.45	5.09
Brassidic acid	5.55	5.06
Lauryl alcohol	5.25	4.79

If the effect of temperature is neglected, it will be noted that the dimension x increased on melting. Since for the solid both the x and l dimensions decrease as the temperature approaches absolute zero, it is possible that the length of the molecules as measured in the liquid state represents the minimum possible length. This would mean that the molecules on melting came together forming long chains, thus causing an increase in the dimension x as a result of the redistribution of the available volume.

The effect of temperature on the measured molecular dimensions has not been extensively investigated, but it is relatively small. The estimated accuracy of the values given in Table 4 is ±0.05 Å.

CRITICAL DENSITY, ρ_c. The critical density for a number of liquids is given in reference (*13*), and additional values may be found in *20*. For other liquids Watson's method of generalized liquid densities (*23*) is recommended.

RATIO OF CRITICAL TO MINIMUM MOLECULAR VOLUME, v_c/v_0. A number of empirical methods (*6, 10, 18, 19*) have been proposed for determining the molecular volume at absolute zero. The method presented here is based on the law of rectilinear diameter, according to which the arithmetical average of the densities of a pure unassociated liquid and its saturated vapor (orthobaric densities) is a linear function of the temperature. In equation form

$$\frac{1}{2}(\rho_L + \rho_G) = a - bT \qquad (16)$$

Although not exact, this relation is accurate for many substances and provides a very useful method for calculating the critical density, a quantity not readily measurable.

At absolute zero Equation (16) reduces to

$$\frac{1}{2}\rho_o = a \qquad (17)$$

At the freezing point the density of the vapor is very small and may be neglected, and so Equation (16) reduces to

$$\frac{1}{2}\rho_f = a - bT \qquad (18)$$

At the critical temperature the density of the vapor and liquid is the same and Equation (16) reduces to

$$\rho_c = a - bT_c \qquad (19)$$

Equations (17), (18), and (19) may be combined to eliminate the constants a and b. This results in

$$\rho_o/\rho_c = 2\left\{1 + \left(\frac{\rho_f/2 - \rho_c}{\rho_c}\right)\left(\frac{T_c}{T_c - T_f}\right)\right\} \qquad (20)$$

Equation (20) gives the ratio of the critical to minimum molecular volume v_c/v_0 from a knowledge of the critical density and temperature, density at freezing point, and freezing temperature.

In these calculations the freezing density was determined by Watson's relation (*23*)

$$\rho_f = \left(\frac{\rho_{68°F.}}{\omega_{68°F.}}\right)\omega_f \qquad (21)$$

The expansion factor was calculated by the equation (*23*)

$$\omega = 0.1745 - 0.0838\,T_r \qquad (22)$$

for $T_r < 0.65$. Values of the critical temperature will be found in the same tables giving the critical density. Other values for hydrocarbons may be estimated by the method of Michael and Thodos (*12*). Values for other liquids may be estimated by the method proposed by either Watson (*22*) or Meissner and Redding (*11*).

Equation (20) was found to be applicable for both normal and associated liquids. A few values will be given as an example:

Liquid	Method of Measurement	$v_c/v_{o\ obs.}$	$v_c/v_{o\ calc.}$ [Eq. (20)]
n-Pentane	Density*	3.80	3.82
Ethyl alcohol	Gas law	4.02	3.94
Ethyl alcohol	Compressibility†	4.10	3.94
Ethyl ether	Compressibility†	3.91	3.89

*The lowest density measured was 47.9 lb./cu. ft. at 246°R. This value was extrapolated to 0°R.
†The volume at absolute zero may be regarded as given by the limiting volume of a liquid under infinite pressure, which can be calculated from the compressibility. In the case of liquids, at 68°F. and 11,600 atm. the reduction in volume is about 30%. Hence the density at 0°R. is obtained by ρ 68°F., 1 atm ÷ 0.70.

Presented at A.I.Ch.E. New York meeting

Fundamentals of the Hydrodynamic Mechanism of Splitting in Dispersion Processes

J. O. Hinze, Royal Dutch Shell-Laboratory, Delft, Holland

The splitting of globules is an important phenomenon during the final stages of disintegration processes. Three basic types of deformation of globules and six types of flow patterns causing them are distinguished.

The forces controlling deformation and breakup comprise two dimensionless groups: a Weber group N_{We} and a viscosity group N_{Vi}. Breakup occurs when N_{We} exceeds a critical value $(N_{We})_{crit}$. Three cases are studied in greater detail: (a) Taylor's experiments on the breakup of a drop in simple types of viscous flow, (b) breakup of a drop in an air stream, (c) emulsification in a turbulent flow.

It is shown that $(N_{We})_{crit}$ depends on the type of deformation and on the flow pattern around the globule. For case (a) $(N_{We})_{crit}$ shows a minimum value ~ 0.5 at a certain value of N_{Vi} and seems to increase indefinitely with either decreasing or increasing ratio between the viscosities of the two phases. For case (b) $(N_{We})_{crit}$ varies between 13 and ∞, depending on N_{Vi} and on the way in which the relative air velocity varies with time, the lowest value refers to the true shock case and $N_{Vi} \to 0$. For case (c) $(N_{We})_{crit}$, which determines the maximum drop size in the emulsion, amounts to ~ 1, and the corresponding values of N_{Vi} appear to be small. A formula is derived for the maximum drop size.

Efficient dispersion with a view to obtaining large interfacial areas is of great importance for heat and mass transfer processes in gas-liquid systems (atomization, froth-formation) and liquid-liquid systems (emulsification).

Most of the ordinary diminution processes function by injection of one phase into the other or by inducement of turbulence in the continuous phase. In the case of injection the potential energy of the phase to be dispersed is converted into kinetic energy, and at the same time usually interaction takes place with another medium, which may be gaseous, liquid, or solid. This interaction generates forces in the phase to be dispersed which may result in its breaking up. In the case of turbulence it is the kinetic energy of the turbulent motion in the continuous phase that brings about the breakup of the other phase.

In general the disintegration process takes place in stages. When one fluid is just squirted into another or when stirring processes have just started, the fluid to be dispersed is at first present in bulk. The deformation of this bulk of fluid and its initial breakup into chunks of fluid, which may break up further into smaller parts, has been much studied (*8, 6, 4*). There seems to be a mechanism that is common to such disintegration of liquids, to emulsification, and to atomization, namely the penetration of lamellae and ligaments of one fluid into the other. These ligaments then break up into globules, which may further split up into smaller parts.

When parts of a drop are separated or when a long ligament breaks up into droplets, in most cases secondary small droplets are also formed. Moreover, the ligaments at the moment of breakup will in general not all be equally thick. Hence during these disintegration processes drops of different sizes are formed. As the sizes seem to depend on many uncontrollable conditions, at present it is practically impossible to predict theoretically the final size distribution of a dispersion. Of course this does not exclude the possibility of making predictions from empirical correlations.

Concerning the various stages of disintegration processes, important contributions have already been made by theoretical and experimental studies of the instability of liquid films and cylindrical liquid ligaments and of the breakup of drops (*6, 15*). These theories can be applied to some simple types of atomization, but for the reasons stated above they still fail to describe quantitatively "chaotic" disintegration processes. More knowledge is required concerning the detailed mechanisms of breaking-up processes, as for instance the splitting up of small fluid lumps of the dispersed phase during the final stages of disintegration. For this case an attempt is made in the present paper to systematize the various ways in which single globules can break up. These considerations are applied to the breakup of globules in a viscous flow, to drops exposed to an air flow, and to emulsification in turbulent flow. In these few cases it appears possible to obtain an expression for the average value of the maximum globule size that can withstand the forces of a known hydrodynamic flow field.

BASIC TYPES OF GLOBULE DEFORMATION AND FLOW PATTERN

Globules can split up owing to hydrodynamic forces in a number of different ways that depend on the flow pattern around them. In general the following three basic types of deformation (illustrated in Figure 1) can be recognized.

Type 1. The globule is flattened, forming in the initial stages an oblate ellipsoid (lenticular deformation). How deformation proceeds during the subsequent stages leading to breakup seems to depend on the magnitude of the external forces causing the deformation. One possibility is that the drop deforms into a torus, which, after being more or less stretched, breaks into many small droplets.

Type 2. Here the globule becomes more and more elongated, forming in the initial stages a prolate ellipsoid, until ultimately a long cylindrical thread is formed, which breaks up into droplets (cigar-shaped deformation).

TABLE 1.—POSSIBLE CONDITIONS FOR BREAKUP OF A GLOBULE

Type of deformation	A. Dynamic pressures			B. Viscous stresses		
	Flow pattern around the globule					
1. Lenticular ..	(*a*) Parallel	(*c*) Axisymm. hyperbol.	(*e*) Rotat.	(*a*) Parallel	(*c*) Axisymm. hyperbol.	(*e*) Rotat.
2. Cigar-shaped	(*b*) Plane hyperbol.	(*d*) Couette		(*b*) Plane hyperbol.	(*d*) Couette	
3. Bulgy	(*f*) Irregular					

Type 3. As the surface of the globule is deformed locally, bulges and protuberances occur, and thus parts of the globule become bodily separated (bulgy deformation).

Of the various flow patterns that may cause a globule to deform in one of these basic ways, those considered here are given in Figure 2. In addition an irregular flow field *f* as occuring in turbulent flow is considered. For the rotating flow pattern *e* it is assumed that the fluid rotates bodily. It is further assumed that the flow patterns considered are large compared with the globule size but are still local flow patterns in the entire flow field. Finally one may distinguish between deformation by external dynamic pressures and that by viscous stresses. The possible combinations of flow patterns and types of deformation, or more precisely the most important of the possible ways in which a globule can be broken up by hydrodynamic forces, are given in Table 1. Thus it is expected that deformation of type 1 will occur if the globule is subjected to the dynamic pressures or viscous stresses produced by the parallel flow *a*, the axisymmetric hyperbolic flow *c*, and the rotating flow *e*. Type 2 deformation (cigar-shaped deformation) can be caused by the plane hyperbolic flow *b* and the Couette flow *d*, and type 3 (bulgy deformation) is brought about only by the dynamic pressures occurring in the irregular flow pattern *f*.

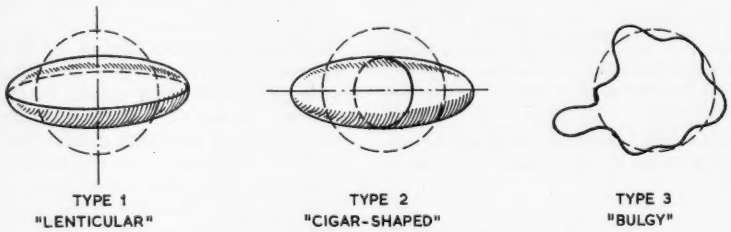

Fig. 1. Basic types of globule deformation.

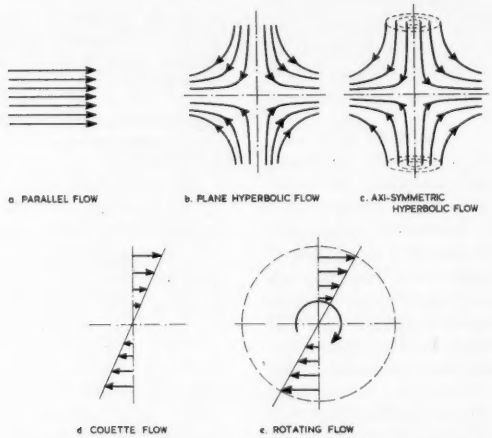

Fig. 2. Flow patterns that can cause one of the basic types of globule deformation.

Breakup will occur if there is a sufficient degree of deformation, that is, if the region of the flow pattern causing a specific deformation is sufficiently large to contain the deformed globule and if the flow pattern persists long enough.

Various possibilities may be considered somewhat more closely.

Lenticular Deformation in Parallel Flow. Here the globule has a translatory motion relative to the ambient fluid. This motion will persist longer if the density of the globule is much greater than that of the ambient fluid. An example of the dynamic case *A1a* (*see* Table 1) is the bursting of a drop in an air flow. If the flow is viscous (case *B1a*), the tangential viscous forces on the interface cause a torodial internal circulation, shown theoretically by Hadamard (*7*) and experimentally by Garner (*5*), which produces at the interface normal forces that in conjunction with the external normal component of the viscous stresses tend to deform the globule.

Lenticular Deformation in Rotating Flow (Cases *A1e* and *B1e*). The globule is assumed to be in a region where the ambient fluid rotates about an axis coinciding with that of the globule. Also here it will in general be necessary to have an appreciable difference in density in order to make the centrifugal forces sufficiently great to bring about breakup of the globule.

Cigar-shaped Deformation in Plane Hyperbolic Flow (Cases *A2b* and *B2b*). The elongation occurs along that axis in the plane of the flow in which the direction of the velocity is away from the origin.

Cigar-shaped Deformation in Couette Flow. In the dynamic case *A2d* the pressure distribution on the globule causes initially an elongation along an axis at 45° to the direction of flow. After this, pressure distribution on the elongated globule will cause further elongation and also a slight rotation, until the elongated globule has reached a position in which only continued elongation with eventual breakup can take

place. In the viscous case *B2d* the tangential forces at the interface cause internal circulation. The normal components of the viscous forces cause the globule to deform into an ellipsoid. The axes of the ellipsoid fall in the principal planes of the stress distribution of the shear flow (that is, the planes with no tangential stress). Also here, after sufficient elongation, breakup may occur.

The third type of deformation takes place if local presure differences at the interface (flow pattern *f*) cause initial bulges which, helped perhaps by a general parallel flow past the globule, may develop into protuberances, which may then possibly split up.

We thus see that a preference for a given type of deformation and breakup depends not only on the local flow pattern around the drop, but also on the physical properties of the two phases, namely their densities, viscosities, and interfacial tension.

In atomization the possibilities *A1a* and *A2d* will be the ones most frequently encountered; sometimes also *A3f* will be possible.

In the case of gas dispersion in liquids (froth-formation), more particularly if the liquid is in violent turbulent motion, the following conditions will often occur: *A1c*, *A2b*, *A2d*, *A1e*, and *A3f*.

In emulsification processes it is reasonable to expect the conditions *B2b* and *B2d*, with the odds on *B2d*, to occur in viscous flows; whereas in turbulent flows the conditions *A1c*, *A2b*, *A2d*, and *A3f* may occur, with the odds perhaps on *A2d*.

FORCES CONTROLLING THE SPLITTING UP OF A GLOBULE

An isolated globule will be considered on the surface of which external forces act in such a way as to cause a deformation of the globule. τ is this force per unit surface area; in general it will vary along the surface and will be a function of time. It may be a viscous stress or a dynamic pressure set up in the surrounding continuous phase.

Owing to the deformation of the globule, internal flows are set up that cause viscous stresses as well as dynamic pressures. Furthermore the interfacial tension σ will give rise to a surface force that will in general counteract the deformation. If D is the diameter of the globule, the surface-tension force will be of the order of magnitude σ/D. In the first instance the dynamic pressure will be of the same order of magnitude as τ, causing flow velocities of the order of magnitude $(\tau/\rho_d)^{\frac{1}{2}}$. Thus the viscous stresses are of the order of magnitude

$$\frac{\mu_d}{D}\sqrt{\frac{\tau}{\rho_d}}$$

where μ_d and ρ_d are the viscosity and density of the globule.

These three forces per unit area

$$\tau,\ \sigma/D,\ \text{and}\ \frac{\mu_d}{D}\sqrt{\frac{\tau}{\rho_d}}$$

control the deformation and breakup of the globule. The ratio between each two of these forces is a dimensionless magnitude. Three dimensionless groups may be formed in this way, only two of which are independent.

For one of the dimensionless groups the combination $N_{We} = \tau D/\sigma$, a generalized Weber group, was chosen. The qualification "generalized" was added because, strictly speaking, the Weber group usually refers to $\rho U^2 D/\sigma$ where ρU^2 is the dynamic pressure of a fluid flow.

For the other dimensionless group either

$$\frac{\mu_d}{\sigma}\sqrt{\frac{\tau}{\rho_d}}\ \text{or}\ \frac{\tau D}{\mu_d}\sqrt{\frac{\rho_d}{\tau}} = \frac{\rho_d D}{\mu_d}\sqrt{\frac{\tau}{\rho_d}}$$

may be chosen, the latter being the Reynolds group. However, since the two groups contain the external force τ, the ratio between these two groups was preferred. It contains only the properties of the globule

$$N_{Vi} = \frac{\mu_d}{\sqrt{\rho_d \sigma D}},\ \text{a viscosity group.}$$

This group is called a viscosity group because it accounts for the effect of the viscosity of the fluid in the globule.

Of course the two groups N_{We} and N_{Vi} will immediately result from applying formal dimensional analysis and taking into account the magnitudes τ, D, σ, μ_d, and ρ_d.

The greater the value of N_{We}, that is, the greater the external force τ compared with the counteracting interfacial-tension force σ/D, the greater the deformation. At a critical value $(N_{We})_{crit}$, breakup occurs.

Experiments have shown that the mechanism of breakup is quite simple when N_{We} is equal to or slightly higher than $(N_{We})_{crit}$. The more N_{We} exceeds its critical value, the more complicated this mechanism becomes. For $N_{We} >> (N_{We})_{crit}$ this mechanism is very complex, and the disintegration process is more or less chaotic. This subject will be considered when the bursting of a drop in an air stream is described.

If the breakup of a globule is one of the final stages of a general disintegration process, then usually the N_{We} for breakup does not greatly exceed the critical value, and so the mechanism of breakup remains the simple type.

Since the deformation process can be described in terms of the two dimensionless groups, in general, $(N_{We})_{crit}$ will be a function of N_{Vi}. For this relation the following form is chosen

$$(N_{We})_{crit} = C[1 + \varphi(N_{Vi})] \quad (1)$$

where the function φ decreases to zero when $N_{Vi} \to 0$. In this form C is the value of We_{crit} for vanishing viscosity effect of the globule liquid. In this relation C and φ are still dependent on the external conditions, since the force τ is determined by the flow conditions in the continuous phase around the globule, which can also be described in terms of other dimensionless groups. The $(N_{We})_{crit}$ will be different for the three basic types of deformation and will also be dependent on the local flow pattern around the globule.

If the flow pattern is the same throughout the entire flow region, all globules larger than their critical size will break up according to the same mechanism. For all these globules the same value of $(N_{We})_{crit}$ is valid.

In more complicated flow fields where locally and temporarily different flow patterns of varying flow velocities occur, as for instance when the continuous phase is in turbulent motion, the $(N_{We})_{crit}$ will not be the same for all the globules present in the flow field. Some statistical mean value of $(N_{We})_{crit}$ will then determine the average size of the largest globules that can still withstand the breakup forces of the flow field. To arrive at this statistical mean value a higher weight must be assigned to those flow patterns and types of deformation which produce a lower value of $(N_{We})_{crit}$.

DEFORMATION OF GLOBULES IN VISCOUS FLOW

Fundamental work on the splitting up of drops in viscous flow was done by Taylor (*16*) and Tomotika (*18*). Taylor developed a theory based upon a few obvious assumptions, such as small deformations, no slip at the interface, and con-

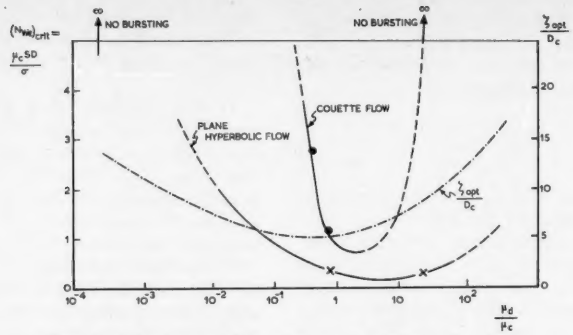

Fig. 3. $(N_{We})_{crit}$ and S_{opt}/D_c as functions of μ_d/μ_c.

tinuous shear stress across the interface. He considered two types of flow, namely the Couette flow (type *d* of Figure 2) and the plane hyperbolic flow (type *b* of Figure 2).

Because of the shear flow of the continuous phase the originally spherical drop is deformed into an ellipsoid (basic type 2), the cases *B2b* and *B2d* of Table 1.

According to Taylor's theory the deformation of the globule is predominantly determined by the generalized Weber group.

$$N_{We} = \frac{\mu_c S D}{\sigma},$$

where S is the maximum velocity gradient in the flow field of the continuous phase.

In two apparatuses which simulate the Couette flow and the plane hyperbolic flow respectively, Taylor has studied the deformation of a single drop as a function of S; he determined the value of S at which the breakup of the drop occurs, that is, $(N_{We})_{crit}$. This has been done with liquids that show the following ratios between the viscosities:

$$\frac{\mu_d}{\mu_c} = 0.0003, 0.5, 0.9, \text{and } 20.$$

Throughout the experiments the viscosity of the continuous phase was essentially the same, namely about 100 c.g.s. units.

The few data of Taylor's experiments are given in Figure 3. They show that in all cases a drop bursts more easily in the plane hyperbolic flow than in the Couette flow. If [$(N_{We})_{crit}$ for hyperbolic flow]/[$(N_{We})_{crit}$ for Couette flow] is determined, the curves in Figure 3 seem to indicate a maximum value of about 0.4 at $\mu_d/\mu_c \sim 1$. For both types of flow a minimum value of $(N_{We})_{crit}$ of less than 1 is obtained at a value of $\mu_d/\mu_c > 1$ (roughly at 5).

In the case of the Couette flow Taylor observed the remarkable fact that at $\mu_d/\mu_c = 20$ there was no breakup of the drop; the drop was only slightly deformed and showed a slow rotation in the direction of flow. Such a rotation, however, cannot occur in the plane hyperbolic flow; indeed, in that flow breakup did ultimately occur.

In neither type of flow was there any breakup at all during the experiments at the viscosity ratio $\mu_d/\mu_c = 0.0003$, even at the highest rates of flow applied. This result can be explained by the results of Tomotika's theoretical investigations (*17*). He considered the stability of an infinitely long cylindrical column of a viscous liquid surrounded by another viscous liquid when subjected to disturbances of rotational symmetry. He found that the optimum wave length ζ_{opt}, at which the rate of increase of the disturbance is at its maximum, increases to infinity if the viscosity ratio μ_d/μ_c becomes either infinite or zero. This means that the chance of the breakup of a drop deformed into a cylindrical thread is very slight at those extreme viscosity ratios.

The values of ζ_{opt}/D_c, where D_c is the diameter of the cylindrical thread, are also given in Figure 3. Apparently a minimum value of ζ_{opt} occurs at $\mu_d/\mu_c = 0.28$, that is, at $\mu_d/\mu_c < 1$. Hence, for the same diameter of the column the smallest drops caused by the breakup of the column are obtained at this viscosity ratio.

If the energy necessary to deform the drop is neglected, the power input must be equal to the dissipation in the flow of the continuous phase. This dissipation per unit mass ε is equal to $\mu_c S^2/\varrho_c$ for the Couette flow, and to $4\,\mu_c S^2/\varrho_c$ for the plane hyperbolic flow.

From Figure 3 it may be concluded that the energy input required to break a given drop reaches its minimum at $\mu_d/\mu_c > 1$. But in view of the results obtained by Tomotika (*17, 18*) it is possible that smaller drops are formed at a $\mu_d/\mu_c < 1$. One can estimate from Figure 3 that the energy input required for breaking the same drop is smaller for the hyperbolic flow than for the Couette flow.

Although it would be very desirable to have more data available from experiments such as those carried out by Taylor, yet it is possible to draw conclusions, albeit with some reserve, from his few experimental results:

1. It will be very difficult to disperse fluids that show a high viscosity ratio. This becomes obvious if one considers the extreme cases: dispersion of gas bubbles in viscous liquid flow, and dispersion (atomization) of liquid drops in viscous gas flow. This explains why in practice dispersion by pure viscous flow is restricted to emulsification processes.
2. For a given energy input per unit time and mass of the continuous phase, the drop that can resist the shear flow without breaking will be smaller if the liquid with the greater viscosity is the dispersed phase ($\mu_d/\mu_c > 1$).
3. A dispersion in which $\mu_d/\mu_c < 1$ can contain a larger fraction of small drops than one in which $\mu_d/\mu_c > 1$, although for the same energy input the largest drops may be larger; that is, the dispersion may be less uniform.

If relation (1) is applied to the results given in Figure 3, the assumption that at least C must be a function of μ_d/μ_c, becoming infinite for $\mu_d/\mu_c \to 0$ and probably also for $\mu_d/\mu_c \to \infty$, is obvious. The function φ may also increase indefinitely with increasing N_{Vi}. If $(N_{We})_{crit}$ is plotted against N_{Vi}, the minimum value for $(N_{We})_{crit}$ is obtained at rather high values of N_{Vi}, namely 100 and more. From the relation between $(N_{We})_{crit}$ and μ_d/μ_c one may conclude that the minimum value of $(N_{We})_{crit}$ will occur at lower values of N_{Vi} as the viscosity of the continuous phase decreases.

BREAKUP OF A DROP IN AN AIR STREAM

Investigation into the bursting of drops in an air stream has a long history, dating to before 1904, when Lenard published his experiments (*14*). Shortly after World War I Hochschwender made similar experiments (*11*), and in recent years drop deformation and breakup have been studied both experimentally and theoretically (*2, 9, 10, 12, 19, 20*) in various countries.

If a drop exposed more or less suddenly to a parallel air flow (flow

pattern *a* of Figure 2) is considered for not too small drops and for a relative air velocity sufficiently great to bring about breakup of the drop, the Reynolds number for the flow around the drop will in general be sufficiently great for the external dynamic pressure forces to overshadow the external viscous forces. The external forces can then be expressed in terms of $\rho_c U_o^2$, where ρ_c is the density of the continuous phase and U_o the maximum value of the air velocity relative to the drop. In this case the Weber group has its original notion:

$$N_{We} = \frac{\rho_c U_o^2 D}{\sigma}.$$

Hinze(*9, 10*) has shown theoretically that $(N_{We})_{crit}$ depends not only on N_{Vi} but also on the way in which the relative velocity varies with time. Two cases have been studied by the various investigators, namely that of the true shock exposure and that of the falling drop. $(N_{We})_{crit}$ turns out to be much smaller for the first case.

For $N_{Vi} = 0$ and true shock exposure $(N_{We})_{crit} \simeq 13$, whereas for a falling drop $(N_{We})_{crit} \simeq 22$(*10*). $(N_{We})_{crit}$ increases with increasing N_{Vi}. Figure 4 shows results of laboratory experiments studying this effect of the viscosity of the drop on its breakup. Figure 4 also shows theoretical curves for the case of true shock exposure. These two theoretical curves refer to the cases of slight viscosity effect and great viscosity effect respectively. For great viscosity effects, which occur when $N_{Vi} > 0.5$, the rate of deformation is so low that the relative air velocity decreases substantially during the process of deformation and breakup, and so consequently do the breakup forces. Theoretical considerations show (*see* Figure 4) that $(N_{We})_{crit} \to \infty$ for indefinitely increasing N_{Vi}. The experimental results seem to indicate that already at $N_{Vi} > 2$ breakup will cease.

All investigators of the mechanism of breakup observed that during the breakup process the drop passes in succession through the stages of extreme flattening, formation of a torus with attached hollow-bag—shaped film of increasing size, bursting of the film, and breakup of the torus. Experiments at Delft showed that this mechanism still remains even for large effects of the drop viscosity.

Lane(*12*) was the first to draw attention to the fact that at

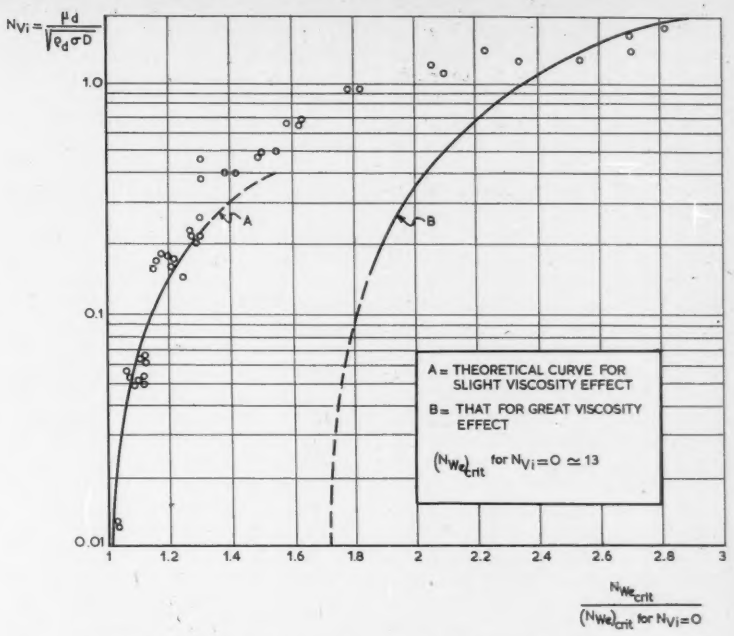

Fig. 4. Effect of N_{Vi} on $(N_{We})_{crit}$ in the case of a drop suddenly exposed to an air stream.

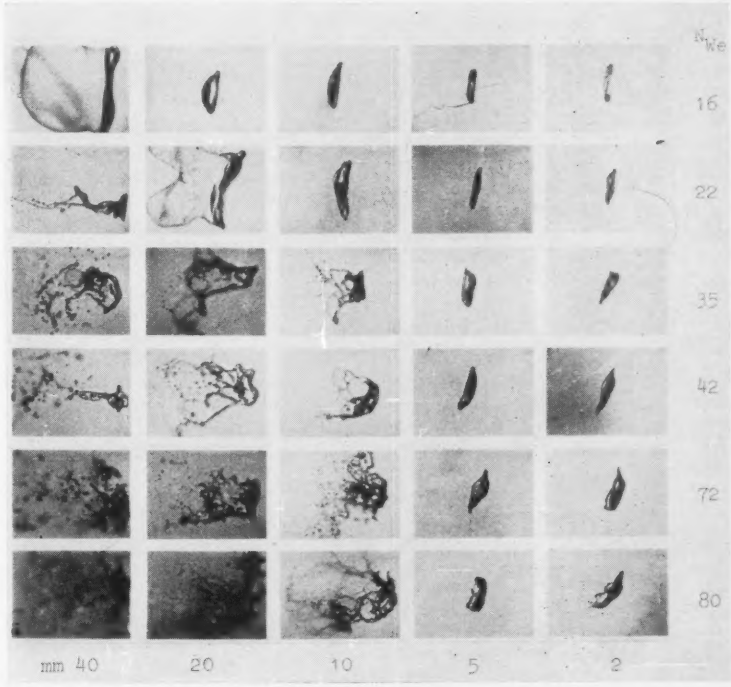

Fig. 5. Short-flash photographs showing the breakup of a drop at increasing values of N_{We}. Gas oil; $D = 3.9$ mm.; $(N_{We})_{crit} \simeq 13$.

$N_{We} >> (N_{We})_{crit}$ the mechanism of breakup is different from the one just described. Figure 5 shows a series of short-flash photographs taken during the Delft experiments of drops launched in a horizontal air flow. With increasing N_{We} the nature of breakup changes in the direction of a more chaotic disintegration process. One may notice that the shape of the bulk of the drop during the initial stages of deformation is different for the two mechanisms. In the case of the first mechanism, that is at low N_{We}, the drop during deformation has the convex part directed downstream, whereas in that of the second mechanism, at large N_{We}, the the convex part is directed upstream. The nonuniform pressure distribution along it causes an acceleration of the drop. The acceleration forces acting on the fluid particles of the drop produce a deformation in addition to that caused along the drop by the pressure distribution, which is assumed to be steady. The first kind of deformation mentioned above is more comformable to the pressure distribution along the drop alone, whereas the second kind is more comformable to what might be expected of the acceleration effects alone. Moreover for $N_{We} >> (N_{We})_{crit}$ a kind of stripping off of the drop surface takes place owing to waves and ripples generated there.

Although the transition from the first mechanism to the second with increasing N_{We} is more or less gradual, it appears possible to introduce a second critical N_{We} pertaining to this transition. An analysis of the experimental results concerning this second critical N_{We} shows it to be a quite complicated function of the dimensionless groups N_{Vi}, N_{Re} pertinent to the flow around the drop, and ρ_d/ρ_c.

EMULSIFICATION IN TURBULENT FLOW

The dispersion of one liquid into another as the result of keeping the latter in violent turbulent motion is restricted here to the case of emulsification under noncoalescing conditions, which can be realized, for instance, by taking low concentration of the dispersed phase so that the chance of coalescing, in so far as it is determined by statistical mechanical conditions, is very slight.

More or less unconsciously guided by the mechanism observed by Taylor in viscous shear flow, investigators have commonly believed hitherto that also in turbulent flow splitting up of drops is the result of viscous shearing action (*4, 16*). However, a first requisite for such breakup of drops is that not only the undeformed drop, but also the elongated drop, must be small compared with the local regions of viscous flow. For not too small values of the Reynolds number the spatial dimensions of such local regions are very small, compared at least with the largest drops observed in the emulsion. Hence it is more logical to assume that the dynamic pressure forces of the turbulent motions are the factor determining the size of the largest drops. These dynamic pressure forces are caused by changes in velocity over distances at the most equal to the diameter of the drop. In regard to the area just around the drop, the plane hyperbolic, the axisymmetric and Couette flow patterns are the ones most likely to be responsible for breaking up the largest drops (compare the possibilities *A2b*, *A1c*, and *A2d* of Table 1). The kinetic energy of a turbulent fluctuation increases with increasing wave length. Thus velocity differences due to fluctuations with a wave length equal to $2d$ will produce a higher dynamic pressure than those due to fluctuations with a shorter wave length. If these fluctuations are assumed to be responsible for the breakup of drops, for $(N_{We})_{crit}$ in the relation (1) may be placed

$$(N_{We})_{crit} = \frac{\rho_c \overline{v^2} D_{max}}{\sigma},$$

where $\overline{v^2}$ is the average value across the whole flow field of the squares of velocity differences over a distance equal to D_{max}. To relate this average kinetic energy to this distance, one considers the simplest case, namely an isotropic homogeneous turbulence. For this case of turbulence the main contribution to the kinetic energy is made by the fluctuations in the region of wave lengths where the Kolmogoroff energy distribution law is valid. In this region the turbulence pattern is solely determined by the energy input ϵ per unit mass and unit time. It can be shown that for this region

$$\overline{v^2} = C_1 (\epsilon D)^{2/3}$$

where $C_1 \simeq 2.0$ according to Batchelor (*1*).

If for the moment one assumes that $N_{Vi} << 1$, then one obtains from 1:

$$\frac{\rho_c D_{max}}{\sigma} C_1 (\epsilon D_{max})^{2/3} = \text{const}$$

or

$$D_{max} \left(\frac{\rho_c}{\sigma}\right)^{3/5} \epsilon^{2/5} = C \qquad (2)$$

This simple result also follows directly from dimensional reasoning once it has become evident that only the quantities ρ_c, σ, and ϵ determine the size of the largest drops.

If this result is to be applied to fields of nonisotropic turbulent flow, it must be assumed that the turbulence pattern is practically isotropic in the region of wave lengths comparable to the size of the largest drops. Indeed, many actual, nonisotropic, turbulent flows do show an energy spectrum the high-energy part of which can often be approximated by the Kolmogoroff spectrum (*13*).

Furthermore, nonisotropic turbulent flows are not usually homogeneous, and so the energy input and dissipation are not constant across the flow field; moreover there is no equilibrium between energy input and dissipation at

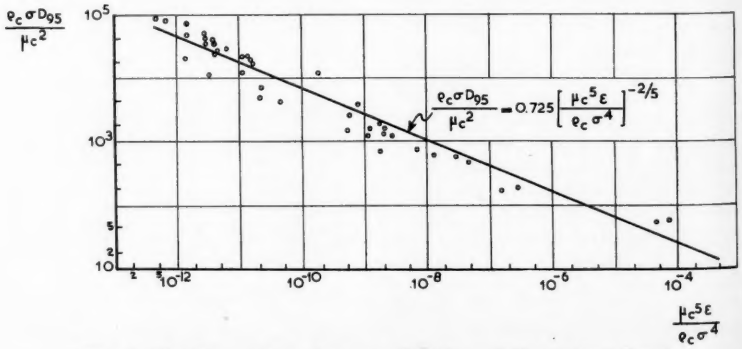

Fig. 6. Maximum drop size as a function of the energy input according to experimental data by Clay.

each point. In this case, even if local isotropy is present, the drop size as determined by (2) is still a function of the space coordinates.

If in the emulsifying apparatus the flow field is not too inhomogeneous, the powerful diffusive action of turbulence causes the average size of the largest drop in the whole field to correspond to the average energy input across this field.

With these assumptions formula (2) has been applied to the results obtained by Clay (*3*) with his model arrangement consisting of two coaxial cylinders, the inner one of which rotated. Clay determined drop-size distributions and from these calculated the value of D_{95}; this is the value for which 95% by volume is contained in the drops with $D<D_{95}$. If one takes $D_{max}\simeq D_{95}$ and applies the theory to this D_{95}, one obtains for (2):

$$D_{max}\left(\frac{\rho_c}{\sigma}\right)^{3/5}\epsilon^{2/5}=0.725$$

with a standard deviation of 0.315.

Figure 6 shows that notwithstanding the wide scatter the data follow pretty well the relation (2). In this figure the relation is written:

$$\frac{\rho_c\,\sigma\,D_{95}}{\mu_c^2}=0.725\left[\frac{\mu_c^5\,\epsilon}{\rho_c\sigma^4}\right]^{-2/5} \qquad (3)$$

An appreciable scatter of test data is quite usual in phenomena with processes governed by statistical laws, but the very large scatter obtained here is most probably due to the rather crude way in which the drop-size distributions were obtained, which made the determination of D_{95} very inaccurate.

It would be interesting to know how far the relation (3) is applicable to other emulsifying apparatus. If the flow field is not too inhomogeneous (for instance, if there is emulsification by turbulence in pipe flow) the relation might well be applied; but in stirring apparatus, with paddles and the like, the intensity of turbulence will vary appreciably, being highest close to the paddles. Although perhaps the maximum drop size may still follow roughly the -2/5 law of the energy input, it is reasonable to expect a much smaller value at least for the numerical constant.

From the relation (3) it is possible to calculate the value of $(N_{We})_{crit}$. This, of course, will be a statistical mean value. If one substitutes $\overline{v^2}=2.0(\epsilon D_{max})^{\frac{2}{3}}$ in the expression $(N_{We})_{crit}=\rho_c\overline{v^2}\,D_{max}/\sigma$, one obtains $(N_{We})_{crit}=2.0\rho_c\epsilon^{2/3}D_{max}^{5/3}/\sigma$; thus with the empirical relation (3): $(N_{We})_{crit}=2.0(0.725)^{5/3}\simeq 1.18$. This value of roughly 1.2 is nearer to the value pertinent to the breakup of a drop in viscous shear flow, that is, according to type 2, than to that found for the breakup in a parallel air flow, that is, according to type 1.

Calculation of the values of N_{Vi} pertinent to D_{95} showed that in all cases N_{Vi} was smaller than 0.3 and in most cases even smaller than 0.1. Obviously the duration of the fluctuating turbulence forces that were responsible for the breakup of drops larger than D_{max} was too short to allow of an appreciable viscosity effect.

CONCLUDING REMARKS

In three cases of the breakup of drops, namely that in a viscous shear flow, that in an air flow, and that in a turbulent flow, it has been shown that there may be various mechanisms of breakup in dispersion processes and that $(N_{We})_{crit}$ will then be different too. Apparently $(N_{We})_{crit}$ is appreciably smaller in breakup according to deformation type 2 than in breakup according to the other types of deformation. The difference in density between the dispersed and the continuous phase has an important effect on the way in which breakup occurs.

Thus if one wants to apply values for $(N_{We})_{crit}$ obtained in one way to other dispersion processes, one has first to make sure that there is not a basic difference between the two dispersion processes; if there is, incorrect results might be obtained. This has too often not been realized.

ACKNOWLEDGMENT

The author expresses his thanks to N. V. De Bataafsche Petroleum Maatschappij (Royal Dutch Shell Group) for permission to publish this paper. He also wishes to thank his coworkers J. Groenhof, J. W. de Fluiter, and M. P. W. van Leerdam, who carried out the experimental part of the investigations in the laboratory.

NOTATION

D = globule diameter, cm.
D_{max} = largest drop size, cm.
D_{95} = value of D for which 95% by volume is contained in the drops with $D<D_{95}$, cm.
D_c = diameter of cylindrical thread, cm.
S = maximum velocity gradient in external flow field, sec.$^{-1}$
$\overline{v^2}$ = average value of square of difference in turbulence velocity, sq. cm./(sec.)^2
U = relative velocity with respect to globule, cm./sec.
U_o = maximum value of U, cm./sec.
τ = surface force per unit area, dyne/sq.cm.
σ = interfacial tension, dyne/cm.
μ = absolute viscosity, g./(cm.)(sec.)
ρ = density, g./cm.^{3}
ζ_{opt} = optimum wave length (cm.)
ϵ = energy input per unit mass and time, or dissipation per unit mass, sq.cm./sec.^{3}
N_{Vi} = viscosity group $=\mu_d/\sqrt{\rho_d\sigma D}$
N_{We} = Weber group $=\tau D/\sigma$, or $\rho_c U_o^2 D/\sigma$, or $\rho_c\overline{v^2}D/\sigma$
$(N_{We})_{crit}$ = critical value of N_{We} for breakup

Subscripts

c = continuous phase
d = dispersed phase

c.g.s. units are used.

LITERATURE CITED

1. Batchelor, G. K., *Proc. Cambridge Phil. Soc.*, 47, 359 (1951).
2. Blanchard, D. C., *Trans. Am. Geophys. Union*, 31, 836 (1950).
3. Clay, P. H., *Proc. Roy. Acad. Sci. (Amsterdam)*, 43, 852, 979 (1940).
4. Clayton, W., "The Theory of Emulsions and Their Technical Treatment," p. 481, 5 ed., J. and A. Churchill, Ltd., London (1954).
5. Garner, F. H., *Trans. Inst. Chem. Engrs. (London)*, 29, 315 (1951).
6. Giffen, E., and A. Muraszew, "The Atomization of Liquid Fuels," Chapman and Hall, Ltd., London (1953).
7. Hadamard, J., *Compt. rend.*, 152, 1735 (1911).
8. Hinze, J. O., Sixth Intern. Congress Appl. Mech., Paris (1946).
9. Hinze, J. O., *Appl. Sci. Research*, A1, 263 (1948).
10. *Ibid.*, 273 (1948).
11. Hochschwender, E., Ph.D. thesis, Univ. Heidelberg (1949).
12. Lane, W. R., *Ind. Eng. Chem.*, 43, 1312 (1951).
13. Laufer, J., *Natl. Advisory Comm. Aeronaut., Tech. Note* 2954 (1953).
14. Lenard, P., *Meteor. Zs.*, 21, 249 (1904).
15. Squire, H. B., *British J. Appl. Phys.*, 4, 167 (1953).
16. Taylor, G. I., *Proc. Roy. Soc. (London)*, A146, 501 (1934).
17. Tomotika, S., *Proc. Roy. Soc. (London)*, A153, 302 (1936).
18. *Ibid.*, A150, 322 (1935).
19. Volynsky, M. S., *Repts. Acad. Sci. U.S.S.R.*, 62, No. 3 (1948).
20. *Ibid.*, 68, No. 2 (1949).

Presented at A.I.Ch.E. New York meeting

Efficiency and Capacity Factors in Lube Extraction

J. R. Felix and C. H. Holder, Esso Research and Engineering Company, Linden, New Jersey

Premium-grade lubricating oils can be manufactured by phenol extraction of high-grade lube feed stocks. Aromatics of low viscosity index dissolve preferentially in the continuous phenol phase to form an extract, and paraffins and naphthenes of high viscosity index are relatively insoluble and form a discontinuous raffinate phase. Contacting is done in multistage plate-type towers using countercurrent flow between stages and cocurrent flow within stages. Phenol is recovered from both raffinate and extract for recirculation to the system. The process is very versatile and with relatively minor variations in process conditions is used to process stocks ranging from light napthenic base oils having a viscosity of 37 SSU at 210°F. to paraffinic premium-grade motor-oil bright stocks having a viscosity of 200 SSU at 210°F.

The results reported here were obtained during an experimental program aimed at increasing the contacting efficiency and capacity of the towers used in the extraction step. Factors considered are the effects of extraction temperature and interstage entrainment on extraction efficiency and of phase physical properties on capacity.

EFFICIENCY STUDIES

Definition of Extraction Efficiency

A simple, accurate measure of stage efficiency was needed to interpret the laboratory data and since some of the experimental work was done in a single-stage unit, the efficiency used had to be translated to multistage commercial towers.

Earlier work in these laboratories showed that refractive index (R.I.) was a good measure of lube-oil quality—viscosity index or paraffin plus naphthene content of the oil increasing with decreasing R.I. Thus the removal of aromatics is related to the decrease in R.I. of the raffinate oil as it passes through a stage. Efficiency measurements were therefore based on this inspection. Stage efficiency was defined as the ratio of the R.I. decrease actually obtained in the stage to that obtained by batch contacting to equilibrium at stage temperature, feed oil, and phenol in the same volume proportions as fed to the stage. This ratio was called "cocurrent" efficiency, defined as

$$\eta_c = \frac{I_F - I_R}{I_F - I_R^*} \qquad (1)$$

Commercial-tower contacting ability is commonly expressed as over-all and/or Murphree efficiency. A relationship between these and the cocurrent efficiency was needed to relate results from the experimental single-stage unit to commercial extractors. The relation between Murphree and over-all efficiencies has been derived(*3*) and for lube extraction is given by

$$\eta_o = \frac{\log\left[1 + \eta_M\left(\frac{s}{m} - 1\right)\right]}{\log\left(\frac{s}{m}\right)} \qquad (2)$$

The relationship between cocurrent and Murphree efficiencies is given by

$$\eta_M = \frac{\eta_c}{1 + \left(1 - \eta_c\right)\frac{s}{m}} \qquad (3)$$

This expression in conjunction with Equation (2) relates the cocurrent and over-all efficiencies, a plot of the relationship being shown in Figure 1.

Equations (2) and (3) are based on straight operating and equilibrium lines. Study of a large number of lube extraction diagrams based on refractive index has shown that this requirement is fairly well approximated in many commercial extractions, at least over sections of the extractor.

Temperature Effect on Efficiency

Lube extraction plants generally process feed stocks of widely different viscosities in a single tower, and it was recognized qualitatively that extractor efficiency tended to be lower on high-viscosity stocks. This was studied to get a more quantitative effect of temperature and, hence, viscosity on extraction efficiency. Three lube-base stocks of different origin covering a wide viscosity range were used. Physical inspections on these oils are given in Table 1.

A single-stage extractor was used in the work, and a schematic diagram of it and the auxiliary

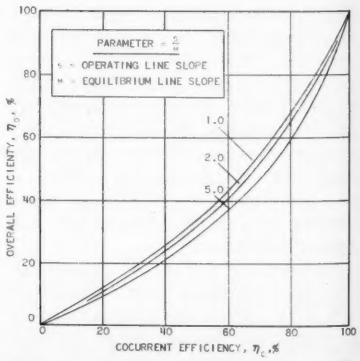

Fig. 1. Over-all and cocurrent efficiencies.

TABLE 1.—FEED STOCKS USED IN TEMPERATURE STUDIES

Feed stock	Gravity, °A.P.I.	Viscosity @ 100° F. SSU	Viscosity @ 100° F. Centistokes
Light Coastal	27.9	80	25.5
Canadian	25.7	160	34.3
Venezuelan	19.6	100 @ 210° F.	20.5 @ 210° F.

equipment is shown in Figure 2. The extractor was 4 in. thick with 20- by 30-in. glass front and rear faces with spotlights placed at the rear to permit observation of phase flows. Phenol was introduced to the stage through an internal downcomer; oil entered the stage just downstream of the downcomer outlet. Both phases then flowed through the mixing section of the stage and into the settling section. Phase mixing was caused entirely by the density difference between the phases. The vertical baffle in the mixing section and the oil-feed arrangement were the same in this series of experiments. Oil and phenol were fed to the

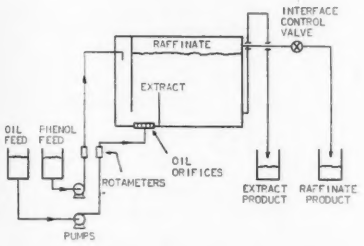

Fig. 2. Extraction equipment.

unit with small gear pumps, flow rates being measured with calibrated rotameters. The oil was saturated with phenol prior to being fed to the unit to avoid the indeterminate effect which saturation within the stage would have on efficiency and to simulate partially operation of an intermediate tray in a commercial tower. Phenol was the continuous phase. The volume of oil holdup in the mixing section of the stage was measured by withdrawing a sample of total mixing-zone liquid through a sampler tube installed so that it might be swung across the mixing zone area at any stage height. These samples were allowed to settle at stage temperature and the fraction of oil phase was then obtained.

Table 2 lists the various temperatures and operating conditions used in the work together with phase physical properties and measured efficiencies. These data show that efficiency is increased by extracting at higher temperatures. With Venezuelan stock, for example, going from 139° to 200°F., at otherwise constant conditions, increased the efficiency nearly twofold. The effect of oil-phase viscosity on efficiency is illustrated by comparing the run on the Canadian oil at a volume flow ratio of 1.5 (line 2) with that on the Venezuelan oil at 139°F. (line 6). The change in raffinate viscosity from 7.7 to 31.5 centistokes caused a reduction in efficiency from 69 to 37%. The data illustrate also that the oil holdup in the mixing zone is an important variable. Comparison of the first two runs on the Canadian oil (lines 2 and 3) shows that increasing the oil holdup from 14 to 24% gave an increase in efficiency from 69 to 88%. The oil holdup was found to be dependent upon the oil rate, the volume flow ratio of phenol to oil, and the oil content of the extract phase.

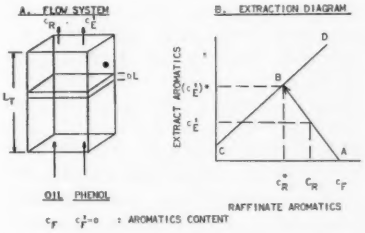

Fig. 3. Cocurrent extraction system.

To assist in understanding these results and to extrapolate them to conditions not directly measured, the extraction system was analyzed by assuming that back mixing of the oil and phenol did not occur in the mixing zone. Observation of the flow pattern in the cocurrent mixing zone indicated this to be approximately correct. It was assumed also that the extraction in the single stage could be represented by considering only the transfer of aromatics from the paraffins plus naphthenes to the phenol and that a straight equilibrium line existed over the limited concentration change in the stage. With these assumptions, the system can be represented by Figures 3 *a* and 3*b*.

With reference to Figure 3*a*, the aromatics transferred from raffinate oil to phenol in the length dL are given by

$$-R\,dc = K_R\,aA\,(c - c^*)\,dL \quad (4)$$

Rearranging and integrating over the mixing-zone height L_T with constant K_R and R give

$$-\int_{c_F}^{c} \frac{dc}{c - c^*} = \frac{K_R a A L_T}{R} \quad (5)$$

For a straight equilibrium line, CD in Figure 3*b*,

$$c' = mc^* + b_1 \quad (6)$$

By an aromatics material balance from the stage inlet to height L,

$$c' = (R/E)\,(c_F - c) = s\,(c_F - c) \quad (7)$$

where s is the slope of the operating line AB in Figure 3*b*.

For oil drops of average diameter D and a fractional oil holdup in the mixing section of f the drop surface area per unit volume of mixing zone is

$$a = \left(\frac{6f}{D}\right) \quad (8)$$

It was assumed further that the major mass transfer resistance was in an oil film at the surface of the drop, and so the over-all mass transfer coefficient K_R was equal to the oil film coefficient k_R. This latter coefficient, in turn, was considered to be related to the oil-phase physical properties by a power function of the form:

$$k_r = b_2\,(v_o)^{b_3} \quad (9)$$

This simplification is limited to extraction systems having the same general physical properties, for example interfacial tension. Substitution of Equations (6) through (9) into Equation (5) gives

$$-\int_{c_F}^{c_R} \frac{cd}{c\left(1+\frac{s}{m}\right) - \left[\left(\frac{s}{m}\right)c_F - b_1/m\right]} = \frac{6b_2 f A L_T\,(v_o)^{b_3}}{DR} \quad (10)$$

The integral in Equation (10) can be evaluated to give a function of the cocurrent efficiency η_{oc}. Direct integration of the left-hand side of Equation (10) gives

$$\int_{c_F}^{c_R} f(c)\,dc = \left(\frac{1}{1+\frac{s}{m}}\right) \ln\left[\frac{c_F + (b_1/m)}{c_R + (b_1/m) - \left(\frac{s}{m}\right)(c_F - c_R)}\right] \quad (11)$$

From Figure 3*b*

TABLE 2.—VISCOSITY EFFECT ON EFFICIENCY

Feed stock	Extraction conditions: Oil rate, bbl./hr./sq. ft.*	Temp., °F.	Mix.-zone oil holdup, %	Vol. flow ratio, phenol to oil	Phase viscosity, centistokes† Raffinate	Extract	Cocurrent efficiency, %
Light Coastal	15.9	78	14	1.0	12.8	6.8	53
Canadian	15.9	141	14	1.5	7.7	3.1	69
	15.9	141	24	0.5	7.7	3.1	88
	5.0	145	7	1.0	7.2	2.9	79
	16.5	150	28	1.0	6.7	2.7	91
Venezuelan	11.9	139	12	1.0	31.5	3.0	37
	11.9	155	12	1.0	18.2	2.4	44
	11.9	200	14	1.0	9.1	1.3	70

* Based on mixing zone area.
† At extraction temperature.

$$c_E^* = mc_R^* + b_1 = s\,(c_F - c_R^*)$$

or

$$\frac{s}{m} = \frac{c_R^* + \dfrac{b_1}{m}}{c_F - c_R^*}$$

and

$$\eta_c = \frac{c_F - c_R}{c_F - c_R^*}$$

From these definitions of s/m and η_c there results

$$\left(1 + \frac{s}{m}\right) = \frac{c_F + \dfrac{b_1}{m}}{c_F - c_R^*} \qquad (12)$$

$$\left(1 + \frac{s}{m} - \eta_c\right) = \frac{c_R + \dfrac{b_1}{m}}{c_F - c_R^*}$$

Hence if the ln term in Equation (11) is divided through by $(c_F - c_R^*)$, and Equation (12) and the definition for η_c are substituted there results:

$$\int_{c_F}^{c_R} f(c)\,dc = \left(\frac{1}{1 + \dfrac{s}{m}}\right) \ln \frac{1}{1 - \eta_c} \qquad (13)$$

Substituting (13) into (10) and rearranging to solve for η_c give

$$\eta_c = 1 - e^{\dfrac{-b_4\left(1 + \dfrac{s}{m}\right) fAL_T (v_o)^{b_3}}{R}};$$

where

$$b_4 = \frac{6b_2}{D} \qquad (14)$$

Equation (14) is the result used in interpreting the experimental data in Table 2. Superficial oil contact time is given by fAL_T/R. Hence directionally a decrease in oil rate, an increase in mixing-zone area or height, or an increase in the fractional holdup of oil will increase extraction efficiency. As pointed out above, additional studies have shown that for lube-phenol systems, the fractional oil holdup f depends on the oil and phenol flow rate and the oil content of the phenol phase. Since f and c_3 depend on the physical properties of the extraction system and the dispersion method used, quantitative results from Equation (14) will depend on the specific physical and mechanical system under study; however, the general approach used to interpret the data is believed to be generally applicable and could be applied to other extraction systems.

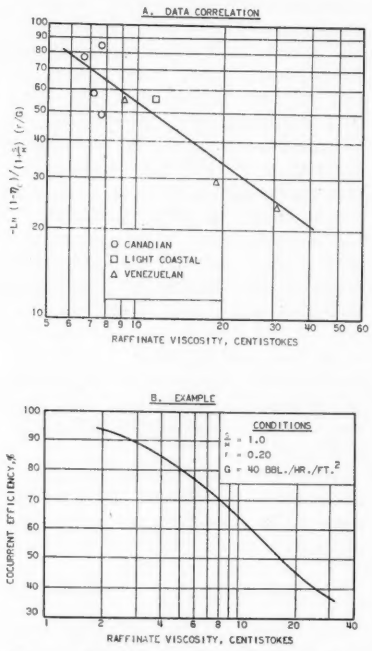

Fig. 4. Efficiency increased by reducing oil-phase viscosity.

Rearrangement of (14) gives

$$-\frac{\ln(1-\eta_c)}{\left(1+\dfrac{s}{m}\right)(f/G)} = (b_4 L_T)\,(v_o)^{b_3} = b_5\,(v_o)^{b_3} \qquad (14a)$$

where G = the oil flow rate per unit of mixing-area cross section. By Equation (14a), a plot of the left-hand side vs. μ_o on log-log paper should yield a straight line. Figure 4a shows the data of Table 2 plotted in this manner. The agreement of the data with theory is considered satisfactory in view of the assumptions made in the analysis. That oil-phase viscosity may control in lube extractions is indicated by this analysis as the efficiency data of Table 2 are not correlated by the efficiency function if plotted vs. the phenol-phase viscosity.

The large effect of temperature and hence viscosity on efficiency is shown more clearly in Figure 4b. This plot was prepared for an s/m value of unity, a mixing-zone oil holdup of 20%, and an oil-flow rate of 40 bbl./hr./sq.ft. In the range of oil-phase viscosities greater than 4 centistokes, a 50% reduction in viscosity for these conditions will increase cocurrent efficiency by about 16%, for example, from 50 to 66% efficiency.

Interfacial tension between phases also affects stage efficiency by affecting drop size. With lube-phenol systems the interfacial tension is relatively constant at about 2.5 to 4.0 dynes/cm. and so oil drop diameters are relatively constant at about 1/16 to ⅛ in. To extend the range of interfacial

tension, phenol was extracted from kerosene with water. Table 3 shows the extraction efficiency obtained in comparison with that for a typical lube-phenol system under comparable extraction conditions and with the same extractor. The relatively low lube efficiency was due to the use of a stage arrangement somewhat different from that used in the temperature-efficiency work.

The large drop size and low mixing-zone oil holdup caused by the high interfacial tension of the kerosene-water system reduced the available surface area and holding time more than enough to counterbalance the greater turbulence in the large kerosene drops. Efficiency was therefore reduced.

Table 3.—Extraction Efficiency Reduced by High Interfacial Tension

System	Lt. Coastal oil-phenol	Kerosene-water
Oil viscosity, SSU @ 80° F.	69	33
Interfacial tension, dynes/cm.	3.1	17.0
Mixing zone oil holdup, %	17	6
Oil drop size (approx.), in.	1/16–1/8	1/4–1/2
Cocurrent efficiency, %	44	25

EFFECT OF ENTRAINMENT ON EFFICIENCY

In any extraction, entrainment of internal phases occurs if the settling capacity of the stage is exceeded. This becomes critical in certain lube extractions where the phenol and lube stock form slow separating emulsions. The entrainment will affect the contacting efficiency of the stages.

A brief literature review showed no estimate for the effect of dual-phase entrainment on efficiency in liquid extraction. Accordingly, an expression was derived to estimate the relative effect of raffinate phase entrainment vs. extract phase entrainment and to set some limit on the amount of entrainment to be tolerated in an extraction without seriously affecting over-all tower efficiency.

The following major assumptions were made in deriving the result:

1. The equilibrium and operating lines are linear.
2. Equal entrainment occurs in all internal stages.
3. The stages operate at 100% efficiency.
4. Oil solubility is constant in each phase.

The extraction system assumed in the derivation is shown in Figure 5. The normal raffinate flow from stage n is accompanied by entrained extract and recycle raffinate carried into the stage by incoming extract; similarly, the normal extract flow from stage $(n+1)$ is accompanied by entrained raffinate and recycle extract carried into stage $(n+1)$ by stage-n raffinate. For perfect stages the entrained phase from any stage will be in equilibrium with the main flow of the other phase in that stage. If it is assumed that oil refractive indexes are additive on a volumetric basis, the following balance can be written around the top of the extractor and stage n:

$$(X+\epsilon_x Y)\, I_n S_x + \epsilon_y X I'_n S_y = R I_N S_R + (Y+\epsilon_y X)\, I'_{n+1} S_y + \epsilon_x Y I_{n+1} S_x \quad (15)$$

Division of Equation (15) by $(S_y Y)$, S_x and S_y being assumed constant, with the ratio $(S_x X/S_y Y)$ called s and the ratio (S_x/S_y) called R_s, gives

$$s I_n + I_n \epsilon_x R_s + I'_n \epsilon_y \left(\frac{s}{R_s}\right) = s I_N + I'_{n+1} I'_{n+1}\, \epsilon_y \left(\frac{s}{R_s}\right) + I_{n+1}\, \epsilon_x R_s \quad (16)$$

For a linear equilibrium line with the R.I. coordinates chosen to make this line go through the origin,

$$I'_i = m I_i, \text{ for the } i \text{ th stage.} \quad (17)$$

Substitution of (17) into (16) with rearrangement gives

$$I_{n+1} - A\, I_n = B I_N \quad (18)$$

where

$$A = 1 + \frac{1}{\epsilon_f}\left(\frac{s}{m} - 1\right)$$

$$B = -\frac{s}{m\epsilon_f}$$

$$\epsilon_f = \left(1 + \frac{\epsilon_y s}{R_s} + \frac{\epsilon_x R_s}{m}\right)$$

Equation (18) is a first-order, linear difference equation which can be solved (2) to give

$$I_n = b_1 (A)^n + \frac{B I_N}{1-A} \quad (19)$$

The boundary condition on Equation (19) is that at the feed stage the raffinate-oil refractive index equals that of the feed. Thus

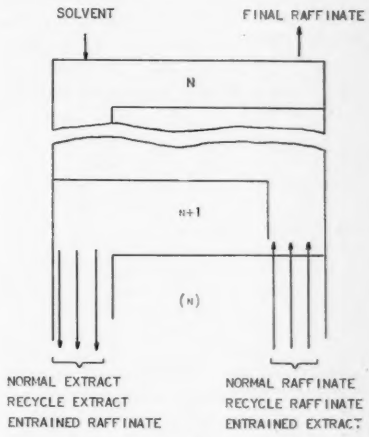

Fig. 5. System for phase entrainment.

$$I_n = I_F \text{ for n} = 0$$

Substitution of this condition into Equation (19) gives

$$b_1 = I_F - \left(\frac{B I_N}{1-A}\right)$$

Substituting this value for b_1 into Equation (19) and setting $n = N$, where N is the top stage of the entrained extractor, gives after rearrangement

$$\frac{I_F - I_N}{I_F} = \frac{(1-A-B)\,(1-A^N)}{(1-A) - B\,(1-A^N)} \quad (20)$$

The result in Equation (20) can be expressed in terms of only the (s/m) ratio and the entrainment factor ϵ_f by substitution of the definitions for A and B. This substitution gives

$$\frac{I_F - I_N}{I_F} = \frac{1 - \left[1 + \frac{1}{\epsilon_f}\left(\frac{s}{m} - 1\right)\right]^N}{1 - \left(\frac{s}{m}\right)\left[1 + \frac{1}{\epsilon_f}\left(\frac{s}{m} - 1\right)\right]^N} \quad (21)$$

Solving Equation (21) for N with $(I_F - I_X)/I_F = \phi$ gives

$$N = \frac{\log \dfrac{(\phi - 1)}{\left(\dfrac{\phi s}{m} - 1\right)}}{\log\left[1 + \dfrac{1}{\epsilon_f}\left(\dfrac{s}{m} - 1\right)\right]}$$

If no internal entrainment occurs and the extractor operates on the same feed to produce the same final raffinate, the number of theoretical stages required will be

$$N_t = \frac{\log \dfrac{(\phi - 1)}{\left(\dfrac{\phi s}{m} - 1\right)}}{\log\left(\dfrac{s}{m}\right)}$$

as $\epsilon_f = 1.0$.

Hence, if the efficiency of an internally entrained extractor is defined as the ratio of the number of theoretical stages needed for a given feed improvement to those needed when internal entrainment occurs, the efficiency will be

$$\eta_a = N_t/N = \frac{\log\left[1 + \dfrac{1}{\epsilon_f}\left(\dfrac{s}{m} - 1\right)\right]}{\log \dfrac{s}{m}},$$

$$\frac{s}{m} \neq 1.0 \qquad (22)$$

If $s/m = 1.0$, the efficiency follows from Equation (21) by differentiating both numerator and denominator with respect to s/m and evaluating at $s/m = 1.0$. Doing this and solving for efficiency, as above, gives

$$\eta_a = \frac{1}{\epsilon_f}, \quad \frac{s}{m} = 1.0 \qquad (23)$$

where ϵ_f is the entrainment factor. A plot of Equations (22) and (23) is shown in Figure 6.

An estimate of the effect of phase entrainment on the extraction efficiency by use of Equation (22) with typical plant values for the variables is shown in Table 4. For this typical lube extraction the efficiency of a perfect stage decreases rapidly with increase in entrainment in either stream, and simultaneous entrainment in both streams is very serious. The calculation shows also that efficiency is most reduced by entrainment in the extract.

TABLE 4.—EXTRACTION EFFICIENCY REDUCED BY ENTRAINMENT

Operating conditions
Oil in raffinate (S_x), vol. % = 88
Oil in extract (S_y), vol. % = 20
Equilibrium line slope (m), average = 2.5
Operating line slope (s), average = 2.3

A. Entrainment in one phase

Entrainment in	Extract				Raffinate			
Amount entrained, %	2	5	10	20	2	5	10	20
Over-all efficiency, %*	96	91	83	69	99	97	94	88

B. Entrainment in both phases

Entrainment, %, in			
Extract	5	10	5
Raffinate	10	5	15
Over-all efficiency, %*	87	81	84

*Over-all efficiency = apparent efficiency.

The results are only directional for an actual stage which operates at less than 100% efficiency when running entrainment free. It is probable that they do set a limit on the harmful effect of entrainment, as the efficiency of an actual stage would be expected to be less affected by a given amount of entrainment as the unentrained efficiency of the stage decreased. It would appear, therefore, that up to about 5% entrainment in the extract or 10% entrainment in the raffinate would not seriously reduce the efficiency of an actual stage in typical lube extraction service.

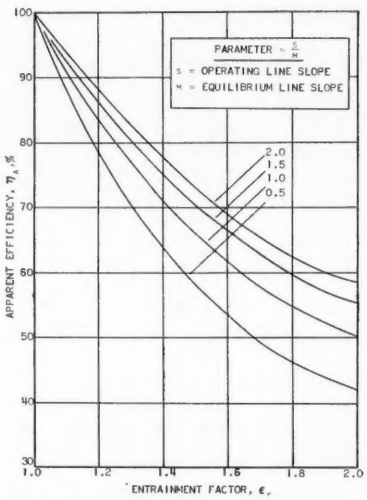

Fig. 6. Effect of internal entrainment on efficiency.

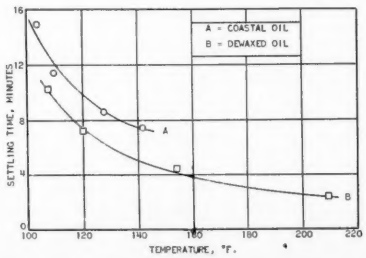

Fig. 7. More rapid separation of phases at higher temperatures.

CAPACITY STUDIES

Maximum stage efficiency, though very desirable, is not the sole criterion of the performance of a commercial extraction tower. Tower capacity, or the maximum flow rates that can be successfully handled without entrainment, must also be considered for a true rating of over-all tower performance. These factors are interrelated, as the presence of entrainment shows that the capacity has been exceeded, and entrainment decreases efficiency. For high capacity the intimate mixture of phases in the mixing section of the stage must separate quickly, and this separation depends on the phsyical properties of the phases and the flow pattern in the settling section of the stage. For a given stage design the physical properties will govern capacity.

Temperature Effect

An arbitrary, though quantitative, test of the settling characteristics of lube-phenol systems was devised to study the effects of phase viscosity and differential density. Equal volumes of phenol and oil were put in a small graduate and mixed with a standard stirrer for a fixed number of strokes while the graduate was maintained at constant temperature. This mixing gave an intimate mixture, or "emulsion," of oil droplets in phenol. The time required for the emulsion to settle into two clear phases was used as a measure of the ease of separation of the phases.

The effect of temperature on the rapidity of phase separation was in-

TABLE 5.—CAPACITY INCREASED BY HIGHER EXTRACTION TEMPERATURES

Type of run	Low temperature	High temperature
Tower top temperature, °F.	180	215
Tower bottom temperature, °F.	160	195
Phenol-water content, vol. %	6.2	8.5
Phenol treat on feed, vol.%	124	124
Final extract-oil content, vol.%	15.8	15.3
Maximum oil rate without entrainment, gal./hr.	0.5 to 0.8	2.0
Settling time, min., in Stage:		
9 (second from top)	6	3
2	8	4

vestigated by getting settling-test data at various temperatures on a wide variety of lube-phenol systems. The oil content of the extract, or phenol phase, was maintained constant at 25 vol. % by varying the phenol water content. Phase viscosity was estimated on the assumption that fluidities were additive on a volume basis. The rapid decrease in settling time associated with increasing temperature, illustrated for two of these stocks in Figure 7, indicates that higher capacity should result with higher extraction temperatures.

The temperature effect was tested experimentally in a 20-stage pilot plant extractor(*1*). For the test work a paraffinic base stock was used which had a gravity of 18.7° A.P.I. and a viscosity of 225 SSU at 100°F. The extractor was operated with a total of ten stages and a final extract oil content of 15%. Extractor feed rate was increased at two temperature levels, while the raffinate quality was maintained, until the entrained oil phase appeared in the final extract. Agitation speed was kept constant in these runs. Results of these tests are shown in Table 5.

With the higher extraction temperature, oil throughput was increased about threefold. As the phenol treat was held constant, the extractor over-all capacity increased by this same amount. It is seen that the increased capacity was accompanied by a decrease in the settling time of the internal tower phases. The results of this study coupled with the effects of temperature on extraction efficiency indicate that extraction temperature is a powerful variable in lube-oil extractions.

Effect of Physical Properties

The settling-test data were generalized by considering that the settling characteristics of the systems could be represented by Stokes' Law. Expressed in terms of the time required to settle a fixed distance, Stokes' Law gives.

$$\frac{1}{\theta} = \frac{g\,(\rho_y - \rho_z)\,D^2}{18\,L\mu_y} \qquad (24)$$

Hence a plot of the reciprocal of settling time vs. the ratio of the differential density to extract-phase viscosity should plot as a straight line. Figure 8 shows the settling-test data plotted in this way; data on kerosene-water were included to take advantage of the low extreme of oil viscosity. The data correlation is quite good with the kerosene-water data falling in line with those for lube-phenol systems. The plot shows that settling time is decreased by an increase in the density difference between phases or a reduction of the extract-phase viscosity. Stages where capacity is critical in a lube extractor will, therefore, be those where the density difference is least and the extract-phase viscosity the greatest. Figure 9 shows the changes in phase densities, differential density, and phase-settling time at flow conditions through a commercial extractor when a paraffin base oil is extracted from a Canadian crude source. The operation was run with the oil feed entering the bottom stage, this stage temperature being about 25°F. lower than the top stage. It is seen that the density differential is smallest and essentially constant in the bottom four or five stages, owing to the extract density reaching a minimum value near the middle of the extractor because of the opposing effects of increasing oil content and decreasing temperature. Since the settling time of the stage phases increases progressively down the extractor, the results indicate that extract-phase viscosity is the governing property in the bottom stages and that the capacity critical stages are the feed stages and those near them.

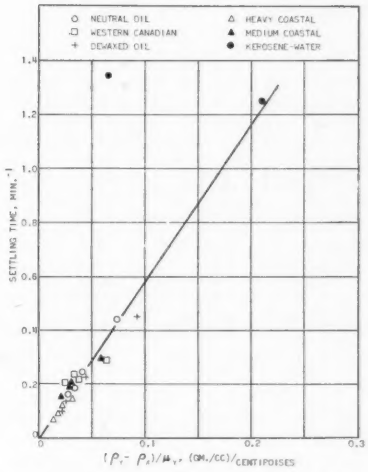

Fig. 8. Lube-phenol settling test following Stokes' Law.

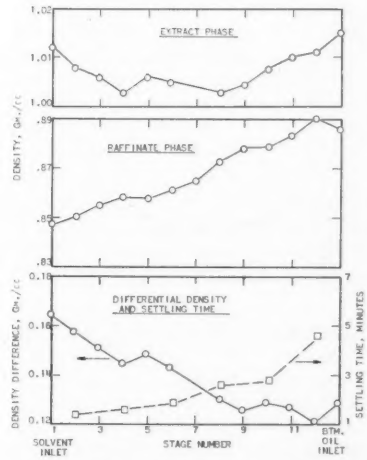

Fig. 9. Phase density and settling time in commercial extractor oil feed: Western Canadian paraffinic lube distillate; viscosity at 100°F. = 78 SSU; gravity = 21.9° A.P.I.

SUMMARY

The principal findings of the extraction studies reported here are as follow.

1. Extraction temperature has a very marked influence on stage efficiency in lube-phenol extractions; higher temperatures give higher efficiencies by reducing oil-phase viscosity. Interfacial tension, though not a major variable in lube extraction, also has a major effect on stage efficiency by affecting drop size.

2. Interstage entrainment in either one or both phases in lube-phenol extraction reduces efficiency markedly, entrainment in the extract being most serious.

3. The flow capacity of extractor towers used in lube service increases with increasing extraction temperature. The capacity limiting stages are the feed stage and the stages near it. Viscosity of the continuous phase in these stages appears to be the governing physical property.

ACKNOWLEDGMENT

The authors wish to acknowledge the assistance and suggestions of W. T. Knox, R. L. Weeks, R. B. Long, W. M. Basch, and J. A. Carver during the course of the laboratory work and to express appreciation to the Esso Research and Engineering Company for permission to publish the results.

NOTATION

A = cross-sectional area, L
a = surface area per unit volume, L^{-1}
b_1, b_2, etc. = constants
c = fractional concentration of aromatics in raffinate
c' = fractional concentration of aromatics in extract
D = drop diameter, L
E = extract oil flow, L^3/θ
f = fractional holdup of oil in mixing zone
G = oil flow per unit cross section, L/θ
g = acceleration of gravity, L/θ^2
I = raffinate-oil refractive index
I' = extract-oil refractive index
K = over-all mass transfer coefficient
k = individual film mass transfer coefficient
L = mixing section length or distance, L
m = equilibrium line slope
R = raffinate oil flow, L^3/θ
$R_s = S_x/S_y$ = phase solubility ratio
S = fraction of oil in phase
s = operating line slope in extraction
X = raffinate-phase flow, L^3/θ
Y = extract-phase flow, L^3/θ
ε_x = entrainment of raffinate phase in extract phase, L^3/L^3
ε_y = entrainment of extract phase in raffinate phase, L^3/L^3
ε_f = entrainment factor
η_a = apparent efficiency
η_c = cocurrent efficiency
η_M = Murphree efficiency
η_o = over-all efficiency
μ = absolute viscosity, $M/L\theta$
υ = kinematic viscosity, L^2/θ
ρ = density, M/L^3
θ = time

Subscripts

E = extract
F = feed
R = raffinate
o, x = raffinate phase
y = extract phase

LITERATURE CITED

1. Fenske, M. R., and R. B. Long, paper presented at Am. Inst. Chem. Engrs., Washington meeting (March, 1954).
2. Marshall, W. R., Jr., and R. L. Pigford, "Applications of Differential Equations to Chemical Engineering Problems," Univ. Delaware. Newark (1947).
3. Perry, J. H., "Chemical Engineers' Handbook", 3 ed., McGraw-Hill Book Company, Inc., New York (1950).

Presented at A.I.Ch.E. New York meeting.

Thermodynamic Properties of Air

E. M. Landsbaum, W. S. Dodds, W. F. Stevens, B. J. Sollami, and L. F. Stutzman
Northwestern University, Evanston, Illinois

In recent years the development of new sources and uses for high pressure air has emphasized the need for thermodynamic charts covering a wider pressure range than do the published charts. To fill this need, the chart by Williams (*9*) has been extended to cover pressures from 1 to 1,000 atm. in the temperature range of 300° to 675°R. Previously published temperature-entropy charts for air, all including isoenthalpic lines, are those of

	Temp., °R.	Press., atm.
Gerhart (*2*)..	460 to 1,010	1 to 238
N.D.R.C. (*8*).	140 to 760	1 to 238
Williams (*9*).	125 to 500	1 to 220

The charts of both Gerhart (*2*) and Williams (*9*) were calculated from Joule-Thompson expansion data; the values obtained are also given in tabular form. The method for determining the values for the N.D.R.C. (*8*) chart is not reported; this chart is small and difficult to use and tabular results are not given.

The additional values required for the chart presented here were calculated by the thermodynamic techniques outlined below and serve as an independent check on the calculations of both Williams (*9*) and Gerhart (*2*), which differ by less than 0.5% from those given in this paper.

The sources of the data utilized and the range over which each source applied are as follows:

	Temperature, °R.	Pressure, atm.
Amagat (*1*)	460 to 675	100 to 1,000
Holborn and Otto (*4, 5*)	492 to 675	1 to 100
Nelson, Obert "Z" charts (*7*)	300 to 500	220 to 1,000
Williams (*9*)	125 to 500	1 to 220

There are some P.V. data by Koch (*6*) and Witkowski (*10*) in the range 300° to 492°R. and 1 to 220 atm. but they are not of sufficient quantity to be usable. The data which were available, as P.V. data or as Z charts, required calculations and graphical solutions to give the required enthalpy and entropy values (*3*). As a basis for construction of the chart the value of zero entropy has been arbitrarily assigned to saturated liquid air at 1-atm. pressure, and an enthalpy value of 100 B.t.u./lb. has been arbitrarily assigned to gaseous air at zero pressure and 0°R.

The enthalpy of the air at any pressure and temperature is obtained from Equations (1), (2), (3), and (4).

$$H_{PT} = H^*_T - (H^* - H_P)_T \quad (1)$$

$$H^*_T = \int_0^T C^*_p \, dT + 100 \quad (2)$$

$$(H^* - H_P)_T = \int_0^P \frac{RT^2}{P}\left(\frac{\partial Z}{\partial T}\right)_P dP \quad (3)$$

W. S. Dodds is at present with General Foods, Hoboken, New Jersey.

Note: Figure 1, measuring 17 by 22 in., is available from the authors at a cost of 25 cents for handling and mailing.

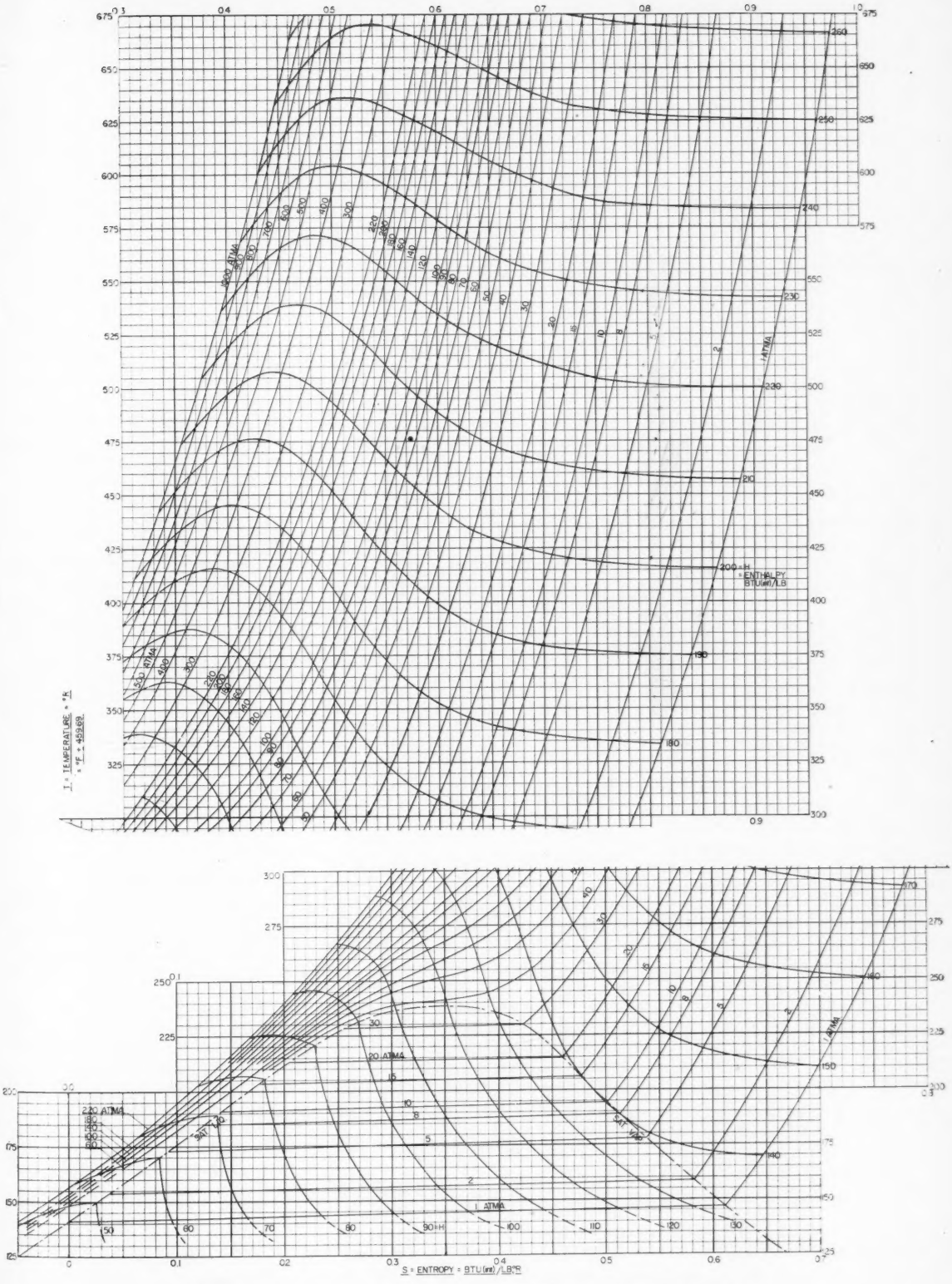

Fig. 1. Air-temperature chart: upper, 50 to 500 atm.; lower, 1 to 50 atm.

TABLE 1.—THERMODYNAMIC PROPERTIES OF AIR

T = °F. H = enthalpy, B.t.u. (int.)/lb.
P = pressure, atm. S = entropy, B.t.u. (int.)/(lb.) (°R.)

P		−126	−76	−40	−4	32	78	104	140	176
1	H	.....	.....	.....	.....	217.84	226.47	235.23	243.82	252.51
	S	.....	.....	.....	.....	0.9037	0.9226	0.9361	0.9507	0.9644
5	H	.....	.....	.....	.....	217.49	226.19	234.96	243.70	252.39
	S	.....	.....	.....	.....	0.7925	0.8115	0.8251	0.8398	0.8542
10	H	.....	.....	.....	.....	216.88	225.70	234.59	243.38	252.69
	S	.....	.....	.....	.....	0.7438	0.7630	0.7768	0.7916	0.8054
20	H	.....	.....	.....	.....	215.02	224.15	233.28	242.13	251.02
	S	.....	.....	.....	.....	0.6929	0.7127	0.7270	0.7419	0.7561
50	H	.....	.....	.....	.....	212.25	221.68	230.97	240.05	249.12
	S	.....	.....	.....	.....	0.6254	0.6457	0.6603	0.6756	0.6902
100	H	153.10	174.97	187.46	198.14	207.45	217.39	227.00	236.65	246.49
	S	0.436	0.491	0.520	0.543	0.5693	0.5908	0.6058	0.6221	0.6378
200	H	141.50	163.54	175.41	189.30	200.54	211.08	221.45	232.14	242.87
	S	0.359	0.418	0.451	0.479	0.5085	0.5313	0.5476	0.5657	0.5828
300	H	138.27	159.67	170.96	185.00	196.54	207.54	218.55	229.83	240.93
	S	0.324	0.381	0.414	0.441	0.4712	0.4950	0.5125	0.5316	0.5492
400	H	137.95	159.07	169.88	183.90	195.12	206.30	217.58	229.03	240.42
	S	0.301	0.358	0.389	0.417	0.4457	0.4697	0.4878	0.5073	0.5270
500	H	139.12	160.02	170.15	184.50	195.43	206.61	217.94	229.42	240.93
	S	0.284	0.340	0.370	0.398	0.4269	0.4508	0.4691	0.4885	0.5067
600	H	141.05	161.67	172.13	185.78	196.79	207.87	219.19	230.59	242.18
	S	0.271	0.326	0.357	0.384	0.4121	0.4359	0.4540	0.4733	0.4917
700	H	143.32	163.87	174.21	187.63	198.78	209.79	221.01	232.36	243.99
	S	0.260	0.315	0.343	0.371	0.4000	0.4236	0.4415	0.4607	0.4792
800	H	145.85	166.50	176.64	189.90	201.16	212.09	223.24	234.63	246.20
	S	0.250	0.305	0.333	0.361	0.3895	0.4131	0.4308	0.4499	0.4682
900	H	148.57	169.33	179.37	192.53	203.75	214.65	225.73	237.00	248.72
	S	0.241	0.297	0.325	0.352	0.3803	0.4037	0.4213	0.4404	0.4590
1000	H	151.46	172.08	182.31	195.45	206.49	217.42	228.36	239.67	251.45
	S	0.233	0.289	0.320	0.344	0.3719	0.3954	0.4128	0.4319	0.4507

$$Z = Z_s \frac{PV}{P_s V_s} \times \frac{T_s}{T} = 0.99941 \frac{PV}{T} \times \frac{459.69}{1.0} \quad (4)$$

The solution of Equation (3), which is necessary to solve Equation (1), is accomplished graphically from a plot of $RT^2 (\partial Z/\partial T)_P$ vs. P or a plot of $(\partial Z/\partial T)_P$ vs. P. The value of $(\partial Z/\partial T)_P$ is obtained from a plot of Z vs. T at constant pressure. Smoothed values of $(\partial Z/\partial T)_P$ are obtained by plotting the observed slopes against temperature and using values obtained from the resulting curve.

The entropy of the air at any pressure and temperature is obtained from Equations (5), (6), and (7).

$$S_{PT} = S^*_{PT} - (S^*_P - S_{P_T}) \quad (5)$$

$$S^*_{PT} = \int_{492^\circ \text{R.}}^{T} C^*_p \frac{dT}{T} - R \ln\left(\frac{P}{1}\right) + 0.9045 \quad (6)$$

$$(S^*_P - S_{P_T}) = \frac{(H^* - H_P)_T}{T} - \int_0^P \frac{R(1-Z)}{P} dP \quad (7)$$

The value of 0.9045 is the entropy of air at 492°R. and 1 atm. referred to zero entropy for saturated liquid air at 1 atm. The value of the group $(H^* - H_P)_T$ had been previously determined (*see* above), and the value of the integral of Equation (7) was determined graphically from a plot of $(1-Z)/P$ vs. P.

Calculations carried out according to the foregoing procedures resulted in the values given in Table 1. These values plus additional values (*9*) served as the basis for construction of Figure 1.

ACKNOWLEDGMENT

The chart and data presented here were prepared for use in a research project sponsored by the Wright Air Development Center, to which appreciation is due for permission to publish this information. The suggestions of G. M. Brown in carrying out the work were also very much appreciated.

NOTATION

C_p = heat capacity at constant pressure

H_{PT} = enthalpy at a given temperature, T, and pressure P

H^*_T = enthalpy of an ideal gas at a temperature, T

P = pressure

P_s = pressure, standard condition

R = gas constant

S_{PT} = entropy at a given temperature, T, and pressure, P

S^*_{PT} = entropy of an ideal gas at a given temperature, T, and pressure, P

T = temperature

T_s = temperature, standard condition

V = volume

V_s = volume, standard condition

Z = compressibility factor

Z_s = compressibility factor at standard conditions (0.99941)

LITERATURE CITED

1. Amagat, M. E. H., *Ann chim. et phys.*, Series 6, **29**, 68, (1893).
2. Gerhart, R. V., F. C. Brunner, H. S. Mickley, B. H. Sage and W. N. Lacey, *Mech. Eng.*, 64, 270 (1942).
3. Hougen, O. A., and K. M. Watson, "Chemical Process Principles," p. 493, John Wiley and Sons, Inc., New York (1947).
4. Holborn, L., and J. Otto, *Z. Physik*, **23**, 77, (1924).
5. *Ibid.*, **33**, 1 (1925).
6. Koch, P. P., *Ann. phys.*, **27**, 311 (1908).
7. Nelson, L. C., and E. F. Obert, *Chem. Eng.*, **61**, *No. 7*, 203 (July, 1954).
8. N.D.R.C., Div. 11, Vol. 1, *Oxygen Research*, OSRD, Washington, D. C. (1946).
9. Williams, V. C., *Trans. Am. Inst. Chem. Engrs.*, **39**, 93 (1943).
10. Witkowski, A. W., *Philosophy Magazine*, **41**, 288 (1896).

Diffusional Film Characteristics in Turbulent Flow: Dynamic Response Method

John J. Keyes, Jr.
Union Carbide Nuclear Company, Oak Ridge, Tennessee

Application of a dynamic or unsteady-state technique to the problem of radial mixing in a tube is described. Measurement of the amplitude attenuation suffered by a sinusoidally modulated gas composition wave as it flows within an open (unpacked) tube makes possible the direct determination of an "equivalent gas film thickness" from which a mass transfer film coefficient may be readily calculated.

A brief summary of the method employed for obtaining the necessary mathematical relationships is presented, along with descriptions of the techniques developed for measurement of small amplitude differences at wave frequencies as high as 10 cycles /sec.

Experimentally, conditions were varied to include a range of Schmidt number from 0.18 to 1.24 and of Reynolds number from 4,000 to 50,000. The results of this work appear to fall nearly in line with the semitheoretical equation of Martinelli as written for mass transfer. Generally speaking, α was found to be an increasing function of N_{Sc}, varying from about 0.5 to a maximum of 0.77; β, in turn, was found to increase with N_{Re} from 0.3 to 0.5.

A suggestion for extending the method to measurement of eddy diffusivities in the axial direction is included.

The fact that transfer of material between a flowing gas stream and an interface does not take place instantaneously is of prime significance in the design of equipment for separation and purification of fluid mixtures. Consequently, much work has been done, both theoretically and experimentally, to ascertain the dependence of mass transfer rates on measurable quantities, such as gas properties and flow rates. The dynamic or unsteady-state method(*7*) shows promise as a new research tool for investigation of these and other fundamental problems. It is the intent of this paper to present the basic theory and to describe experimental techniques as developed for application of the method to mass transfer in open tubes, together with some preliminary data which seem to bear out the validity of the method. It is felt, further, that the techniques here described are applicable in general to other problems where the dynamic method might be contemplated.

The method makes use of the fact that a fluid stream which has a cyclically varying composition undergoes a decrease in amplitude and a corresponding phase shift by virtue of radial mass transfer. To visualize the mechanism involved one may find it helpful to consider the combined resistance to transfer by both eddy and molecular diffusion as lumped into an "equivalent" diffusional film of such thickness, B_F, that the entire concentration gradient between gas and interface would be just sufficient to cause *molecular* diffusion through the film at the proper rate. The influence of the cyclic composition variation, then, is to impose a fluctuating radial concentration gradient, the effect of which in combination with the hold-up or "capacity" of the gas film is to smooth out the variations and to introduce some phase shift as the wave progresses down the tube.

The experimental procedure consists in comparing amplitude, and where necessary, phase of the outlet with that of the inlet stream. From these measurements it is possible by application of the appropriate functional relationships to determine the equivalent gas film thickness, and herefrom the film coefficient, k_g, directly. No measurement of compositions within the tube need be made, and in contrast to wetted-wall techniques no liquid phase is required. This latter feature makes the dynamic method particularly well suited for studies on noncondensable gas pairs.

PREVIOUS WORK

The cyclic method was employed by Bell and Katz(*1*) to determine surface heat transfer coefficients by utilizing sinusoidal temperature input. Later Dayton et al.(*2*) by an improved method obtained good agreement with conventional heat transfer data for several geometries.

The original application to mass transfer was made by Rosen and Winsche(*5*), who investigated rate processes in absorption beds with sine wave input.

Perhaps the most lucid exposition of the method is that of Deisler(*3*), who extended the theory to a determination of three independent rate mechanisms and applied the results to diffusion in a packed bed. Indeed, it was Deisler's work which suggested the application of the dynamic method to the problem considered here.

APPARATUS AND INSTRUMENTATION

The dynamic response method requires a means for generating the sinusodial composition wave at constant total flow rate and pressure together with a means for measuring the wave amplitude and phase. Frequencies in the range from 3 to

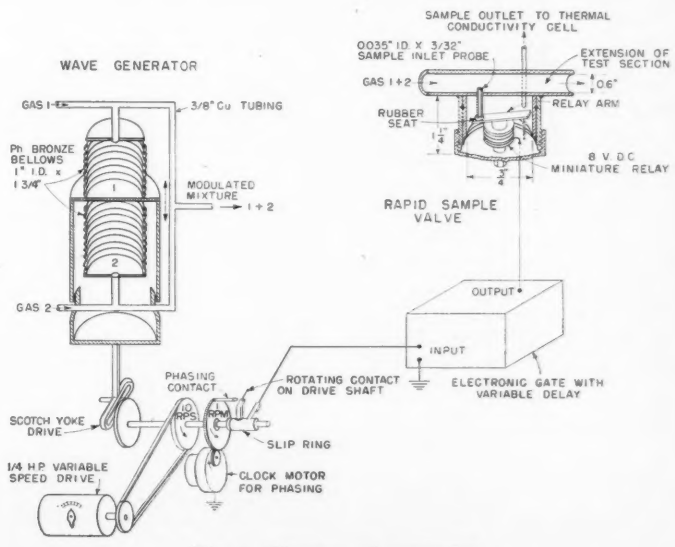

Fig. 1. Diagram of apparatus.

10 cycles/sec. are required, depending on conditions, to give measurable attenuation.

Figure 1 includes a sketch of the wave generator. It consists of a pair of matched bellows mounted rigidly at the ends and separated by a movable central partition, the latter being attached to a scotch-yoke drive mechanism to give reciprocating motion. Each bellows chamber communicates directly with a gas supply line as indicated. Because of push-pull action of the bellows, pressure and flow variations are canceled, giving as output the pure composition function desired. Operation as high as 15 cycles/sec. is feasible with this design, maintaining reasonably good wave form.

Analysis of the modulated wave is basically by thermal conductivity; however direct, continuous sampling from the test section through the thermal element proved unsatisfactory. Even with a specially designed rapid-response cell, short lines, and low pressure, the output signal was found to fall off rapidly above 1 cycle/sec., mainly because of mixing in the sample lines and chambers. Figure 2 is a block diagram of the apparatus as finally developed, capable of responding to as high as 10 cycles/sec. but utilizing only standard thermal conductivity cells and recorder. This scheme enables simultaneous measurement of attenuation and phase shift.

The test section consists of an 8-ft. length of glass tubing, 0.61 in. I.D., preceded by a 6-ft. entrance section and an expanded section of open pipe for attenuation of any harmonics present in the generated wave. Two relay operated rapid sampling valves are provided at either end of the test section for the purpose of monitoring the gas wave. These valves act to withdraw a small volume of sample gas when energized for a predetermined fraction of a cycle (2 to 5%) by means of the rotating contact on the generator shaft. Provision for delaying (or advancing) the action of valve B with respect to valve A is provided by an electronic delay gate variable from 0 to 250 msec.

Operation of the sampling system can best be understood by reference to Figure 3. If points indicated by x represent withdrawal of a sample at each cycle of the fundamental wave at some arbitrary time, the output of the valve is a constant gas composition with magnitude depending on the relationship in phase (or time) between the wave generator stroke and the signal to the sampling relay. To obtain a complete representation of the wave it is necessary simply to scan through 360° by continually rotating the phase of the synchronizing contact with respect to the generator shaft. Thus, the sampling point is made to traverse the wave, as indicated by the points marked •, at sufficiently low frequency for the analytical system to follow. The over-all result is a reproduction of the original wave in amplitude and phase but at greatly reduced frequency. A scanning rate of about 1 cycle/min. is satisfactory. Figure 4 is the trace of a typical wave form so obtained. Figure 1 shows an isometric view of the relay valve and scanning mechanism. Figures 5 and 6 are, respectively, photographs of the wave generator and of the over-all apparatus.

The method of determining attenuation and phase is straightforward. Outputs of the two samplers, at 7 cm. Hg, flow to opposite sides of a thermal conductivity bridge (Gow-Mac Company, NRL Model), the output of which depends on amplitude and phase relationships of the two input waves. If these are

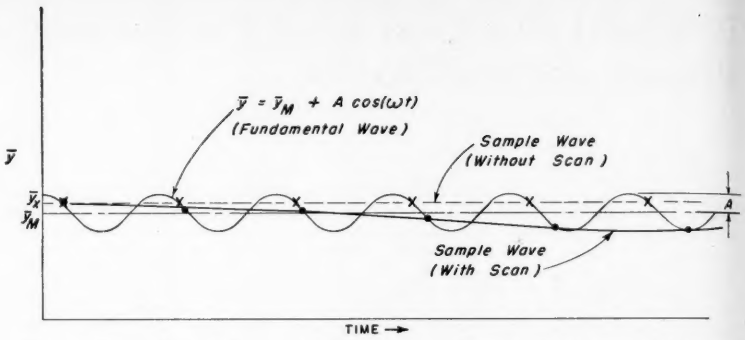

Fig. 3. Operation of the rapid sampling system, illustrating reduction in output frequency.

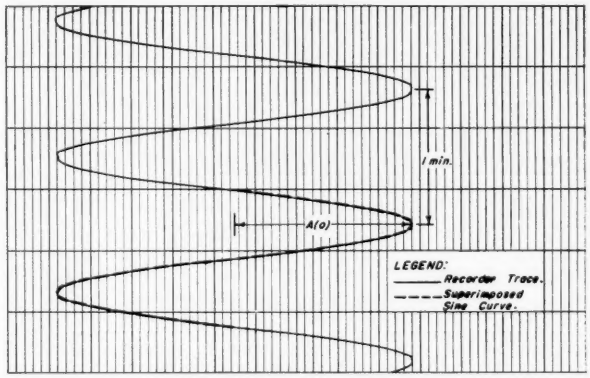

Fig. 4. Typical wave trace; fundamental frequency, 7 cycles/sec.

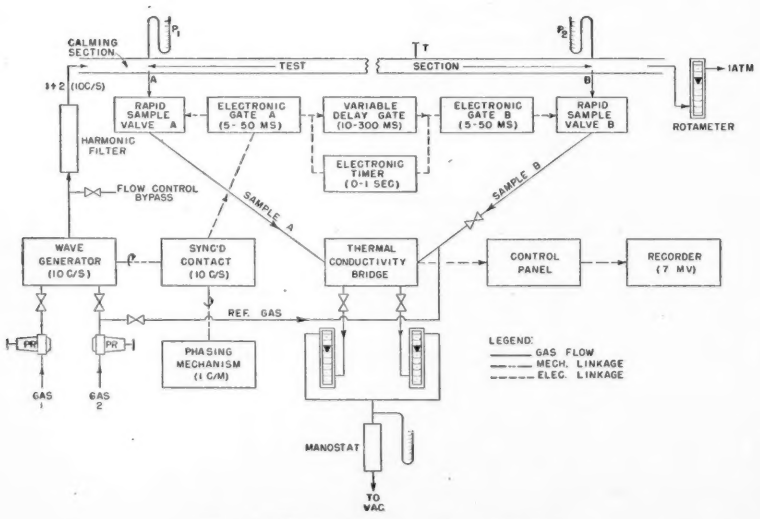

Fig. 2. Block diagram of apparatus.

Fig. 5. Wave generator and phasing mechanism.

exactly in phase, a sensitive recorder connected across the bridge will indicate amplitude difference directly. Thus, when the variable delay on B is adjusted for minimum output amplitude, which will approach a true null as $A(L) \rightarrow A(O)$, the two sample waves are in phase, and the delay as read on the timer is a measure of the phase lag between the sample points. The attenuation ratio of the wave

$$\frac{A(L)}{A(O)} = 1 - \frac{A(O) - A(L)}{A(O)}$$

is obtained from the indicated amplitude difference and the initial amplitude $A(O)$.

ANALYTICAL TREATMENT AND DISCUSSION

An understanding of the mechanism by which equivalent film thickness is related to attenuation and phase shift of the sinusoidal composition wave can best be attained by consideration of the behavior of the wave with reference to its radial and longitudinal travel. Attention is here confined to the case of an open (unpacked) tube through which the gas is flowing.

As indicated in the introductory remarks, use is made of the equivalent gas film concept in the analysis. This simplifying approach is probably adequate provided consistency in the definition of the transfer coefficient is maintained. Accordingly, the gas film coefficient, k_g, is related to film thickness, B_F, as follows:

$$k_g = \frac{\rho D}{B_F} \qquad (1)$$

where ρ and D are respectively gas density and molecular diffusivity. Equation (1) is simply the expression of Fick's law for equimolar, countercurrent diffusion. Since the experimental measurements yield values for B_F directly, as will be seen, it was decided to report the results in terms of the latter quantity, with the understanding that the mass transfer coefficient which would obtain for a given N_{Re} and N_{Sc} is directly calculable from Equation (1).

The interior of the tube of diameter d is divided into a central turbulent core of uniform radial composition y and constant mass velocity G, based on the inside tube area, and a peripheral nonturbulent film of thickness B_F, uniform velocity V (the assumption of uniform velocity in the film being necessary to obtain a solution in closed form), and varying radial composition y, as indicated in Figures 7 and 8. As the gas wave progresses along the tube, there is exchange by diffusion between the core and film, the net result of which is equivalent to mixing of the components of the wave (amplitude reduction) and lagging behind of the wave crests (phase shift). Note that there is no net radial flow. only transient flow alternately toward and away from the wall. In addition, there may also be mixing in the axial direction, depending on the magnitude of the longitudinal eddy diffusion coefficient, D_L, and the concentration gradient. It is desired to obtain a quantitative expression for the relationships among these variables.

The differential material balance over a cylindrical core volume element in the direction of flow is first written (*see* Figure 7):

Core Equation

$$\frac{4N(1+2B_F/d)}{d} + \frac{V_M}{\overline{V}}\left(G\frac{\partial \overline{y}}{\partial z} - D_L\rho\frac{\partial^2 \overline{y}}{\partial z^2}\right) + \rho\frac{\partial \overline{y}}{\partial t} = 0 \qquad (2)$$

N is the rate of transport of one component from the core to the film, based on the inside film perimeter and evaluated at $x = B_F$. $V_M/\overline{V}$, the ratio of maximum to average velocity, depends on the particular choice of the film velocity, V:

1. $V = 0$: $V_M/\overline{V} \cong 1 + 4\frac{B_F}{d}$
2. $V = V_M/2$: $V_M/\overline{V} \cong 1 + 2\frac{B_F}{d}$
3. $V = V_M$ $V_M/\overline{V} \cong 1$

N is obtained from an independent material balance across the film (*see* Figure 8):

Film Equation

$$V\frac{\partial y}{\partial z} + D\frac{\partial^2 y}{\partial x^2} + \frac{\partial y}{\partial t} = 0 \qquad (3)$$

Obviously,

$$N = Dp\frac{\partial y}{\partial x}\bigg|_{x=B_F} \qquad (4)$$

Boundary conditions for (3) are

$$\frac{\partial y}{\partial x}\bigg|_{x=0} = 0 \qquad (5)$$

$$y = \overline{y}\bigg|_{x=B_F} \qquad (6)$$

It is desired to obtain a solution of (2) at $z = L$, subject to the harmonic boundary condition at the inlet, $z = 0$:

$$\overline{y} = \overline{y}_M + A(O)\cos\omega t \qquad (7)$$

Equations (2) and (3) can be readily solved by the method of separation of variables, if the coefficients V, ρ, D, D_L, etc., are as-

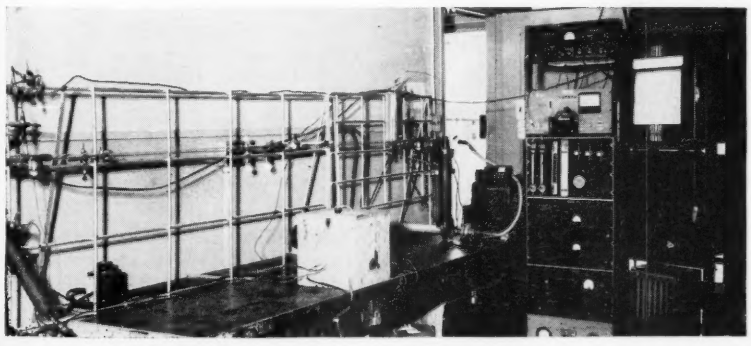

Fig. 6. Over-all view of the apparatus.

sumed to be constants,* and exp $(i\omega t)$ is taken as the time dependent factor, a consequence of (7). In the final step imaginary terms are dropped, and a solution to (2) of the following form is reached:

$$\bar{y}(z) = \bar{y}_M + A(O) \exp[-R(z)] \cos[(\omega t - \phi(z)] \quad (8)$$

$$\therefore \frac{A'(L)}{A_1(O)} = \exp[-R(L)] \text{ attenuation ratio} \quad (9)$$

R, the attenuation exponent, and ϕ, the phase shift, are functions of known quantities G, ρ, D, etc., and of B_F, which is to be determined. Solutions have been obtained for the three assumed film velocities already discussed. The result for R is essentially independent of V, and one may conclude that knowledge of the velocity profile is not necessary so far as amplitude measurements are concerned. Since, on the other hand, ϕ does exhibit a strong dependence on assumed velocity distribution, it was decided to base all results on the attenuation measurements and to leave for a possible future program the interpretation of phase shift data.

*This is essentially true for small amplitudes, say, <10%.

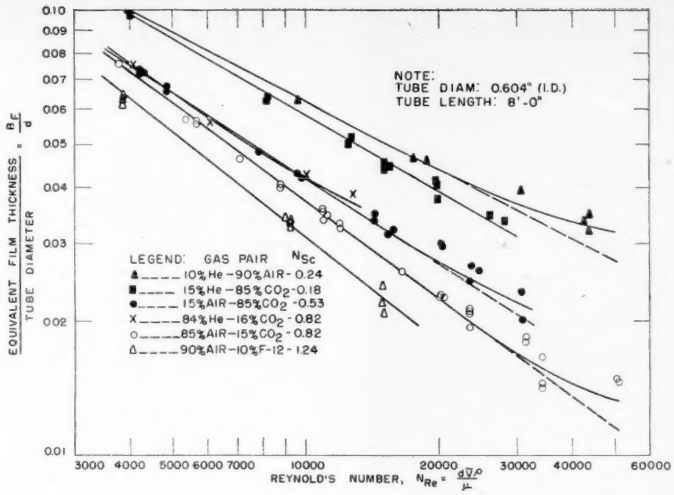

Fig. 9. Summary of experimental results: $-\frac{B_F}{d}$ vs. N_{Re}

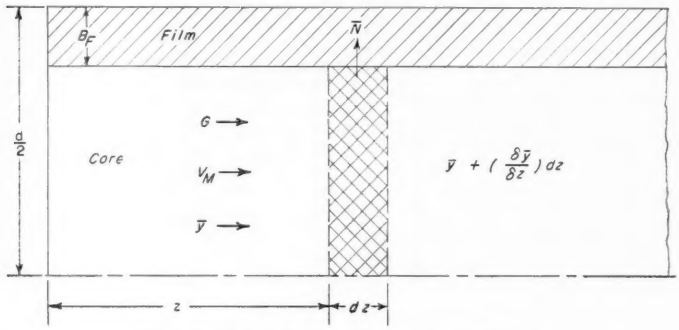

Fig. 7. Nomenclature for core equation.

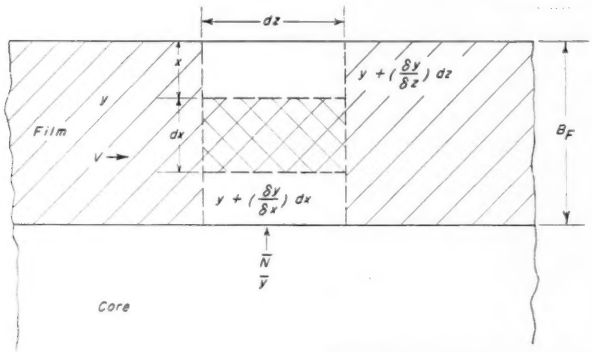

Fig. 8. Nomenclature for film equation.

Attenuation Exponents

Case 1. Longitudinal diffusion is negligible in comparison with radial diffusion.

This situation obtains normally, since longitudinal concentration gradients are very much smaller than the radial gradients. (Wave lengths of the order of 2 to 10 ft. were employed in this work.) Hence, the second order term in (2) is dropped:

$$R(L) = \frac{2\rho L (2\omega D)^{\frac{1}{2}} \left(1 - \frac{2B_F}{d}\right)}{dG} \left[\frac{\sinh\gamma - \sin\gamma}{\cosh\gamma + \cos\gamma}\right]$$

where $\gamma = \left(\frac{2\omega}{D}\right)^{\frac{1}{2}} B_F$ (10)

When γ is sufficiently small that the hyperbolic and trigonometric functions can be represented by their respective series with only first and third degree terms included, the preceding result simplifies considerably:

$$R(L) \cong \frac{4\rho L \omega^2 B_F^3 (1 - 2B_F/d)}{3dGD} \quad (10a)$$

Equation (10a) holds to within about 1% when solved for B_F, with γ as great as 1.0. It is apparent that the attenuation will be a strong function of frequency and of film thickness in particular. The method is therefore quite sensitive for determination of the latter quantity.

Case 2. Perfect radial mixing is assumed and $B_F = 0$ is set in Equations (2) and (3), only the longitudinal mixing effect being left.

For this case

$$R'(L) = \frac{\rho^3 \omega^2 L D_L}{G^3} \quad (11)$$

Some notion of the magnitude of the longitudinal effect can be obtained by substitution of typical values in Equation (11):

$V = G/\rho = 28$ ft./sec. (corresponding to $N_{Re} \cong 10{,}000$ in 0.6-in. I.D. tube)

$\omega = 2\pi f = 24$/sec.
$D_L = D = 1.8\times10^{-4}$ sq.ft./sec. (air-CO_2)
$L = 8$ ft.,
giving

$$\left.\frac{A\,(L)}{A\,(O)}\right|_{\text{axial mixing}} = \exp(-R') = 0.9995$$

Even though D_L were 100 times as great as D, which might possibly be true at very high N_{Re}, the effect of longitudinal diffusion is probably negligible as assumed, since under these same conditions

$$\left.\frac{A\,(L)}{A\,(O)}\right|_{\text{radial mixing}} \cong 0.9.$$

EXPERIMENTAL CONSIDERATIONS AND RESULTS

Film thickness determinations covering a wide range of Reynolds and Schmidt numbers were desired. Because of their availability and sensitivity to analysis by thermal conductivity, the following gas pairs were employed:

Gas pair	Light comp., %	μ cp.	ρ, lb./cu. ft.	D, sq. ft./sec.	N_{Sc}
He-CO_2	15	1.61×10^{-2}	9.76×10^{-2}	6.2×10^{-4}	0.18
He-Air	10	1.81	6.76	7.5	0.24
Air-CO_2	15	1.50	10.72	1.77	0.53
Air-CO_2	50	1.61	9.36	1.77	0.65
He-CO_2	84	1.85	2.67	6.2	0.82
Air-CO_2	85	1.73	8.02	1.77	0.82
Air-Freon-12	90	1.73	9.88	0.95	1.24

(values given at 25°C., 1 atm.)

Reynolds numbers were varied from about 4,000 to 50,000 for the 85% air–15% CO_2 system; the upper limit for the other systems was 20,000 to 30,000.

Because of difficulty in interpretation of the phase shift measurements, as well as some uncertainties in the data, discussion of this portion of the work has been omitted.

Typical amplitude data for 85% air–15% CO_2 are listed in Table 1. Repeat runs at approximately constant N_{Re} but varying frequency are included for the purpose of ascertaining any second-order frequency dependence. In addition, some runs at varying initial amplitude, $A(O)$, were made to detect possible nonlinearity. Results of the attenuation measurements are summarized in Figure 9.

Discussion of the Results

Logarithmic plots of B_F/d vs. N_{Re}, with N_{Sc} as parameter, Figures 9 and 10, are suggested by conventional mass transfer correlations of the form

TABLE 1.—TYPICAL DYNAMIC RESPONSE AMPLITUDE DATA

15% CO_2—85% Air (N_{Sc}=0.82)
Tube length L=8.03 ft.
Tube diameter d=5.07×10⁻² ft
Temperature: approx. 25°C.
Pressure: approx. 1 atm.

Run number	Flow rate, cu. ft./min. 25°C. 1 atm.	Frequency, cycles/min.	Initial amplitude $A(O)$, %	Measured attenuation $\frac{A(L)}{A(O)}$	N_{Re}	γ	$\frac{B_F}{d}$ from Eq. (11)
11	1.310	162	7.6	0.409	3770	1.402	0.0760
25a	1.850	208	6.2	0.592	5330	1.240	0.0566
12a	1.956	161	5.6	0.739	5640	1.082	0.0556
b	1.956	211	6.5	0.613	5640	1.227	0.0553
83	2.44	206	8.0	0.801	7080	1.005	0.0462
13a	3.035	202	5.5	0.872	8750	0.913	0.0397
b	3.035	290	7.1	0.742	8750	1.127	0.0407
24c	3.81	251	5.6	0.886	10960	0.918	0.0358
b	3.81	291	6.5	0.874	10960	0.928	0.0339
a	3.81	363	7.6	0.794	10960	1.077	0.0352
82	3.85	205	—	0.936	11100	0.775	0.0346
14	4.10	273	6.5	0.886	11820	0.925	0.0347
10a	4.10	275	7.8	0.895	11820	0.888	0.0323
c	4.10	323	6.0	0.838	11820	1.018	0.0328
23d	5.73	246	—	0.969	16450	0.668	0.0259
a	5.73	363	—	0.905	16450	0.910	0.0280
80	6.93	231	6.0	0.984	20100	0.570	0.0229
79	6.95	307	6.0	0.968	20150	0.680	0.0228
78	7.56	382	—	0.962	21900	0.720	0.0228
17a	8.10	321	6.0	0.977	23500	0.640	0.0209
22	8.10	323	5.0	0.977	23500	0.640	0.0213
15d	8.10	329	5.0	0.981	23500	0.660	0.0193
18c	8.10	382	5.6	0.955	23500	0.786	0.0235
15b	8.10	470	8.5	0.930	23500	0.888	0.0241
73	10.84	261	4.0	0.9930	31400	0.495	0.0182
74	10.91	335	5.2	0.9875	31500	0.574	0.0186
27a	11.75	303	4.6	0.9948	34100	0.442	0.0145
b	11.75	341	5.2	0.9903	34100	0.535	0.0166
d	11.75	494	6.9	0.970	34100	0.740	0.0193
81a	17.45	383	—	0.9941	50500	0.505	0.0149
76	17.60	415	5.2	0.9928	51000	0.532	0.0147

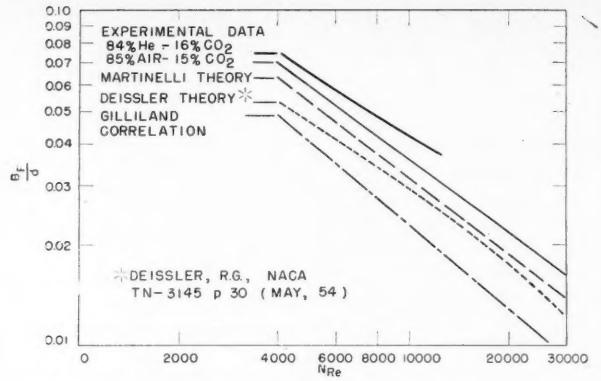

Fig. 10. Comparison of theory and experiment for $N_{Sc} = 0.82$.

$$B_F/d = k\,N_{Re}^{-\alpha} N_{Sc}^{-\beta} \quad (12)$$

A dependence on a Reynolds number of this form does indeed seem to fit the experimental results for $N_{Re}<20{,}000$, with α an increasing function of N_{Sc} as indicated in Figure 11. At high N_{Re}, however, there is some apparent leveling off of the dependence, attributable possibly to certain experimental difficulties:

1. At the higher flow rates there appears to be a small frequency effect, as shown in Table 1, tending to raise the film thickness as frequency is increased at constant N_{Re}. This effect may be due in part to increased wave distortion.

2. Spread in the results for B_F/d at constant N_{Re}, increasing at the higher flow rates, may be attributed also to exaggeration of random errors, a consequence of the increased sensitivity required to measure smaller and smaller amplitude differences.

3. Longitudinal mixing may contribute to the observed attenuation at high N_{Re}, although this seems unlikely.

It might be pointed out, on the other hand, that variation in initial amplitude $A(O)$ from 2% to 8% had no significant effect on the results. (This conclusion might have to be qualified under extreme conditions, such as the case of a high proportion of He in CO_2, where gas density changes significantly with composition.)

Figure 12 illustrates the observed dependence on Schmidt number at constant Reynolds number. In this case the data do not indicate a linear relationship over the entire range of N_{Sc} as ordinarily assumed. Only at the high range, say $0.6<N_{Sc}<1.2$, could one interpret such a relationship to hold. Figure 13 illustrates the observed variations in slope, $-\beta$, based on the above limited range, with N_{Re}.

Comparison with Theory

It is apparent from the variation in slopes of both N_{Re} and N_{Sc} diagrams that the simplest form of Equation (12), obtained by assuming constant exponents, does not represent the results here reported. Some previous work with the equation of Martinelli (*4*), as written for mass transfer, had been encouraging; consequently, it was decided to compare the results with this semitheoretical equation:

$$\frac{B_F}{d} = \frac{32.95R_c\left[\alpha N_{Sc} + \ln(1+5\,\alpha N_{Sc}) + \frac{1}{2}\ln 2.53\times10^{-3}\,N_{Re}^{0.9}\right]}{\alpha N_{Sc}\,N_{Re}^{0.9}} \quad (13)$$

R_c is the ratio of mean to maximum concentration difference. Equation (13) was derived from a more general form of the equation as given by Sherwood and Pigford (*6*) by substitution of the simplified Blasius friction factor expression

$$f = \frac{0.046}{N_{Re}^{0.2}}$$

The value of the parameter

$$\alpha\left(=\frac{\epsilon H}{\epsilon M}\right)$$

was taken as 0.9, based on a comparison of some earlier data.

Comparison of the results with Equation (13) is included in Figures 10 and 11. The Martinelli

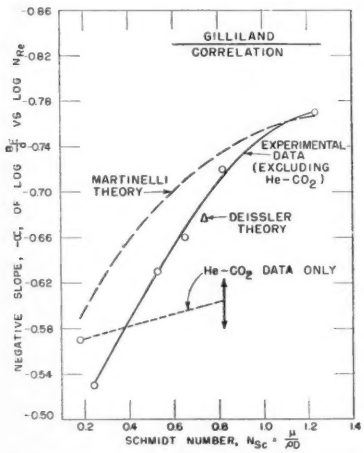

Fig. 11. Schmidt-number dependence of Reynolds-number exponent, $-\alpha\left(\frac{B_F}{d} = KN_{Re}^{-\alpha} N_{Sc}^{-\beta}\right)$.

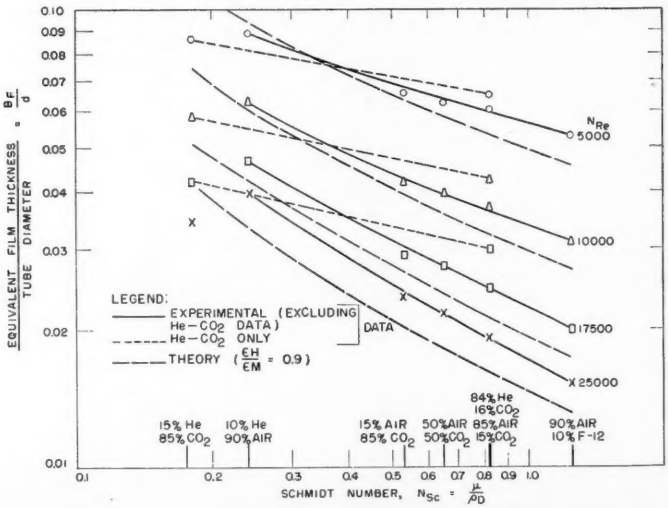

Fig. 12. Comparison of results with Martinelli theory: $\frac{B_F}{d}$ vs. N_{Sc}.

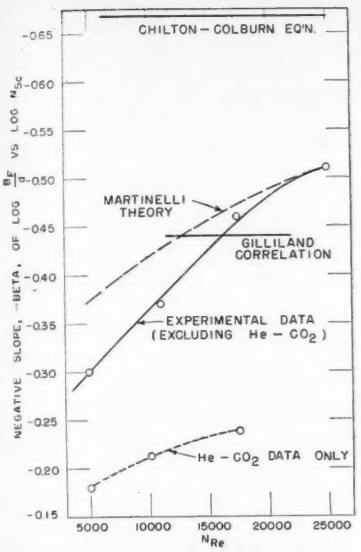
CHILTON – COLBURN EQ'N.
MARTINELLI THEORY
GILLILAND CORRELATION
EXPERIMENTAL DATA (EXCLUDING He – CO_2)
He – CO_2 DATA ONLY
NEGATIVE SLOPE, –BETA, OF LOG $\frac{B_F}{d}$ VS LOG N_{Sc}
N_{Re}

Fig. 13. Reynolds number dependence of Schmidt number exponent, $-\beta$, for $0.6 < N_{Sc} < 1.24$ $\left(\frac{B_F}{d} = KN_{Re}^{-\alpha} N_{Sc}^{-\beta}\right)$.

equation plots nearly linearly with N_{Re} at constant N_{Sc}, over the range of interest, falling a little below the measured results. Note that the experimental and theoretical slopes, $-\alpha$, compared in Figure 11, exhibit similar variations with N_{Sc}, with particularly good agreement for $N_{Sc} > 0.8$.

Figure 12 is a further comparison of results with Equation (13). B_F/d is considered a function of N_{Sc} at constant N_{Re}. The anomalous behavior of He-CO_2 is observed in Figure 10 as a lack of agreement with air–CO_2 data at the same Schmidt and Reynolds numbers and is evidenced further by the abnormally low N_{Re} and N_{Sc} dependence (Figures 11 and 13). These effects are not at present understood.

Variations in experimental and theoretical slopes, $-\beta$, with N_{Re}, as plotted in Figure 13, show surprising similarities. There seems to be a leveling off in β with increasing N_{Re} toward a value somewhat above 0.44 obtained by Gilliland.

An interesting potentiality of the dynamic method for measurement of axial eddy diffusivity in open tubes exists, for it can be shown that phase shift of the modulated wave should occur independently of longitudinal mixing. From simultaneous measurements of attenuation and phase, therefore, D_L may be determined. Difficulty in obtaining and interpreting phase measurements has thus far prevented attainment of this end.

Discussion of Experimental Errors

Aside from ever-present errors, such as those in calibration and flow metering, certain difficulties associated with generation and detection of the modulated wave might be mentioned. Wave distortion may be introduced at the generator by bellows mismatch, play in bearings and yoke, excessive pressure differences between bellows, etc. If not too serious, such distortions can be removed by the expanded tube filter, which attenuates the higher order harmonics.

The rapid sampling technique in itself may introduce apparent wave distortion, particularly if the phasing rate is too great compared with the fundamental frequency or if the sampling time is too long. In general, the phasing frequency should not exceed 0.5% of the fundamental, and the sampling time 5% of a cycle. Figure 4, previously discussed, illustrates the good sinusoidal wave form attainable.

CONCLUSION

The dynamic response method shows promise as a tool for fundamental studies related to gas mixing and mass transfer, where conventional methods are unwieldy or in some cases inapplicable. The work described here is an illustration of the sensitivity and flexibility of the method and of the nature of experimental techniques found applicable to the specialized problems of generating and monitoring a high frequency gas composition wave. Experimental evidence of deviations from the commonly utilized mass transfer correlations is discussed. Because of the preliminary nature of the results, no attempt to present a specific correlation of the data has been made other than to point out the similar trend to that predicted by the semitheoretical Martinelli equation.

ACKNOWLEDGMENT

The author wishes to express appreciation to G. A. Kuipers, for suggesting the design of the wave generator, to D. F. Smith for the basic idea of rapid sampling, and to J. H. Lykins and H. S. McKown for design and for development of the electronic equipment.

NOTATION

A = interfacial area, sq. ft.
$A(L)$ = amplitude at distance L from inlet
$A(O)$ = amplitude at inlet
B_F = equivalent film thickness, ft.
d = inside tube diameter, ft.
D = molecular diffusivity, sq.ft./sec.
D_L = longitudinal (eddy) diffusivity, ft./sec.
f = friction factor
G = axial mass velocity, lb./(sec.)(sq.ft.)
k_g = gas film transfer coefficient, lb./(sec.)(sq.ft.)(mole fraction)
K_g = over-all gas film mass transfer coefficient, lb./(sec.)(sq. ft.)(mole fraction)
L = tube length, ft.
N = radial mass velocity of one component, lb./(sec.)(sq.ft.)
N_{Re} = Reynolds number, $d\overline{V}\rho/\mu$
N_{Sc} = Schmidt number, $\mu/\rho D$
$R(L)$ = radial attenuation exponent
$R'(L)$ = axial attenuation exponent
R_c = ratio mean to maximum Δy
t = time, sec.
V = velocity of film, ft./sec.
$\overline{V}$ = average velocity, ft./sec.
V_M = maximum velocity, ft./sec.
W' = radial mass rate of diffusing component, lb./sec.
x = radial distance from tube wall, ft.
y = film concentration
$\overline{y}$ = core concentration
y_M = mean core concentration
z = distance from tube inlet, ft.

Greek Letters

α = Reynolds number exponent, also $\alpha = E_H/E_M$ (= eddy diffusivity for heat or mass/eddy diffusivity for momentum)
β = Schmidt number exponent
$\gamma = (2\omega/D)^{\frac{1}{2}} B_F$
μ = mean viscosity, lb./(ft.)(sec.)
ρ = mean density, lb./cu.ft.
ϕ = phase shift
ω = angular frequency, radian/sec.

LITERATURE CITED

1. Bell, J. C., and E. F. Katz, "Heat Transfer and Fluid Mechanics Institute," Am. Soc. Mech. Engrs., Berkeley, Calif. (June 22, 1949).
2. Dayton, R. W., et al., *Rept. BMI-747*, Battelle Memorial Institute (1952).
3. Deisler, P. F., Jr., Ph.D. Dissertation, Princeton University (June, 1952).
4. Martinelli, R. C., *Trans. Am. Soc. Mech. Engrs.* 69, 947-959 (1947).
5. Rosen, J. B., and W. E. Winsche, *J. Chem. Phys.*, 18, 1587 (1950).
6. Sherwood, T. K., and R. L. Pigford, "Absorption and Extraction," 2 ed., p. 63, McGraw-Hill Book Company, Inc., New York (1952).
7. Wilhelm, R. H., *Chem. Eng. Progr.*, 49, No. 3, 153 (1953).

Total Pressure Method for Vapor-liquid Equilibria at Low Absolute Pressures: Aniline-nitrobenzene Systems

G. W. Holtzlander and J. W. Riggle
E. I. du Pont de Nemours and Company, Wilmington, Delaware

Binary vapor-liquid equilibrium data for use in the successful design and operation of mass transfer equipment at pressures down to approximately 5 mm. Hg may be advantageously obtained by the method of total pressures. In this method the desired equilibrium data are derived from pressure vs. temperature measurements on a convenient number of made-up solutions covering the entire composition range.

With a modified Smith and Menzies isoteniscope, it is possible to measure accurately the data required for making the equilibrium calculations down to 2 mm. abs. pressure without the "bumping," supercooling, and superheating encountered with equilibrium stills. The isoteniscope is simple to construct and operate from 1 atm. to 2 mm. abs.

The use of the total pressure method and the isoteniscope is illustrated by the determination of the vapor-liquid equilibrium in the aniline-nitrobenzene system at 5 and 10 mm. abs. In nineteen out of twenty instances the vapor compositions for a given liquid composition are precise to within ± 0.9% and the relative volatility, which varied between 2.54 and 1.85 over the composition and temperature ranges, is precise within ± 1.5%.

One of the basic types of data required for the successful design and operation of mass transfer equipment such as distillation columns, absorbers, strippers, and condensers is equilibrium vapor-liquid composition. Numerous methods of measuring and calculating vapor-liquid compositions as well as data on many specific systems have been reported in the literature, but comparatively few applications of the method of total pressure are reported for obtaining vapor-liquid data in the range of pressures from 5 mm. Hg to 1 atm. Only a few binary systems have been reported at pressures of 5 to 10 mm. which might be used for studying operating characteristics such as plate efficiencies of vacuum distillation columns.

This paper is concerned with the explanation and application of the total pressure method to a specific system as well as a description of apparatus which has been successfully used to measure the data required for this method. A large part of the discussion presupposes a knowledge of the theory of nonideal vapor-liquid phase behavior, as space will not permit a complete review of the development and reasoning behind many of the statements and equations. The reader desiring background information is referred to the papers published by Carlson and Colburn (*1*) and Wohl(*14*).

The total pressure method of obtaining vapor-liquid equilibrium data on binary systems was theoretically explored to some extent by Redlich, Kister, and Turnquist (*10*) and by Carlson and Colburn (*1*). Redlich and Kister(*9*) used a slightly modified form of the total pressure method to obtain values of α, the relative volatility, for the binary systems formed by the three isomers of xylene with ethylbenzene and for the system isopentane *n*-pentane. The values of the relative volatility obtained(*9*) were precise to ±0.10%.

Briefly stated, the total pressure method for measuring binary vapor-liquid equilibrium data consists of the following steps:

1. Measurement of the total pressure vs. temperature relationships for four to eight made-up solutions throughout the composition range of the binary system.
2. Use of curve-fitting techniques to obtain the constants in one of the integrated forms of the Gibbs-Duhem equation (a differential equation of thermodynamics which relates the composition of any phase to the activity of any given component).
3. Calculation of the vapor-liquid equilibrium from the constants and vapor-pressure data for any constant pressure within the range of data.

Since total pressure data may be measured in static equilibrium apparatus where no boiling takes place, the total pressure method eliminates the bumping and unsteady boiling frequently found in stills operating at low pressures. It is nearly always possible, therefore, to obtain low-pressure vapor-liquid data by this method which are much more precise than the data taken in equilibrium stills. Furthermore, in some systems where there are no convenient analytical methods for measuring the composition of the phases and where no contamination of the components occurs during experimental work, the total pressure method offers a means for obtaining vapor-liquid values, as data can be obtained from made-up solutions.

The apparatus best adapted for obtaining the total pressures at low absolute pressures is a slightly modified form of the isoteniscope reported by Smith and Menzies (*12*). This apparatus in combination with gauges, ballast tanks, and vacuum pumps has been used up to this time only to measure the vapor pressure of pure materials. For this work on the aniline-nitrobenzene system, the Smith and Menzies isoteniscope was modified, the vapor volume being decreased in relation to the liquid volume to minimize changes in liquid composition caused by vaporization of the more volatile component during operation. In addition, means for providing adequate agitation were included in the modifications, and a few other minor changes were made to aid in the operation of the device.

The total pressure method and isoteniscope were applied to the problem of obtaining precise vapor-liquid equilibrium data for the system aniline nitrobenzene at 5 and 10 mm. abs. pressure as an illustration of the techniques involved. This system was selected because it may be advantageously employed as a test system for determining operating characteristics of vacuum distillation columns. Its advantages for such use are (*a*) boiling temperatures are in the range of 50° to 100°C. at 5 to 10 mm.; (*b*) analytical determinations may be readily performed on the mixtures; (*c*) the components are completely miscible and there is no azeotrope in the system; (*d*) the relative volatility is of such value that a reasonable number of plates or

transfer units may be included in any test column; and (*e*) the components have nearly equal molal latent heats. Data on the vapor-liquid behavior of this system, therefore, will prove valuable for the study of distillation column behavior as well as for the design of process equipment.

The following paragraphs describe the operation and construction of the apparatus used in obtaining the total pressure data and the techniques used in converting the information into the desired vapor-liquid compositions. The *x-y* data for the aniline-nitrobenzene system at 5 and 10 mm. abs. pressure are presented in tabular and graphical form.

APPARATUS AND EXPERIMENTAL PROCEDURE

The modified Smith and Menzies (*12*) isoteniscope used to measure the total pressures of the aniline-nitrobenzene solutions is shown in Figure 1. For this system the size of the liquid bulb was increased to 200 ml. to prevent appreciable change in the liquid composition when vaporization occurs. A stopcock was added to the outlet of the isoteniscope to give better control of the apparatus, and a magnetic stirrer was incorporated in the bulb to ensure intimate contacting of the vapor and liquid phases and also the rapid attainment of thermal equilibrium of the contents of the bulb with the surrounding bath liquid.

The following procedure was used during each run. The isoteniscope was connected to a vacuum pump and evacuation was allowed to proceed for several minutes. Stopcock *A* (Figure 1) was closed and the connection to the vacuum pump broken. A leveling bulb containing about 175 ml. of test liquid was connected by means of glass tubing and short lengths of gum-rubber hose to the isoteniscope. Stopcock *A* was then opened, the leveling bulb raised to a higher level than the isoteniscope, and the test fluid allowed to run into the isoteniscope, which then was placed in a bath of suitable heat transfer oil. The cold traps *C*, *F*, and *I* (Figure 2) were charged with dry ice–acetone mixture, and the magnetic stirrer and the vacuum pump were started. When the liquid in the bulb began to vaporize, the pressure in the system was fixed by setting the Cenco electronic manostat (*G*, Figure 2) to allow slow vaporization. Usually it was found necessary to keep the bath temperature between 60° and 80°C. while this step was performed. About 10% of the charge in the bulb was distilled over into the first dry-ice trap, where it was frozen and held for the remainder of the run. It was found necessary to do this with the aniline-nitrobenzene system in order to remove all traces of dissolved and adsorbed air from the bulb. When the desired amount of material had been distilled into the dry-ice trap, the condensate which had collected in the U leg was mixed thoroughly with the contents of the bulb by tilting the apparatus repeatedly, care being taken to continue boiling rapidly enough to exclude air from the bulb contents during the operation. An amount of this mixed liquid sufficient to act as manometer fluid was transferred to the U leg. The two legs of liquid in the U leg then were equalized by resetting the inert gas pressure on the system. With the aid of a small spirit level any setting in the range of 2 to 20 mm. Hg abs. could be maintained to within 0.5 mm. of the fluid in the manometer or 0.04 mm. Hg.

A series of pressure-temperature readings was taken on each charge to the apparatus over the pressure range of 2 to 20 mm. Hg abs. pressure, starting at the lower pressure and progressing upward. Less than 10 min. was required for the system to come substantially to equilibrium when a measurement was made. At the end of a run the isoteniscope was disconnected from the rest of the apparatus, taken from its bath, and connected to a nitrogen cylinder by a flexible hose. Stopcock *A* was opened and nitrogen allowed to bleed into the isoteniscope until a pressure of ½ to 1 lb./sq.in. gauge registered on the regulator of the nitrogen cylinder. Stopcock *A* was then closed and the flexible tubing disconnected from the end of the isoteniscope. The isoteniscope then was inverted over a suitable container and a sample taken by opening Stopcock *A*.

A mercury-filled Dubrovin gauge (*4* and *5*), calibrated against a McLeod gauge, was used to measure all pressures. These readings were reproducible to within ±0.05 mm. Hg. After each run the zero point of the gauge was checked by closing the stopcock on the isoteniscope, closing the air bleeds on the pressure regulator, and allowing the vacuum pump to exhaust the system. Use of a relatively large quantity of suitable heat transfer oil in the bath as thermal ballast maintained the temperature manually to within ±0.02°C. All temperatures were measured with a Leeds and Northrup semiprecision potentiometer in conjunction with a copper-constantan thermocouple which had been calibrated against a National Bureau of Standards certified platinum resistance thermometer.

The materials used in the experiments were C. P. grade aniline and nitrobenzene, which were redistilled at 10 mm. Hg abs. pressure at a reflux ratio of 20 to 1 in an 8-ft. frac-

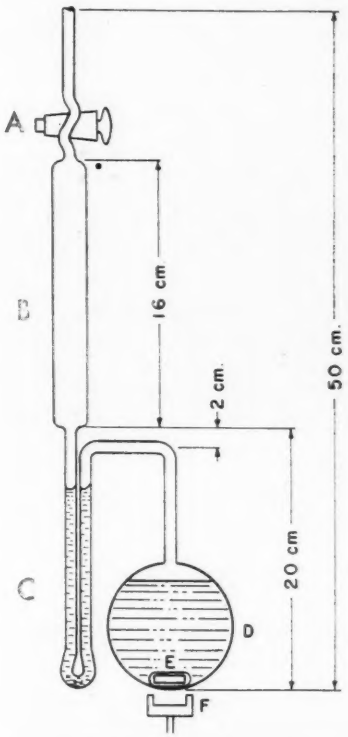

Fig. 1. Modified isoteniscope: *A*, 4-mm. oblique vacuum stopcock; *B*, entrainment trap and partial condenser (14-mm. tubing); *C*, U-tube manometer (10-mm. heavy-wall tubing); *D*, 200-ml. balloon flask; *E*, glass-covered magnetic stirrer bar; *F*, rotating bar magnet.

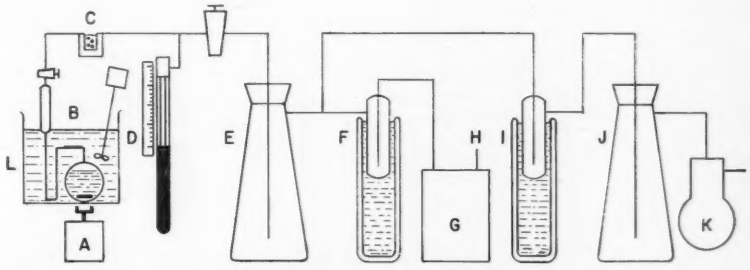

Fig. 2. Total pressure apparatus: *A*, magnetic stirrer; *B*, isoteniscope; *C*, cold trap; *D*, Dubrovin gauge; *E*, 4-liter ballast flask; *F*, cold trap; *G*, Cenco electronic manostat; *H*, air bleed; *I*, cold trap; *J*, 4-liter ballast flask; *K*, vacuum pump; *L*, oil bath.

TABLE 1.—EXPERIMENTAL DATA

Pressure, mm. Hg	Temperature, °C.	Pressure, mm. Hg	Temperature, °C.
100 mole % nitrobenzene		9.98 mole % aniline	
2.07	55.27	2.26	55.32
2.77	60.22	3.12	60.30
3.76	65.20	4.20	65.27
4.99	70.25	5.57	70.30
6.55	75.17	7.33	75.20
8.58	80.25	9.60	80.30
11.01	85.25	12.30	85.30
13.93	90.25	15.67	90.32
17.62	95.42	19.83	95.42
16.03 mole % aniline		25.45 mole % aniline	
1.83	50.55	2.08	50.40
2.52	55.45	2.74	55.32
3.42	60.35	3.73	60.32
4.60	65.25	5.02	65.30
6.04	70.35	6.64	70.32
7.90	75.30	8.72	75.22
10.33	80.35	11.30	80.20
13.23	85.27	14.48	85.29
16.66	90.32	18.29	90.25
39.01 mole % aniline		47.41 mole % aniline	
2.29	50.42	3.32	55.40
3.11	55.32	4.49	60.35
4.21	60.32	5.93	65.32
5.66	65.25	7.93	70.37
7.46	70.35	10.39	75.27
9.81	75.22	13.44	80.35
12.72	80.30	17.16	85.30
16.28	85.30		
59.52 mole % aniline		76.40 mole % aniline	
2.65	50.47	2.08	45.62
3.56	55.30	2.91	50.70
4.68	59.82	3.91	55.50
6.40	65.22	5.34	60.40
8.50	70.27	7.19	65.40
11.10	75.17	9.50	70.45
14.41	80.27	12.44	75.40
18.40	85.30	16.13	80.47
		19.19	83.72
100 mole % aniline			
3.25	50.57		
5.96	60.30		
8.01	65.25		
10.70	70.42		
13.90	75.45		
18.05	80.32		

tionating column, 1.5 in. in diam., packed with protruded stainless steel half rings. First cuts from the column were discarded. After a steady head temperature had been reached, the condensate product was collected in the distillate receivers. The contents of the receivers were stored under a nitrogen blanket in dark glass bottles until they were used in the experimental work. No tests for purity for either component were made other than the measurement of vapor pressure. These pressure-temperature relationships are tabulated in Table 1 and plotted in Figure 3. In addition to the pure components, seven mixtures of aniline and nitrobenzene covering the composition range were prepared and run in the apparatus as described in the preceding paragraphs. After each run with the mixtures the contents of the isoteniscope were removed and analyzed for aniline content by the method of Markunas and Riddick(7). A weighed portion of sample was titrated with $N/10$ perchloric acid in glacial acetic acid. Results of analyses were reproducible within 0.2 wt. % aniline.

EXPERIMENTAL DATA

The experimental data are presented in Table 1, in which readings of pressure and temperature are recorded for each mixture and for the pure components. These data are plotted in Figure 3 to enable the reader to visualize the pressure-temperature relationships. In order to facilitate mathematical treatment of the raw data, an Antoine vapor-pressure equation was fitted to each set of readings. This equation empirically expresses the relationship between pressure and temperature and has the following form:

$$\log_{10}(p^\circ \text{ or } P_t) = C + \frac{D}{E+t} \quad (1)$$

The constants C, D, and E were obtained by a least squares technique for the pressure range between 2 and 20 mm. Hg. The precision with which each curve represents the experimental data was determined by statistical analysis to be ± 0.15 mm. in nineteen out of twenty observations. A tabulation of the constants is presented in Table 2.

Literature data for completely determining the absolute accuracy of the total pressure measurements by comparison are not available. A rough idea of the accuracy to be expected, however, may be obtained by comparing the experimental pressure-temperature relationships for pure aniline with measurements

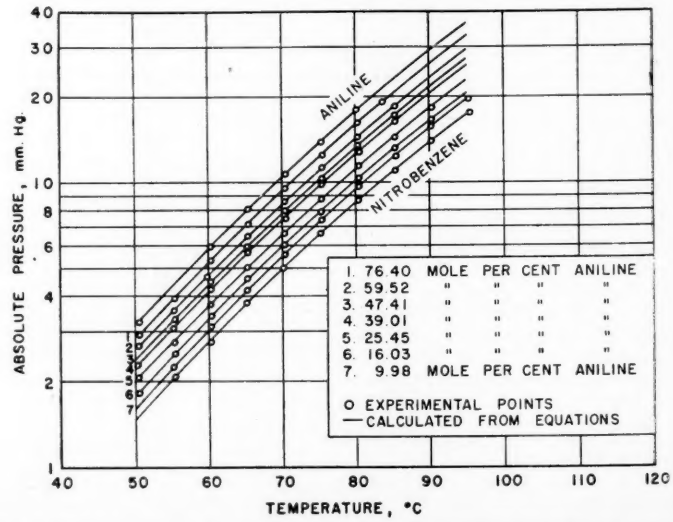
ABSOLUTE PRESSURE, mm Hg
TEMPERATURE, °C
ANILINE
NITROBENZENE
1. 76.40 MOLE PER CENT ANILINE
2. 59.52 " " " "
3. 47.41 " " " "
4. 39.01 " " " "
5. 25.45 " " " "
6. 16.03 " " " "
7. 9.98 MOLE PER CENT ANILINE
O EXPERIMENTAL POINTS
—CALCULATED FROM EQUATIONS

Fig. 3. Total pressures vs. temperature for the aniline-nitrobenzene system.

TABLE 2.—TABULATION OF CONSTANTS IN TOTAL PRESSURE EQUATION

Composition, mole %	C	D	E
100 Nitrobenzene	6.2576	−1279.117	159.90
9.98 Aniline	6.7021	−1449.532	173.09
16.03 Aniline	6.1114	−1184.762	152.04
25.45 Aniline	7.6387	−1950.693	215.84
39.01 Aniline	7.0323	−1586.584	187.33
47.41 Aniline	7.1491	−1639.674	191.98
59.52 Aniline	7.2130	−1665.063	194.71
76.40 Aniline	7.2520	−1635.551	190.23
100 Aniline	6.8102	−1400.285	171.76

already in the literature. That is, between 5 and 20 mm. Hg, the measured temperatures are from 0.21°C. higher to 0.08°C. lower than the data of Rechenberg(*8*), from 0.41°C. higher to 0.94°C. lower than the data of Stull(*13*), and 0.07°C. higher than the single data point of Gould, Holzman, and Niemann(*5*). Unfortunately the vapor pressures of nitrobenzene cannot be compared in a similar manner because literature data cannot be found which appear accurate enough for this purpose in the range of 1 to 20 mm. abs.

Comparison of vapor pressures does not give complete information on the accuracy of total pressure measurements. Additional obvious errors which might occur when the pressure of a mixture is measured are (*a*) the change in the liquid composition caused by vaporization of more volatile constituent into the vapor space above the solution and (*b*) errors in analysis of solutions. The maximum vaporization error may be estimated by assuming that the entire space is filled with vapors of the more volatile constituent at the maximum pressure and average temperature of the measurements. For the isoteniscope used in the experiments the error resulting from "vapor holdup" is —0.04 mole % in the liquid based on the assumptions previously described. From analysis of made-up solutions of aniline and nitrobenzene, the analytical error appeared to be a maximum of ±0.10 mole %. The maximum over-all error originating with composition changes, therefore, is estimated to be —0.14, +0.06 mole %.

CALCULATION OF VAPOR-LIQUID DATA FROM EXPERIMENTAL DATA

Two assumptions were used in computing vapor-liquid data from the total pressure data: (*a*) the vapor phase will behave as an ideal gas at 5 and 10 mm. and (*b*) activity coefficients can be expressed by some integrated form of the Gibbs-Duhem equation. It should be pointed out that any integrated form of the Gibbs-Duhem equation applies only at constant temperature and pressure. Guggenheim(*6*), however, shows that the external pressure has little effect upon the liquid-phase activity coefficient at total pressures up to several atmospheres. He integrates the differential form of the Planck function defined as

$$dY = \frac{H}{T^2}dT - \frac{V}{T}dP_t - R\ln P_1 dn_1 - R\ln P_2\, dn_2 \quad (2)$$

at constant temperature and composition into the form

$$\ln\left(\frac{P_{1_{P_t=P_t}}}{P_{1_{P_t=0}}}\right) = \frac{(P_t-0)\ V_1'}{RT} \quad (3)$$

The quantity $\gamma_1 x_1 p_1^\circ$ may be substituted for P_1 so that Equation (3) may be written

$$\ln\left(\frac{\gamma_{1_{P_t=P_t}}}{\gamma_{1_{P_t=0}}}\right) = \frac{(P_t-0)\ V_1'}{RT} \quad (4)$$

which expresses the change in the activity coefficient with external pressure. Even at several atmospheres $P_t V_1' << RT$, and so the effect of pressure on the activity coefficient in the pressure region of 2 to 30 mm. Hg is negligible. The effect of temperature change on the activity coefficients, however, usually is quite large, and the calculations must include such effects. The following discussion will present the calculation procedures employed.

The calculation is started by drawing up several pressure-vs.-composition plots (each plot at constant temperature) from the total pressure equations or from the graph of total pressure vs. temperature. These plots cover the entire range of boiling temperatures of the mixtures at 5 and 10 mm. For each constant-temperature plot the constants in the integrated form of the Gibbs-Duhem equation are determined by curve-fitting techniques. These constants are then correlated as a function of temperature by a graph. Another cross plot of the total pressure data is made, this time at the pressure for which the vapor-liquid data are desired (actually a boiling point curve). For ten or twelve liquid compositions the boiling temperatures are read from the boiling point curve, and the constants for the integrated form of the Gibbs-Duhem equation are obtained from the plot of constants vs. temperature. The activity coefficients then are calculated for the proper liquid composition. The next step is to use activity coefficients, liquid compositions, and vapor pressures to calculate the vapor compositions. A few trial calculations may be necessary to obtain the exact boiling temperature which makes the summation of the vapor mole frac-

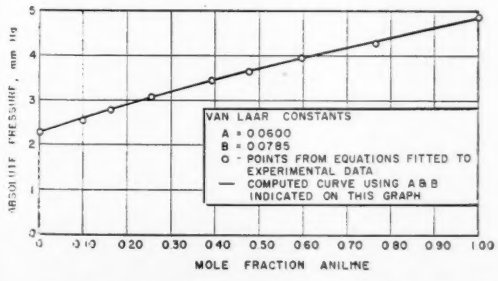
ABSOLUTE PRESSURE, mm Hg
VAN LAAR CONSTANTS
A = 0.0600
B = 0.0785
O - POINTS FROM EQUATIONS FITTED TO EXPERIMENTAL DATA
— COMPUTED CURVE USING A & B INDICATED ON THIS GRAPH
MOLE FRACTION ANILINE

Fig. 4. Total pressure at 57°C.

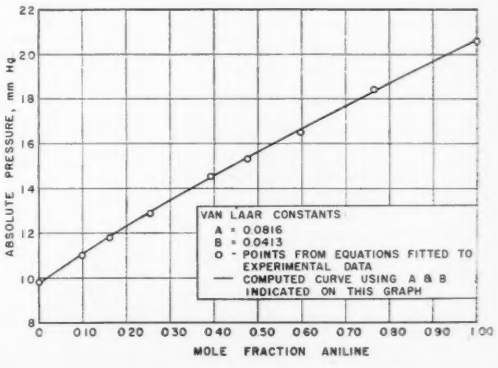
ABSOLUTE PRESSURE, mm Hg
VAN LAAR CONSTANTS
A = 0.0816
B = 0.0413
O - POINTS FROM EQUATIONS FITTED TO EXPERIMENTAL DATA
— COMPUTED CURVE USING A & B INDICATED ON THIS GRAPH
MOLE FRACTION ANILINE

Fig. 5. Total pressure at 83°C.

tions equal to unity. These adjustments are usually small and represent minute inaccuracies in the data and/or the empirical nature of the integrated form of the Gibbs-Duhem equation used. The following paragraphs will illustrate the application of the procedure to the calculation of the vapor-liquid equilibrium for aniline nitrobenzene at 5 and 10 mm. Hg abs.

Figures 4 and 5 are representative pressure-vs.-composition plots at constant temperatures of 57° and 83°C. These plots were obtained by substituting the respective temperatures into the total pressure equations derived from the experimental data. They might as easily be obtained directly from Figure 3, but with somewhat less accuracy than by using the equations. In addition to Figures 4 and 5 constant-temperature plots were also made at 62°, 67°, 72°, and 77°C. in the calculations. For the sake of brevity, these plots are not included. Table 3, however, tabulates the total pressure-vs.-composition data at the chosen temperatures of 57°, 62°, 67°, 72°, 77°, and 83°C.

Before the calculations were started, it was necessary to select the type of solutions to the Gibbs-Duhem equation which would express the activity coefficients for this system. As discussed by Carlson and Colburn(*1*), the choice of the type of solutions depends upon the value of AV_2/BV_1 as well as whether or not $V_2 = V_1$. At the start of the computations an estimation of AV_2/BV_1 for the aniline-nitrobenzene system indicated that the ratio might approximate 1.0 at the average temperature. In addition, at the midtemperature, V_1 is nearly equal to V_2. It appeared, therefore, that either the van Laar or Margules solutions might be applicable. Since, however, the van Laar equations gave good fits to the experimental data and are somewhat more easily handled in calculations than the Margules equations, they were selected for making the computations. The van Laar equations are

$$\log \gamma_1 = \frac{A}{\left(1+\frac{Ax_1}{Bx_2}\right)^2} \qquad (5)$$

$$\log \gamma_2 = \frac{B}{\left(1+\frac{Bx_2}{Ax_1}\right)^2} \qquad (6)$$

The constants in the van Laar equations were obtained by successive trial calculations for each of the constant-temperatures, 57° through 83°C. These calculations were carried out by use of the following equation, which relates the total pressure to the activity coefficients as well as vapor pressures and liquid compositions:

$$P_t = \gamma_1 x_1 p_1^\circ + \gamma_2 x_2 p_2^\circ \qquad (7)$$

The activity coefficients, of course, are functions of the A and B values as shown in Equations (5) and (6). The labor in fitting a set of A and B values to the constant-temperature plots was shortened by machine computation. In these computations a number of sets of A and B values were tried until the deviations from the experimental total pressures were minimized. The computed total-pressures-vs.-composition curve appears as a solid line on Figures 4 and 5, and the best values of the van Laar constants for each particular temperature are listed in Table 3. Temperature variation of A and B throughout the boiling-temperature range of the solutions was correlated by fitting the A and B values determined in the previous step on a graph (*see* Figure 6).

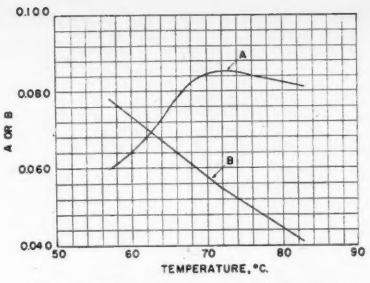

Fig. 6. Change in A and B with temperature.

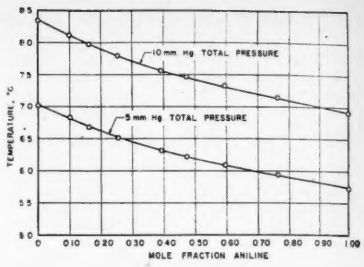

Fig. 7. Boiling-point curves for the aniline-nitrobenzene system.

TABLE 3.—TOTAL PRESSURES IN MM. HG ABS. OF THE EXPERIMENTAL SOLUTIONS AT THE INDICATED TEMPERATURES, AND THE VAN LAAR CONSTANTS GIVING THE BEST FIT TO THE TOTAL PRESSURES AT THE SAME TEMPERATURE

Temperature, °C.	Compositions, mole % 100% Nitrobenzene	9.98 Aniline	16.03 Aniline	25.45 Aniline	39.01 Aniline
57°C.	2.29	2.53	2.77	3.08	3.46
62°C.	3.11	3.44	3.81	4.15	4.67
67°C.	4.17	4.62	5.04	5.52	6.22
72°C.	5.52	6.13	6.66	7.27	8.20
77°C.	7.21	8.06	8.68	9.49	10.72
83°C.	9.81	11.01	11.77	12.92	14.56

Compositions, mole % 47.41 Aniline	59.52 Aniline	76.40 Aniline	100 Aniline	van Laar constants A	B
3.66	3.96	4.33	4.89	0.0600	0.0785
4.93	5.33	5.85	6.61	0.0680	0.0706
6.57	7.09	7.83	8.82	0.0805	0.0640
8.66	9.33	10.35	11.63	0.0857	0.0540
11.30	12.16	13.54	13.13	0.0840	0.0495
15.35	16.88	18.45	20.54	0.0816	0.0413

The boiling point curves for the system at 5 and 10 mm. Hg were obtained from the total pressure equations and are shown in Figure 7. They could also be cross-plotted from Figure 3 but with a decreased accuracy. These curves are used to get an approximate starting point for the final calculations and also for a comparison with computed boiling temperatures. In most situations, therefore, a simple cross plot of the total pressure data is all that is required.

The final calculations for obtaining the vapor composition in equilibrium with a given liquid composition were made by trial computations using the boiling point curve, vapor pressure curves, and the van Laar constants curves. For a given liquid composition a boiling temperature was obtained from the boiling point curve. This temperature was inserted in the vapor pressure equation for aniline and nitrobenzene, and the respective vapor pressures were computed. A and B were obtained at the same temperature from Figure 6. The activity coefficients, γ_1 and γ_2, were calculated from Equations (5) and (6). Vapor pressures, liquid composition, activity coefficients, and

TABLE 4.—VAPOR-LIQUID COMPOSITIONS AT 5 MM.

x_1, mole fraction aniline in liquid	γ_1, activty coefficient of aniline	γ_2, activity coefficient of nitrobenzene
0.050	1.1825	1.0006
0.100	1.1551	1.0024
0.200	1.1125	1.0080
0.300	1.0821	1.0160
0.400	1.0594	1.0264
0.500	1.0418	1.0398
0.600	1.0277	1.0569
0.700	1.0163	1.0792
0.800	1.0077	1.1079
0.900	1.0021	1.1456
0.950	1.0005	1.1691

y_1, mole fraction aniline in vapor	t, °C., boiling point	α, relative volatility
0.118	69.2	2.54
0.216	68.1	2.48
0.372	66.1	2.37
0.495	64.5	2.29
0.595	63.1	2.21
0.682	61.9	2.14
0.757	60.8	2.08
0.824	59.9	2.01
0.886	59.0	1.95
0.944	58.2	1.89
0.972	57.8	1.85

TABLE 5.—VAPOR-LIQUID COMPOSITIONS AT 10 MM.

x_1, mole fraction aniline in liquid	γ_1, activity coefficient of aniline	γ_2, activity coefficient of nitrobenzene
0.050	1.1674	1.0008
0.100	1.1381	1.0030
0.200	1.0958	1.0103
0.300	1.0665	1.0204
0.400	1.0452	1.0329
0.500	1.0294	1.0476
0.600	1.0179	1.0641
0.700	1.0096	1.0824
0.800	1.0042	1.1035
0.900	1.0010	1.1248
0.950	1.0003	1.1370

y_1, mole fraction aniline in vapor	t, °C., boiling point	α, relative volatility
0.116	82.3	2.49
0.212	81.1	2.42
0.366	79.0	2.31
0.488	77.2	2.23
0.590	75.7	2.16
0.678	74.3	2.10
0.755	73.1	2.05
0.824	72.0	2.00
0.887	71.1	1.96
0.945	70.1	1.91
0.973	69.7	1.89

total pressure were inserted in the following equations and the vapor compositions were calculated:

$$y_1 = \frac{\gamma_1 \, x_1 \, p_1^\circ}{P_t} \qquad (8)$$

$$y_2 = \frac{\gamma_2 \, x_2 \, p_2^\circ}{P_t} \qquad (9)$$

In all calculations use of the temperatures from the boiling point curve resulted in the summation of the vapor mole fractions being equal to 1 within the precision of the vapor pressure data.

For each pressure the vapor compositions for eleven liquid compositions were computed. Tables 4 and 5 present the x-y data activity coefficients, and boiling temperatures obtained and also values of α, the relative volatility, as a function of liquid composition. Since the computed boiling point curve is identical with the curve obtained by cross-plotting the data on Figure 3, no attempt was made to include it on Figure 7 in addition to the experimental curve. A statistical estimate of the precision of the data was made in which it was found that in nineteen out of twenty instances the vapor compositions will be expressed within ±0.9% and the relative-volatility values obtained will be precise within ±1.5%.

Just as in the case of the vapor pressure of nitrobenzene, paucity of data makes it difficult to compare these results with others to obtain an estimate of the absolute accuracy. Docksey and May (*2*), however, determined vapor-liquid data for aniline nitrobenzene at 10 mm. total pressure by the method of Rosanoff, Bacon, and White (*11*). Unfortunately, they presented only a graph of the equilibrium compositions and did not include a tabulation of the x-y values or of the boiling temperatures. It is impossible, therefore, to test the thermodynamic consistency of their data and to draw direct comparisons for estimating accuracies. Relative volatilities, however, may be estimated from the Docksey and May data. Such estimations indicate a value of α between 1.90 and 2.00 over the composition range. These values may be compared with the relative volatilities in Tables 4 and 5, which are from 1.85 to 2.54.

It will be noted from Figure 6 that the van Laar constant A goes through a maximum at about 72°C. and the value of B decreases steadily with increasing temperature. As pointed out by Carlson and Colburn (*1*), the variation of A and B with temperature may be related to the heat of mixing. The change in the trend of A with temperature, therefore, may indicate that the heat of mixing changes sign within the range of temperatures over which the data for this system were obtained. Since no data on heats of mixing for this system are available in the literature, calculations cannot be made which might indicate the validity of the A curve.

ACKNOWLEDGMENT

The authors wish to thank A. E. Hoerl for his assistance in making the computations.

NOTATION

A, B = constants in van Laar solutions to the Gibbs-Duhem equation

C, D, E = constants in the Antoine equation

p° = general vapor pressure, mm. Hg

$P_{1,2}$ = partial pressure of components (1) and (2), mm. Hg

P_t = total pressure, mm. Hg

t = temperature, °C.

V = molar volume, cc./g.mole

V_1' = partial molal volume, $(\partial V/\partial n_1)_{T, P, n_2}$

x = mole fraction in liquid

y = mole fraction in vapor

γ = Raoult's law activity coefficient

α = relative volatility, y_1x_2/x_1y_2

subscript 1 refers to aniline

subscript 2 refers to nitrobenzene

LITERATURE CITED

1. Carlson, H. C., and A. P. Colburn, *Ind. Eng. Chem.*, **34**, 581-589 (1942).
2. Docksey, P., and C. J. May, *J. Inst. Petroleum Tech.*, **21**, 175-199 (1935).
3. Dubrovin, J., *Instruments*, **6**, 194 (1933).
4. Germann, F. E. E., and K. A. Gagos, *Anal. Chem.*, **15**, 285-286 (1943).
5. Gould, C., G. Holzman, and C. Niemann, *Anal. Chem.*, **19**, 204-206 (1947).
6. Guggenheim, E. A., "Thermodynamics," Interscience Publishers, New York (1949).
7. Markunas, P. C., and J. A. Riddick, *Anal. Chem.*, **23**, 337-339 (1951).
8. Rechenberg, C. von, "Einfache und fraktionierte Destillation," Schimmel and Co., Leipzig (1923).
9. Redlich, O., and A. T. Kister, *J. Am. Chem. Soc.*, **71**, 505-507 (1949).
10. Redlich, O., A. T. Kister, and C. E. Turnquist, *Chem. Eng. Progr., Symposium Series*, No. 2, **48**, pp. 49-61 (1952).
11. Rosanoff, M. A., C. W. Bacon, and R. H. White, *J. Am. Chem. Soc.*, **36**, 1803-1825 (1914).
12. Smith, A., and A. W. C. Menzies, *J. Am. Chem. Soc.*, **32**, 1412 (1910).
13. Stull, D. R., *Ind. Eng. Chem.*, **39**, 517-540 (1947).
14. Wohl, K., *Trans. Am. Inst. Chem. Engrs.*, **42**, 215-249 (1946).

Presented at A.I.Ch.E. Washington meeting

Low-temperature Oxidation of Ammonia in Fixed and Fluidized Beds

H. F. Johnstone, J. D. Batchelor, and C. Y. Shen, University of Illinois, Urbana, Illinois

The oxidation of ammonia in the presence of manganous oxide-bismuth oxide catalyst supported on small alumina spheres was studied in both fixed and fluidized beds in the temperature range from 205° to 250°C. The column used was 4½ in. in diameter and 43 in. high. The experiments were made so that the transport effects in the fluidized bed might be separated from the chemical kinetic effects.

In accordance with the theory of two-phase fluidization proposed in a previous paper, comparison is made between the reaction rate associated with the discontinuous phase and that associated with the continuous phase as estimated from the results in the fixed bed. The over-all reaction-rate constants in the fluidized bed can be related to those in the fixed bed by an exponential term in the superficial gas velocity, V^n; n is a constant which depends on the reaction system and the size and type of the reactor.

Little information has been published on reaction kinetics in fluidized beds. Gilliland, Mason, and Oliver reported that at the same space velocity a fluidized bed gives a lower conversion for a homogeneous gas reaction than does a fixed bed (*4*). This was attributed to mixing and by-passing in the bed. On the basis of pressure drop studies, Toomey and Johnstone (*10*) suggested that a fluidized bed may be considered to be composed of two phases: a continuous phase consisting of uniformly dispersed particles in a supporting gas stream and a discontinuous phase consisting of pure gas in the form of bubbles, channels, or slugs. On this basis an equation was developed for the variation of pressure drop with gas velocity.

In a fluidized catalytic reactor the two-phase concept implies that the type and degree of contact between the gas and solid will be completely different for the two phases. For the most part the gas in the continuous phase supports the catalyst particles and flows through the interstices in a manner analogous to the flow in a fixed bed. As the rate of flow of gas in the continuous phase is limited by the formation of the discontinuous phase, the flow in this phase is always laminar, at least for beds of small spherical particles. For a given bed the reaction rate in the continuous phase should depend on molecular diffusivities and be independent of the presence of the discontinuous phase. The actual concentrations of the reactants, however, will usually depend on the rate of transfer between the phases, which will be affected by the motion of the discontinuous phase.

In general there will be some supplementary reaction in the discontinuous phase, or at the phase boundary, which cannot be assigned definitely to the continuous phase. At the point of incipient two-phase fluidization, however, all the reaction may be assigned to the continuous phase; any increase in reaction rate at higher gas velocities must be associated directly or indirectly with the discontinuous phase. It will be interesting to apply this concept to actual kinetic data and to develop a method of estimating the rate in a fluidized bed from the constants obtained for a fixed bed.

The reaction used for studying the effect of fluidization on the re-

J. D. Batchelor's present address is Pittsburgh Consolidation Coal Company, Library, Pennsylvania; C. Y. Shen is with Monsanto Chemical Company, Dayton, Ohio.

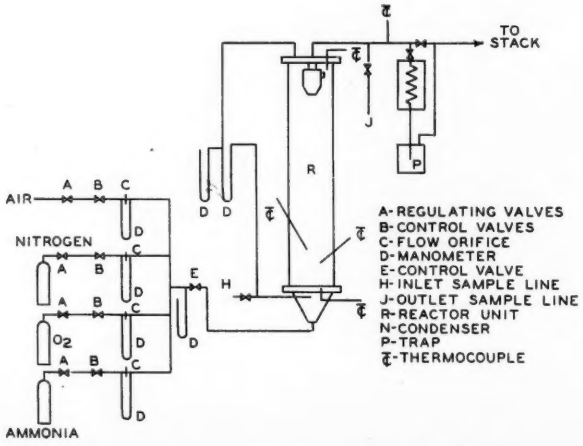

Fig. 1. Flow diagram of experimental equipment.

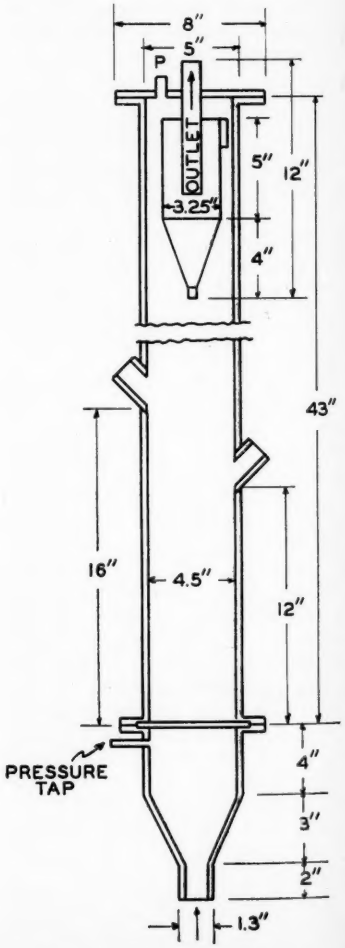

Fig. 2. Fluidized-bed unit.

TABLE 1.—PROPERTIES OF CATALYST FRACTIONS

Fraction	Geometric mean diameter, μ	Geometric standard deviation	Particle density,* g./cc.	Apparent density, g./cc.	%MnO (dry basis)	$\%Bi_2O_3$ (dry basis)
165-200 mesh	103	1.19	2.08	1.10	3.51	3.75
120-165 mesh	139	1.14	2.05	1.05	3.48	3.63
+120 mesh	178	1.23	2.01	1.00	3.43	3.51
Unsized	103	1.36	2.06	1.08	4.20	4.15

*By displacement of mercury.

action kinetics in a fluidized bed was the low-temperature oxidation of ammonia. This reaction has been investigated thoroughly in a tubular reactor (*5*), and the catalyst, manganous oxide and bismuth oxide, was shown to have a constant activity over several hundred hours.

The mechanism of ammonia oxidation of temperatures around 1,000°C. has been studied by Bodenstein (*2*) and Zawadzki (*11*). At lower temperatures, in the range from 200° to 300°C., Nagel (*9*) found that nitrous oxide is the principal product of the reaction. A more detailed study with metallic oxide catalysts was made by Krauss (*8*). In a fixed bed of manganous oxide–bismuth oxide, Kobe and Hosman (*7*) obtained a maximum yield of 71% nitrous oxide in the temperature range from 175° to 300°C. at space velocities of 3.5 to 6 $min.^{-1}$ The mechanism studies at low temperatures in the tubular reactor (*5*) showed that the rate depends on the amount of adsorbed oxygen on the catalyst and the concentration of ammonia in the gas phase.

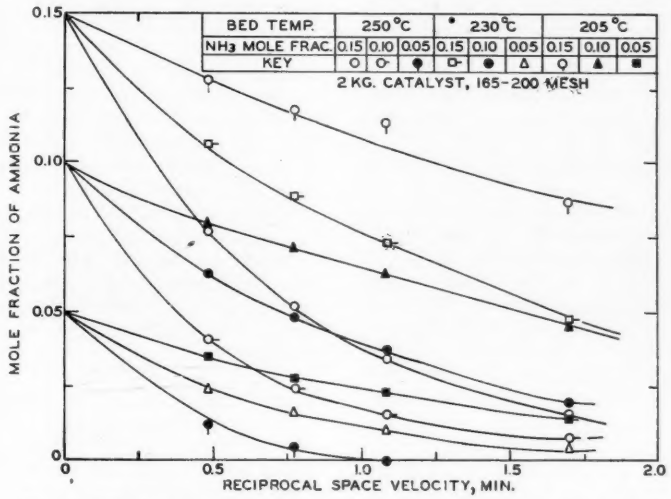

Fig. 3. Effect of temperature, concentration, and contact time on ammonia oxidation in fixed-catalyst beds.

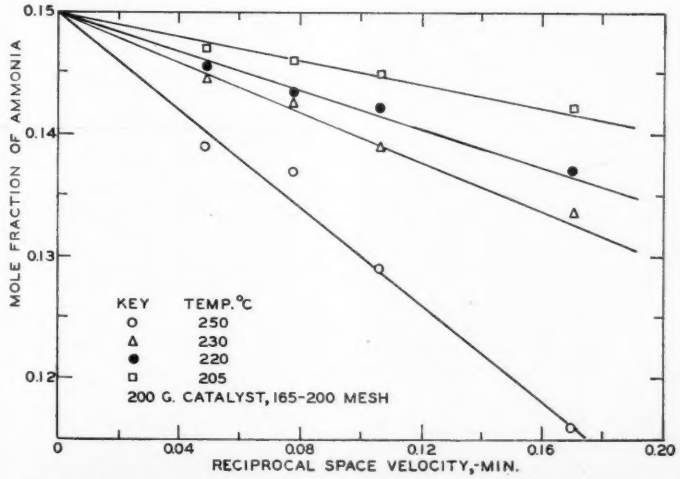

Fig. 4. Effect of temperature on oxidation rate at high ammonia concentration and low contact time in fixed beds.

EXPERIMENTAL

Apparatus

The equipment used is shown in Figure 1. The flow of cylinder gases was regulated with ½-in. needle valves and measured through calibrated sharp-edged flowmeters. The reactor, 4½ in. I. D. and 43 in. high, was constructed from type-310 stainless steel. The lower flange was connected to a conical inlet section and held a stainless steel porous plate which supported the bed and distributed the gas flow uniformly. The upper flange supported the cyclone separator for removing the catalyst particles from the gas. The small amount of catalyst collected in the cyclone was returned to the reactor at the end of each series of runs. Details of the reactor are shown in Figure 2. It was heated by six 750-watt Chromalox resistance strip heaters which were controlled automatically. Later the heaters were replaced by three sections of chromel ribbon wound on alundum insulation to give more uniform temperature distribution. Temperatures of the fluidized bed were measured by two iron-constantan thermocouples in stainless steel wells located in the axis of the column. Thermocouples were also installed on the porous plate and on the reactor walls near the geometric centers of the heated sections. The exit gas lines were heated electrically to prevent condensation of water.

Catalyst

The catalyst was made by impregnation of Alcoa XF-21-Si (low soda) alumina fluid-cracking catalyst. One kilogram of the alumina particles was first dampened with 250 cc. of a solution containing 100 g. manganous nitrate and 35 g. bismuth nitrate. The impregnated catalyst was dried in a steam heated vacuum oven for 5 days prior to heating in a large electric furnace at 375°C. for 2 days. Part of the dried catalyst was separated by sieving on 120-, 165-, and 200-mesh screens. Final size distributions in each fraction were determined by measuring 300 particles under a microscope. The geometric mean diameters, standard deviations, and other properties of the catalysts are shown in Table 1. The catalyst particles were generally smooth and rounded but not truly spherical.

Procedure

Before a reaction run was made, a weighed portion (3 to 6 kg.) of one

of the impregnated catalyst fractions was placed in the reactor through the top of the column, which was then heated to the reaction temperature while the bed was fluidized with air. When the reaction temperature was reached and the temperature controller was operating smoothly, a series of measurements was made on the pressure drop across the bed; the air rate was started much higher than required to fluidize the bed and was reduced in steps to a value below the fluidization rate. The pressure-drop curve was determined by decreasing the air rate to avoid any static friction effects near the minimum fluidization point.

The oxygen-ammonia gas stream was then substituted for the air flow. At least 2 hrs. was allowed for the attainment of steady state. The gauge pressure at the bed outlet was set at about 9 cm. of water, and the absolute pressure at E (Figure 1) was regulated to 820 mm. Hg. Simultaneous inlet and outlet gas samples were drawn through weighed tubes of magnesium perchlorate and Ascarite for the determination of water vapor, ammonia, and nitrogen peroxide(*5*). The volumes of gas sampled at the rate of about 0.01 cu.ft./min. were measured with wet test meters. The oxygen and ammonia flow rates, the pressure drop across the bed, the orifice downstream pressure, and the temperature were also noted.

A sample of the gas leaving the absorption tubes was mixed with a measured volume of pure hydrogen in an Orsat-type gas burette and the oxygen content determined by absorption in Oxsorbent. The nitrous oxide was then reacted with the hydrogen in a slow combustion pipette, and the decrease in volume was equivalent to the volume of nitrous oxide present. Nitrogen was determined from the volume of the remaining gas.

RESULTS IN FIXED-BED REACTOR

In the low-temperature oxidation of ammonia, several simultaneous reactions can occur to give various products. In order to interpret the results in the fluidized bed, experiments were made at low gas velocities in the same apparatus under the same conditions but with the catalyst stationary. A gas mixture containing 10% ammonia and 90% oxygen was first passed at various rates through the empty reactor at 250°C. to determine whether the metallic surface of the reactor wall and the porous support might have some catalytic effect. No reaction took place under these conditions.

The results obtained with a bed of 2 kg. of 165- to 200-mesh catalyst at 250°, 230°, and 205°C. at different space velocities are shown in Figure 3. At high temperatures and low gas velocities the extent of conversion is high and the possible error is greater than it is at low temperatures and low velocities.

To overcome the high conversion at high temperatures, the weight of catalyst was reduced to 200 g. The results at the higher space velocities are shown in Figure 4. For each temperature the rate of oxidation is independent of the concentration above 12% ammonia in the gas mixture. Thus under these conditions the reaction follows approximately an over-all zero-order process.

In a previous paper the mechanism of the low-temperature oxidation was shown to be a bimolecular surface reaction involving adsorbed oxygen atoms and ammonia diffusing to the surface(*5*). The reaction may be expressed by

$$NH_3 + [O]_{ads} \longrightarrow \text{intermediate} \longrightarrow \text{oxidized product} \qquad (1)$$

The suggested intermediates are hydronitrous acid, hydroxylamine, or imide(*2, 11*). The rate is represented by the equation

$$\frac{d(NH_3)}{d\tau} = k[O]_{ads}[NH_3] \qquad (2)$$

where τ is the reciprocal space velocity expressed as volume of catalyst per unit of volumetric gas-feed rate. The volume of the catalyst is obtained from the weight of catalyst in the bed and the absolute density shown in Table 1. The reciprocal space velocity obtained in this way differs from the conventional definition by a factor of $1/(1-\varepsilon)$, where ε is the void fraction. The expression can be extended to the fluidized region without the confusion of uncertain values of ε in the expanded catalyst bed. Furthermore, if a Langmuir type of isotherm describes the adsorption of oxygen, Equation (1) becomes

$$-\frac{d(NH_3)}{d\tau} = \frac{k'\sqrt{(O_2)}}{1+\sqrt{K(O_2)}}(NH_3) \qquad (3)$$

where K is the adsorption equilibrium constant. At atmospheric pressure the concentration of each reactant may be replaced by its respective partial pressure.

$$-\frac{dp_{NH_3}}{d\tau} = \frac{k' p_{NH_3}\sqrt{p_{O_2}}}{1+\sqrt{K p_{O_2}}} \qquad (3a)$$

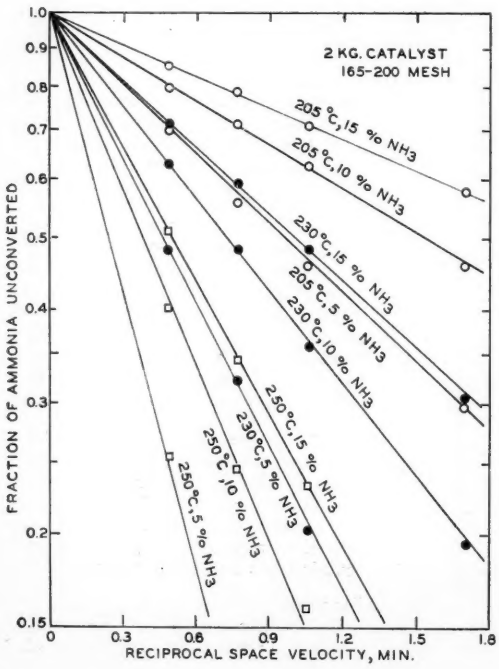

Fig. 5. Oxidation of ammonia following first-order reaction in fixed beds.

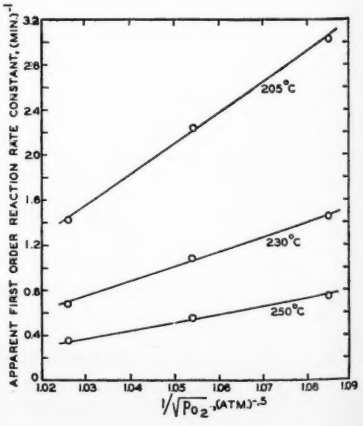

Fig. 6. Effect of temperature and oxygen pressure on apparent first-order reaction.

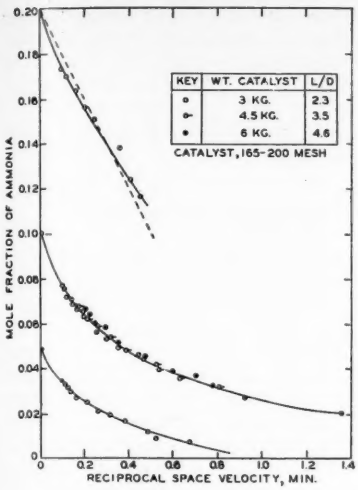

Fig. 7. Effect of initial concentration of NH_3 on oxidation rate at 250°C. in fluidized beds. Dotted line represents zero-order rate calculated from data for fixed-bed reactors.

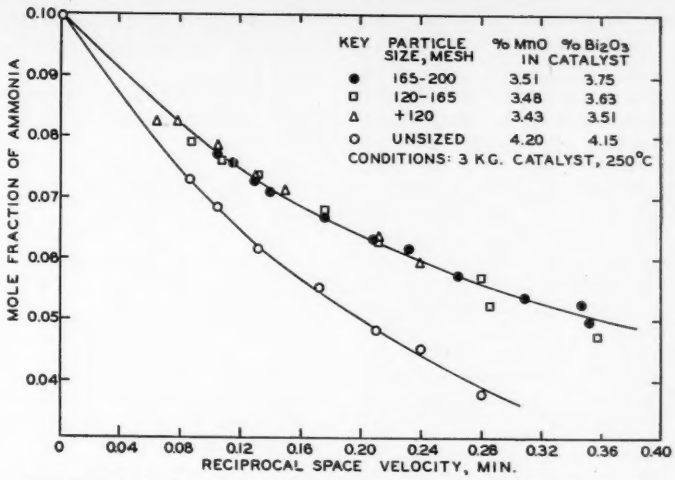
KEY | PARTICLE SIZE, MESH | % MnO IN CATALYST | % Bi2O3 IN CATALYST
165-200 | 3.51 | 3.75
120-165 | 3.48 | 3.63
+120 | 3.43 | 3.51
UNSIZED | 4.20 | 4.15
CONDITIONS: 3 KG. CATALYST, 250°C
MOLE FRACTION OF AMMONIA
RECIPROCAL SPACE VELOCITY, MIN.

Fig. 8. Effect of catalyst size and composition on oxidation rate in fluidized beds.

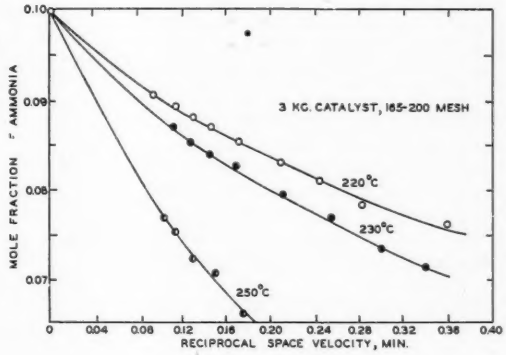

Fig. 9. Effect of temperature and contact time on oxidation rate in fluidized beds.

In the present work a high oxygen: ammonia ratio was used so that the concentration of oxygen remained essentially constant. Thus, Equation (3*a*) represents a pseudo first-order reaction which on integration becomes

$$\ln (1 - \alpha) = -k'_1 \tau \qquad (4)$$

where α is the fraction conversion. Figure 5 is a replot of the data in Figure 3, which show that the results are in agreement with the first-order equation. The rate constant k'_1 depends on the average partial pressure of oxygen as indicated by

$$k'_1 = \frac{k' \sqrt{p_{O_2}}}{1 + \sqrt{K p_{O_2}}} \qquad (4a)$$

A plot of $1/k'$ vs. $1/\sqrt{p_{O_2}}$ yields a straight line at a given temperature, as shown in Figure 6, from which the value of k' and the adsorption equilibrium constant can be determined. When the right-hand side of Equation (4) is small, $\exp(-k'_1\tau)$ can be expanded into a series and all terms except the first are negligible, or

$$\alpha = k'_1 \tau \qquad (5)$$

It is this apparent zero-order reaction that is shown in Figure 4. At 250°C. k'_1 is 1.33 min.$^{-1}$ The error in $(1-\alpha)$ resulting from using only the first two terms of $\exp(-k'\tau)$ at τ equal to 0.2 min. is about 5%. Since the product yield in a zero-order process depends only on the time of contact with the catalyst, the reaction rate in this range is substantially the same in a fluidized bed as in a fixed bed under the same conditions.

RESULTS IN FLUIDIZED BEDS

The work on fluidized beds was carried out in the same apparatus but at higher gas velocities (*1*). The velocity for minimum fluidization was determined from pressure-drop measurements. The pressure drop was plotted against the gas velocity, and the sharp break extrapolated from the fixed- and fluidized-bed regions was assumed to be the minimum fluidization point.

The complete results of the kinetic studies, showing the effects of ammonia concentration, particle size of catalyst, and temperature on the reaction rate, are shown in Figures 7 to 9. The space velocity was calculated in the same way as for the fixed bed. The method does not differentiate between the bubbles of gas and the gas that supports the catalyst; however, it does allow a correlation of the data from fixed beds with those from fluidized beds. Increasing the bed depth maintained the same space velocity in the fluidized bed as was used for the fixed-bed studies. The effect of temperature is approximately the same as for the fixed bed, but the over-all conversion cannot be correlated with the first-order relationship of Equation (4). In Figure 7 the dotted line represents the zero-order rate determined from Figure 6 by use of the corresponding average partial pressure of oxygen.

The particle size of the catalyst does not have much effect on the reaction rate in the range from +120 to 165-200 mesh, as shown in Figure 8. The higher activity of the unsized catalyst may be caused by its higher content of active metallic oxides.

DISCUSSION OF RESULTS

The change in conversion rate in going from a fixed-bed to a fluidized reactor depends on the effect on the rate of chemical reaction and on the physical nature of

the gas-solid contact in the bed. If only a portion of the gas contacts the catalyst and the rest bypasses the bed in the form of bubbles, then the over-all rate depends on the rate of transfer from the discontinuous phase to the continuous phase in contact with the solids and on the rate of chemical reaction at the surface. If one assumes that the effective contact and the transfer rate between the gas and the catalyst particles may be expressed as an exponential function of the gas velocity, the over-all rate constant for the fluidized bed for a constant temperature becomes

$$k'_f = AV^n \qquad (6)$$

The constant A is related to the fixed-bed reaction-rate constant, because when the velocity approaches that of minimum fluidization, the rate constant defined by Equation (6) should agree with the value obtained from the fixed bed. Then

$$k'_1 = AV_{mf}^n \qquad (7)$$

and

$$\frac{k'_f}{k'_1} = \left(\frac{V}{V_{mf}}\right)^n \qquad (8)$$

Substitution of Equation (6) into the first-order rate equation gives

$$-\frac{dp_{NH_3}}{d\tau} = AV^n (p_{NH_3}) \qquad (9)$$

This involves the assumptions that the over-all rate is proportional to the partial pressure of ammonia in the gas, and the partial pressure of oxygen remains constant in the reactor.

Since $\tau = W/\rho V$, integration under isothermal and isobaric conditions gives

$$\int_p^{p(1-\alpha)} \frac{dp}{p} = \frac{AW}{\rho} \int_\infty^V V^{n-2} dV \qquad (10)$$

If n is less than one, then

$$\ln(1-\alpha) = \frac{AW}{\rho(n-1)} V^{n-1} \qquad (11)$$

A plot of—$\ln(1-\alpha)$ vs. the volumetric gas velocity on a logarithmic scale is shown in Figure 10. In the fluidized range of velocities, the lines are parallel. From the slope, the value of n is 0.17. Since n is positive, the reaction rate is faster in the fluidized bed than in the fixed bed at the same space velocity. A similar conclusion was reached by Kivnick and Hixson (*6*) for the reduction of nickel oxide in a fluidized bed, although no measurements were made in the fixed-bed region. The value of n obtained by them was approximately 0.70. Thus n is determined by the nature of the gas-solid reaction, but it appears to be independent of particle size, as shown in Figure 10.

For reactions that are not zero order, either by-passing of the gas as bubbles or mixing of the gas in the fluidized bed will result in a lower reaction rate in a fluidized reactor than in a fixed bed. Although the mass transfer constant in a fluidized bed was found by Chu (*3*), it is not possible to draw the conclusion that the reaction mechanism in a fluidized bed is changed to a diffusion — controlling step. The vigorous movement of particles inside a fluidized bed may also increase the effectiveness of the particle surface for a chemical reaction.

The relative values of A estimated from the intercepts in Figure 10 are shown in Figure 11 together with the reaction-rate constants from the fixed-bed data. The activation energy obtained from the slope of the lines is 14.8 kcal./g. mole. It is the same as for the fixed bed when the same catalyst is used.

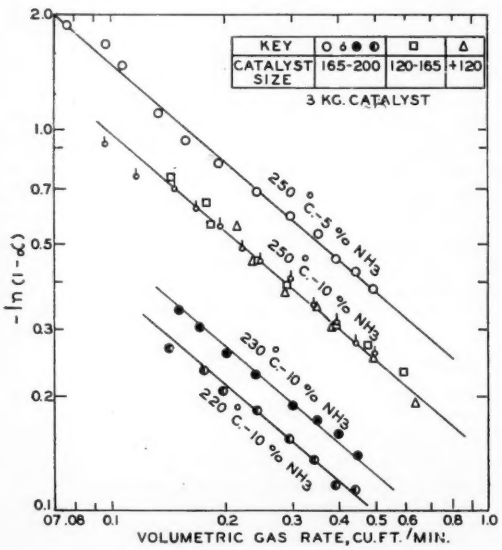

← Fig. 10. Effect of gas velocity on conversion rate in fluidized beds.

TWO-PHASE FLUIDIZATION THEORY

The concept of two-phase fluidization may be used to explain the observed kinetic data. When the gas rate is sufficient to produce two-phase fluidization, the total reaction is the sum of that in each phase. From the flow characteristics alone, the formation of the discontinuous phase is expected to decrease the over-all percentage conversion. However, if there is mass transfer between the phases, or any supplementary reaction in the discontinuous phase, the over-all rate may increase. The increase in pressure drop with gas velocity above the point of two-phase fluidization (*10*) is given by

$$\frac{\Delta p_{ke}}{\Delta p_{mf}} = (lD_p^{0.5} - m) \ln \frac{V}{V_v} \qquad (12)$$

Δp_{ke} is the kinetic-energy loss caused by bubbles of the discontinuous phase passing through the continuous phase. This should also be a measure of the degree of contact of the two phases, and the effect of the discontinuous phase on the reaction rate should in a similar manner depend on the flow rate.

The pressure-drop measurements showed that the flow rate at minimum fluidization is 70 to 85% of the value at incipient two-phase fluidization. Since there was no way of observing the initial formation of the second phase in the reactor, the lower value was used

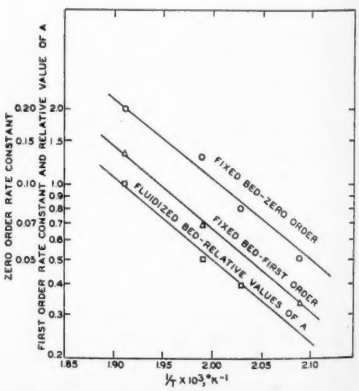
ZERO ORDER RATE CONSTANT
FIRST ORDER RATE CONSTANT AND RELATIVE VALUE OF A
FIXED BED-ZERO ORDER
FIXED BED-FIRST ORDER
FLUIDIZED BED-RELATIVE VALUES OF A
1/T X 10³, °K⁻¹

Fig. 11. Variation of reaction-rate constants with temperature.

to estimate the flow rate at which the discontinuous phase was just formed in the kinetic studies. The corresponding value of the fractional conversion, α_c, was found from Figures 7 and 9 and the rate of reaction in the continuous phase was calculated from

$$R_c = (\alpha_c)\,(V_v)\,(y_1) \qquad (13)$$

The reaction rate in the discontinuous phase was then found from

$$R_d = R - R_c \qquad (14)$$

The ratios R_d/R_c for all the data obtained with the fluidized bed are plotted in Figure 12. The lines are represented by

$$\frac{R_d}{R_c} = K_s \log \frac{V}{V_v} \qquad (15)$$

The slopes and intercepts evaluated by the method of least squares are shown in Table 2.

For the pressure-drop data, the slope of the $\Delta p_{ke}/\Delta p_{mf}$ vs. log V lines is a function of $Dp^{0.5}(10)$. A slight effect of the size of the column was also noted, as was to be expected. For the reaction-rate data, the effect of particle size is quite different, since the surface area related to the reaction rates is not the same as that affecting the pressure drop. The reaction rate in the continuous phase should be directly proportional to the surface area per unit volume of the bed. Thus

$$R_c \propto \frac{6\,(1-\epsilon)}{D_p} \qquad (16)$$

At constant gas velocity the reaction rate in the discontinuous phase is determined by the surface area of the bubbles. It may be postulated that the initial size of the bubbles is proportional to the interstitial space between the particles. The bubbles initially formed coalesce and become larger as they ascend. Thus the bubble surface is proportional to D_p^{-2} or

$$\frac{R_d}{R_c} \propto \frac{1}{D_p} \qquad (17)$$

Since $\Delta p_{ke}/\Delta p_{mf}$ is proportional to $D_p^{0.5}$, then

$$\frac{R_d}{R_c} \propto D_p^{-1.5}\,\frac{\Delta p_{ke}}{\Delta p_{mf}} \qquad (18)$$

or

$$\frac{R_d}{R_c} \propto D_p^{-1} \ln \frac{V}{V_v} \qquad (19)$$

In a comparison of Equations (19) and (15), the slope K_s is seen to be inversely proportional to the diameter of the catalyst particles.

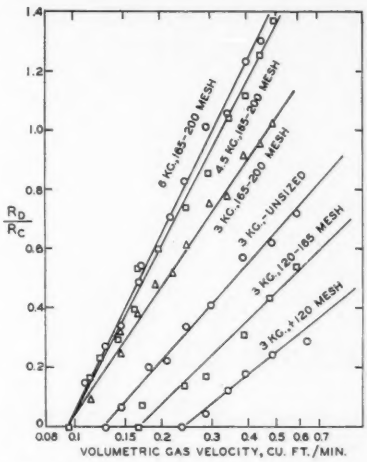

Fig. 12. Effect of gas velocity on reaction rates in discontinuous phase. Initial ammonia concentration 10%, 250°C.

TABLE 2.—VALUES OF THE CONSTANTS K_s AND V_v IN EQUATION (15)

Fluidized bed Weight, kg.	Size	K_s	Gas rate at incipient fluidization, V_v, std. cu.ft./min.
3	165-200 mesh	1.44	0.094
4.5	165-200 mesh	1.87	0.094
6	165-200 mesh	2.01	0.094
3	+120 mesh	0.73	0.238
3	120-165 mesh	0.97	0.173
3	unsized	1.09	0.125

CONCLUSIONS

The reaction rate at incipient fluidization can be estimated from the rate in the fixed bed; hence Equation (15) should be useful for estimating the reaction rate in a fluidized bed. Since the value of K_s undoubtedly depends on the type and size of reactor, this effect should be investigated with other reactions before Equation (15) can be accepted for general scale-up purposes. The results indicate that the reaction rate in a fluidized bed can be divided into two parts: the part that is related only to the chemical kinetics can be predicted from the rate in a fixed bed; the part that depends on mass transfer from the discontinuous phase is a function of the gas velocity and is independent of the particle size.

ACKNOWLEDGMENT

The authors express their appreciation to the Dupont Company for support of a graduate fellowship during part of the work, which was completed as part of the program of the Engineering Experiment Station.

NOTATION

A = a constant defined by Equation (6)
D_p = diameter of catalyst particle, ft.
k, k' = reaction-rate constants
k'_1 = first-order rate constant, min.$^{-1}$
k'_f = reaction-rate constant in fluidized bed
K = adsorption equilibrium constant
K_s = slope defined by Equation (16)
l, m, n = constants
p = partial pressure; subscript NH_3 and O_2 denote ammonia and oxygen, respectively, atm.
Δp = pressure drop; subscript mf refers to incipient fluidization of ke to excess drop above fluidization, lb./sq.in.
R = conversion rate; subscript c refers to continuous phase, and d refers to discontinuous phase, lb.moles/min.
T = temperature, °K.
V = volumetric gas velocity; subscript v refers to incipient fluidization, cu.ft./min.
W = weight of catalyst, lb.
y = concentration of ammonia; subscript l refers to inlet, moles/cu.ft.

Greek Letters

α = fraction conversion
τ = reciprocal space velocity, min.
ρ = absolute density of catalyst, lb./cu.ft.
ϵ = void fraction

LITERATURE CITED

1. Batchelor, J. D., Ph.D. thesis, University of Illinois (1952).
2. Bodenstein, M., *Trans. Electrochem. Soc.*, 71, 353 (1937).
3. Chu, J. C., J. Kalil, and W. A. Wetteroth, *Chem. Eng. Progr.*, 49, 141 (1953).
4. Gilliland, E. R., E. A. Mason, and R. C. Oliver, *Ind. Eng. Chem.*, 45, 1177 (1953).
5. Johnstone, H. F., E. T. Houvouras, and W. R. Schowalter, *Ind. Eng. Chem.*, 46, 702 (1954).
6. Kivnick, A., and A. N. Hixson, *Chem. Eng. Progr.*, 48, 394 (1952).
7. Kobe, K. A., and R. D. Hosman, *Ind. Eng. Chem.*, 40, 397 (1948).
8. Krauss, W., *Z. Electrochem.*, 53, 320 (1949).
9. Nagel, A. V., *Z. Electrochem.*, 36, 754 (1930).
10. Toomey, R. D., and H. F. Johnstone, *Chem. Eng. Progr.*, 48, 220 (1952).
11. Zawadzki, J., *Discussions Faraday Soc.*, No. 8, 140 (1950).

(Presented at A.I.Ch.E. New York meeting)

Liquid-liquid Extraction in Continuous-flow Agitated Extractors

A. W. Flynn and R. E. Treybal
New York University, New York

Extraction studies were made with the systems toluene water benzoic acid and kerosene water benzoic acid in two dimensionally similar cylindrical extractors, one 6 in. in diameter by 6 in. high, the other 12 in. in diameter by 12 in. high. Each extractor contained four radial baffles, of width equal to 16.7% of the extractor diameter. The extractors were agitated by six-bladed dimensionally similar turbine impellers, the diameters of which were in each case one third the diameter of the extractor.

When the extractors were full of liquid, i,e., in the absence of an air-liquid interface, the power required for a given impeller speed was independent of the rate of flow of liquid. However, such operation required more power than the equivalent open-tank agitator, and more baffling was required to produce fully turbulent flow.

Flow rates were varied from 0 to 4,000 lb./hr. and solvent-to-water mass ratios from 3:1 to 1:6. Extraction stage efficiencies were found to be appreciable even at zero agitator speed.

The additional stage efficiency produced by agitation was found to be a function of the power input per unit volume of liquid flowing. This relationship permitted the correlation of all extraction efficiency data for a given system at a constant solvent-to-water ratio over eight-fold range of power input. It was found possible to predict the performance of an extractor in continuous flow from batch-extraction measurements through the methods of MacMullin and Weber.

In the case of transfer of material between two immiscible liquid phases by agitation in a vessel, the relationship between rate of mass transfer and power required for agitation is of interest. The power consumption of agitators operating in a single liquid phase has been investigated by Rushton and coworkers (*12* and *13*) and Mack and his associates (*4, 5, 6*). They have presented methods of predicting the power consumption of an agitator based on size, speed, and liquid properties. Miller and Mann (*9*) studied the operation of agitators in various systems composed of two immiscible liquid phases. In all these studies there was no flow of liquid through the tank.

In the case of mass transfer, batch systems were studied by Mack and Marriner (*7*) and Hixson and Smith (*2*), and more recently continuous-flow systems were studied by Oldshue and Rushton (*10*), Hein (*1*), Karr and Scheibel (*3*), and Overcashier and his associates (*11*).

The present study was undertaken to determine the effect of agitator speed and power, vessel size, rate of flow, and phase ratio on the stage efficiency of agitated extractors and to confirm if possible the published procedures for predicting continuous-flow performance from batch-operation tests.

EQUIPMENT

Two dimensionally similar extraction vessels, as shown in Figure 1, were made for the tests. Constructed of commercially available glass tubing clamped between two flat metal plates, each vessel was provided with four radial baffles each 16.7% of the

This paper is an abridgment of the thesis of Arthur W. Flynn submitted in partial fulfillment of the requirements for the degree of Doctor of Engineering Science at New York University (1953).

A. W. Flynn is at present with Nuclear Development Associates, White Plains, New York.

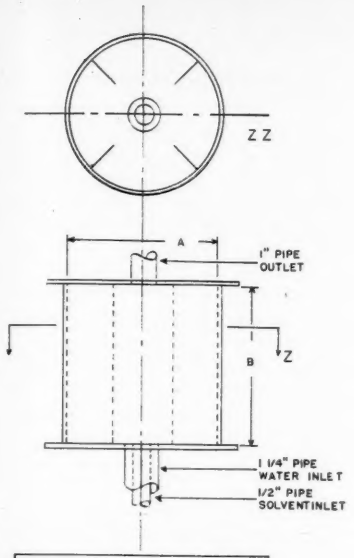

SIZE	A	B
6" EXTRACTOR	5 3/4"	6 1/8"
12" EXTRACTOR	11 1/8"	12 1/4"

Fig. 1. Extraction vessel.

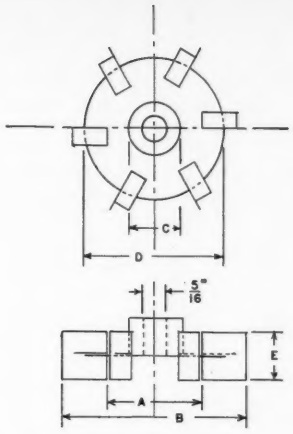

SIZE	A	B	C	D	E
2" IMPELLER	1	2	1/2	1 1/2	13/32
4" IMPELLER	2	4	1	3	13/16

Fig. 2. Agitator impeller.

vessel diameter in width. The agitator impeller, the diameter of which was one third the vessel diameter, was driven by a shaft passing through the vertical outlet pipe and was located at the center of the vessel. The agitator impellers, as shown in Figure 2, were flat-bladed radial turbines constructed by welding six flat plates to a circular plate and stiffening the assembly by welding small reinforcing tabs to the backs of the radial blades.

The tests were performed in the equipment arrangement shown in Figure 3. All extraction studies were made with the top cover and wall baffles in place and with all entrapped air removed from the equipment. There were four parts to the investigation: (1) power measurements, (2) measurements of the phase ratio of the liquid in the vessel, (3) extraction measurements during continuous flow, and (4) batch-extraction measurements.

POWER MEASUREMENTS

The power input to the impellers was determined as a function of speed, phase ratio of liquids, and rate of flow. In all cases the baffles were in place and the liquid level was maintained in the "chimney" to prevent aeration of the liquid. The power measurements were taken by varying the speed of the agitator from 300 to 1,100 rev./min. for the 6-in. extractor and 100 to 350 rev./min. for the 12-in. and reading the tachometer and dynamometer. Power was determined electrically at low inputs where the dynamometer scale read less than 1 lb.

The determination of small power values of agitator power input required a number of precautions to ensure accuracy. The drive motor was a small D.C. shunt motor with oil-lubricated bearings. Before each test the bearings were freshly oiled and the motor operated for between 45 and 60 min. to permit stabilizing the bearing and winding temperatures. The motor was operated at constant field current to eliminate that variable from consideration. The armature resistance was determined at the normal operating temperature and the armature input power was measured by meters of 0.5% accuracy. The motor-power output was determined by subtracting the armature resistance losses and the stray power losses from the armature power input. The no-load power input was checked frequently to detect any change in the motor or tachometer friction. The agitator power measurements are believed accurate to within ±5%.

Physical properties of the various liquids used in the tests are listed in Table 1.

The measured power data were used to calculate the power numbers and the Reynolds numbers. Figure 4 shows the individual power numbers for agitation of single liquids plotted against the corresponding Reynolds numbers for 16.7% baffles.* This type of plot was previously used by Rushton, Costich, and Everett(*13*). Whereas at high Reynolds numbers the water, toluene, and sucrose-solution power numbers lie on a single straight line for both sizes of vessel, those for kerosene do not.

The width of the baffles in the 6-in. extractor was then increased to 25% of the vessel diameter and the tests were repeated. In Figure 5 the impeller power numbers are plotted against Reynolds number for the 25% baffles. Identical curves were obtained for the sucrose solution, kerosene, and water, but not for the more viscous motor oil. When, however, the tests were repeated after the liquid level in the vessel was lowered until a small air space was formed under the top cover, all the liquids provided a single curve, as shown by the dotted curve in Figure 5.

TABLE 1.—PHYSICAL PROPERTIES OF LIQUIDS USED

Liquid	Density, lb./cu.ft.	Viscosity, centipoises
Water	62.2	0.95
Toluene	54.0	0.59
Kerosene	51.2	2.52
Sucrose-water solution	69.3	3.38
Motor oil	55.8	87.5

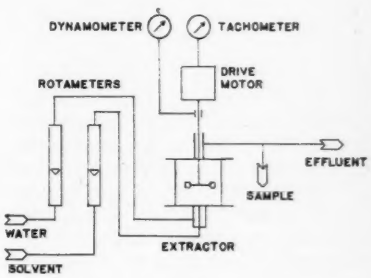

Fig. 3. Flow diagram.

Rushton(*12*) has shown that for reliable prediction of the performance of a large-scale agitator from measurements on a small-scale one it is necessary that both operate fully baffled. In addition when a given agitator is operated fully baffled the power number is a function solely of the Reynolds number. For open vessels operated with an air-liquid interface, a fully baffled condition (or "standard" baffling) is provided by four radial baffles each one-twelfth the tank diameter in width. From Figures 4 and 5 it can be seen that neither arrangement of agitator and baffles meets the condition of full baffling when vessels are operated without an air-liquid interface. This condition has not been reported in the literature as existing

*Complete tabular data are obtainable as document 4653 from the Photoduplication Service, American Documentation Institute, Library of Congress, Washington 25, D.C., for $1.25 for photoprints or microfilm.

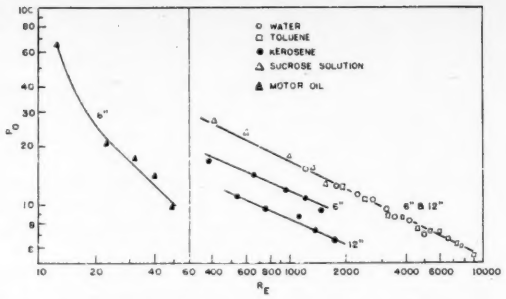

Fig. 4. Power number correlation; 6- and 12-in. extractors, 16.7% baffles.

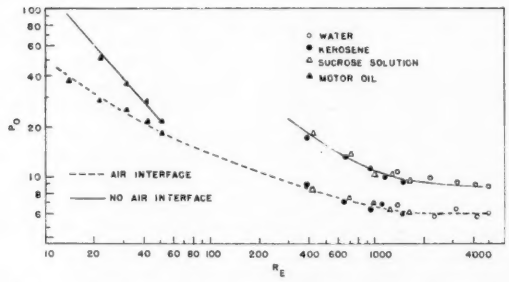

Fig. 5. Power number correlation; 6-in. extractor, 25% baffles.

in large commercial-size vessels although the baffles in such vessels are much narrower than the ones employed in these tests. The need for more baffling to provide for a fully baffled condition when the agitators are operated full of liquid may be a characteristic which is limited to small-scale vessels. The present conclusion is that more work must be done on these matters, and they are being explored further.

The effect of rate of liquid flow through the equipment on the power required for a given agitator speed was too small to be detected.

The power required for agitation of the single liquids water, toluene, or kerosene is so nearly the same for each that reliable measurements of the effect of mixing two insoluble phases could not be made. For the toluene-water mixtures encountered in extraction measurements, the power requirement was calculated from Figure 4 by use of the average viscosities and densities of Miller and Mann (*10*). Because the behavior of kerosene was different from water and did not produce a common power - number–Reynolds - number curve with 16.7% baffles, it was felt that the Miller and Mann interpolation should not be used with mixtures of kerosene and water. Experimentally the power required for agitating these mixtures could scarcely be distinguished from that for water alone, and the latter is used in reporting the subsequent extraction data.

PHASE RATIO OF VESSEL CONTENTS

A comparison was made between the ratio of the insoluble liquids in the feed to the extraction vessel during continuous operation and the ratio in the vessel contents at steady state. This was done by operating at fixed rate of flow of liquids, phase ratio, and impeller speed until steady state was reached. The liquid flow and the impeller rotation were then suddenly stopped, the liquids in the vessel allowed to separate into two layers, and their relative volumes measured. Tests were made only on the 12-in. vessel because its larger dimensions permitted greater accuracy in the measurements. The results are presented in Table 2. The holdup of organic liquid was very small at zero agitator speed. With a rotating agitator, at all but the slowest speeds the ratio of the phases in the vessel approached that in the feed mixture.

CONTINUOUS EXTRACTION

The equipment in Figure 3 was operated by extracting the benzoic acid from the organic phase into

TABLE 2.—ORGANIC LIQUID HOLD-UP

12-in. Extractor, 16.7% Baffles

Flow rate, lb./hr.		Solvent holdup, % of feed composition			
		Impeller speed, rev./min.			
Solvent	Water	0	150	250	350
		Solvent = toluene			
250	250	3.92	86.0	100	100
500	500	4.75	97.0	100	100
1,000	1,000	9.60	100	100	100
1,500	1,500	12.5	100	100	100
2,000	2,000	14.4	100	100	100
250	750	8.90	100	100	100
500	1,500	11.0	100	100	100
750	2,250	12.2	100	100	100
285	1,715	15.4	100	100	100
400	2,400	19.3	100	100	100
750	250	50.0	100	100	100
1,500	500	90.0	100	100	100
		Solvent = kerosene			
250	250	3.38	88.0	98.0	98.0
500	500	5.16	79.5	91.2	98.5
1,000	1,000	6.75	77.8	88.0	98.0
1,500	1,500	7.60	77.6	88.0	98.0
2,000	2,000	8.50	77.6	88.0	98.0
250	750	8.50	95.0	98.0	100
500	1,500	8.50	87.9	100	100
750	2,250	8.50	81.0	95.0	100
285	1,715	8.50	90.0	100	100
400	2,400	11.80	82.5	100	100
750	250	4.50	97.0	100	100
1,500	500	6.80	96.0	100	100

pure water. The effluent stream was sampled at the extractor outlet by collection of the mixed effluent in a 500-ml. graduate. The sample was allowed to separate into two layers. Samples for analysis were immediately pipetted from the settled liquids and titrated with fresh sodium hydroxide solution, phenolphthalein being used as an indicator. Alcohol was used with the organic layer to produce a single-phase mixture. In many of the runs the concentration change in the organic liquid was so small that it was difficult to check material balances exactly. In a typical run, for example, 9.25 cu.ft./hr. of a toluene–benzoic acid solution containing 0.0148 lb. mole of acid/cu.ft. was contacted with 9.01 cu.ft. of water/hr., acid free. The effluent water analyzed 0.000900 lb. mole of acid/cu.ft. The effluent toluene analyzed 0.0141 lb. mole of acid/cu.ft., which represents a discrepancy of 11% between the acid transferred from the toluene and that transferred to the water. On the other hand, a perfect material balance requires the toluene effluent to analyze 0.01402, which agrees with the observed value within the error of analysis. Similar agreement of observed and calculated effluent analysis of the organic liquid was obtained in 91% of the runs made. The remaining rates were not included in the final correlations. Mass transfer rates were calculated on the basis of water analyses owing to the larger percentage change in composition for that liquid.

A total of 149 extraction measurements was made on these systems, covering a range of from 500 to 4000 lb./hr. total flow, solvent-to-water ratios from 3:1 to 1:6, and dimension changes of 2:1.* Stage efficiencies were expressed as Murphree efficiencies based on water concentrations,

$$E = 100(C_{W2} - C_{W1})/(C_{We} - C_{W1}) \quad (1)$$

and since in every case C_{W1} equaled zero, this expression becomes simply $E = 100\ C_{W2}/C_{We}$. The stage efficiency E_0 at zero agitator speed was found to be appreciable even at low flow rates. This efficiency without agitation varied from 44.5% on the 6-in. extractor passing 250 lb./hr. of water and 250 lb./hr. of toluene to 92% for the same extractor passing 250 lb./hr. of water and 750 lb./hr. of toluene. Similar but lower values were found with kerosene. It was necessary to correct for this large initial efficiency in order to study the effect of agitation. This was done through the expression

$$E_A = 100(E - E_0)/(100 - E_0) \quad (2)$$

where E_A is the stage efficiency attributable to agitation, E is the over-all stage efficiency at any agitator speed, and E_0 that at zero agitator speed for the same liquid flow rate.

*See footnote, p. 325.

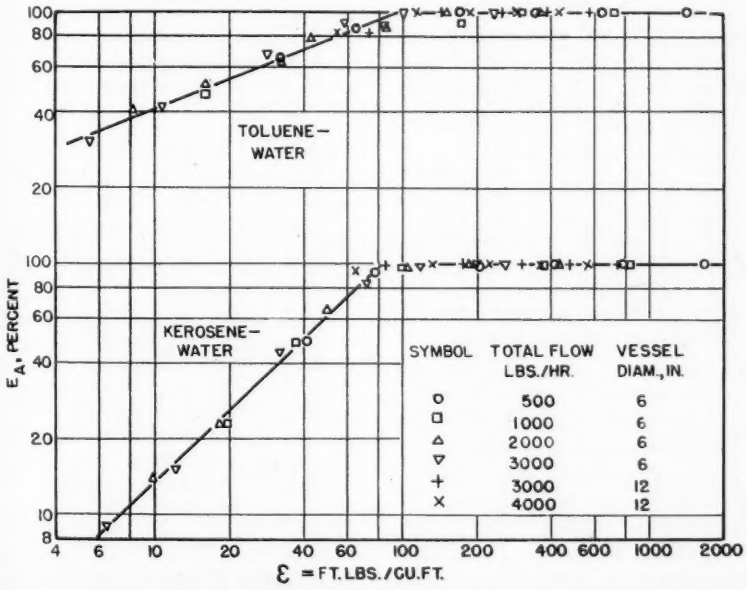

Fig. 6. Extraction of benzoic acid for equal rates of flow of organic and aqueous liquids.

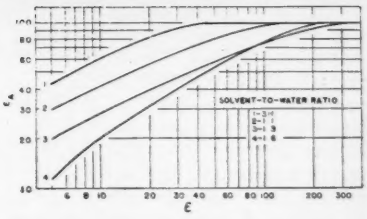

Fig. 7. Extraction efficiency summary, toluene water benzoic acid.

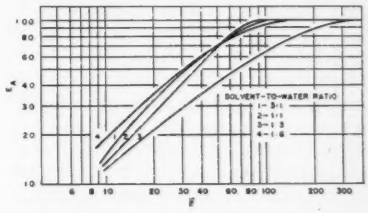

Fig. 8. Extraction efficiency summary, kerosene water benzoic acid.

The efficiency attributable to agitation for each system and each phase ratio when plotted against the agitator energy per unit volume of liquid flowing through the vessel, $\varepsilon = Pt/V$, gave rise to a single curve for all flow rates and for both vessel sizes. Figure 6, for example, shows the curves for the one-to-one flow ratio which result for the two systems. The remaining data are summarized in Figures 7 and 8. This provided the best correlation among the data and suggests a means of predicting the performance of larger scale equipment which is dimensionally similar.

In general greater solvent-to-water ratios increased the extraction efficiency, in opposition to the findings of Miller and Mann (*9*) and Hixson and Smith (*2*), who worked only with batch systems. The difference may be explained by the fact that in continuous operation the feed streams were directed into the impeller, which then did not have to lift the heavy liquid from the bottom of the vessel in order to mix it into the dispersion. In a batch operation the agitator must lift the heavy liquid, and when the proportion of heavy liquid is small, any of it which remains on the bottom of the vessel unmixed with the dispersion lowers the measured agitator efficiency. This is true whether the

efficiency is indicated by the mixing index of Miller and Mann(*9*) or the extraction rate as described by Hixson and Smith (*2*).

The continuous-flow extractor operates with complete and uniform mixing once the agitator speed exceeds a certain low value. Where the solvent-to-water ratio is high, the work required to produce the amount of interfacial area required for a given efficiency is less than when the ratio is low. This may be due to the fact that the degree of initial dispersion in the vessel is more a function of solvent than of water flow rate. This is confirmed by a study of many photographs made of the vessel in operation. When the initial dispersion is good, the initial E is high and only a small amount of work is required from the agitator to raise E to 100%. This small increase in E, however, represents a change in E_A between zero and 100%. Therefore, with large solvent-to-water ratio, less agitator power is required to increase E_A from zero to 100% than for the case of small ratios, where E is low. The exceptional behavior of the 6:1 solvent-to-water ratio mixtures in both systems may be related to the beginnings of emulsification which were observed with this ratio.

It was not found possible to produce a good correlation between the data for the two systems studied.

BATCH EXTRACTION

The effect of time on the extraction efficiency in batch operation was determined. Measured quantities of solvent containing benzoic acid and water were placed in the vessel without mixing. The agitator was then started and run for a measured length of time at constant speed. The time at which the clear layers of water and solvent disappeared was recorded as the time at which thorough agitation was attained. At the end of the agitation time the agitator was stopped and the mixture allowed to separate into two liquid layers. Samples of the solvent and water layers were then analyzed. All batch measurements were made in the 12-in. extractor because it held a sufficient quantity of material to ensure accuracy.

Over-all extraction efficiencies were calculated and used to predict the extraction efficiency of the equipment in continuous flow through the use of the method of MacMullin and Weber(*8*). As an example of the results for a flow of 2000 lb./hr. of toluene and 2000 lb./hr. of water the E_A measured in continuous flow was 79% while that calculated from batch data was 80%. For the kerosene system at the same flow rates the measured value was 92.4% and the calculated value was 88%. The good agreement between the calculated over-all efficiencies and the efficiency attributable to agitation indicates that it is possible to predict the extraction efficiency in continuous flow from batch measurements if all the extraction in both cases is attributable to agitation.

SUMMARY

1. It is tentatively concluded that an agitated vessel without an air-to-liquid interface may not behave as a fully baffled vessel even though it contains baffles considerably larger than those required by the same vessel operating with an air-to-liquid interface.

2. The extraction efficiency attributable to agitation is a function of the agitator energy input per unit volume of total liquid flowing. This relationship may be used to predict the performance of dimensionally similar equipment at a constant solvent-to-water ratio. This has been verified over a range of 8 to 1 in flow rate, 2 to 1 in dimensions, and 100 to 1 in agitator power input, with the same solvents and solute.

3. It is possible to predict the performance of the extraction equipment in continuous flow from batch measurements through the method of MacMullin and Weber provided that all extraction is attributable to agitation.

NOTATION

C = concentration of benzoic acid, lb.mole/cu.ft.
d = diameter of impeller, ft.
E = extraction stage efficiency, %
E_A = extraction stage efficiency attributable to agitation, %
g_c = conversion factor, 32.2 ft. (lb. force)/(sec.^{2}) (lb. mass)
n = impeller speed, rev./sec.
P = agitator power, ft.lb./sec.
P_o = power number $= Pg_c/\rho n^3 d^5$, dimensionless
Q = flow rate, cu.ft./sec.
R_E = Reynolds number $= d^2 n\rho/\mu$, dimensionless
t = holdup time, sec.
V = extractor volume, cu.ft.

Greek Letters

ε = specific energy, ft.lb./cu.ft.
μ = viscosity, lb./ft.sec.
ρ = density, lb./cu.ft.

Subscripts

K = kerosene
S = organic solvent
T = toluene
W = water
e = equilibrium condition
0 = zero impeller speed
1 = initial condition
2 = final condition

LITERATURE CITED

1. Hein, R. F., Ph.D thesis, University of Minnesota (1951).
2. Hixson, A. W., and M. I. Smith, *Ind. Eng. Chem.*, 41, 973 (1948).
3. Karr, A. E., and E. G. Scheibel, *Chem. Eng. Progr. Symp. Series* No. 10, 50, 73 (1954).
4. Mack, D. E., *Chem. Eng.*, 58, No. 3, 109 (1951).
5. Mack, D. E., and A. E. Kroll, *Chem. Eng. Progr.*, 44, 189 (1948).
6. Mack, D. E., and V. W. Uhl, *Chem. Eng.*, 54, No. 10, 115 (1947).
7. Mack, D. E., and R. A. Marriner, *Chem. Eng. Progr.*, 45, 545 (1949).
8. MacMullin, R. B., and M. Weber, *Trans. Amer. Inst. Chem. Engrs.*, 31, 409 (1935).
9. Miller, S. A., and C. A. Mann, *Trans. Amer. Inst. Chem. Engrs.*, 40, 709 (1944).
10. Oldshue, J. Y., and J. H. Rushton, *Chem. Eng. Progr.*, 48, 297 (1952).
11. Overcashier, R. H., H. A. Kingsley, Jr., and R. B. Olney, paper presented to Amer. Inst. Chem. Engrs., Washington (1954).
12. Rushton, J. H., *Chem. Eng. Progr.*, 47, 485 (1951).
13. Rushton, J. H., E. W. Costich, and H. J. Everett, *Chem. Eng. Progr.*, 46, 395 (1950).

Effect of Drying Conditions on Drying Rate and Physical Properties of a Porous Solid

E. H. Lebeis and T. A. Burtis
Houdry Process Corporation, Marcus Hook, Pennsylvania

Rate data are presented for both the constant – and the falling-rate drying of closely sized spheres of silica-alumina hydrogel. This hydrogel, which contains a fine powder, is the starting material from which petroleum cracking catalysts may be prepared. During the constant-rate period the drying rate is directly proportional to the difference between the dry- and wet-bulb temperatures of the air. In the falling-rate period the rate is proportional to the free water content, the proportionality factor being an undetermined function of the dry-bulb–wet-bulb differential.

Drying severity during the falling-rate period is shown to be the major determinant of the final pellet density. At constant wet-bulb temperature, density is inversely related to the dry-bulb–wet-bulb differential. If this differential is held constant, density is directly related to the wet-bulb temperature.

The variation in drying rate with position in the bed for through-circulation constant-rate drying of deep beds of particles is analyzed for the case where the direction of air flow is periodically reversed for equal time intervals. It is indicated that uniformity of drying should increase with an increase in air velocity, but decrease as bed depth is increased. At constant conditions and bed depth, large particles should dry more uniformly than small. Within normal operating ranges, air temperature and humidity should have little effect on drying uniformity.

In chemical processes in which solid catalysts are required, the physical as well as the catalytic properties of the solid are of great importance. This is especially true of petroleum cracking catalysts prepared from hydrogels. The properties of the final product are usually dependent upon the drying conditions employed. In the drying of hydrogels, from 5 to 15 lb. of water must be evaporated for every pound of catalyst produced. Drying equipment and operating costs therefore are generally high. This paper presents the results of an experimental study of the drying of spherical hydrogel catalyst particles undertaken to obtain basic rate data for equipment selection and design and to explore the effects of drying conditions on the physical properties of the catalyst.

When small particles of this type are dried by through circulation of air, the material is usually spread in a relatively deep multilayer bed(4). By use of this technique, a fairly high degree of heat economy can be achieved because the dry-bulb temperature of the air leaving the bed closely approaches the wet-bulb temperature. However, because of this change in dry-bulb temperature as the air passes through the bed, there is considerable variation in drying rate from one side of the bed to the other in this type of operation.

In order to eliminate this variation in the laboratory, the experimental work was limited to the drying of a single layer of particles. A small-scale dryer was built specifically for this program. The drying-rate data obtained should, strictly speaking, be applicable only

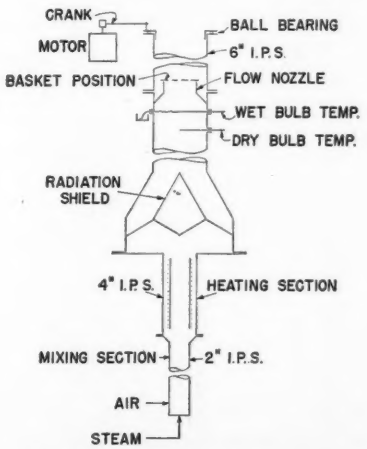

Fig. 1. Sectional view of dryer.

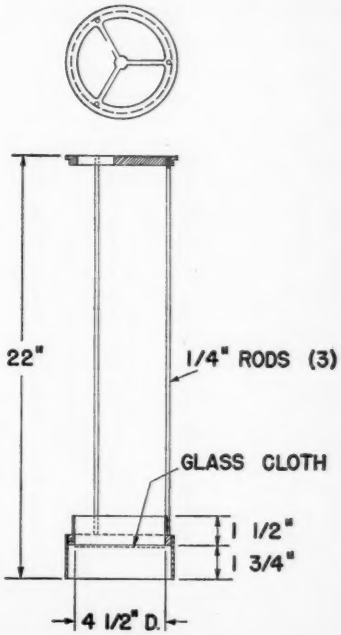

Fig. 2. Detail of dryer basket.

E. H. Lebeis is at present affiliated with Catalytic Construction Company, Philadelphia, Pennsylvania.

to single layers and not to deeper beds, as heat and mass transfer rates will differ somewhat for multiple layers because of the difference in air turbulence. For design purposes, however, the use of single-layer data is conservative. A method is given for predicting the degree of drying uniformity obtainable with multilayer beds. The effects of particle size, air velocity, temperature, and bed depth are discussed.

EQUIPMENT AND OPERATING PROCEDURE

A sectional drawing of the experimental dryer is shown in Figure 1. Metered quantities of preheated air and steam were introduced to the bottom section, which served as a mixing chamber. The mixed stream then flowed upward over an electrical heating element, which raised the temperature to the desired dry-bulb level.

A baffle was placed above this section to serve as a radiation shield between the material being dried and the heating element. Above this baffle the air dry- and wet-bulb temperatures were measured. The air was then passed through the layer of hydrogel spheres, or beads, and discharged from the dryer.

The basket in which the charge was suspended is shown in detail in Figure 2. The beads rested upon an open-meshed "leno-weave" glass cloth of 13 by 25 mesh. Glass cloth was used to minimize heat transfer by conduction. The glass cloth was held in place by a skirt which extended below the level of the glass cloth. This skirt fitted down inside the flow nozzle shown in Figure 1 when the basket was in the dryer, an arrangement that prevented air from bypassing the beads. In some runs the space into which the skirt extended was filled with Dow silicone fluid of very high boiling point to provide a liquid seal. The presence or absence of fluid had no discernible effect on drying rates, which indicated that little air was by-passed when the apparatus was operating with a dry seal.

The basket proper was rigidly connected to a ring above by three rods. The top ring fitted into the race of a ball bearing mounted at the top of the dryer. A small motor and crank imparted to the ball bearing a reciprocating rotary motion, which was in turn imparted to the top ring and, through the rods, to the basket below. This motion effectively agitated the beads to promote drying uniformity.

The top ring and basket were fabricated from aluminum. The basket skirt was formed from light-gauge 18-8 stainless steel. The rods which connected ring and basket were Dowmetal. These metals satisfactorily combined corrosion resistance and light weight.

Standard steel pipe was used for the dryer shell, and the inside surfaces were painted with aluminum paint to retard both corrosion and radiation.

External electrical heating circuits were provided at the top of the dryer to prevent condensation on the walls during high humidity runs. The steam transfer line connecting the metering orifice with the dryer was similarly wired to avoid condensation in the line and to provide some superheat. The compressed-air feed was preheated in a steam-jacketed double-pipe heat exchanger.

The operating procedure was as follows. The dryer was heated on air alone until the dry-bulb temperature exceeded the wet-bulb temperature to be employed. Steam flow was then started. The steam and air flow rates were set to give the desired total flow rate and wet-bulb temperature. When all temperatures, including those at the wall, were lined out, the basket containing the wet beads was lowered into place without cessation of air or steam flow. At the end of the drying period the basket was removed, again without stopping the flow.

The beads were weighed before and after each run. The unit was originally set up to weigh the basket and beads during the run, but it was found impossible to weigh accurately with air flowing. Stopping the air flow during the time of weighing produced undesirable temperature fluctuations. The best method found for obtaining reliable drying-rate data was to dry successive batches of the same charge for various times, discharging the product immediately into airtight weighing bottles.

The solid studied in this investigation was a silica-alumina hydrogel prepared essentially according to a method which has been previously described (*3*). A feature of this method is the incorporation of finely ground dried gel powder in the hydrogel. This powder reduces the amount of breakage in drying and helps to create large pores, or macropores, in the catalyst structure. In the absence of this powder the catalyst would contain only micropores smaller than 1,000 Å. in radius. With the powder present, pores larger than 1,000 Å. may be created during the drying operation. These large pores are desirable because, among other things,

TABLE 1.—SUMMARY OF DRYING DATA

	Primary drying conditions				Secondary drying conditions				Heat-treated properties	
Run	Dry bulb, °F.	Wet bulb, °F.	Time, min.	H_2O, wt. %	Dry bulb, °F.	Wet bulb, °F.	Time, min.	H_2O, wt. %	Porosity, vol. %	Pellet density, g./cc.
4	220	160	15	224	220	160	60	9.9	61.1	0.928
5	200	160	15	..	200	160	60	12.4	60.0	0.963
7	240	180	13	308	240	180	46	7.5	61.5	0.932
8	190	150	18	319	190	150	35	28.3	60.1	0.968
9	180	140	18	265	180	140	40	24.2	61.6	0.952
10	200	140	15	292	200	140	26	25.7	61.7	0.948
11	210	150	13	312	210	150	27	..	60.8	0.953
13	160	140	31	389	160	140	100	42.8	54.7	1.050
14	170	140	25	353	170	140	80	22.1	58.2	0.974
15	170	150	30	400	170	150	100	52.0	60.5	0.993
16	180	150	22	393	180	150	100	17.0	58.1	0.989
17	180	150	22	386	245	212	80	21.9	58.1	1.051
18	180	150	25	364	180	150	100	16.6	61.0	0.957
19	180	150	25	359	210	150	45	10.6	62.5	0.920
20	180	150	25	336	210	180	80	19.8	59.1	1.006
21	180	150	25	350	240	180	45	9.0	61.3	0.948
22	180	150	25	338	272	212	45	10.6	58.0	1.01
23	210	150	13	325	180	150	100	14.3	60.4	0.955
24	210	150	13	336	210	150	47	7.7	61.5	0.917
25	210	150	13	314	210	180	80	16.7	56.9	1.023
26	210	150	13	322	240	180	40	10.5	59.3	0.973
27	210	150	13	316	242	212	80	22.9	56.8	1.046
28	210	150	13	309	272	212	45	9.5	57.2	1.034

they increase the speed of regeneration when coke is burned from used catalyst. As charged to drying, this material has the consistency of very stiff, elastic gelatin.

Because the particles were formed as very regular, slightly flattened spheres, it was possible to obtain a very closely sized fraction by screening. The effect of particle diameter on drying rate was eliminated by using one size of fraction throughout the study. The major diameter of the beads charged to the dryer varied from 8.5 to 10.5 mm., the average being 9.6 mm. The diameter of the completely dried beads was about one half this figure. The water content of the wet beads averaged 6.40 lb./lb. of dry gel. Moisture contents were determined by measuring the weight loss of a sample after 16 hr. in a standard laboratory drying oven in an air atmosphere at 220°F. All moistures are expressed on the dry at 220°F. basis.

All runs were made at an air velocity of 200 std.cu.ft./sq.ft. of bed/min. The drying was separated into two stages in order to differentiate between the constant- and the falling-rate periods. The first drying stage was terminated when the water content had reached about 3.0 lb./lb. of dry gel. Earlier work had shown that the critical moisture content at which the rate changed from constant to falling was about 1.5 lb./lb. of dry gel. In the second drying stage the water content was lowered from approximately 3.0 to between 0.1 and 0.2 lb./lb., which is close to the equilibrium water content.

Physical properties of the beads were studied after calcination. Porosity and pellet density were determined by measurement of the volume of water absorbed and of the volumetric displacement of the water-soaked beads. Large-pore volume was determined by measuring the volume of mercury absorbed by previously evacuated catalyst under 1,000 lb./sq.in. gauge pressure. This method gives the volume of the pores larger than 1,000 Å. in radius.

DISCUSSION OF EXPERIMENTAL RESULTS

Drying Rates

A summary of drying data is presented in Table 1. In the first series of experiments (runs 4 to 16, Table 1) the effects of air temperature and humidity on the first-stage drying rates were studied. Because the drying rates were very high, no attempt was made to obtain incremental rate data. Drying times varied between 13 and 31 min., depending upon the conditions employed. The over-all drying rates were obtained by subtracting the moisture content of the discharged beads from that of the charge and dividing by the drying time.

The results of these experiments are shown in Figure 3, where the first-stage drying rate is plotted vs. the difference between dry- and wet-bulb temperature. It can be seen that drying rate is directly proportional to this temperature difference. The fact that the line passes through the origin shows that the bead temperature must be close to the air wet-bulb temperature or, in other words, that air-to-solid temperature-driving force approximates the difference between dry- and wet-bulb temperatures.

In order to aid in determining the drying mechanism, beads discharged from the first-stage operation were visually examined before and after being immersed in water. The discharged beads were similar

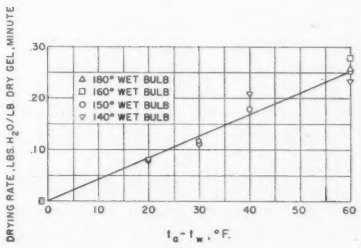

Fig. 3. Primary drying rate vs. dry-bulb—wet-bulb temperature difference.

in translucence to the charged beads, although they were smaller in size. No pickup of water or displacement of air was apparent on immersion in water. These facts show that no vapor spaces had been created within the structure during this part of the drying operation. In the absence of internal vapor spaces evaporation had to take place only from the outside surface, and water removal was accompanied by shrinkage of the bead. Had any evaporation occurred within the structure, a diffusional resistance large in relation to the resistance of the gas film would have been imposed. In this case the diffusion rate and therefore the drying rate would be influenced by the wet-bulb temperature. The fact that no significant variation of drying rate with wet-bulb temperature can be noted in Figure 3 is a further indication that no internal vapor diffusion occurred. The effect of wet-bulb temperature on the gas-film transfer coefficients was apparently less than the experimental error.

Drying-rate data during the second stage were taken at two sets of conditions. In both cases the wet-bulb temperature was maintained at 180°F. In one case the dry-bulb temperature was 240°F.; in the other, 210°F. Samples from successively longer drying runs were weighed and analyzed for moisture content. In addition, the diameter was measured. At each set of conditions one sample was held in the dryer until its weight was constant. The moisture content of this sample was taken as the equilibrium moisture content. The moisture analyses were then converted from total moisture on the dry at 220°F. basis to free moisture on the equilibrium dry basis.

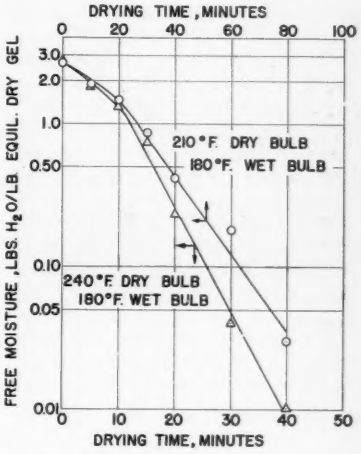

Fig. 4. Secondary drying curves.

The data obtained in these two runs are plotted in Figure 4. Free-moisture content is plotted vs. time. These curves follow the normal pattern closely. On semilog paper a curve should be obtained during the period when drying rate is constant. After the critical moisture content is passed and the drying rate falls with moisture content, a straight line should be obtained, provided drying rate is strictly proportional to moisture content. The exact location of the critical point is not obvious by inspection of the curves, but it appears to be in the neighborhood of a moisture content of 1.5 lb. water/lb. of equilibrium dry gel.

The drying rates in the falling-rate period can be expressed in the form (*5*)

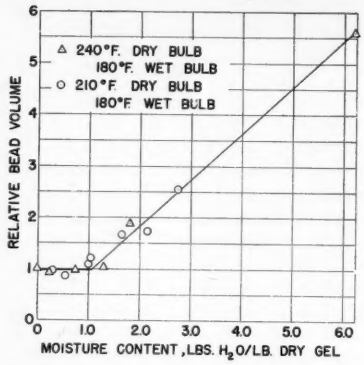

Fig. 5. Bead shrinkage during drying.

$$\frac{dW}{d\theta} = -k\,(W - W_e)$$

where k is the slope of the straight lines in Figure 4. The value of k for the run at 60°F. differential between dry- and wet-bulb is about 2.7 times the value at 30°F. differential, an indication that although k is related to this differential, it is not directly proportional. Further study is needed to define the relationship. A possible explanation is that evaporation takes place in both runs at a temperature higher than the wet-bulb temperature.

The shrinkage data taken in these runs are plotted in Figure 5, where relative bead volume is plotted against moisture content. The data show that shrinkage is linear with moisture content until a moisture content between 1.0 and 1.5 has been reached. Below this range shrinkage is less than can be picked up by this test. In the absence of a significant amount of shrinkage, the water removal must be from pores within the structure.

These data, together with the drying-rate curves, indicate that the critical moisture content is between 1.0 and 1.5. Down to this point shrinkage keeps pace with drying and so all evaporation is from the surface and the rate is essentially constant. Below the critical there is little shrinkage and evaporation is from internal pores. The rate falls as the diffusional resistance is increased.

Effect of Drying Conditions on Physical Properties

A series of twelve experiments (runs 17 to 28, Table 1) was made to determine the effect of drying conditions on the final physical properties of the beads. Two first-stage drying conditions were employed. Six runs were made at 180°F. dry bulb, 150°F. wet bulb, and 25 min. drying time. The other six runs were made at 210°F. dry bulb, 150°F. wet bulb, and 13 min. drying time. Six sets of second-stage drying conditions were selected. The samples originally slow-dried and those originally fast-dried were both finally dried at these six final drying conditions. Three wet-bulb temperatures were used: 150°, 180°, and 212°F. At each wet-bulb level two dry-bulb temperatures were used, one 30°F. above the wet bulb, and one 60°F. above the wet bulb. With the 30° differential the drying time was 80 to 100 min.; with the 60° differential the drying time was 45 min.

The results of these experiments are given in Table 2. The runs are grouped by wet-bulb temperature level at which the secondary drying was conducted. It can be seen that at each secondary drying condition essentially the same density and porosity were obtained with those originally slow-dried as with those originally fast-dried. This indicated that the drying conditions during the constant-rate period had relatively little effect.

The conditions during the falling-rate period, however, had profound effects on the final bead-catalyst density. At each wet-bulb level the density is higher for the sample dried at the lower dry-bulb temperature, that is, dried at the lower rate. At constant temperature difference between dry and wet bulb the density increases as the wet-bulb temperature is raised. All the density variations noted can be explained by the changes in porosity within the limits of experimental error.

Included in Table 2 are large-pore data for some of the catalysts. It is apparent that some relationship exists between density and large-pore volume. To determine that relationship better, the large-pore-volume data were used to calculate the gel density, which is the pellet density that would be obtained if no large pores were present. The formula used is

$$\text{gel density} = \frac{1}{\dfrac{1}{\text{pellet density}} - \text{large-pore volume}}$$

The gel densities calculated for those samples for which large-pore data were available are given in Table 3. The data are arranged in order of increasing pellet density and decreasing large-pore volume. The uniformity of the calculated gel-density values indicates that practically all the pellet density variation is the result of differences in large-pore volume.

The conclusion is drawn that increasing the drying severity, either by increasing the dry-bulb temperature at constant wet-bulb temperature or by decreasing the wet bulb at any given differential between dry and wet bulb, results in greater structural strains in drying. The physical manifestation of the greater strain is increased large-pore volume and decreased pellet density. In order to obtain a particular catalyst density, the permissible drying rate is a function of the wet-bulb temperature. The higher the wet-bulb temperature, the faster the catalyst may be dried. Because this material is so sensitive to drying conditions in the falling-rate period, it is evident that the drying conditions must be kept as uniform as possible in order to produce a high-quality product.

TABLE 3.—GEL DENSITIES CALCULATED FROM LARGE-PORE VOLUMES

Pellet density, g./cc.	Large-pore vol., cc./g.	Calc. gel density, g./cc.
0.917	0.14	1.05
0.957	0.12	1.08
0.973	0.09	1.07
1.034	0.03	1.07
1.051	0.01	1.06

TABLE 2.—EFFECT OF DRYING CONDITIONS ON PHYSICAL PROPERTIES

Secondary drying conditions		Slow primary drying(*)			Fast primary drying(†)		
Dry-bulb temp., °F.	Wet-bulb temp., °F.	Pellet density, g./cc.	Porosity, vol. %	Large pore vol., cc./g.	Pellet density, g./cc.	Porosity, vol. %	Large pore vol., cc./g.
210	150	0.920	62.5	..	0.917	61.5	0.14
180	150	0.957	61.0	0.12	0.955	60.4	
240	180	0.948	61.3	..	0.973	59.3	0.09
210	180	1.006	59.1	..	1.023	56.9	
272	212	1.01	58.0	..	1.034	57.2	0.03
242	212	1.051	58.1	0.01	1.046	56.8	

*Slow drying—180°. dry bulb, 150°F. wet bulb, 25 min.
†Fast drying—210°F. dry bulb, 150°F. wet bulb, 13 min.

This study shows, then, that the drying operation could logically be divided into two separate operations: a primary stage in which the catalyst is rapidly dried at a relatively low wet-bulb level and a secondary stage in which the catalyst is further dried at as high a wet-bulb temperature as possible and at a rate which will give the desired physical properties. The main reason for this separation of operations is that corrosion of the dryer becomes increasingly severe as the wet-bulb temperature is raised. Therefore, cheaper construction can be used for the low wet-bulb primary stage than for the higher wet-bulb secondary stage. The exact wet-bulb temperature at which the secondary drying is performed is selected by an economic balance which considers both the effect of wet bulb on material costs and the effect of rate on dryer size.

It is obviously desirable to evaporate as much water as possible in the cheaper first-stage dryer. On the other hand, it is also essential that no particle be dried past the critical moisture content at these relatively severe drying conditions. Because this portion of the drying operation must be stopped before the fastest drying particle reaches the critical moisture content, uniformity of drying becomes a factor of great importance. Stated another way, total dryer investment cost will be lowest when when maximum drying uniformity is achieved in the first stage of operation. Even for more conventional single-stage drying operations, uniformity is important, as the dryer must be sized to lower the moisture content of the slowest drying particle to the desired level. Therefore, the following analysis of the factors influencing uniformity of drying during the constant-rate period was made. It has been shown that uniformity during the falling-rate period is also essential. Although an analysis was not made for the falling-rate period, many of the conclusions may be applied to that period.

UNIFORMITY OF DRYING IN DEEP BEDS

It was previously mentioned that materials of the type studied in this investigation are often dried commercially in moving-belt tunnel dryers by circulation of heated air through relatively deep beds. The bed thickness is usually between ½ and 3 in. Reversal of the direction of air flow through the bed in successive zones is frequently practiced. This technique materially minimizes the nonuniformity of drying through the bed. The analysis which follows is based upon this reversing-flow technique for the constant-rate period.

The first case to be considered is that of air flow in one direction only. It is assumed that air flows upward through the bed. The amount of heat transferred per hour in a square foot of bed of unit thickness may be expressed as

$$\frac{q}{A} = G\,c_p\,\Delta t_a \qquad (1)$$

when the relatively small amount of sensible heat imparted to the vaporized water is neglected. The amount of heat transferred is also related to the heat transfer coefficient as follows:

$$\frac{q}{A} = \frac{(ha)\,L'\,\Delta t_m}{12} \qquad (2)$$

where

$$\Delta t_m = \frac{\Delta t_1 - \Delta t_2}{2.3 \log \Delta t_1/\Delta t_2} \qquad (3)$$

and

L' = bed thickness, in.

If, in accordance with the findings of this investigation, the solid temperature is constant and equal to the air wet-bulb temperature,

$$\Delta t_a = \Delta t_1 - \Delta t_2 \qquad (4)$$

Substituting this value in Equation (3) gives

$$\Delta t_m = \frac{\Delta t_a}{2.3 \log \Delta t_1/\Delta t_2} \qquad (5)$$

Combining Equations (1), (2), and (5) and solving for log $\Delta t_1/\Delta t_2$ yield

$$\log \frac{\Delta t_1}{\Delta t_2} = \frac{0.0362\,(ha)\,L'}{G\,c_p} \qquad (6)$$

All the constants in the right-hand side of Equation (6), except L', can be evaluated by selecting the air-mass velocity and dry- and wet-bulb temperatures, provided the relationship between the heat transfer coefficient and these conditions is known. Combining these constants into one constant, C, gives

$$\log \frac{\Delta t_1}{\Delta t_2} = CL' \qquad (7)$$

It has been shown (*see* Figure 3) that drying rate during the constant-rate period is directly proportional to the difference between air dry- and wet-bulb temperatures. In accordance with the basic assumption of this derivation, the temperature of the solid may be substituted for air wet bulb. Then Δt_1 and Δt_2 are proportional to the drying rates at those points. If a value of unity is assigned to Δt_1, then Δt_2 represents the ratio of the drying rate at a point L' in. from the entrance of the bed to the drying rate at the entrance. This relationship is illustrated by the line labeled *upflow* in Figure 6.

Figure 6 was plotted by use of a value for the heat transfer coefficient of 2,100 B.t.u./(hr.)(cu. ft.)(°F.) calculated from constant-rate drying runs at the following conditions: $G = 750$ lb./(sq.ft.)(hr.), $t_a = 240$°F., $t_w = 180$°F. This value agrees well with a value calculated from a previously published correlation (*1*).

If the direction of air flow is periodically reversed for equal time intervals instead of remaining constant, the variation in drying rate with bed position may be determined for any particular bed depth by the method shown in Figure 6 where a bed 2 in. deep is assumed. Here a mirror image of the original curve is drawn to represent downflow operation. The ordinates of the two curves are then averaged to yield the concave curve representing cumulative drying-rate variation with position in the bed.

At the conditions upon which Figure 6 was calculated, the ratio of the drying rate at the center of the bed to that at the edges of the bed is $0.48/0.615 = 0.78$. It may be readily seen that the concavity of the reversing-flow curve will increase as the bed thickness is increased. This states the logical expectation that drying uniformity will suffer as the bed thickness is increased.

With reference to Equation (6), increasing the heat transfer coefficient while otherwise maintaining constant conditions will result in up- and downflow lines of greater slope in Figure 6. The reversing-flow curve will then have greater concavity. The only way to increase the heat transfer coefficient without changing air velocity, humidity, or temperature is by decreasing the particle size of the material being dried (*1* and *2*). It may be expected then that small particles will dry less uniformly than large, all conditions including bed depth being equal. It must be noted, though, that the over-all drying rate will be higher for the smaller particles.

The effect of air velocity on drying uniformity may be readily interpreted with the aid of equation (6). The heat transfer coefficient has been shown (*1*) to vary approximately as the six-tenths power of the velocity. Then

$$\log \frac{\Delta t_1}{\Delta t_2} = \varphi \frac{G^{0.6}}{G} = \varphi G^{-0.4} \quad (8)$$

indicating that an increase in air velocity should result in more uniform drying. The maximum velocity is dictated by pressure-drop considerations.

The effect on drying uniformity of varying bed thickness with reversal of air flow is best illustrated by Figure 7. This curve was derived as follows. Equation (7) was converted to

$$\Delta t_2 = \frac{\Delta t_1}{e^{C'L'}} \quad (9)$$

where $C' = 2.303C$. The relative drying rate at the center of the bed is proportional to

$$\Delta t_{0.5L} = \frac{\Delta t_1}{e^{0.5\ C'L'}} \quad (10)$$

Likewise, at either edge of the bed the relative drying rate with reversal is proportional to the average of Δt_1 and Δt_2 for unidirectional flow, or

$$\frac{\Delta t_1 + \Delta t_2}{2} = \frac{\Delta t_1 + \Delta t_1/e^{C'L'}}{2} \quad (11)$$

Calling the ratio of drying rate at the center of the bed to that at either edge R, dividing Equation (10) by (11), and simplifying give

$$R = \frac{2}{e^{0.5\ C'L'} + e^{-0.5\ C'L'}} = \operatorname{sech}\ 0.5\ C'L' \quad (12)$$

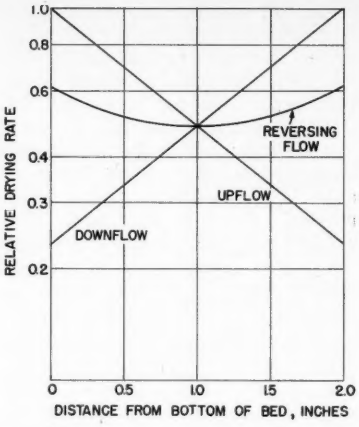

Fig. 6. Drying rate vs. position in a 2-in.-deep bed (through circulation).

R may then be readily plotted vs. L'.

The same type of analysis has not been applied to the falling-rate period; however the various factors should have the same qualitative effect as in the constant-rate period. The fact that drying rate falls as the moisture content falls has a compensating effect which should tend to make the falling-rate drying inherently more uniform than the constant-rate drying.

Although experimental confirmation of the findings of this analysis is not available, it is believed that they may be used qualitatively with confidence. The selection of drying equipment requires considerable experimental work. If uniformity of drying is a consideration, the method can be used to indicate the practical limits of operating conditions and to indicate the qualitative effect of each variable. Limiting the field can significantly decrease the amount of experimental work necessary.

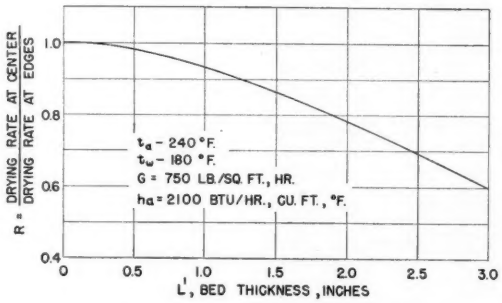

Fig. 7. Drying rate vs. bed thickness (through circulation with reversal of air flow).

CONCLUSIONS

1. The drying rate of the hydrogel studied is proportional to the difference between air dry- and wet-bulb temperatures during the constant-rate period.

2. During the falling-rate period the rate is proportional to the free-moisture content. The proportionality factor is a complicated and undetermined function of the difference between dry- and wet-bulb temperatures.

3. Wet-bulb temperature level and drying rate during the falling-rate period are the major determinants of the density and large-pore volume of cracking catalysts prepared from this hydrogel. The higher the wet-bulb temperature, the faster the catalyst may be dried to obtain the desired density.

4. According to theoretical analysis, the important factors influencing uniformity of drying during the constant-rate period when deep layers are dried are bed depth, air velocity, and particle size.

ACKNOWLEDGEMENT

The aid of E. H. Ivey, Jr., and J. B. Holiman is gratefully acknowledged. Permission by Houdry Process Corporation to publish this paper is appreciated.

NOTATION

a = surface area, sq.ft./cu.ft.
c_p = specific heat, B.t.u./(lb.) (°F.)
h = heat transfer coefficient, B.t.u./(hr.) (sq.ft.) (°F.)
k = a constant
q = heat transfer rate, B.t.u./hr.
Δt_a = change in air temperature passing through bed, °F.
Δt_1 = temperature difference between air and solid at entrance of bed, °F.
Δt_2 = temperature difference between air and solid at exit of bed, °F.
A = bed area normal to flow, sq.ft.
C, C' = constants
G = mass velocity, lb./(hr.) (sq. ft.)
L' = bed thickness, in.
W = moisture content, lb. H_2O/lb. bone dry solid
W_e = equilibrium moisture content, lb. H_2O/lb. bone dry solid
θ = time, hr.

LITERATURE CITED

1. Gamson, B. W., G. Thodos, and O. A. Hougen, *Trans. Am. Inst. Chem. Engrs.*, 39, 1 (1943).
2. Marshall, W. R., Jr., and O. A. Hougen, *Trans. Am. Inst. Chem. Engrs.*, 38, 91 (1942).
3. Milliken, T. H., Jr., U. S. Pat. 2,487,065 (Nov. 8, 1949).
4. Perry, J. H., ed., "Chemical Engineers' Handbook," p. 823, McGraw-Hill Book Company, Inc., New York (1950).
5. *Ibid.*, p. 807.

Presented at A.I.Ch.E. New York meeting

Extraction of Petroleum Fractions by Ammonia Solvents

M. R. Fenske, R. H. McCormick, H. Lawroski, and R. G. Geier
The Pennsylvania State University, University Park, Pennsylvania

In developing a solvent for the separation of complex hydrocarbon mixtures many factors must be considered, some of the more important of which are listed in Table 1. It is easy to get some of these properties but difficult to get all of them in a single solvent.

TABLE 1.—FACTORS IN SOLVENT SELECTION

1. Selectivity, β
2. Solubility—β relationship
3. Adaptability to various feed stocks
4. Ease of recovery (volatility, etc.)
5. Density
6. Stability
7. Corrosiveness
8. Cost
9. Viscosity
10. Interfacial tension
11. Toxicity
12. Freezing point
13. Latent heat

Consequently the choice has to be based upon a composite evaluation. For example, prime emphasis can be placed on solvent selectivity as defined by β (Table 2), but unless the solvent has a relatively high dissolving power under the conditions for having a good β, the solvent is handicapped because excessive solvent treats may be needed. What is desired (but difficult to obtain) is a high solubility and a high β throughout the concentration range over which the separation is being made. Solubility is the weight percentage of hydrocarbon in solution in the solvent phase.

It is obviously desirable to be able to use the same solvent system for various feed stocks. In this way a plant can be shifted from one feed to another without a new solvent-extraction facility having to be built.

Since some separations will involve circulating large amounts of solvent, the regeneration of the solvent should be easy. Distillation is a convenient method when large amounts of high heat are not needed. However, other methods, such as chilling to separate the solvent or washing with another solvent, can sometimes be used. For a solvent to find its widest use, when distillation is employed for its recovery, the solvent should

TABLE 2.—DEFINITION OF β AND EQUATIONS FOR MINIMUM CONDITIONS

1. Stages $\left(\frac{x_a}{x_b}\right)_e = \beta^N \left(\frac{x_a}{x_b}\right)_r$

2. Reflux ratio $\left(\frac{O_o}{P_e}\right)_{min} = \frac{1}{\beta - 1}\left[\frac{(x_a)_e}{(x_a)_f} - \beta\frac{(x_b)_e}{(x_b)_f}\right]$

3. Solvent: oil ratio $S/O_{min} = \left[\frac{O_o}{P_e} + 1\right]\left[\frac{\text{wt. \% } S}{\text{wt. \% } O}\right]_{sf}\left[\frac{P_e}{O_f}\right]$

Notation

x_a = wt.% more soluble component, solvent-free basis
x_b = wt.% less soluble component, solvent-free basis
N = total perfect stages (minimum)
β = average β in stage equation (1); β at feed point in reflux ratio equation (2)
O_o = pounds of oil overflow at feed
P_e = pounds of oil removed as extract product
S/O = solvent-to oil ratio, by weight (neglecting solvent removed with final raffinate)
$[\text{Wt.\% } S/\text{Wt.\% } O]_{sf}$ = ratio of wt.% solvent to wt.% oil in solvent phase leaving feed point
O_f = pounds of oil fed to system

Subscripts

e refers to final extract
f refers to oil feed point
r refers to final raffinate

boil either below the materials being separated or well above them. A solvent boiling coincident with some of the materials being separated offers many problems.

The other properties, 5 to 13 in Table 1, relate to extractor design, the cost of the operation, and the character of the equipment employed. Density, viscosity, and interfacial tension are important in phase mixing and phase separation. These properties affect the capacity and efficiency of an extractor.

EXTRACTION VARIABLES

To make a given sharp separation by extraction, it is important to know at least three of the requirements, namely, the number of theoretical stages, the reflux ratio, and the solvent-to-oil ratio. "Oil" is used here to denote generally the material to be separated. Table 2 lists the equations for calculating the minimum values of these three operating variables. These equations are for the usual engineering bases, namely continuous and steady-state operation.

Figure 1 illustrates the use of these relationships for the separation of a binary *A-B* mixture containing 25% *A* to produce 95% *A* in the extract and 5% *A* in the raffinate when the solubility in the solvent is 20% at the feed point (*1*). Many separations can be made by extraction if ten to twenty-five theoretical stages are used, even if β is as low as 1.5.

In dealing with a practical extraction case something more than the minimum conditions, shown on Figure 1, is needed.

Figure 2 shows how actual and minimum extraction conditions are related. This is an empirical relationship. The band was calculated using more than 40 points from 4 different hydrocarbon-solvent systems employing reflux. The ranges in values used in these calculations are (*a*) extract to raffinate purity from 90 to 99%, (*b*) solubility of hydrocarbon in the solvent from 5 to 20%, (*c*) β from 1.07 to 10, and (*d*) the feed to the extractor from 20 to 50% in extractable component (*1*).

SELECTIVITY OF VARIOUS SOLVENTS

There are so many mixtures that are amenable to extraction and so many liquids potentially useful as solvents that a detailed discussion of all these combinations cannot be given here. A few comparisons, nevertheless, are possible for two hydrocarbon systems, (*a*) methylcyclohexane and *n*-heptane, a naphthene-paraffin pair difficult to separate by distillation, and (*b*) toluene and methylcyclohexane, an aromatic-naphthene pair illustrating the separation of aromatics from hydrocarbon mixtures.

The behavior of different solvents with these two systems is shown in Tables 3 and 4. In Table 3 these β's are to be compared with an α of 1.07 for distillation and a γ of about 1.3 for vapor-liquid extraction for most solvents.

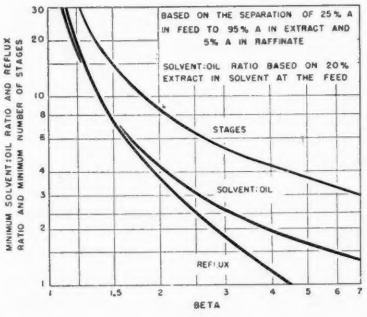
BASED ON THE SEPARATION OF 25% A IN FEED TO 95% A IN EXTRACT AND 5% A IN RAFFINATE
SOLVENT:OIL RATIO BASED ON 20% EXTRACT IN SOLVENT AT THE FEED
STAGES
SOLVENT:OIL
REFLUX
MINIMUM SOLVENT:OIL RATIO AND REFLUX RATIO AND MINIMUM NUMBER OF STAGES
BETA

Fig. 1. Variation of minimum solvent: oil ratio, minimum reflux ratio and minimum stages with β.

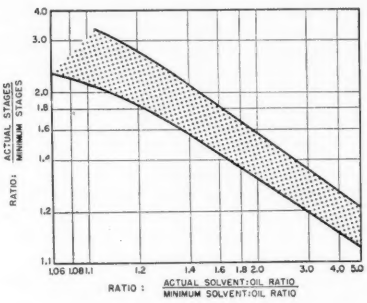

Fig. 2. Estimation of practical operating conditions from minimum values.

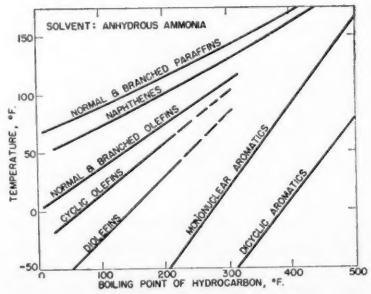

Fig. 3. Temperature for 10 wt. % solubility.

The toluene - methylcyclohexane system (Table 4) differs from the other system in that most of the solvents are completely miscible with toluene. This means that toluene cannot be made pure by liquid extraction unless some way is found to change the solubility behavior as the concentration of toluene increases in the extractor. The limiting purity is listed in the last data column on Table 4. In general there are three ways to open up this type of phase diagram so as to permit the most soluble component (viz. toluene) to be produced in pure form.

1. In one case the temperature can be successively lowered in the extractor as the solvent phase becomes progressively richer in the extractable component. This lower temperature will reduce the solubility, as illustrated in Figure 6. This is an effective procedure when applicable. The limitations are that the solvent or the material being extracted must not solidify or become too viscous to flow readily and that the maintenance of the lowest required temperature must not be too difficult or expensive.

2. A precipitant, or antisolvent, can be injected along the main solvent flow path to reduce gradually the dissolving power of the solvent as it flows toward the extract end of the extractor. For example, the precipitant may be water when the solvent is alcohol, phenol, or liquid ammonia. This is an effective procedure and obviates extensive temperature reductions. It is necessary, however, to separate the precipitant from the solvent because usually it is not needed at the raffinate end of the extractor, or the point of solvent entry.

3. Another solvent incompletely miscible with the main solvent but having good dissolving power for the material being extracted can be introduced at the extract end of the extractor to take the place of the usual reflux phase. Thus there is always a two-phase liquid-liquid system present and the process of extraction can continue to any desired purity if the β and the stages are adequate. This second solvent flows countercurrently to the main solvent. The principal disadvantage of this two-solvent system is that two solvents, instead of one, have to be handled and recovered. This double-solvent procedure is particularly valuable when the mixture being separated is very viscous or even solid. Extraction, or the separation of the mixture, can occur as long as there are adequate solubility in the solvents and a suitable β.

LIQUID AMMONIA AS A SOLVENT

It has been recognized for some time that liquid ammonia is a use-

TABLE 3.—METHYLCYCLOHEXANE–*n*-HEPTANE-SOLVENT

Solvent	Temp., °F.	Solubility*, wt. % hydrocarbon in solvent phase	β (average)	Ref.
Methanol	−4	14	1.2	3
Sulfur dioxide	50	10	1.2	6
Ammonia	110	10	1.3	4
Acetonitrile	104	14	1.3	3
2, 4-Dimethylthia-cyclopentane dioxide	113	10	..	7
Methyl cellosolve	50	15	1.3	3
Acetonylacetone	86	14	1.3	3
Methyl carbitol	140	13	1.3	3
Furfural	140	15	1.4	3
Aniline	102	15	1.4	3
Phenyl cellosolve	122	15	1.4	3
Gamma valerolactone	102	14	..	4

*Hydrocarbon charge composition is 50 vol.% *n*-heptane and 50 vol.% methylcyclohexane. The solvent:oil-weight ratio is 1:1.

ful solvent, resembling water in some of its characteristics. Being an inorganic compound, it has not been used extensively heretofore for hydrocarbon separations; however, liquid ammonia has good solvency and selectivity for separating several hydrocarbon types. When its solubility becomes too low the use of a low-molecular-weight amine, such as monomethylamine, has been found satisfactory for increasing the solvent power. This is an alternative to raising temperature. When the solubility becomes too high, water is a good antisolvent. Thus this three-component solvent system, comprised of water, liquid ammonia, and monomethylamine, enables a great variety of hydrocarbon mixtures to be separated (*5*).

Figure 3 illustrates the solubility relationships for various hydrocarbon types when liquid ammonia contains 10 wt.% of these in solution. The temperature at which 10 wt.% solubility is obtained is plotted against the boiling point of the various hydrocarbon types. It is evident from this diagram that the use of a prosolvent, such as methylamine, is desired when the higher boiling hydrocarbons and those which are less polar are extracted. Similarly, water is desirable in the solvent when low-molecular-weight hydrocarbons, and particularly those high in polarity such as aromatics, are extracted.

β-SOLUBILITY RELATIONSHIP

For this solvent system a correlation has been obtained between selectivity, defined as β, and the differences in temperatures in degrees Fahrenheit for 10 wt.% solubility for any pair of hydrocarbons. This is shown in Figure 4. Upon combining it with Figure 3 one can ascertain the feasibility of separating hydrocarbons with liquid ammonia. These relationships are applicable for separating gasolines, kerosenes, gas oils, and lubricating distillates.

β is strongly dependent on the solubility. Thus, to be able to use this ammonia solvent system effectively, it is important to control the solubility throughout the concentration range prevailing in an extractor. This is particularly true for difficult separations and separations involving both high yield and high purity. Figure 5 illustrates the dependency of β on solubility.

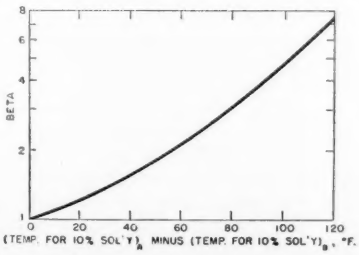

Fig. 4. β for hydrocarbon binary (*A*-*B*) in liquid ammonia.

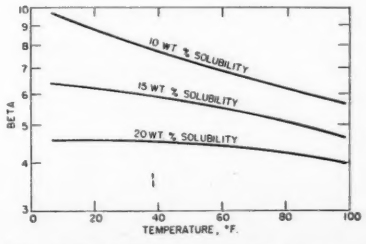

Fig. 5. Variation of β with temperature: toluene-methylcyclohexane-ammonia.

TOLUENE METHYLCYCLOHEXANE AMMONIA

This system is shown in Figure 6 for anhydrous ammonia. To make a complete separation of both hydrocarbons with anhydrous ammonia, an extractor would have a very pronounced temperature gradient: the raffinate end would be about 100°F. and the extract end below 10°F.

This high gradient can be eliminated by using water as an antisolvent, as shown in Figure 7. To limit the solubility of toluene in anhydrous ammonia to 20 wt.%, the temperature has to be below 0°F. On the other hand, the temperature can be 100°F. if liquid ammonia contains about 13 wt.% water. Figure 8, which shows these relationships as a triangular diagram, illustrates the desirability of having a solubility pattern typified by the line *CJ*.

OTHER HYDROCARBON SYSTEMS

Table 5 illustrates the selectivity of liquid ammonia for separating various binary hydrocarbon systems at 10 wt.% solubility.

The *C*-7 binary series is of interest. Here one of the components involves the carbon skeleton of methylcyclohexane and one of the components decreases successively in hydrogen content from the other by two hydrogen atoms. Ammonia is selective enough to recognize this difference.

Other naphthene-paraffin separations have been made with these ammonia solvents. Table 6 illustrates the importance of selecting the proper boiling-point relationships for a naphthene-paraffin separation. Since the solvent recognizes differences in molecular weight as well as molecular type, narrow boiling cuts are preferred for naphthene-paraffin separations.

PILOT PLANT SEPARATIONS

A twenty-stage stacked extractor (*2*) has been used to carry out a variety of separations with this liquid-ammonia system. Both batch and continuous extractions have been made, but this discussion relates only to continuous steady-state operation. These separations do not necessarily represent the optimum. Instead they are intended to illustrate the range of feeds and the versatility of the ammonia type of solvents. Both stripping and enriching stages are employed, for what takes place in the enriching zone determines the purity of the

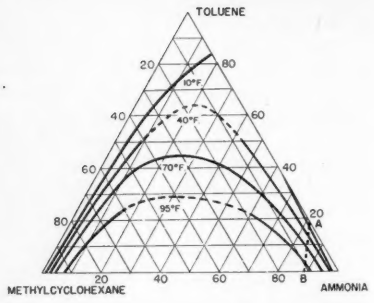

Fig. 6. Toluene-methylcyclohexane-ammonia; for solubilities along *AB*, $\beta = 4.0$ to 5.5.

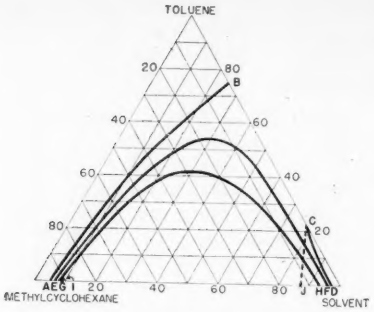

Fig. 8. Toluene-methylcyclohexane-solvent at 110°F.

Solvent composition, wt. %

Area	NH_3	H_2O
AB-CD	86	14
EF	90	10
GH	95	5
IJ	100	0

For solubilities along *CJ*, $\beta = 3.5$ to 5.5.

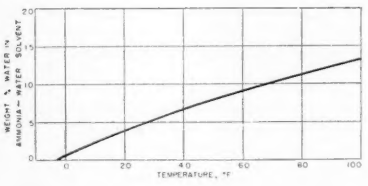

Fig. 7. Relation between temperature and water content to maintain 20 wt. % solubility of toluene in ammonia.

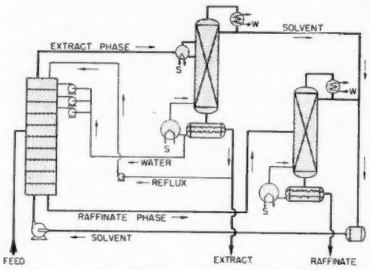

Fig. 9. Liquid-extraction pilot plant.

TABLE 4.—TOLUENE–METHYLCYCLOHEXANE–SOLVENT

Solvent	Temp., °F.	β at 20% hydrocarbon solubility*	At plait point: Wt. % hydrocarbon solubility ($\beta = 1.0$)	At plait point: Wt. % toluene in hydrocarbon	Ref.
Phenyl cellosolve	0	3.1	58	38	3
Methyl carbitol	0	3.8	59	51	3
Methyl cellosolve	−20	4.2	65	32	3
Aniline	−10	4.5	58	42	3
Ammonia	70	4.7	62	73	..
2, 4-Dimethylthia-cyclopentane dioxide	0	5.0	57	45	7
Furfural	10	5.0	63	48	3
Gamma valerolactone	0	6.0	..	..	4
Acetonitrile	10	6.3	78	48	3
Acetonylacetone	−10	6.6	65	43	3
Sulfur dioxide	−40	17.7	59	44	6

*Hydrocarbon charge composition is 50 vol.% toluene and 50 vol.% methylcyclohexane. The solvent:oil weight ratio is 1:1.

TABLE 5.—SEPARATION OF HYDROCARBONS WITH LIQUID AMMONIA

Hydrocarbon system	β at 10 wt. % solubility	Min. theo. stages to make 95% pure extract and 95% pure raffinate
Isobutylene:isobutane	2.2	8
Butadiene:isobutylene	2.0	9
Trimethylethylene:n-pentane	1.9	10
Isoprene:pentene–1	2.0	9
Methylcyclohexane:*n*–heptane	1.3	20
4–Methylcyclohexene–1:methylcyclohexane	1.5	15
1–Methyl–1,3–cyclohexadiene:methylcyclohexene	1.6	13
Methylcyclohexadiene:toluene	1.6	13
Styrene:ethylbenzene	1.8	10
Octene–1:isopropylbenzene	2.8	6

most soluble component. What happens in the stripping zone determines its yield.

TABLE 6.—SELECTIVITY OF NAPHTHENE-PARAFFIN SYSTEMS

B.P. naphthene − B.P. paraffin, °F.	β at 15 wt.% solubility
−30	1.45
−10	1.32
0	1.25
20	1.15
50	1.10

$$\beta = \left(\frac{\text{wt.\% naphthene}}{\text{wt.\% paraffin}}\right)_{ext.} \times \left(\frac{\text{wt.\% paraffin}}{\text{wt.\% naphthene}}\right)_{raff.}$$

Figure 9 is a diagram of the pilot plant. Because ammonia and monomethylamine are low boiling, pressure distillation is used to separate and regenerate the solvent. Open steam stripping is used to separate the solvent from the extract and raffinate portions. Part of the water is recycled, as shown, to get solubility control in the extractor.

This pilot plant is operated at a pressure sufficient to maintain the solvent within the extractor in a liquid phase. The pressure required is in the range of 150 to 200 lb./sq.in.abs.

SOLVING EXTRACTION PROBLEMS

This solvent and the twenty-stage extractor comprise a calculating machine to study and solve a variety of extraction problems. Because of the ease of sampling the phases in the extractor and the ease of removing solvent from these samples, extensive operating-line–equilibrium-curve analyses can readily be made. Figure 10 illustrates the type of data obtainable on a simple system. In this case the distribution of stages and the choice of reflux and of solvent treat was such that most of the stages were used effectively. In a separation of this type where the solubility changes through the extractor can be very large, constant solvent composition and temperature being used, it is important to have the solubility on the stages properly controlled either by temperature reduction or water injection or both. Because of these solubility changes, which affect β, the equilibrium curve is not really a smooth continuous line as shown. Instead, it is actually saw-toothed

TABLE 7.—LIQUID EXTRACTION OF PETROLEUM FRACTIONS

	A Catalytic naphtha 200–330				B Catalytic naphtha 236–458				C Thermal naphtha 100–400			D Catalytic naphtha 140–195		E Dearomatized catalytic naphtha 195–250	250–320
Petroleum fraction															
Boiling range, °F.															
Solvent composition, wt.%															
Ammonia	80	80	80	35	85	85	85	85	85	85		100		68	68
Monomethylamine	20	20	20	15	15	15	15	15	15	15		0		32	32
Run	1	2	3	4	5	6	7	8	9	10		11		12	13
Operating conditions															
Stage distribution, *E/F/S*	12/*F*/7	12/*F*/7	12/*F*/7	8/*F*/11	8/*F*/11	8/*F*/11	8/*F*/11	8/*F*/11	8/*F*/11	8/*F*/11		12/*F*/7		7/*F*/12	12/*F*/7
S:O wt. ratio	4.5	4.5	3.0	5	5	3	3	2	5	3		1.6		20	22
Reflux ratio (top of extractor)	5.7	4.0	4.3	2.2	3.7	0.7	5.5	0.8	0.8	0.3		3.0		6.0	4.2
Temperature, °F., (top-bottom stage)	72–95	63–72	72–104	71–73	68–75	68–81	61–73	63–70	79–100	68–86		43–66		72–78	63–72
H_2O injection, wt.% of solvent	12	0	12	0	3	2.5	6	0	0	0		17.5		0	0
Feed															
Vol. % olefins	43	43	43	16	16	16	16	16	24	24		8		53	45
Vol. % *P+N*	31	31	31	33	33	33	33	33	51	51		73		46	54
Vol. % aromatics	26	26	26	51	51	51	51	51	25	25		19*		1	1
Raffinate															
Vol. % of feed	80	62	80	40	55	30	75	45	50	75		85		50	48
Vol. % olefins	48	43	46	23	24	12	20	18	18	26		10		21	19
Vol. % *P+N*	43	55	45	77	61	88	40	50	78	60		85		79	81
Vol. % aromatics	9	2	9	0	15	0	40	32	4	14		5*		0	0
Extract															
Vol. % of feed	20	38	20	60	45	70	25	55	50	25		15		50	52
Vol. % olefins	5	32	10	6	7	16	5	12	21	15		0		86	73
Vol. % *P+N*	0	2	0	3	1	10	0	10	19	11		0		12	25.5
Vol. % aromatics	95	66	90	91	92	74	95	78	60	74		99.5+*		2	1.5
Yield															
% of feed aromatics in extract	72	94	71	100	85	100	45	70	95	65		78		100	100
% of feed olefins in extract	3	31	5	80	20	80	5	40	55	11		0		80	80
Research octane No.															
Feed						87			71						
Raffinate						10			46						
Extract						101			97						

P+N = Paraffins + Naphthenes. *E/F/S* = Enriching/Feed/Stripping Stages. * Aromatic is benzene.

and the jogs occur at abrupt solubility changes.

By means of a unit such as this twenty-stage extractor, complex separational problems can be attacked profitably from an experimental rather than a wholly theoretical basis. The problem becomes one of being able to analyze the various stage samples, especially when multicomponent mixtures are used.

CRACKED NAPHTHAS

Ammonia solvents have been used to separate catalytic naphthas, as shown in Table 7-*A*. The symbol *E/F/S* denotes the proportion among the enriching stages, the feed stage, and the stripping stages in the stacked extractor. The data are believed self-explanatory.

Figure 11 shows an operating diagram for the aromatic:nonaromatic separation in this catalytic naphtha. This plot illustrates how the stages in the extractor have been utilized and demonstrates solubility control. Whenever the solubility dropped, water injection was used to produce this change on the stages indicated.

Since this ammonia system is inert to hydrocarbons, it is effective in extracting stocks containing olefins and diolefins. Table 7-*C* illustrates the separation of a relatively wide-cut thermally reformed naphtha. This type of separation is useful for octane improvement as well as for making aromatic solvents and petrochemicals.

Table 7-*B* and Figure 12 present data on the separation of a heavy catalytic naphtha boiling in the range of 236° to 458°F. The separations between aromatics and olefins, or between olefins and saturates, were relatively good. The research octane numbers again show the usefulness of this process in naphtha refining.

Figure 12 illustrates the compositions of the feed, extract, and raffinate for one of these separations. Since this is a wide boiling feed, the most difficult separation is between the lowest boiling olefins and the highest boiling aromatics. The composition diagram for the extract shows that low-boiling olefins were present in the extract; the diagram for the raffinate illustrates the extent to which the high-boiling aromatics were not removed.

TABLE 8.—LIQUID EXTRACTION OF A CATALYTIC CYCLE OIL (600° TO 1,000°F.)

Solvent composition, Wt. % = 33NH_3, 67MMA
Feed composition = 47 vol. % aromatics
Stages, $E/F/S = 4/F/4$

Operating conditions			
S:O, wt. ratio	3	3.6	2.2
Reflux ratio (top of extractor)	1	2.6	1.3
Temperature, °F.	88–102	81–100	86–104
H_2O injection, wt.% of solvent	4	3	4
Raffinate, vol% of feed	55	50	50
Vol.% aromatics	15	11	18
Extract, vol.% of feed	45	50	50
Vol.% aromatics	88	81	79
Yield, % of feed aromatics in extract	83	88	79

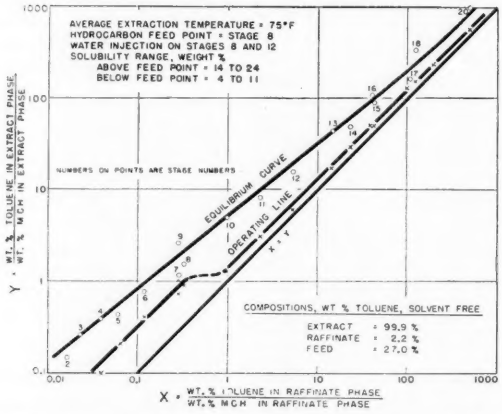
AVERAGE EXTRACTION TEMPERATURE = 75°F
HYDROCARBON FEED POINT = STAGE 8
WATER INJECTION ON STAGES 8 AND 12
SOLUBILITY RANGE, WEIGHT %
ABOVE FEED POINT = 14 TO 24
BELOW FEED POINT = 4 TO 11
NUMBERS ON POINTS ARE STAGE NUMBERS
EQUILIBRIUM CURVE
OPERATING LINE
COMPOSITIONS, WT % TOLUENE, SOLVENT FREE
EXTRACT = 99.9 %
RAFFINATE = 2.2 %
FEED = 27.0 %
Y = WT. % TOLUENE IN EXTRACT PHASE / WT. % MCH IN EXTRACT PHASE
X = WT. % TOLUENE IN RAFFINATE PHASE / WT. % MCH IN RAFFINATE PHASE

Fig. 10. Operating diagram for the extraction of toluene-methylcyclohexane with ammonia.

BENZENE SEPARATION

Liquid ammonia can be used to separate benzene from straight-run and cracked naphthas containing olefins. A typical separation of benzene from a cracked-naphtha fraction boiling in the 140° to 195°F. range is shown in Table 7-*D*. Water injection was used to control the solubility in the extractor. In this extraction twelve stages were used in the enriching section and seven in the stripping section.

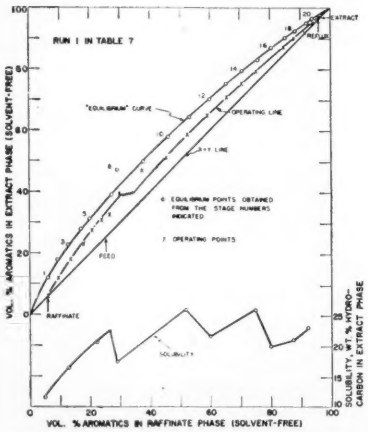

Fig. 11. Volume % aromatics in extract phase (solvent free).

OLEFIN: SATURATE SEPARATIONS

Olefin:saturate separations are not easy with feed stocks with a wide boiling range. The problem here is one of dissolving the highest boiling olefin without taking into solution the lowest boiling saturate. Accordingly, narrower boiling feeds help materially in getting both high-olefin yields and purities.

Table 7-*E* illustrates this separation for two feeds. The separation would have been much sharper had these feed stocks been of narrower boiling range. These stocks cannot be separated by distillation or extractive distillation to the extent shown by these liquid extractions.

CYCLE STOCKS AND LUBRICATING OILS

This liquid ammonia system has been used to extract hydrocarbons ranging in boiling point from 0° to about 1,000°F. at atmospheric pressure. In the higher range the separation frequently relates to taking out aromatics. Table 8 typifies separations in a catalytic cycle oil. Olefins and diolefins present in such feeds are not troublesome. Cycle-stock separations are relatively easy, the selectivity is good, phase separation is rapid, and the solvent is easily recovered.

In the Colombian distillate extraction, shown in Table 9, the object was to reduce neutralization number and to remove the highly condensed or cyclic aromatics. Complete dearomatization was not required. In addition to extracting Coastal distillates, this solvent system has been used on paraffinic lubricating distillates to obtain improvements in viscosity index, cleanliness, bearing corrosion, and oxidation stability.

SUMMARY

Liquid ammonia properly controlled is a versatile solvent for extracting a wide variety of hydrocarbon mixtures. Separations by liquid extraction can be effected between aromatics and olefins, olefins and saturates, and in some cases between naphthenes and paraffins. Solubility varies widely for different types and sizes of hydrocarbons. Because the selectivity of the solvent is dependent upon solubility, it is important that the dissolving power of the ammonia solvent be controlled so that the amount of hydrocarbon in solution in the solvent usually lies between about 10 and 30 wt.%. Thus at all points in a multistage, compound, countercurrent extractor the solvent is incompletely miscible with the hydrocarbons undergoing extraction.

From a practical viewpoint extraction temperatures are usually between 50° and 150°F.

To effect the necessary solubility control of these ammonia solvents in a multistage extractor, water (in concentrations between 0 and 15 wt.%) is used at appropriate extraction stages to reduce the dissolving power of liquid ammonia. To enhance or increase this dissolving power, methylamine has been found very suitable; it is usually in concentrations between 0 and 50 wt.% for many hydrocarbon extractions.

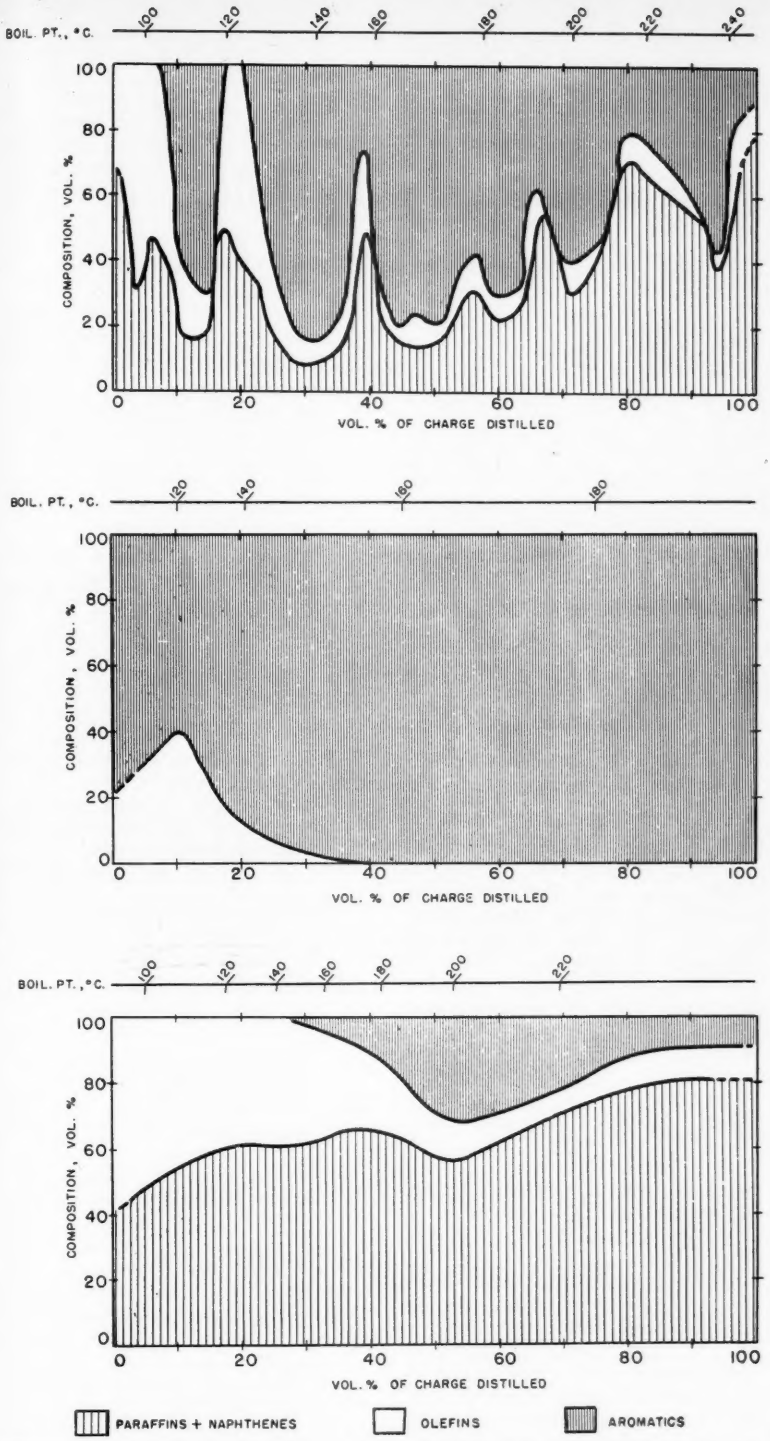

Fig. 12. Fractional distillation of extraction products from catalytic heavy naphtha, 236° to 458°F. (run *B* in Table 9): top, feed; middle, extract (45 vol. % of feed); bottom, raffinate (55 vol. % of feed).

A twenty-stage, countercurrent, stainless steel extractor, with both stripping and enriching zones, has been employed for batch as well as continuous liquid extractions. The hydrocarbon feed rates are usually between 0.5 and 3 gal./hr. and the solvent-to-oil ratios usually range from 1 to 1 to as high as 10 to 1.

Extractions of pure binary mixtures show what goes on in a compound extractor and how the solubility control is realized.

Other data on thermally and catalytically cracked naphthas, catalytic cycle stocks, and Coastal-type lube oils show how this solvent system is applied to petrochemicals, octane improvement, the making of solvents and aviation blending stocks, and the upgrading of lube distillates.

TABLE 9.—LIQUID EXTRACTION OF COLOMBIAN DISTILLATE

Solvent composition, wt.% = 40 NH_3, 60 MMA

Operating conditions		
Stages, *E/F/S*	8/*F*/4	8/*F*/4
S:O wt. ratio	1.0	1.7
Temperature, °F.	112	100
Raffinate, vol.% of feed	88	81
S.U.S. at 100°F.	743	716
Viscosity index	29	38
Neut. No.	0.1	0.1
Vol.% aromatics	23	20
Extract, vol.% of feed	12	19
S.U.S. at 100°F.	1,465	1,490
Viscosity index	−107	−97
Neut. No.	8.7	3.5
Vol.% aromatics	86	80
Feed		
S.U.S. at 100°F.	880	
Viscosity index	18	
Neut. No.	1.7	
Vol.% aromatics	30	

ACKNOWLEDGMENT

The authors wish to acknowledge the assistance of R. A. Rusk, E. C. Kruse, and J. M. Jordan. They are also grateful to the Rohm and Haas Company for help in the initial phases of this study and to the Esso Laboratories for help in the developmental phases.

LITERATURE CITED

1. Cummings, G. H., Ph.D. thesis, The Pennsylvania State University (June, 1941).
2. Fenske, M. R., and R. B. Long, *Chem. Eng. Progr.*, 51, 194 (1955).
3. Herbolsheimer, G., Ph. D. thesis, The Pennsylvania State University (December, 1942).
4. Long, R. B., M.S. thesis, The Pennsylvania State University, (September, 1947).
5. Sweeney, W. J., M. R. Fenske, and G. H. Cummings, U. S. Pat. 2,396,299 (March 12, 1946).
6. Tegge, B. R., M.S. thesis, The Pennsylvania State University (January, 1940).
7. West, A. S., M.S. thesis, The Pennsylvania State University (June, 1946).

(Presented at A.I.Ch.E. New York meeting)

Effect of Void Volume and Prandtl Modulus on Heat Transfer in Tube Banks and Packed Beds

Joel Weisman

Brookhaven National Laboratory, Upton, New York

A correlation is presented relating the heat transfer characteristics of cross-flow heat exchangers to the void-volume-and-tube-pitch ratio. A similar correlation is found to be applicable to heat and mass transfer in packed and fluidized beds and through screens.

A limited amount of data has been obtained on the effect of the Prandtl modulus at high Reynolds numbers. These data seem to indicate, as do those for flow through tubes, that the Prandtl number exponent is a function of Reynolds number.

EFFECT OF VOID VOLUME

The rate of heat transfer for fluids flowing normally to banks of circular tubes is of interest in the design not only of cross-flow exchangers, but also of the more common baffled exchangers. Heat transfer in cross flow has therefore been the subject of a number of investigations. Despite the considerable quantity of data in the literature, there is no generalized correlation relating heat transfer characteristics to lattice geometry. It is the object of the first part of this paper to present such a correlation and to show how this may be applied to packed and fluidized beds.

The first correlation of cross-flow data was made by Colburn (*5*) in 1933. He assigned the letter j to the quantity $(h/CpG_{max})(Pr)^{\frac{2}{3}}$ and found that the data then available for staggered tube banks were represented by

$$j = 0.33\left(\frac{DG_{max}}{\mu_f}\right)^{-0.4} \qquad \left(\frac{DG_{max}}{\mu_f}\right) > 300 \qquad (1)$$

Since that time the extensive data of Pierson (*23*) and Kays, London, and Lo (*19*) for air in turbulent flow have appeared. These data show that the lattice arrangement has a definite effect on the heat transfer coefficients obtained. Pierson found that the variation due to lattice spacing increased with decreasing Reynolds number. Grimison (*15*) correlated the data of Pierson by

$$\frac{hD}{k_f} = 0.28\,\mathrm{Fa}\left(\frac{DG_{max}}{\mu_f}\right)^{0.61} \qquad (2)$$

where Fa was an empirical factor, depending on lattice arrangement and Reynolds number, which varied from 0.65 to 1.3.

Bergelin et al. (*1*) (*2*) investigated the effect of lattice spacing in the intermediate and laminar regions. The lattice arrangement was found to have a noticeable effect, which was greater at the lower Reynolds numbers. At the lowest Reynolds numbers investigated it was found that there was more than a twofold variation in exchanger performance.

Present Correlation

The variation in the heat transfer characteristics of various lattices can be related to the ratio of the tube pitches and the void fraction, ε, of the lattice. The void fraction is defined as

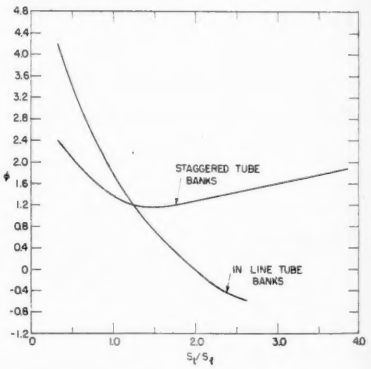

Fig. 1. Variation of arrangement of coefficients with s_t/s_l.

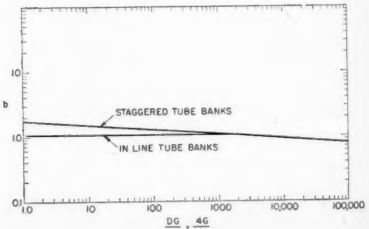

Fig. 2. Variation of arrangement of coefficients with Reynolds number.

Present Address: Westinghouse Commercial Atomic Power, Pittsburgh, Pennsylvania.

$$\epsilon = \frac{\text{total volume of lattice} - \text{volume of tubes}}{\text{total volume of lattice}} \qquad (3)$$

By means of the void-fraction concept it is possible to use a Reynolds number based on the average velocity through the lattice.

$$Re = DG/\mu\epsilon \qquad (4)$$

Using this Reynolds number, one may define a j factor as follows:

$$j' = \left(\frac{\bar{h}\epsilon}{C_{pf}G}\right)\left(\frac{C_{pf}\mu_f}{k_f}\right)^{\frac{2}{3}} =$$

$$f(s_t/s_l, \epsilon, Re) \qquad (5)$$

or rearranging,

$$j = \left(\frac{\bar{h}}{C_{pf}G}\right)\left(\frac{C_{pf}\mu_f}{k_f}\right)^{\frac{2}{3}} =$$

$$f(s_t/s_l, \epsilon, Re) \qquad (6)$$

Equation (6) will be used since it is in harmony with the treatment now given to packed and fluidized beds. It is found that the effects of void-volume-and-tube-pitch ratio may be accounted for by using an equation of the form

$$j\,\epsilon^{\phi b} = f(Re) \qquad (7)$$

where ϕ = arrangement exponent depending on the ratio, s_t/s_l, of transverse to longitudinal tube pitch
b = coefficient depending on the Reynolds number (fixed at 1 for $DG/\mu\epsilon = 4{,}000$).

The values of ϕ and b were obtained by correlating the available data (*1, 2, 19, 23*), which include values of ϵ from 0.415 to 0.91. It was found that the exponents required for in-line arrangements differed from those required for staggered tube banks. Figure 1 shows ϕ as a function of s_t/s_l for both arrangements, and Figure 2 shows b as a function of Reynolds number. For staggered tube banks

$$b = 1.75\,(DG/\mu\epsilon)^{-0.07} \qquad (8)$$

For in-line tube banks, b remains constant at a value of 1.1 until a Reynolds number of 1,200 is reached. At higher Reynolds numbers the values of b for both arrangements coincide.

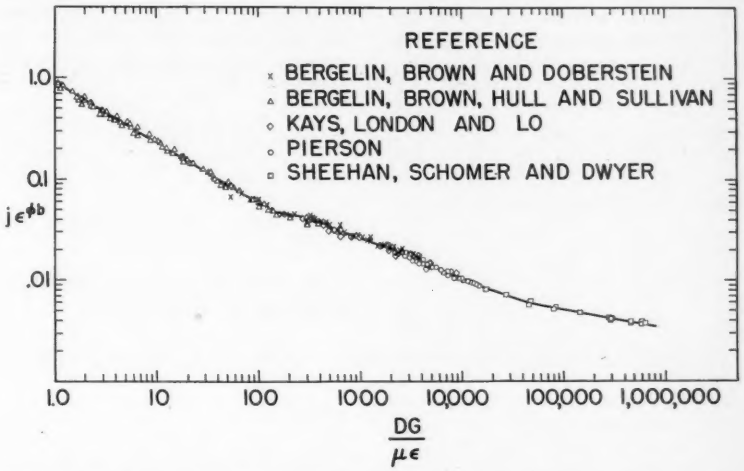

Fig. 3. Correlation of data for heat transfer rates in staggered tube banks.

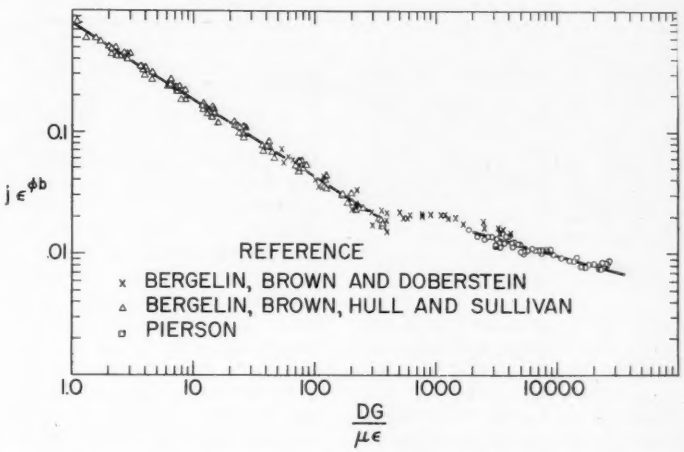

Fig. 4 Correlation of data for heat transfer rates in in-line tube banks.

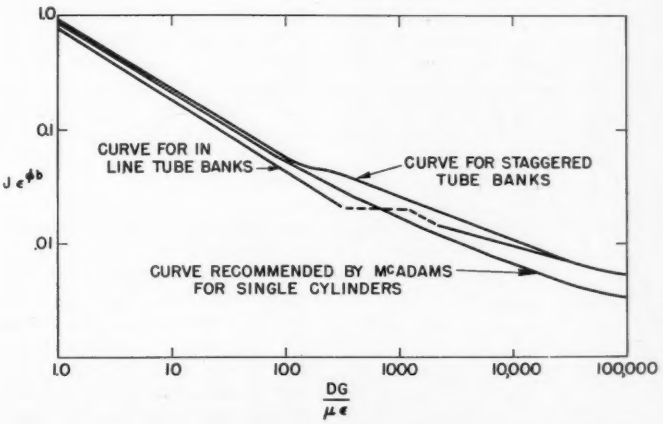

Fig. 5. Comparison of the rate of heat transfer from single cylinders with data obtained in tube banks.

The data of Bergelin and coworkers (*1* and *2*) for staggered tube banks together with points from each set of data for the different staggered arrangements of Pierson (*23*) and Kays, London and Lo (*19*) are plotted in Figure 3. In the laminar and intermediate regions Bergelin et al. found that the effect of physical properties was best accounted for by using $Pr^{\frac{2}{3}}$ together with the Sieder and Tate (*29*) correction. Therefore, in the data of Bergelin and coworkers

$$j = \left(\frac{\bar{h}}{C_p G}\right)\left(\frac{C_{pB}\mu}{k_B}\right)^{\frac{2}{3}}\left(\frac{\mu_W}{\mu}\right)^{0.14} \quad (9)$$

A single smooth curve is obtained from the data of the several investigations. In both the viscous and turbulent regions the curve can be very closely approximated by straight lines on logarithmic coordinates. The equations in these regions are

$$j\,\epsilon^{\phi_b} = 0.895\,(DG/\mu\epsilon)^{-0.59}$$

where

$$(1 < (DG/\mu\epsilon) < 100) \quad (10)$$

$$j\,\epsilon^{\phi_b} = 0.38\,(DG/\mu\epsilon)^{-0.39}$$

where

$$(300 < (DG/\mu\epsilon) < 40{,}000) \quad (11)$$

A very good correlation is found to exist. The lattice spacings investigated by Pierson (*23*) and Kays, London, and Lo (*19*) and Bergelin et al. (*1* and *2*) show no deviation from the curve in excess of 10% although a few individual points show deviations in excess of this.

Although only one lattice arrangement was investigated, the data obtained by Sheehan et al. (*28*) for very high Reynolds numbers are also shown in Figure 3. In the plotting of these data it was assumed that correct values of b could be obtained by extrapolation of Equation (8) to these high Reynolds numbers. By this procedure the following is obtained:

$$j\,\epsilon^{\phi_b} = 0.051\,(DG/\mu\epsilon)^{-0.2}$$

where

$$(DG/\mu\epsilon) > 80{,}000 \quad (12)$$

The data of Bergelin et al. (*1* and *2*) together with representative points from each of the in-line lattices studied by Pierson (*23*) are plotted in Figure 4. The discontinuity between the fully turbulent and laminar regions is more marked in the in-line banks than in staggered tube banks. In the viscous region the data are correlated by

$$j\,\epsilon^{\phi_b} = 0.785\,(DG/\mu\epsilon)^{-0.63}$$

where

$$(1 < (DG/\mu\epsilon) < 300) \quad (13)$$

In the fully turbulent region the following is obtained:

$$j\,\epsilon^{\phi_b} = 0.101\,(DG/\mu\epsilon)^{-0.255}$$

where

$$(2{,}000 < (DG/\mu\epsilon) < 30{,}000) \quad (14)$$

The deviation of the experimental points from the foregoing equations appears to be within the experimental error, as no lattice spacing shows a deviation in excess of 15%.

A comparison of the tube-bank correlations (Figure 5) shows that the staggered-tube data lie above the data for in-line banks until a Reynolds number of 30,000 is reached. From this point on, the two curves appear to be coincident. It will be noted that for the intermediate Reynolds number range there is considerable variation between the curves for in-line and staggered tube banks. The use of a single correlation for both arrangements can lead to errors as high as 90%. Both tube-bank correlations lie above the data for single cylinders in the fully turbulent region. In the laminar region the staggered-tube-bank correlation lies above the single-cylinder data but the in-line-tube-bank correlation lies below. The failure of these correlations to extrapolate to $\epsilon = 1$ indicates that they should not be used for situations where the void fraction, ϵ, is much in excess of 0.9.

Heat and Mass Transfer in Packed and Fluidized Beds

The first problem which presents itself when an attempt is made to extend the correlation developed for tube banks to other systems is the choice of a suitable substitute for tube diameter. A quantity which has been found useful in pressure-drop correlations is the specific surface, a.

$$a = \frac{\text{surface area of particle}}{\text{volume of particle}} \quad (15)$$

The Reynolds number then becomes

$$Re = G/a\,\epsilon\mu \quad (16)$$

For a cylinder $1/a$ equals one fourth the diameter; for a sphere $1/a$ equals one sixth the diameter.

The utility of this concept when applied to heat transfer is illustrated in Figure 6. There the heat and mass transfer data for single spheres in air are compared with the curve recommended by McAdams (*21*) for single cylinders. The agreement between the sphere data and cylinder line is good, particularly for the mass transfer data.

By use of the Reynolds number defined by Equation (16), the data of McCune and Wilhelm (*22*) and Chu et al. (*4*) for fluidized beds of spherical particles may be correlated in the same manner as the tube-bank data. The value of ϕ is found to be 1.1, and b is obtained from the curve used for staggered tube banks. (*See* Figure 2.) When so treated, the mass transfer data are correlated by the curve previously obtained for heat transfer in staggered tube banks. (*See* Figure 7.)

The data of McCune and Wilhelm (*22*) agree very well with the curve but some scatter is observed in the data of Chu et al. (*4*). This scatter appears to be inherent in the data, the poorer precision apparently being caused by the difficulty in measuring the bed height, and therefore ϵ, in gas fluidization. The fluidized-bed data shown do not include data for values of ϵ in excess of 0.86. At higher void fractions the data of McCune and Wilhelm (*22*) deviate from the curve and begin to approach those for single particles.

The data for fixed beds may be handled similarly to those for fluidized beds. However, an additional complication is introduced by the fact that not all the area of the packing or particles is effective in the transfer of mass and heat. Gamson (*13*) has suggested that the j factor be divided by an area factor, representing the fraction of the packing area which is effective. The gas-film data of Hougen, Gamson, and coworkers (*14, 30, 33*) are plotted in Figure 8 by means of the area factors recommended by Gamson (*13*). The value of ϕ for packed beds is also found to be 1.1 and b is again

read from the curve for staggered tube banks. (*See* Figure 2.)

Good agreement is obtained between the data for various packing shapes. As seen from Figure 8, above $Re = 10$ the packed data are also correlated by the curve previously obtained for staggered tube banks.

The liquid-film data of various investigators (*7, 10, 12, 13, 22*) for packed beds of spherical particles at low Reynolds numbers are not shown. As pointed out by Dryden, et al. (*7*) in liquid systems at low Reynolds numbers the rate of transfer obtained by packed beds is influenced by free convection, which in turn varies with the Grashof number. It is not to be expected, therefore, that those data can be adequately correlated by use of j factor concept.

Heat Transfer Through Wire-Screen Matrices

The data of Coppage and London (*6*) for heat transfer through beds of wire screens may also be correlated in the manner used for packed and fluidized beds. In this case it is necessary to define ε on the basis of a single screen, as it was found that the spacing between successive screens did not affect the rate of heat transfer. Over the range of Reynolds numbers investigated, the data seemed to be best fitted when ϕb equal to a constant value of 0.8 was used. The data, given in Figure 9, shows good agreement between the various matrices. The points are fitted fairly closely by the curve derived from staggered-tube-bank data (maximum deviation of 30%) but are somewhat better correlated by the dotted line having the following equation:

$$j\,\epsilon^{0.8} = 0.36\,(G/a\,\epsilon\mu)^{-0.5}$$

where

$$(0.5 < (G/a\,\epsilon\mu) < 60) \qquad (17)$$

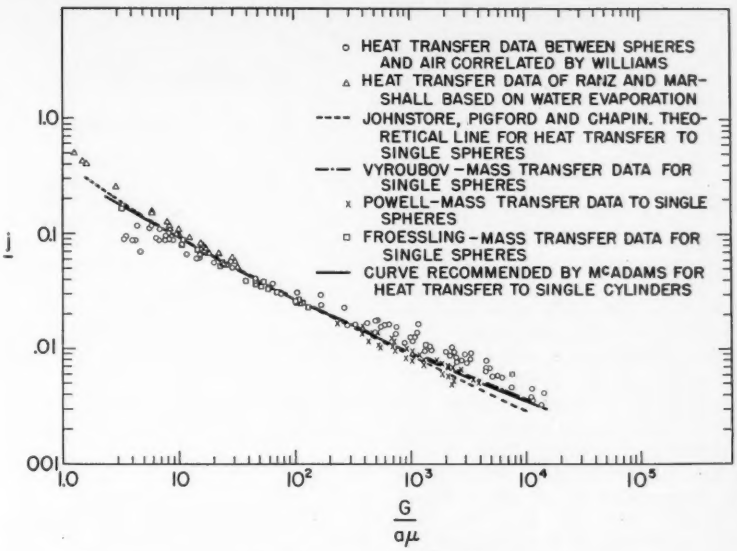
HEAT TRANSFER DATA BETWEEN SPHERES AND AIR CORRELATED BY WILLIAMS
HEAT TRANSFER DATA OF RANZ AND MARSHALL BASED ON WATER EVAPORATION
JOHNSTORE, PIGFORD AND CHAPIN. THEORETICAL LINE FOR HEAT TRANSFER TO SINGLE SPHERES
VYROUBOV – MASS TRANSFER DATA FOR SINGLE SPHERES
POWELL – MASS TRANSFER DATA TO SINGLE SPHERES
FROESSLING – MASS TRANSFER DATA FOR SINGLE SPHERES
CURVE RECOMMENDED BY McADAMS FOR HEAT TRANSFER TO SINGLE CYLINDERS
j
1.0
0.1
.01
.001
1.0
10
10²
10³
10⁴
10⁵
G/aμ

Fig. 6. Comparison of the rate of heat transfer from single cylinders with the data for single spheres.

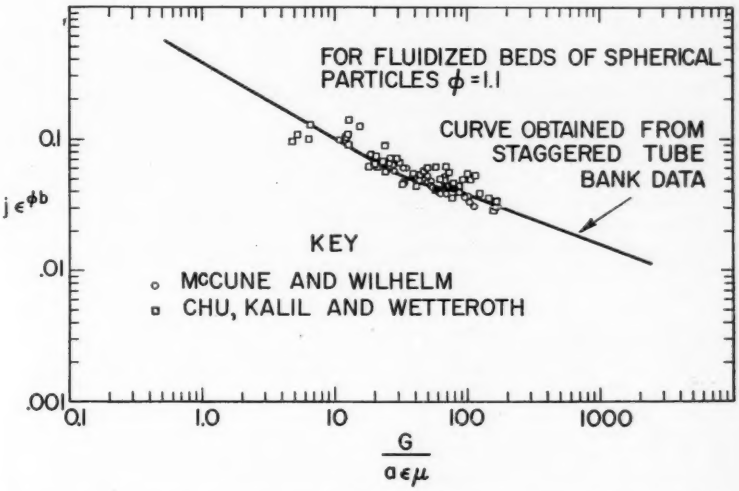

Fig. 7. Comparison of data for beds of fluidized spheres with curve from staggered-tube-bank data.

EFFECT OF PRANDTL NUMBER IN CROSS FLOW

Comparatively little work has been done on the effect of the Prandtl modulus on heat transfer for the case of fluids flowing across tube banks. In general it has been assumed that the effect is the same in cross flow as in the better understood case of flow through tubes. The latter case was first analyzed for the turbulent region by Prandtl (*25*) and Taylor (*31*) and more recently and extensively by Von Karman (*18*), Boelter et al. (*1*), and Reichart (*27*), using velocity-distribution measurements in straight tubes.

Colburn (*5*) showed that over the range of Reynolds numbers then investigated the complex function of Prandtl number appearing in the theoretical derivations could be replaced by the Prandtl number to a constant power. Colburn could thus empirically correlate the data by equations of the form

$$f(Re) = (\bar{h}/C_pG)\,Pr^{\frac{2}{3}} \qquad (18)$$

One of the most recent theoretical analyses is due to Lin, Moulton, and Putnam (*20*), who introduced the concept of a small amount of eddy in what is normally considered the laminar layer. With their analysis they were able to obtain considerably better agreement for heat transfer at Prandtl numbers greater than 1 and for mass transfer data at high Schmidt numbers. They presented their results as a series of curves of h/CpG vs. Reynolds number with Prandtl number as parameter. These curves may be very closely approximated by an equation of the form

$$f(Re) = (\bar{h}/C_pG)\,Pr^{n} \qquad (19)$$

where n is itself a function of the Reynolds number.

The variation in the Prandtl number exponent is shown in Figure 10.

$$n = 1.22\,Re^{-0.07} \qquad (20)$$

It is seen that the Colburn approximation of $n = 2/3$ is a good average value for use at fairly low Reynolds numbers. However, the deviation from this becomes large at high Reynolds numbers.

One might expect a similar situation to obbtain in cross flow. It would also be expected that the effect would be noticeable at lower Reynolds numbers owing to the greater turbulence in cross flow. A small quantity of data which indicate that this may be true were obtained at Brookhaven National Laboratory as part of the previously reported(*8, 9, 28*) extensive investigation of heat ransfer rate for cross flow at high Reynolds numbers.

Both local and average heat transfer coefficients were obtained for two lattice positions at two Reynolds numbers and a Prandtl number of approximately three. The equipment and methods used were those described by Sheehan et al.(*28*) and therefore will not be given in detail here. Briefly the heat transfer coefficients were obtained by measuring the total temperature difference between the bulk water temperature and the inside-wall temperature of a hollow electrically heated nickel tube. The wall temperatures were obtained by means of a revolving pin-point thermocouple probe. The tube bank used consisted of 200 elements 10 rows wide and 20 deep. The elements, 0.810 in. in diameter, were set in an equitriangular spacing with a pitch of 1 9/32 in.

It is found that the 2/3 power of the Prandtl number does not bring the data taken at $Pr \cong 3$ into agreement with the $Pr \cong 1$ data. The discrepancy is found to exist whether the comparison is based on the use of the average film temperature for the determination of fluid properties or on the use of bulk water temperatures together with the Sieder and Tate (*29*) correction. If it is assumed that the effect of the Prandtl number in cross flow is similar to the effect in flow through tubes, this discrepancy can be explained. It is known that for the turbulent region, $n = 2/3$ is a good average value between approximately $(DG/\mu\varepsilon) = 100$ and $(DG/\mu\varepsilon) = 2{,}000$. If

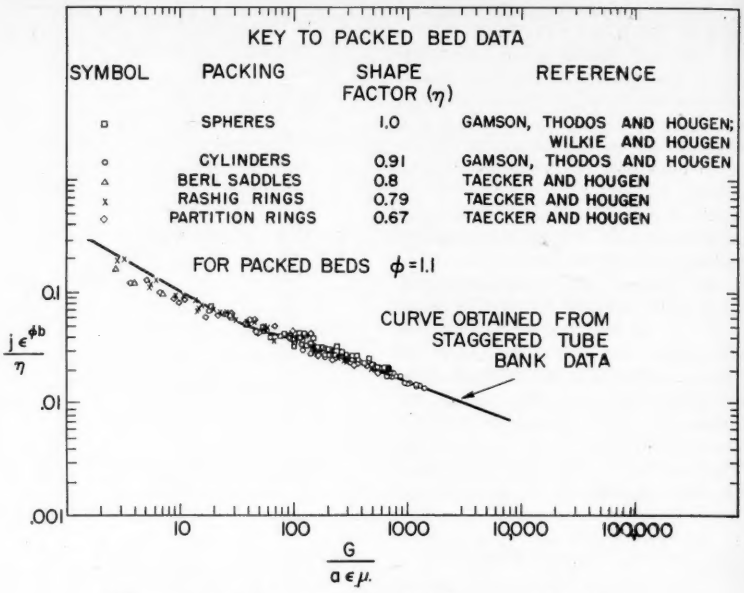

Fig. 8. Correlation of packed-bed heat transfer data.

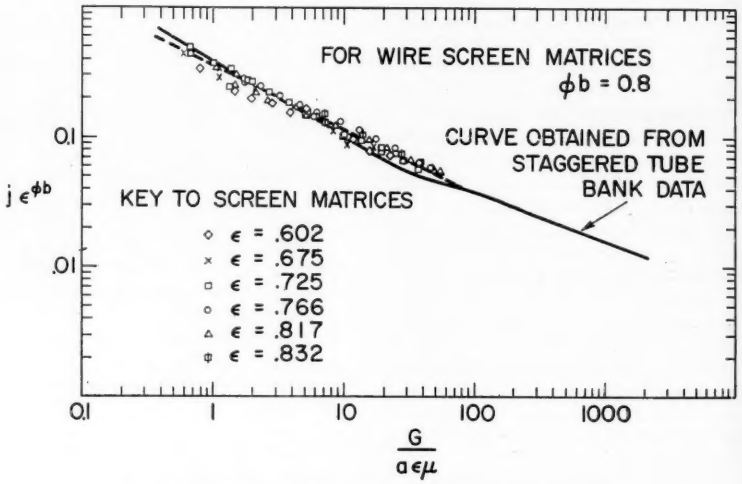

Fig. 9. Correlation of wire-screen heat transfer data.

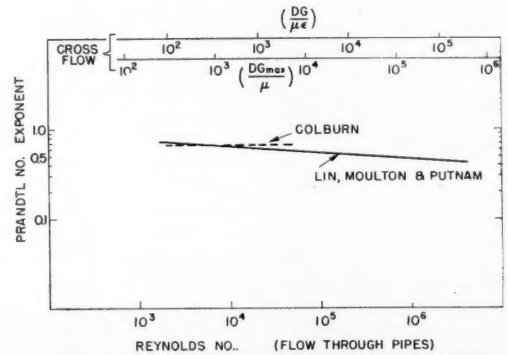

Fig. 10. Variable Prandtl number exponent obtained from work of Lin et al. (*20*).

a line parallel to Equation (20) is drawn through this region, one obtains for staggered tube banks

$$n = 0.985\,(DG/\mu\epsilon)^{-0.07} \quad (21)$$

In Figures 11 and 12 the experimental values for the average film coefficients are compared with the lines obtained by extrapolation of the $Pr = 1$ data for the same lattice positions. It is seen that the line obtained by use of the 2/3 power of Prandtl number falls considerably below the experimental points; however, the line obtained with the variable exponent of Equation (21) appears to fit the data within the experimental error. For the range of Reynolds numbers explored the Prandtl number exponent is about 0.48.

In Figures 13 and 14 a comparison similar to the foregoing is made for the local heat transfer coefficients. The experimental points are compared with the curves obtained by extrapolation of the local-coefficients data of Dwyer, Sheehan, and Weisman (*9*). Again good agreement is obtained with the prediction based on the variable Prandtl number exponent of Equation (21).

It is realized that the results given here must be regarded as tentative in view of the small amount of data available. It is regrettable that budgetary restrictions prevented additional work at other Reynolds and Prandtl numbers, and it is hoped that other workers will investigate this problem.

NOTATION

a = surface area of particle per unit volume of particle, sq.ft./cu.ft.

b = Reynolds number exponent, dimensionless

C_p = specific heat, B.t.u./(lb.) (°F.)

D = diameter of cylinder, ft.

Fa = arrangement of factor of Grimison, dimensionless

G = superficial mass velocity based on total cross-sectional area, lb./(hr.) (sq.ft.)

G_{max} = maximum mass velocity based on minimum flow area, lb./(hr.) (sq.ft.)

h = local heat transfer coefficient for a single point on the circumference of a tube, B.t.u./(hr.) (sq.ft.) (°F.)

h = average heat transfer coefficient, B.t.u./(hr.) (sq.ft.) (°F.)

j = transfer coefficient, dimensionless for heat transfer $j = (h/C_pG)\,(Pr)^{\frac{2}{3}}$ for mass transfer $j = (K'\rho/G)\,(Sc)^{\frac{2}{3}}$

k = thermal conductivity of fluid, B.t.u./(hr.) (sq.ft.) (°F.)/ft.

K' = mass transfer coefficient in concentration units, moles/(hr.) (sq.ft.) (moles/cu.ft.)

n = Prandtl number exponent, dimentionless

Pr = Prandtl number, dimensionless

Re = Reynolds number, dimensionless

s_l = longitudinal tube pitch (distance between tube centers in direction parallel to flow)

s_t = transverse tube pitch (distance between tube centers in direction normal to flow)

S_c = Schmidt number, dimensionless

ε = void fraction, dimensionless

ρ = density, lb./cu.ft.

ϕ = arrangement factor, dimensionless

η = fraction of packing area effective in heat and mass transfer, dimensionless

μ = viscosity, lb./(ft.) (hr.) (evaluated at bulk temperature when no subscript is used)

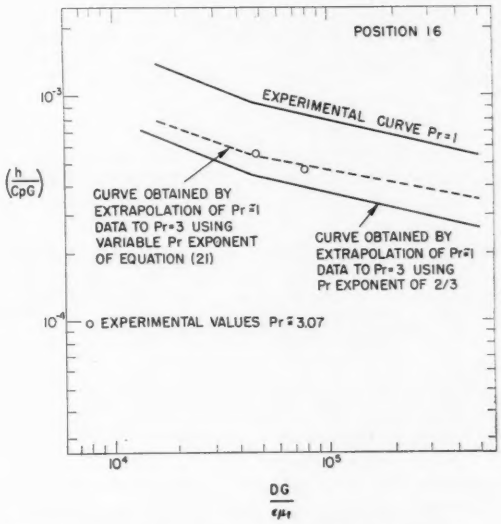
POSITION 16
EXPERIMENTAL CURVE Pr=1
CURVE OBTAINED BY EXTRAPOLATION OF Pr=1 DATA TO Pr=3 USING VARIABLE Pr EXPONENT OF EQUATION (21)
CURVE OBTAINED BY EXTRAPOLATION OF Pr=1 DATA TO Pr=3 USING Pr EXPONENT OF 2/3
o EXPERIMENTAL VALUES Pr=3.07
10⁻³
10⁻⁴
10⁴
10⁵
(h/CpG)
DG/εμf

Fig. 11. Comparison of experimental values of the average coefficients (central position) at $Pr = 3$ with curves extrapolated from $Pr = 1$ data.

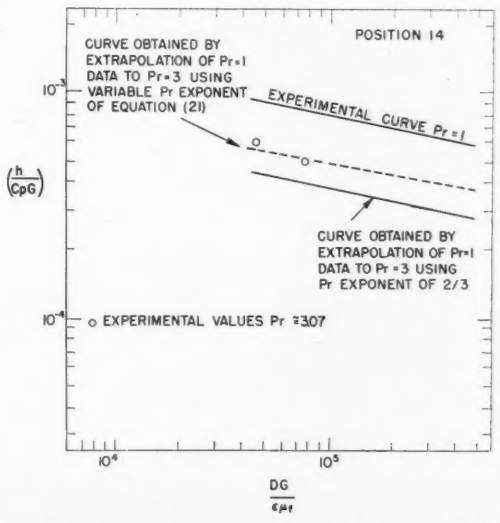
POSITION 14
CURVE OBTAINED BY EXTRAPOLATION OF Pr=1 DATA TO Pr=3 USING VARIABLE Pr EXPONENT OF EQUATION (21)
EXPERIMENTAL CURVE Pr=1
CURVE OBTAINED BY EXTRAPOLATION OF Pr=1 DATA TO Pr=3 USING Pr EXPONENT OF 2/3
o EXPERIMENTAL VALUES Pr=3.07
10⁻³
10⁻⁴
10⁴
10⁵
(h/CpG)
DG/εμf

Fig. 12. Comparison of experimental values of the average coefficients (wall position) at $Pr = 3$ with curves extrapolated from $Pr = 1$ data.

Subscripts

B = evaluated at bulk temperature
f = evaluated at film temperature
W = evaluated at wall temperature

LITERATURE CITED

1. Bergelin, O. P., G. A. Brown, and S. C. Doberstein, *Trans. Am. Soc. Mech. Engrs.*, 74, 969 (1952).
2. Bergelin, O. P., G. A. Brown, H. D. Hull, and F. W. Sullivan, *Trans. Am. Soc. Mech. Engrs.*, 72, 881 (1950).
3. Boelter, L. M., R. Martinelli, and F. Johassen, *Trans. Am. Soc. Mech. Engrs.*, 63, 447 (1941).
4. Chu, J. C., J. Kalil, and W. Wetteroth, *Chem. Eng. Progr.*, 49, 141 (1953).
5. Colburn, A. P., *Trans. Am. Inst. Chem. Engrs.*, 29, 174 (1933).
6. Coppage, J. F., and A. L. London, paper presented at A.I.Ch.E. San Francisco meeting (September, 1953).
7. Dryden, C. E., D. A. Strang, and A. E. Withrow, *Chem. Eng. Progr*, 49, 191 (1953).
8. Dwyer, O. E., F. L. Horn, and J. Weisman, *Am. Soc. Mech. Engrs.*, preprint F-21.
9. Dwyer, O. E., T. V. Sheehan, and J. Weisman, *Am. Soc. Mech. Engrs.*, preprint F-20.
10. Evans, G. C., and C. F. Gerald, *Chem. Eng. Progr.*, 49, 135 (1953).
11. Froessling, N., *Gerlands Beitr. Geophys.*, 32, 170 (1938).
12. Gaffney, B. J., and T. B. Drew, *Ind. Eng. Chem.*, 42, 1127 (1950).
13. Gamson, B. W., *Chem. Eng. Progr.*, 47, 19 (1951).
14. Gamson, B. W., G. Thodos, and O. A. Hougen, *Trans. Am. Inst. Chem. Engrs.*, 39, 1 (1943).
15. Grimison, E. D., *Trans. Am. Soc. Mech. Engrs.*, 59, 583 (1937).
16. Hobson, M., and G. Thodos, *Chem. Eng. Progr.*, 45, 517 (1949).
17. Johnstone, H. F., R. L. Pigford, and J. H. Chapin, *Trans. Am. Inst. Chem. Engrs.*, 37, 95 (1941).
18. Karman, T. Von., *Trans. Am. Soc. Mech. Engrs.*, 61, 205 (1935).
19. Kays, W. M., A. L. London, and R. K. Lo, *Trans. Am. Soc. Mech. Engrs.*, 76, 387 (1954).
20. Lin, C. S., R. W. Moulton, and G. L. Putnam, *Ind. Eng. Chem.*, 45, 636 (1953).
21. McAdams, W. H., 2 ed., "Heat Transmission", p. 221, McGraw-Hill Book Company, Inc., New York (1942).
22. McCune, L. N., and R. H. Wilhelm, *Ind. Eng. Chem.*, 41, 1124 (1949).
23. Pierson, O. A., *Trans. Am. Soc. Mech. Engrs.*, 59, 563 (1937).
24. Powell, R. W., *Trans. Inst. Chem. Engrs. (London)* 18, 36 (1940).
25. Prandtl, L., *Z. Phys.*, 29, 427 (1928).
26. Ranz, W. E., and W. R. Marshall, Jr., *Chem. Eng. Progr.*, 48, 173 (1952).
27. Reichardt, R., *Natl. Advisory Comm. Aeronaut. Tech. Mem.* 1047 (1943).
28. Sheehan, T. V., R. Schomer, and O. E. Dwyer, *Am. Soc. Mech. Engrs.*, preprint F-19.
29. Sieder, E. N., and G. E. Tate, *Ind. Eng. Chem.*, 28, 1429 (1936).
30. Taecker, R. O., and O. A. Hougen, *Chem. Eng. Progr.*, 45, 188 (1949).
31. Taylor, G. J., *Great Britain Advisory Comm. Aeronaut. Rept. Mem.* 2272 (1916).
32. Vyroubov, V., *J. Tech. Phys. (U.S.S.R.)*, 9, 1923 (1939).
33. Wilke, C. R., and O. A. Hougen, *Trans. Am. Inst. Chem. Engrs.*, 41, 445 (1945).
34. Williams, G. C., in W. H. McAdams, "Heat Transmission," 2 ed., p. 236, McGraw-Hill Book Company, Inc.

Presented at the A.I.Ch.E. Louisville meeting

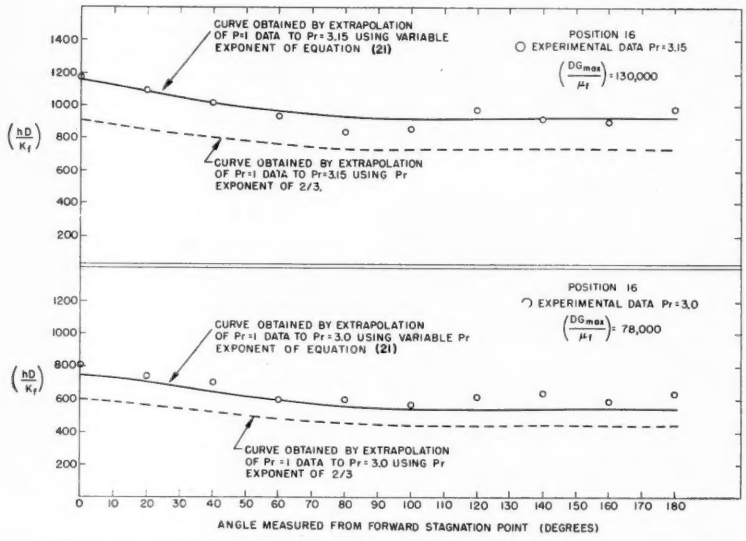
CURVE OBTAINED BY EXTRAPOLATION OF Pr=1 DATA TO Pr=3.15 USING VARIABLE EXPONENT OF EQUATION (21)
POSITION 16
○ EXPERIMENTAL DATA Pr=3.15
(DGmax/μf)=130,000
CURVE OBTAINED BY EXTRAPOLATION OF Pr=1 DATA TO Pr=3.15 USING Pr EXPONENT OF 2/3.
POSITION 16
○ EXPERIMENTAL DATA Pr=3.0
(DGmax/μf)= 78,000
CURVE OBTAINED BY EXTRAPOLATION OF Pr=1 DATA TO Pr=3.0 USING VARIABLE Pr EXPONENT OF EQUATION (21)
CURVE OBTAINED BY EXTRAPOLATION OF Pr=1 DATA TO Pr=3.0 USING Pr EXPONENT OF 2/3
(hD/Kf)
ANGLE MEASURED FROM FORWARD STAGNATION POINT (DEGREES)

Fig. 13. Comparison of experimental values of individual film coefficients (central position) at $Pr = 3$ with curves extrapolated from $Pr = 1$ data.

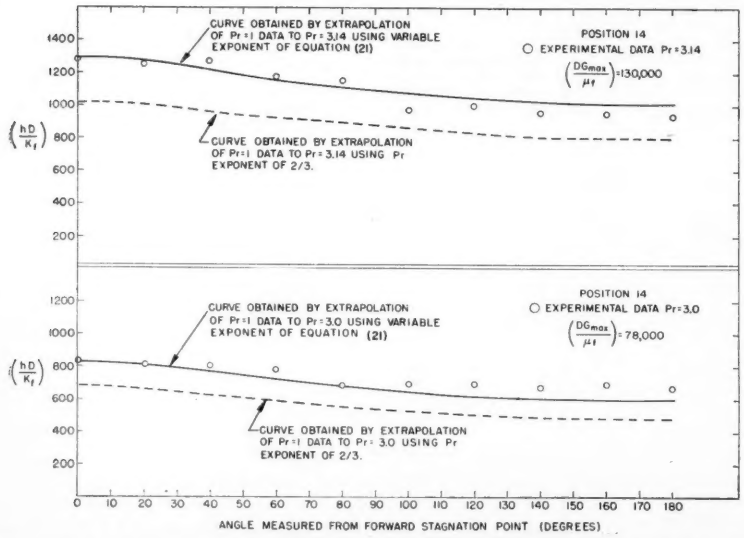
CURVE OBTAINED BY EXTRAPOLATION OF Pr=1 DATA TO Pr=3.14 USING VARIABLE EXPONENT OF EQUATION (21)
POSITION 14
○ EXPERIMENTAL DATA Pr=3.14
(DGmax/μf)=130,000
CURVE OBTAINED BY EXTRAPOLATION OF Pr=1 DATA TO Pr=3.14 USING Pr EXPONENT OF 2/3.
POSITION 14
○ EXPERIMENTAL DATA Pr=3.0
(DGmax/μf)=78,000
CURVE OBTAINED BY EXTRAPOLATION OF Pr=1 DATA TO Pr=3.0 USING VARIABLE EXPONENT OF EQUATION (21)
CURVE OBTAINED BY EXTRAPOLATION OF Pr=1 DATA TO Pr=3.0 USING Pr EXPONENT OF 2/3.
(hD/Kf)
ANGLE MEASURED FROM FORWARD STAGNATION POINT (DEGREES)

Fig. 14 Comparison of experimental values of individual film coefficients (wall position) at $Pr = 3$ with curves extrapolated from $Pr = 1$ data.

Gas-solid Contact in Fluidized Beds

C. Y. Shen and H. F. Johnstone, University of Illinois, Urbana, Illinois

According to the concept of two-phase fluidization, a part of the gas in a fluidized reactor passes through the uniform dispersed solid-gas phase in the form of bubbles, channels, and slugs. Material transport by mixing or diffusion takes place at the phase boundaries. A mass transfer coefficient between the two phases may be used to evaluate the effectiveness of contact between the gas and solid. The reaction rate for the catalytic decomposition of nitrous oxide was determined in a fluidized bed of impregnated alumina particles and compared with the corresponding rate in a fixed bed. Simultaneous rate equations were established based on the assumption that the continuous phase is either completely unmixed or uniformly mixed, and the discontinuous phase passes without mixing. The effects of the velocity of the gas, the particle size, and the bed depth on the transfer coefficient were investigated. Applications to heat transfer in fluidized beds and equipment design are discussed.

In a dense-phase fluidized reactor the gas stream may be considered to exist in two phases, according to the concept proposed by Toomey and Johnstone(*8*). The continuous phase comprises a uniform mixture of a part of the gas which supports the solid particles and flows through the bed at the same velocity as that at incipient fluidization. The excess gas which moves through the bed as bubbles, slugs, and channels is the discontinuous phase. Since the solid particles are for the most part retained in the continuous phase, the reactants in the discontinuous phase must be transferred to the continuous phase before they can react with the solid. This concept provides a simple model for the reaction mechanism in a fluidized bed. In a previous paper(*3*) the part of the reaction rate above that at incipient fluidization was attributed to the presence of the discontinuous phase and was correlated with the gas velocity and particle size by analogy with the pressure-drop relationship(*8*).

Although the mechanism of the formation of bubbles and their behavior in the fluidized bed is not entirely clear, the rate of transfer between the two phases may be expressed in terms of a coefficient which depends on such factors as the rate of gas flow, size of the particles, and depth of the bed. The transfer coefficient is a measure of the intimacy of the gas-solid contact in fluidized beds and should be useful in the design of fluidized reactors. Its value can be calculated from data on reaction kinetics in a fluidized bed by comparison with corresponding data for a fixed bed, a suitable model being used as a basis for establishing the simultaneous rate equations. The following models have been used for the present calculations.

C. Y. Shen is at present with Monsanto Chemical Company, Dayton, Ohio.

Consecutive Mass Transfer and Reaction

The fluidized bed is considered to be comprised of two fluid phases: a gas-solid mixture and a pure gas phase, analogous to a liquid with gas bubbles. For a first-order reaction, assuming that mixing within each phase is negligible, the mass transfer coefficient can be calculated from two simultaneous first-order linear differential equations obtained from a material balance on each phase.

$$\frac{dC_d}{d\theta} = -k_d(C_d - C_c) \quad (1)$$

$$\frac{dC_c}{d\theta} = -k_c C_c - \frac{\theta_d V_d}{\theta_c V_c}\frac{dC_d}{d\theta} \quad (2)$$

where k_d is the transfer coefficient expressed as moles per unit time per unit volume of bed per unit concentration difference between the two phases. This definition is similar to the capacity coefficient for an adsorption tower, which is characteristic of the equipment design. k_c is the first-order reaction rate constant. Since the velocity of the gas is different in the two phases, in order to transform Equations (1) and (2) to distance coordinates the time of detention must be introduced.

$$\frac{dC_d}{dz} = -\frac{\theta_d k_d}{L}(C_d - C_c) \quad (3)$$

$$\frac{dC_c}{dz} = \frac{V_d}{V_c}\frac{\theta_d}{L}k_d(C_d - C_c) - \frac{\theta_c k_c C_c}{L} \quad (4)$$

The solution of Equations (3) and (4) is

$$C_d = A_1 e^{\frac{R_1 z}{L}} + B_1 e^{\frac{R_2 z}{L}} \quad (5)$$

$$C_c = A_2 e^{\frac{R_1 z}{L}} + B_2 e^{\frac{R_2 z}{L}} \quad (6)$$

where

$$R_1 = \frac{1}{2}\left[-b + \sqrt{b^2 - 4c}\right],$$

$$R_2 = \frac{1}{2}\left[-b - \sqrt{b^2 - 4c}\right],$$

$$b = k_d\theta_d\left(\frac{V}{V_c}\right) + k_c\theta_c,$$

$$c = k_c k_d \theta_d \theta_c$$

The arbitrary constants A_1, A_2, B_1, and B_2 can be evaluated from the boundary conditions:

$$\text{At } z = 0,\ C_d = C_c = C_1, \text{ and } \frac{dC_c}{dz} = -\frac{k_c C_1 \theta_c}{L} \quad (7)$$

Therefore,

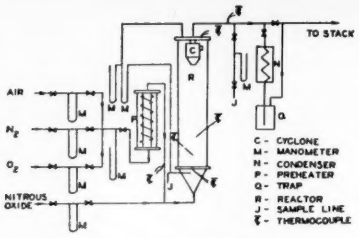

Fig. 1. Diagram of apparatus.

$$\frac{C_d}{C_1}=\frac{1}{R_1-R_2}\left[R_1 e^{\frac{R_2 z}{L}}-R_2 e^{\frac{R_1 z}{L}}\right] \quad (8)$$

$$\frac{C_c}{C_1}=\frac{1}{R_1-R_2}\left[(R_1+k_c\,\theta_c)\,e^{\frac{R_2 z}{L}}-(R_2+k_c\,\theta_c)\,e^{\frac{R_1 z}{L}}\right] \quad (9)$$

Furthermore, from a material balance at the outlet

$$\frac{C_2}{C_1}=\frac{V_c}{V}\left(\frac{C_c}{C_1}\right)+\frac{V_d}{V}\left(\frac{C_1}{C_d}\right) \quad (10)$$

The subscripts 1 and 2 denote the inlet and outlet conditions, respectively. Since C_2/C_1 is measured directly and k_c is known from fixed-bed studies, the value of k_d can be calculated from Equations (8) to (10).

Continuous Reactor Model

The continuous phase is assumed to be equivalent to a well-stirred reactor of constant and uniform composition at a fixed gas velocity. When steady state exists, the amount of reactants flowing into the reactor will equal the amount that flow out plus those that react.

$$Q_c\frac{dC_c}{d\theta}=0=V\,(C_1-C_2)-Q_c\,k_c\,C_c \quad (11)$$

where Q_c = volume of the continuous phase = $V_c\theta_c$
or

$$C_c=\frac{V}{k_c\,V_c\,\theta_c}\,(C_1-C_2) \quad (11a)$$

From Equation (1)

$$k'_d=-\frac{1}{\theta_d}\ln\left[\frac{C_{d2}-C_c}{C_{d1}-C_c}\right] \quad (12)$$

k'_d is the transfer coefficient for the continuous reactor model.

Table 1.—Gas Rates at Minimum Fluidization and Incipient Formation of Two Phases

Catalyst size, mesh	Temperature of air, °F.	Minimum fluidization rate, std. cu. ft./min.	Incipient two-phase fluidization rate, std. cu. ft./min.
165–200	800	0.043	0.059
165–200	750	0.046	0.063
165–200	700	0.049	0.068
120–165	800	0.069	0.105
120–165	750	0.074	0.112
120–165	700	0.080	0.121
60–120	800	0.107	0.149
60–120	750	0.114	0.159
60–120	700	0.123	0.171

The concentration of the reactants in the discontinuous phase at the outlet can be obtained from the material balance at the exit

$$C_{d2}=\frac{1}{V_2}\,(VC_2-V_c\,C_c) \quad (13)$$

The retention time in the discontinuous phase can be estimated from the bed expansion,

$$\theta_d=A\,(L_f-L_{mf})\,/\,(V-V_c) \quad (14)$$

The value of k'_d can be found from Equations (11) to (14)

EXPERIMENTAL

The reaction chosen for study was the catalytic decomposition of nitrous oxide, because the analysis is simple and the catalyst activity remains substantially constant over a long period of time. The rate of decomposition was measured in fixed and fluidized beds in the temperature range from 650° to 800°F. Nitrogen, air, or oxygen streams containing 1 to 2.5% nitrous oxide were used.

The kinetics of the reaction are discussed by Schwab and coworkers (*5* and *6*). Damköhler and Delcker (*1*) studied the decomposition in fixed beds of cupric oxide, alumina and alumina impregnated with cupric oxide, at various flow rates in the region of laminar flow. The reaction is first order and the yield depends on the time of contact and not on the linear velocity; hence the diffusional resistance is not a controlling step.

Apparatus. A diagram of the apparatus is shown in Figure 1. The individual gases were passed through filters, pressure regulators, and flow meters. The reactor was 4½ in. I.D. and 43 in. high and was made of 310 stainless steel. One thermocouple was embedded in the porous stainless steel support plate and two others were mounted through the column wall in the fluidized bed itself.

The reactor was heated electrically by chromel resistance ribbon which was wound in three sections around the reactor. The temperatures of the bottom and top sections were controlled manually with variable transformers, and the temperature of the middle section, which covered the entire catalyst bed, was regulated with an automatic controller.

The preheater was also made of a section of the 4½-in. stainless steel tubing 30 in. long. To secure high rates of heat transfer, the preheater was heated by both internal and external electric elements with variable inputs to keep the inlet gas at the desired temperature.

Sample lines were provided beneath the porous plate and at the top of the reactor. The pressure drop across the catalyst bed and the pressure inside the reactor were measured through pressure taps connected to manometers with ¼-in. copper tubing.

Catalyst. The catalyst was made by mixing 10 kg. of Alcoa XF-21-Si fluid cracking catalyst with 2.5 liters of solution containing 1 kg. of manganous nitrate and 350 g. of bismuth nitrate, drying for 5 days in a steam-heated vacuum oven, and finally roasting at 375°C. for 48 hr. in an electric furnace. The catalyst was separated into three fractions, 165-200, 120-165, and 60-120 mesh. by standard Tyler screens. The size distribution and composition of the catalyst are reported in a previous paper (*3*). The catalyst particles were generally round but not truly spherical.

Procedure. Air was used to fluidize the bed while the reactor was being heated to the desired temperature. After 8 to 12 hr. the reacting gas stream was passed into the apparatus and allowed to flow for 2 hr. at the set conditions. A sample of the exit gas was then taken for infrared analysis. The glass analysis cell, equipped with rock-salt-crystal windows, was flushed out thoroughly while the gas pressure was maintained at 800 mm. before adjustment to the final conditions of 72°F. and 745 mm. Temperatures, pressures, and flow rates were recorded during the sampling period.

Gas Analysis. The gas was analyzed for nitrous oxide in a Perkin-Elmer double-beam infrared spectrometer using the base-line technique de-

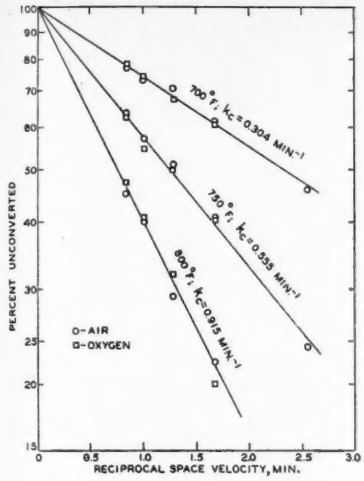

←Fig. 2. Decomposition rate of nitrous oxide in fixed beds: 2 kg. catalyst, 165-200 mesh; inlet-gas concentration, 1% nitrous oxide.

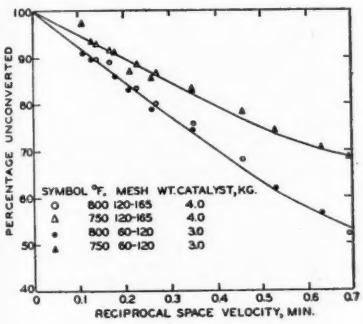

←Fig. 3. Decomposition rate of nitrous oxide in fluidized beds: inlet-gas concentration, 1% nitrous oxide.

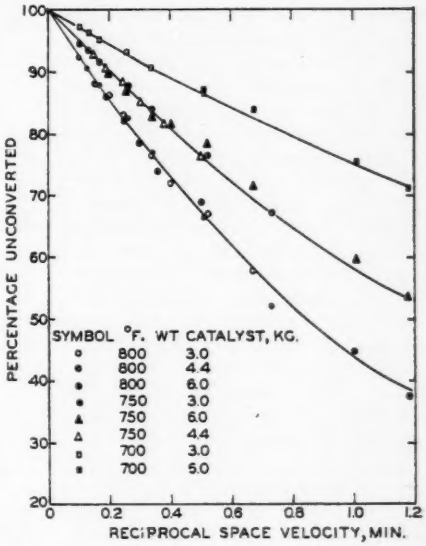

→Fig. 4. Decomposition of nitrous oxide in fluidized beds: effect of temperature and bed depth; inlet-gas composition, 1% nitrous oxide.

scribed by Wright(*11*). The wave number used was 2,180 cm.$^{-1}$

RESULTS

The results with air and oxygen as the diluent gases in the fixed-bed reactor at different temperatures are shown in Figure 2. The reciprocal space velocity shown is the ratio of the volume of the catalyst particles to the volumetric gas-feed rate at standard conditions. The volume of the particles was calculated from the weight of catalyst and the absolute particle density.

The initial nitrous oxide concentration does not affect the fractional rate of decomposition, and the reaction must follow a first-order mechanism. When nitrogen was used instead of air or oxygen, the reaction rate was slightly higher. The probable explanation is that oxygen decreases the number of anion vacancies on the catalyst surface and thus reduces the activity of the catalyst(*9*). The activation energies, calculated from the effect of temperature according to the Arrhenius equation, for the nitrogen and air or oxygen series are about the same, 17 kcal./g.mole. The effect of bed depth and particle size on the decomposition rate in fixed beds is small. The effects of temperature, particle size, and bed depth on the over-all reaction rate in fluidized beds of the same catalyst, with air as the diluent gas, are shown in Figures 3 and 4. The reaction rate in general is lower than that in fixed beds.

The minimum gas rate at which fluidization takes place was determined from the pressure-drop measurements. This was taken as the intersection of the straight lines for the fixed- and fluidized-bed regions in the pressure-drop vs. gas-velocity plots. In a previous paper(*8*) the relation between gas velocity and pressure drop was expressed by

$$\frac{\Delta P_{ke}}{\Delta P_{mf}} = (lD_p^{0.5} - m) \ln \frac{V}{V_v} \quad (15)$$

The incipient two-phase fluidization rate was obtained from the intercept of the straight line on the plot of $\Delta P_{ke}/\Delta P_{mf}$ vs. log V. The results are shown in Table 1.

The expansion of the bed during fluidization was measured in a 3.75-in. I.D., 40-in.-long glass column. Lewis, and Bauer(*4*) have shown that the fractional increase in height above that at minimum fluidization is proportional to the increase in the superficial gas velocity above that at incipient fluidization. This relationship can be expressed by

$$\frac{(L_f - L_{mf})}{L_{mf}} = \frac{0.0188}{D_p^{0.5}} (u - u_v) \quad (16)$$

This equation was used to calculate the height of the fluidized bed at any gas velocity.

TRANSFER COEFFICIENTS

The transfer coefficient between the two phases can be calculated from either of the two models presented above, together with the reaction-rate data in the fixed and fluidized beds. The reaction-rate constant for the fixed bed does not change under isothermal and isobaric conditions. Deviation from this value in the fluidized bed is caused by the presence of the discontinuous phase, and the transfer coefficient can be calculated as follows:

Consecutive Transfer and Reaction Steps. Since the coefficient cannot be expressed explicitly from Equations (8) to (10), its value must be calculated by a trial-and-error method. A value of k_d was first assumed and the outlet concentration was calculated from these equations. The calculated result was then compared with the experimental value and the value of k_d changed until the agreement was good. The values of k_d found by this method varied over a tenfold range from 9.6 to 98.8 min.$^{-1}$ depending on the gas velocity, bed depth, catalyst size, and temperature(*7*).

When the catalyst size is small compared with the diameter of the reactor, dimensional analysis shows that the variables that affect the transfer coefficient can be grouped as follows:

$$\frac{u}{k_d D_p} = \rho\left[\left(\frac{D_p u \rho_g}{\mu}\right)\left(\frac{L}{D_T}\right)\right.$$

$$\left(\frac{\rho_s - \rho_g}{\rho_g}\right)(\epsilon)\Bigg] \qquad (17)$$

In the range studied the gas density, 0.032 to 0.034 lb./cu.ft., had no noticeable effect on the group u/k_dD_p, which may be regarded as a modified Peclet number. The effects of gas velocity, bed depth, and particle size are shown in Figures 5 and 6. Since both the bed expansion and void fraction are functions of gas velocity, the effect of bed depth on the value of the transfer coefficient can be seen from the logarithmic plot of u/k_dD_p vs. gas velocity in Figure 5. The effect of gas velocity on the Peclet number increases with the height-diameter ratio. A possible explanation for this is that there is a greater tendency for channeling, or slugging, with coalescence of bubbles, which affects the gas-flow pattern in deep beds. This decreases the contact between the two phases and lowers the transfer coefficient.

Figure 6 shows that the Peclet number increases with increase in particle size of the catalyst. The average value of k_d for each series of runs is directly proportional to the bed depth and is roughly inversely proportional to the particle diameter. This indicates that k_d is a function of the total surface area of the particles and that the group uL/k_dD_T can be used to correlate all the data involving these variables such as temperature, particle size, and bed depth. This correlation is shown in Figure 7.

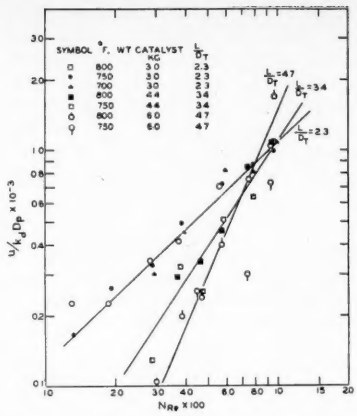

Fig. 5. Effect of bed depth on modified Peclet number: catalyst size, 165-200 mesh.

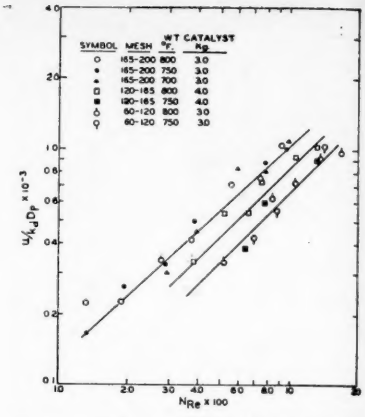

Fig. 6. Effect of particle size on modified Peclet number.

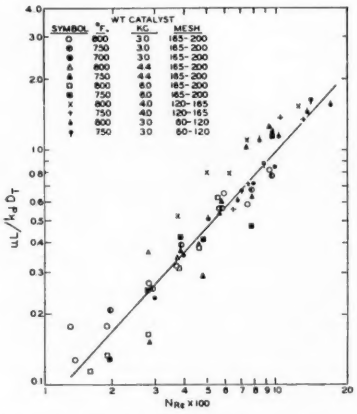

Fig. 7. Correlation of transfer coefficients based on model for consecutive transfer and reaction.

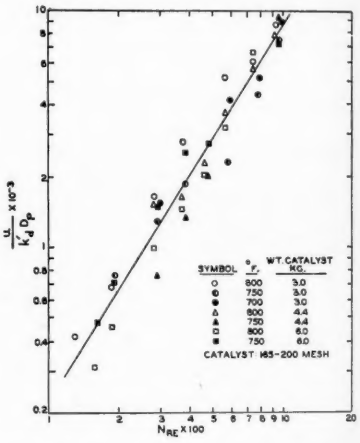

Fig. 8. Correlation of transfer coefficients based on continuous-reactor models.

Continuous Reactor Model. The advantage of the continuous reactor model for representing the fluidized system is that it is simpler to use for higher order reactions and the result on a small unit should be useful for predicting the performance of larger reactors. For the present study a reaction-rate constant calculated from the conversion rate at incipient two-phase fluidization was used to calculate k'_d according to Equations (11) to (14). The modified Peclet number for the continuous reactor model u/k'_dD_p is plotted against the Reynolds number in Figure 8. In this case the data points fall along the line with a slope of 1.6.

Each experimental value of k_d and k'_d was obtained from an average of two or three runs to minimize the fluctuations caused by the unsteadiness of the bed, since a slight error in the outlet concentration was sufficient to introduce a large error in the calculated transfer coefficient. In a few cases, especially at low temperatures, nitrous oxide decomposed in the fluidized bed at high gas velocities was appreciably less than that at incipient fluidization, and the transfer coefficient could not be calculated.

DISCUSSION

Although either the consecutive transfer model or the continuous reactor model can be used for higher order catalytic or homogeneous reactions, the difficulty in using the former lies in the fact that the differential equations become nonlinear. The boundary conditions are known at one end, however, and a solution of the equations can be obtained by a digital computer or by a series solution (7). Since the transfer coefficient does not depend on the reaction order, the value obtained from a first-order reaction should hold for the higher order reactions.

The models and concepts developed for reactions in the fluidized reactor can be applied to heat and mass transfer processes. Experimental measurements of the rate of heat and mass transfer between gas and solid particles in fluidized beds are difficult to make since shallow beds must be used because of the high values of the coefficients. Such fluidized beds behave entirely differently from those used for dense-phase fluidization. Wamsley and Johanson (10) used a transient heating method with beds less than 3 in. deep to determine the heat transfer coefficient between fluidized solids and gas. Their results have been recalculated on the basis of consecutive transfer stops according to the

TABLE 2.—HEAT TRANSFER COEFFICIENTS CALCULATED FROM DATA OF WAMSLEY AND JOHANSON (*10*)

Run	Inlet temp., °F.	Time, hr.×10³	Outlet temp., °F.	T_{p1}, °F.	N_{Re}	h_d B.t.u. (hr.)(°F.)(sq.ft.), obs.	$\frac{\rho_g C_p}{aA} k_d$ B.t.u. (hr.)(°F.)(sq.ft.), calc.
a. 100-115 mesh							
GA12	137.0	90 3	119.9	94.1	1.12	0.0056	0.0292
GA21	137.9	65.0	122.3	98.3	1.86	0.0107	0.0276
GA14	142.1	58.6	128.6	110.2	2.68	0.0215	0.0267
GA17	138.7	62.8	126.3	113.2	3.34	0.0348	0.0260
b. 60-65 mesh							
GA18	138.7	62.2	119.9	101.0	2.93	0.0185	0.0251
GA10	140.8	48.9	124.3	107.1	4.25	0.0326	0.0240
GA13	139.9	47.5	124.3	109.8	5.37	0.0523	0.0235
GA20	139.0	48.3	126.3	114.0	6.43	0.0621	0.0229
c. 32-35 mesh							
GA11	137.2	32.8	113.6	99.8	8.97	0.0197	0.0248
GA16	141.8	44.5	124.3	113.9	11.31	0.0525	0.0230
GA15	139.0	37.8	122.3	111.4	13.25	0.0797	0.0228
GA19	139.4	33.4	122.3	114.5	16.08	0.1850	0.0223

two-phase theory.

From a heat balance the rate of change of temperature of the gas with distance through the bed is given by

$$-w_d C_p \frac{dT_d}{dz} - A\, a\, h_d (T_d - T_c) \tag{18}$$

$$-w_c C_p \frac{dT_c}{dz} = w_d C_p \frac{dT_d}{dz} + h_c\, a\, A\, (T_c - T_p) \tag{19}$$

The time required to bring the temperature of the solid to equilibrium with the gas is very short, as indicated by the experimental results of Johnstone, Pigford, and Chapin (*2*) on heat transfer to clouds of particles. It may be assumed, therefore, that the temperature of the gas in the continuous phase is essentially equal to the particle temperature T_p. This is equivalent to saying that the heat transfer coefficient h_c between particle and gas approaches infinity. The solid particles have a much higher heat capacity than the gas and they mix rapidly; thus the temperature of the solid may be assumed to be constant throughout the bed. With these assumptions, the coefficient h_d can be obtained from the following equations.

$$h_d = \frac{w_d C_p}{a\, A\, L} \ln \frac{T_1 - T_p}{T_{d2} - T_p} \tag{20}$$

$$T_{d2} = \frac{w}{w_d} T_2 - \frac{w_c}{w_d} T_p \tag{21}$$

$$T_p = T_{p1} + \frac{1}{w_s C_s} \int_o^\theta w\, C_p (T_1 - T_2)\, d\theta \tag{22}$$

The inlet temperature T_1 is the corrected value after adjustment for the heat losses, as suggested by Wamsley and Johanson. The temperature of the particles was calculated from Equation (22) by graphical integration of the published data. The time θ was chosen as that at the middle of a run. The values calculated for h_d are listed in Table 2.

When heat or mass is transferred by means of fluid motion near the boundary of the two phases, the same mechanism controls both processes. Therefore, it is reasonable to assume that the rate of heat transfer under a temperature gradient and the rate of mass transfer under a concentration gradient can be correlated by the following equation:

$$h_d = \beta \frac{\rho_g C_p}{a\, A} k_d \tag{23}$$

where β is a proportionality constant nearly equal to unity. The value of the group $\rho_g c_p k_d / aA$, in which k_d is determined from Figure 7 by extrapolation, is also listed in Table 2.

It is to be noted that h_d increases with the gas velocity (it is proportional to $u^{1.6}$); whereas k_d is affected only slightly by velocity. For the smaller particle sizes, 110-115 and 60-65 mesh, the value of h_d follows a similar inverse function of the particle diameter, as shown for k_d in Figure 6, but this is not true for the series of 32-35 mesh size at low velocities. These differences may be due to an error in the assumption of uniform temperature of the solid particles. The large dependence of h_d on velocity may also be a result of using very shallow beds. The agreement of the calculated data with the experimental results, however, is sufficient to show that the concepts of the fluidized bed are useful and approximately correct. Thus the rate of heat transfer between the two phases is the rate-determining step. In practice a greater rate of heat transfer between the gas and particles will be obtained with smaller particles, but more of the gas will pass through the bed as the discontinuous phase. Thus there is a particle size at which the over-all rate of transfer is maximum. The optimum size will also depend on other factors such as the fluidization rate, reaction rate, heat transfer from the wall, etc., which affect economical considerations.

CONCLUSIONS

A fluidized catalyst bed may be considered to be composed of two phases, a continuous phase and a discontinuous phase. In the continuous phase the particles are supported by the gas stream moving at the same velocity as that at incipient fluidization. In the discontinuous phase the excess gas moves through the bed in the form of bubbles, slugs, or channels. In the presence of the discontinuous phase the reactant, for the most part, must be transferred to the continuous phase before reaction can occur. The increase of the over-all reaction rate above that at incipient two-phase fluidization may be attributed to the effect of gas velocity on the mass transfer between the two phases.

From measurements of the catalytic decomposition rate of nitrous oxide, on the assumption that both phases are unmixed, the transfer coefficient was found to be inversely proportional to the particle size. The effect of gas velocity on the transfer coefficient depends very much on the bed depth. The transfer coefficients were also calculated from published data on heat transfer. The approximate agreement between the calculated and observed values shows that the proposed model is sound.

Since the total rate of conversion in a fluidized reactor depends on the transfer rate and the reaction rate in the continuous phase, the rate-determining step evidently depends on the relative magnitude of these rate coefficients. Measurement of the transfer coefficient should enable design calculations and evaluation of the optimum conditions to be made from fixed-bed studies.

NOTATION

a = surface area of particles per unit volume, sq.ft/cu.ft.
A = a constant; area of the reactor, sq.ft.
B = a constant
C = concentration, moles/cu.ft.
C_p = specific heat of gas, B.t.u./(lb.) (°F.)
C_s = specific heat of solid, B.t.u./(lb.) (°F.)
D_p = particle diameter, ft.
D_T = reactor diameter, ft.
h = heat transfer coefficient, B.t.u./(hr.) (°F.) (sq.ft.)
k_d = transfer coefficient for consecutive model, min.$^{-1}$
k'_d = transfer coefficient for continuous model, min.$^{-1}$
k_c = first-order reaction-rate constant, min.$^{-1}$
L = height of bed, ft.
l, m = constants
ΔP_{mf} = pressure drop at minimum fluidization, in. of water
ΔP_{ke} = pressure drop above ΔP_{mf}, caused by kinetic energy losses, in. of water
N_{Re} = Reynolds number, $D_p u \rho_g/\mu$, dimensionless
Q = volume of bed, cu.ft.
T = temperature, °F.
u = linear gas velocity, ft./sec.
V = volumetric gas velocity, cu.ft./min.
w = mass rate of flow of gas, lb./hr.
z = length coordinate, ft.

Greek Letters

β = constant
ε = porosity
θ = time, min.
μ = viscosity, lb./(ft.) (sec.)
ρ = density, lb./cu.ft.

Subscripts

1 = inlet condition
2 = outlet condition
c = continuous phase
d = discontinuous phase
f = fluidization condition
g = gas
s = solid
v = incipient two-phase fluidization
mf = minimum fluidization
ke = kinetic energy

LITERATURE CITED

1. Damköhler, G., and G. Delcker, *Z. Elektrochem.*, **44**, 193 (1938).
2. Johnstone, H. F., R. L. Pigford, and J. H. Chapin, *Trans. Am. Inst. Chem. Engrs.*, **37**, 95 (1941).
3. Johnstone, H. F., J. D. Batchelor, and C. Y. Shen, *A.I.Ch.E. Journal*, **1**, 318 (1955).
4. Lewis, W. K., E. R. Gilliland, and W. C. Bauer, *Ind. Eng. Chem.*, **41**, 1104 (1949).
5. Schwab, G. M., and H. Schultes, *Z. physik. Chem.*, **B9**, 265 (1930).
6. Schwab, G. M., and G. Stager, *Z. physik. Chem.*, **B25**, 418 (1934).
7. Shen, C. Y., Ph.D. thesis, Univ. Illinois (1954); microfilm copies from University Microfilms, Inc., Ann Arbor, Michigan.
8. Toomey, R. D., and H. F. Johnstone, *Chem. Eng. Progr.*, **48**, 220 (1952).
9. Wagner, C., *J. Chem. Phys.*, **18**, 69 (1950).
10. Wamsley, W. W., and L. N. Johanson, *Chem. Eng. Progr.*, **50**, 347 (1954).
11. Wright, N., *Ind. Eng. Chem., Anal. Ed.*, **13**, 1 (1941).

Presented at the A.I.Ch.E. Houston meeting

Prediction of Ternary Vapor-liquid Equilibria from Boiling-point Data

Mitsuho Hirata, Tokyo Institute of Technology, Tokyo, Japan

A knowledge of ternary vapor-liquid equilibrium relations is indispensable to the design of columns for ternary rectification as well as azeotropic and extractive distillations. To determine these relations experimentally requires very involved analyses. It is, therefore, highly desirable to estimate ternary equilibrium relations without those analyses and, better still, without experimentation.

Attempts have been made to predict the ternary vapor-liquid equilibria on the theoretical basis of thermodynamic relations among activity coefficients of three components and by use of three binary equilibrium relations available for three combinations of components from Carlson and Colburn (*3*), Benedict, Johnson, Solomon, and Rubin (*1*), Colburn and Schoenborn (*4*), White (*20*), Wohl (*21*), Redlich and Kister (*16*), and Edwards, Hashmall, Gilmont, and Othmer (*6*). Some of these give good estimations for certain ternary systems but fail in other systems or are laborious to calculate accurately.

Scheibel and Friedland (*17*) proposed an empirical method which gives good agreement with many observed data; however, it is lacking in theoretical background and requires different procedures of calculation for different types of ternary systems concerned.

Othmer, Ricciardi and Thaker (*15*) derived a fundamental thermodynamic equation for ternary systems and used it for checking the vapor-liquid equilibrium data available for a ternary system.

PREDICTION FROM TEMPERATURE-COMPOSITION DATA

A method is here presented for estimating vapor compositions at constant-pressure equilibrium from boiling-point data of ternary systems. This method requires the boiling-point–composition data of the system, but the experimental procedures for determining boiling points of definite ternary liquid mixtures are generally much simpler than those required for determining entire vapor compositions of the system.

The method offered for ternary systems is a natural extension of the method for binary systems developed by the author (*8*) and Othmer, Ricciardi, and Thaker (*15*). It is based on the linear property of the equilibrium relations when

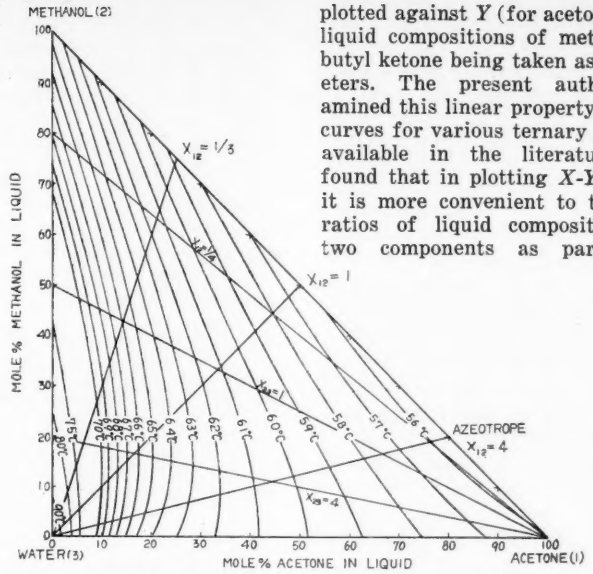

Fig. 1. Triangular diagram of ternary boiling point for the system acetone (1)–methanol (2)–water (3).

they are represented by X-Y curves, $X = x/(1-x)$ vs. $Y = y/(1-y)$, on logarithmic paper.

Othmer et al.(*15*) suggested that ternary systems, such as acetone–chloroform–methyl isobutyl ketone, can also be represented as straight lines on logarithmic paper when X (for acetone, for example) is plotted against Y (for acetone), the liquid compositions of methyl isobutyl ketone being taken as parameters. The present author examined this linear property of X-Y curves for various ternary systems available in the literature and found that in plotting X-Y curves it is more convenient to take the ratios of liquid compositions of two components as parameters rather than the liquid compositions of one component. This manner of indicating parameters for the ternary equilibria was introduced by Colburn and Schoenborn(*4*) in the relation of activity coefficients and liquid compositions. They used as parameters the relative compositions of secondary components instead of the ratios of them, but both are essentially the same.

PREDICTION OF TERNARY SYSTEMS

The calculation procedures of the present method for ternary systems are similar to those for binary systems except for some modifications due to the nature of the ternary system. The entire ternary equilibrium relation may be estimated and determined by the steps given below.

1. Plot available ternary-boiling-point data on a triangular diagram and draw smoothed lines for the constant value of the boiling point, as shown in Figure 1. The system of acetone-methanol-water examined by Uchida, Ogawa, and Hirata(*19*) is used as an example.

2. Plot the boiling point against the liquid composition of any component (preferably the lowest or highest boiling component) along a line on the ternary diagram at a constant ratio of mole fractions of the other two components. Thus the values of the boiling point are plotted against x_1 (in this example, mole fraction of acetone) for a constant value of X_{23}, as in Figure 2, where X_{23} is equal to 1, 4, and ¼. These values of X_{23} indicate in Figure 1 a series of straight lines passing through the corner of component 1 (acetone).

A striking observation in Figure 2 is that some boiling-point curves

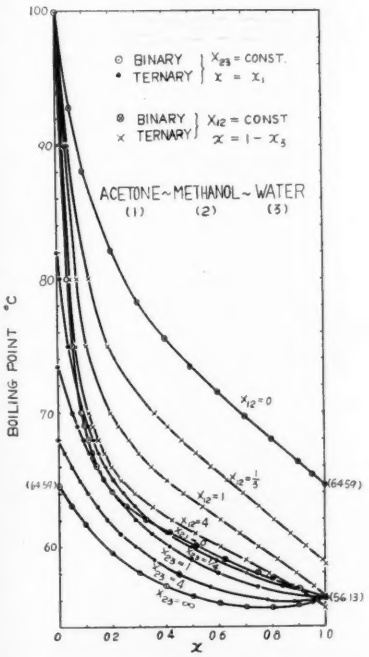

Fig. 2. Plot of boiling point, °C., vs. mole fraction in liquid x for the system acetone (1)–methanol (2)–water (3).

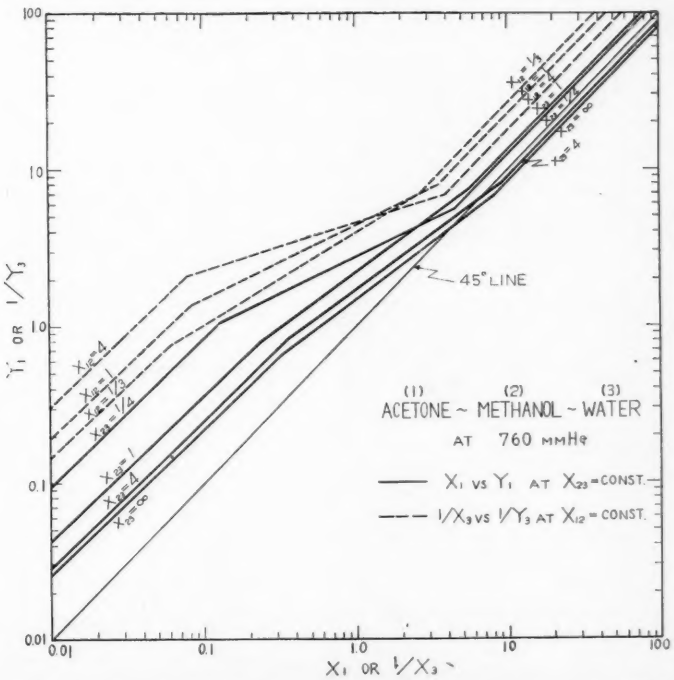

Fig. 3. Ternary X-Y curves calculated for the system acetone (1)–methanol (2)–water (3).

cross the limiting curves for binary systems. In such cases it is obvious that a linear interpolation would be greatly in error.

3. Calculate and determine X_1-Y_1 curves as shown in Figure 3 by using the boiling-point curves of Figure 2 for $X_{23} = 1$, 4, ¼, etc., and by following the same steps developed for binary systems [*cf.* Othmer et al. (*15*) or Hirata (*8* and *10*)]. In these calculations, however, it is usually difficult to find or estimate the latent heat of vaporization of ternary solutions, λ_x, which appears in the term $f(T)$; that is,

$$f(T) = \frac{\lambda_x}{RT^2}\left(\frac{dT}{dx}\right)_P$$

The author proposes here the following approximation for ternary systems:

$$f(T) = \frac{(\lambda_x/RT)}{T}\left(\frac{dT}{dx_1}\right)_P = \text{approx.}\ \frac{(\lambda_1/RT_1)X_1 + (\lambda_{23}/RT_{23})(1-x_1)}{T}\left(\frac{dT}{dx_1}\right)_P \quad (1)$$

where λ_{23}/RT_{23} is the value of λ_x/RT for the binary mixture of component 2 and component 3 at the definite value of X_{23} and may be estimated from binary data.

4. Transform X_1-Y_1 curves into x_1-y_1 curves, as shown in Figure 4. Plot the values of vapor composition y_1 on a ternary diagram and draw lines for the constant value of y_1. (*See* Figure 5.)

5. Calculate and determine X_2-Y_2 curves or X_3-Y_3 curves for another set of lines, X_{13} = constant or X_{12} = constant, by the procedure explained above. Draw lines for the constant value of y_2 or y_3.

6. The constant y_1 lines first obtained, together with the constant y_2 or y_3 lines determined, define the whole vapor-liquid equilibria of the ternary system, as in Figure 5, for the system acetone-methanol-water.

The result calculated by these procedures is compared with the observed data of Othmer, Friedland, and Scheibel (*14*) in Figure 5 and shows fairly good agreement. The method was applied to other systems available, such as acetone–chloroform–methyl isobutyl ketone (*11*), methyl ethyl ketone heptane–toluene (*18*), ethyl acetate–ethanol–water (*7*), carbon tetrachloride–ethanol–benzene (*2*), ethanol-benzene-water (*31*), and isooctane-toluene-phenol (*5*). Comparisons between calculated and observed data show good agreement for the first three systems, but for the latter three systems, mainly owing to the incompleteness of boiling-point data, good agreements are local.

MATHEMATICAL PREDICTION OF VAPOR COMPOSITIONS

As indicated in steps 5 and 6, two sets of X-Y curves must be calculated to determine all the ternary equilibria by the method presented above. If, therefore, only X_1-Y_1 curves are determined, only y_1 and $y_2 + y_3$ have been found, y_2 and y_3 separately are not yet known. In such a case the following mathematical method may be used instead of calculating another set of X_2-Y_2 or X_3-Y_3, though it requires much more laborious calculations. This mathematical method is useful especially when boiling points are measured only along lines such as X_{23} = constant on a triangular diagram.

For ternary systems the fundamental thermodynamic equation may be expressed as follows (*15*), if x_1 is chosen as the independent variable:

$$\frac{x_1}{y_1}\frac{dy_1}{dx_1} + \frac{x_2}{y_2}\frac{dy_2}{dx_1} + \frac{x_3}{y_3}\frac{dy_3}{dx_1} = f(T) \quad (2)$$

For a constant value of X_{23} this relation becomes

$$\frac{d}{dx_1}\left(\ln y_2^{X_{23}+1} y_3\right) = (X_{23}+1)\left(\frac{f(T)}{1-x} - \frac{x_1}{1-x_1}\frac{d\ln y_1}{dx_1}\right) \quad (3)$$

Equation (3) is thermodynamically rigorous and represents the relation between vapor and liquid compositions for a constant value of

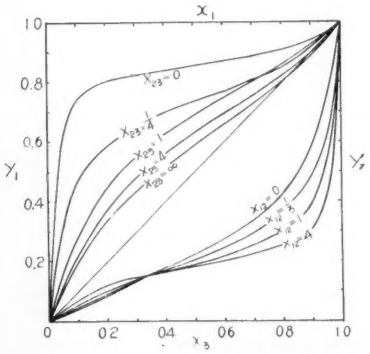

Fig. 4. Ternary x-y curves calculated for the system acetone (1)–methanol (2)–water (3).

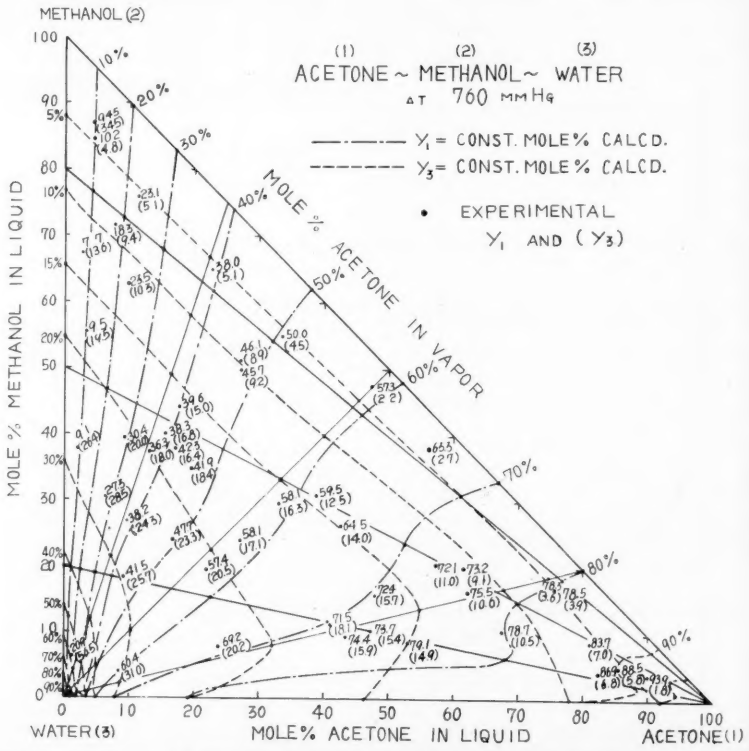

Fig. 5. Comparison between calculated and observed vapor-liquid-equilibrium data for the system acetone (1)–methanol (2)–water (3).

TABLE 1.—CALCULATIONS FOR THE SYSTEM ACETONE (1)—METHANOL (2)—WATER (3). ($X_{23} = 1/4$)

x_1	y_1	t,°C.	$y_2 X_{23} y_3$	y_2	y_3
0.05	0.286	74.0	0.266	0.38	0.334
.1	.412	69.8	.216	.30	.288
.2	.545	65.1	.170	.205	.250
.4	.667	61.1	.121	.13	.203
.6	.750	58.9	.077	.095	.155
.8	.857	57.2	.034	.06	.083

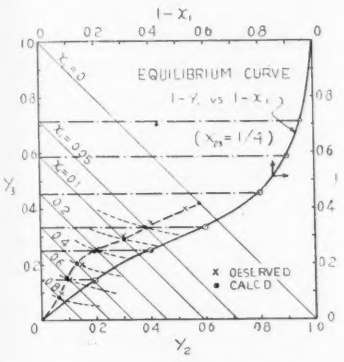

Fig. 6. Determination of ternary vapor compositions for the system acetone (1)–methanol (2)–water (3).

X_{23}. Integrating and rearranging result in the following relation:

$$\log y_0^{X_{23}} y_3 = \left(\log y_2^{X_{23}} y_3\right)_{x_1=0} + \frac{(X_{23}+1)}{2.303}(S_1 - S_2) \qquad (4)$$

where

$$S_1 = \int_0^{x_1} \frac{f(T)}{1-x_1}\,dx_1 \qquad (5)$$

and

$$S_2 = \int_0^{x_1} \frac{x_1}{1-x_1}\frac{d\ln y_1}{dx_1}\,dx_1 = \int_{y_0}^{y} \frac{x_1}{1-x_1}\frac{dy_1}{y_1} \qquad (6)$$

If Equation (1) is substituted in Equation (5), the integration may be simplified as follows:

$$S_1 = \text{approx.}\ \frac{\lambda_1}{RT_1}\int_{T_{23}}^{T} \frac{x_1}{1-x_1}\frac{dT}{T} - \frac{\lambda_{23}}{RT_{23}}\ln\frac{T}{T_{23}} \qquad (7)$$

By use of the aforementioned method of estimating the relation y_1 vs. x_1, the relation T vs. x_1 being known for a constant value of X_{23}, the integrations of S_1 and S_2 are carried out numerically and the term $y_2^{X_{23}} y_3$ may be determined as a function of x_1, say $F(x_1)$. This function, together with the equation $y_2 + y_3 = 1\text{-}y_1$, determines the vapor compositions y_2 and y_3 for the definite value of x_1. Therefore the intercepts of these lines determine y_2 and y_3 at the same time.

An illustrative example is given in Table 1 and Figure 6 for the system acetone (1) -methanol (2) -water (3). The agreement with the observed data(*14*) is fairly good.

CONCLUSION

The method of predicting vapor-liquid equilibrium relations from boiling-point data for binary systems can be used with slight modifications for ternary systems, for which it is particularly useful, as only the boiling-point–composition data are needed to determine the entire vapor-liquid equilibrium relation.

The method may be used also to check the available ternary equilibrium data.

ACKNOWLEDGMENT

The author wishes to acknowledge the kind encouragement of Shun-ichi Uchida and Shigefumi Fujita of Tokyo Institute of Technology and Donald F. Othmer of the Polytechnic Institute of Brooklyn.

NOTATION

$f(T)$ = function defined in Equations (1) and (2)
R = gas constant
T = absolute boiling point of ternary solution
T_1 = absolute boiling point of component 1
T_{23} = absolute boiling point of binary mixture of components 2 and 3, ratio of their compositions being X_{23}
x = mole fraction of component in liquid
x_i = mole fraction of component i in liquid
$X = x/(1-x)$
$X_i = x_i/(1-x_i)$
$X_{ij} = x_i/x_j$, ratio of compositions of components i and j
y = mole fraction of component in vapor
y_i = mole fraction of component i in vapor
$Y = y/(1-y)$
$Y_i = y_i/(1-y_i)$
λ_x = molal latent heat of vaporization of solution
λ_1 = molal latent heat of vaporization of component 1
λ_{23} = molal latent heat of vaporization of binary mixture of components 2 and 3, ratio of their composition being X_{23}

Subscripts 1, 2, and 3 refer to components 1, 2, and 3 respectively

LITERATURE CITED

1. Benedict, M., C. A. Johnson, E. Solomon, and L. C. Rubin, *Trans. Am. Inst. Chem. Engrs.*, **41**, 371 (1945).
2. Campbell, A. N., and W. J. Dulnage, *J. Am. Chem. Soc.*, **70**, 1723 (1948).
3. Carlson, H. C., and A. P. Colburn, *Ind. Eng. Chem.*, **34**, 581 (1942).
4. Colburn, A. P., and E. M. Schoenborn, *Trans. Am. Inst. Chem. Engrs.*, **41**, 421 (1945).
5. Drickamer, H. G., G. G. Brown, and R. R. White, *loc. cit.*, **41**, 555 (1945).
6. Edwards, B. S., F. Hashmall, R. Gilmont, and D. F. Othmer, *Ind. Eng. Chem.*, **46**, 194 (1954).
7. Griswold, J., P. L. Chu, and W. O. Winsauer, *loc. cit.*, **41**, 2352 (1949).
8. Hirata, M., *Chem. Eng. (Japan)*, **13**, 152 (1949); **14**, 65 (1950).
9. *Ibid.*, **15**, 72 (1951); **18**, 14 (1954).
10. ———, *Japan Sci. Rev.*, **2**, 265 (1952).
11. Karr, A. E., E. G. Scheibel, W. M. Bowes, and D. F. Othmer, *Ind. Eng. Chem.*, **43**, 961 (1951).
12. Nagasako, N., and M. Hirata, *Chem. Eng. (Japan)*, **16**, 83 (1952).
13. Norman, W. S., *Trans. Inst. Chem. Engrs. (London)*, **25**, 66 (1945).
14. Othmer, D. F., D. Friedland, and E. G. Scheibel, cited in Ju Chin Chu, "Distillation Equilibrium Data."
15. Othmer, D. F., L. G. Ricciardi, and H. S. Thaker, *Ind. Eng. Chem.*, **45**, 1815 (1953).
16. Redlich, O., and A. T. Kister, *loc. cit.* **40**, 341, 345 (1948).
17. Scheibel, E. G., and D. Friedland, *loc. cit.*, **39**, 1329 (1947).
18. Steinhauser, H. H., and R. R. White, *loc. cit.*, **41**, 2912 (1949).
19. Uchida, S., S. Ogawa, and M. Hirata, *Chem. Eng. (Japan)*, **17**, 193 (1953).
20. White, R. R., *Trans. Am. Inst. Chem. Engrs.*, **41**, 539 (1945).
21. Wohl, K., *loc. cit.*, **42**, 215 (1946).

Analysis of Gas-fluidized Solid Systems by X-ray Absorption

E. W. Grohse

General Electric Company, Schenectady, New York

X-ray absorption is presented as a unique tool for the study of the fundamentals of gas fluidization. For example, bed-density profiles, valuable indexes of the quality of fluidization, are readily determined by means of X-ray absorption. No internal probes, to interfere with the normal action within a fluidized bed, are involved.

As an initial application of X-ray absorption to fluidization, the results of a study of the effect of mode of distribution of gas to a fluidized bed are presented. The importance of this variable, only superficially discussed in previous literature, is clearly shown by these results. Application of X-ray absorption to other chemical engineering operations is readily conceivable.

Although a considerable number of experimental investigations of gas-fluidized solid systems have been reported during the past 5 years or so, with notable exceptions these have been confined to the study of gross phenomena of fluidization. For example, over-all bed expansions and over-all coefficients of heat transfer between fluidized beds and confining surfaces have been rather profusely reported. On the other hand, very little study of local phenomena within fluidized beds has been reported. Furthermore, very little disclosure has appeared in the literature of the important effects of certain variables, such as mode of gas distribution to a bed of solids, upon the quality of fluidization produced.

A major deterrent in the advancement of fundamental knowledge in fluidization is presented by the lack of a reliable, comprehensive index of the quality of fluidization occurring in a given apparatus. Several indexes of quality of fluidization have been proposed (*2, 8, 10*), but none of these appear adequate for general use. Of those already proposed, the index of Morse and Ballou (*8*) holds the most promise, as its calculation is based upon the measurement of local phenomena within a fluidized bed. The correlation of this index, or of the measurements involved, with simultaneous measurements of heat and/or mass transfer between the fluidized solids and the fluidizing gas would be expected to lead to a superior, more nearly complete, index of the quality of performance of a fluidized bed.

This paper represents the initial report of a continuing investigation, the main goals of which are (1) development of fundamental information on the operation of gas-fluidized beds of solids, (2) study of the effects upon fluidization of variables which heretofore have been inadequately investigated, or not at all, and (3) ultimate development of a reliable, comprehensive index of the quality of performance of gas-fluidized beds.

In this paper is presented the use of X-ray absorption as a quantitative tool for the study of local phenomena within fluidized as well as static beds. For example, local bed densities, as well as fluctuations thereof, at any level of a fluidized (or static) bed of solids are readily determined by means of X-ray absorption. As a specific illustration of the utility of this tool, the results of a study of the importance of the mode of distribution of gas to a fluidized bed are presented.

In the use of X-ray absorption there are no internal probes to interfere physically with the normal action within a fluidized bed, or to be affected by detrimental internal conditions such as high temperature and corrosion. Application of X-ray absorption is not restricted to materials of low electric conductivity, as, for example, in the case of the capacitometric technique of Morse and Ballou. By means of special features which were specifically designed into the X-ray equipment employed in the present study, semiquantitative interpretation of the data obtained can be made almost instantly (which is especially useful in exploratory experimentation), and thorough interpretation of data can be effected much more rapidly than would be otherwise possible.

The application of X (or gamma)-ray absorption to other chemical engineering studies, such as, studies of liquid holdup and flooding in packed and wetted-wall columns, entrainment studies, etc., is readily conceivable.

ELEMENTS OF X-RAY ABSORPTION*

X-ray absorption has been employed qualitatively and semiquantitatively for the X-ray examination of the human body, for the location of structural imperfections in equipment, etc., since shortly after the discovery of X-rays by Roentgen in 1895. The use of X rays for these purposes was greatly stimulated by the invention of the modern X-ray tube by Coolidge in 1913. Quantitative applications of X-ray absorption, however, became prevalent only about 10 years ago, when for the first time convenient, precise measurement of X-ray intensities was made possible by the development of the phosphor-activated multiplier phototube (*7* and *11*). The latter is the basis of the most sensitive device generally available today for the measurement of X rays and similar high-energy radiation, the scintillation counter.

Following the development of these convenient, precise instru-

*The principles discussed here also apply for the most part to the absorption of gamma rays.

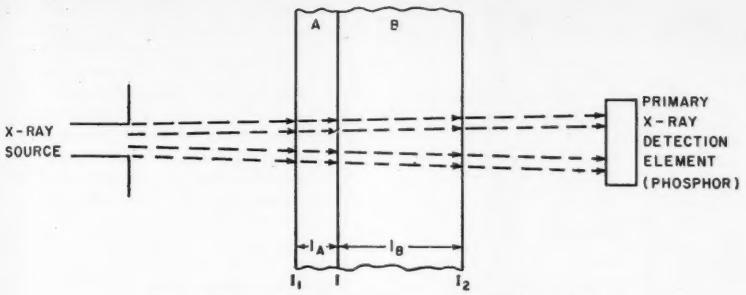

Fig. 1. Schematic diagram for *X*-ray absorption.

ments for the measurement of radiation, extensive applications of X-ray absorption for chemical analysis were made (*4, 5, 6, 9, 12, 17,* and *18*). Indeed, the techniques proposed here for the study of fluidization were developed from many preliminary experiments carried out with the X-ray photometer employed by Smith, Tanis, Liebhafsky, and Winslow in their pioneering quantitative absorption studies (*5* and *11*).

The outstanding characteristic of X rays, from which others derive, is their high energy, or short wave length. Because of this characteristic, the absorption of X rays usually involves only electrons near the atomic nucleus. (The absorption of ultraviolet, visible, or infrared radiation, on the other hand, affects the outer, or valence, electrons, which determine the chemical properties of the elements involved.) X-ray absorption, therefore, which is essentially a process for counting the number, and indicating the kind, of atoms by which the radiation is being absorbed, is virtually independent of the chemical or physical state of the atoms. An oxygen atom per se, for example, will show essentially the same absorption in oxygen gas and in ice, water, steam, and sand.

The absorption of essentially parallel, monochromatic X rays by a homogeneous material of density ρ and thickness l is described by Lambert's law:

$$I = I_o e^{-\mu_m \rho l} \qquad (1)$$

or

$$\ln (I/I_o) = \ln I - \ln I_o = -\mu_m \rho l \qquad (1a)$$

where I_o and I denote the intensities of the incident and transmitted radiation, respectively, and μ_m denotes the mass absorption coefficient of the absorbent. In the application of Equation (1) to a fluidized bed, l becomes the inside diameter of the column and ρ the bulk density of the bed, the variable under study.

The mass absorption coefficient, μ_m, for a given element is independent of the physical state and for chemical compounds is in the first approximation additive from the mass coefficients of the constituent elements. For elements, μ_m depends only upon the wave length of radiation involved; moreover, this dependency is much less complex than for the absorption of radiations of low energy. In the regions of continuous absorption (*1*) most commonly encountered in quantitative X-ray absorption studies, μ_m varies in accordance with the following approximate relationship (*11*a):

$$\mu_m = NCZ^4 \lambda^3/A \qquad (2)$$

where N is Avogadro's number, C is approximately constant in wavelength ranges between adjacent critical absorption wave lengths or "absorption edges," Z is the atomic number, A the atomic weight, and λ the wave length in Angstrom units.

In practice polychromatic X-ray beams are much more frequently employed than monochromatic beams, because they are easier to produce. Equation (1) applies rigorously only to individual monochromatic components of a polychromatic beam, and so for an entire polychromatic beam, use of an integral form of Equation (1) is theoretically required. Fortunately, however, for many practical cases in which polychromatic X radiation is employed, the direct application of Equation (1) serves adequately over the limited ranges of conditions usually encountered.

PRINCIPLES OF X-RAY ABSORPTION APPLIED TO A FLUIDIZED BED

A Pyrex-walled fluidization column was employed in the present study (Figure 3), a simplified representation of which is given in Figure 1. Zone *A* represents the walls of the column, and zone *B* the fluidized (or static) bed. Absorption of the primary radiation by air or by the fluidizing gas is negligible, and consideration of other constant absorbing mediums, such as the protective enclosure of the scintillation crystal, can be included with that of the column walls in zone *A*. For precise work the X-ray beam reaching the phosphor must not be too divergent; otherwise different portions of the beam will have penetrated different thicknesses of the material.* The area of the phosphor should be sufficient to intercept all direct unabsorbed primary radiation, but not so large as to intercept much scattered and background radiation.

Applying Equation (*1a*) to zones *A* and *B* results in

$$\ln I_1 - \ln I = \mu_m^A \rho_A l_A$$

$$\ln I - \ln I_2 = \mu_m \rho_B l_B$$

$$\ln I_1 - \ln I_2 = \mu_m^A \rho_A l_A + \mu_m^B \rho_B l_B$$

$$= \text{"cell constant"} + \mu_m^B \rho_B l_B \qquad (3)$$

If two different absorbers, *B* and *C* (e.g., a fluidized or static bed and a standard thickness of pure aluminum, respectively) produce identical attenuation of a given incident beam (i.e., I_2 as well as I_1 are the same for both cases), the densities and thicknesses of the two absorbers are related by means of Equation (3) as follows:

$$\mu_m^B \rho_B l_B = \mu_m^C \rho_C l_C \qquad (4)$$

$$\rho_B = \frac{\mu_m^C}{\mu_m^B} \frac{\rho_C}{l_B} l_C = K l_C \qquad (4a)$$

$$K = \frac{\mu_m^C}{\mu_m^B} \frac{\rho_C}{l_B} \qquad (4b)$$

$$K = \frac{\rho_B}{l_C} \qquad (4c)$$

*For purpose of simplification of the present discussion, it is assumed that on a time-average basis, the small localized volume of a fluidized bed (or static bed) under examination at a given time is effectively homogeneous: i.e., it is uniformly fluidized (or uniformly packed). This in no way precludes the possibility of gross instantaneous variations in bed densities within a column, as illustrated in later sections of this paper.

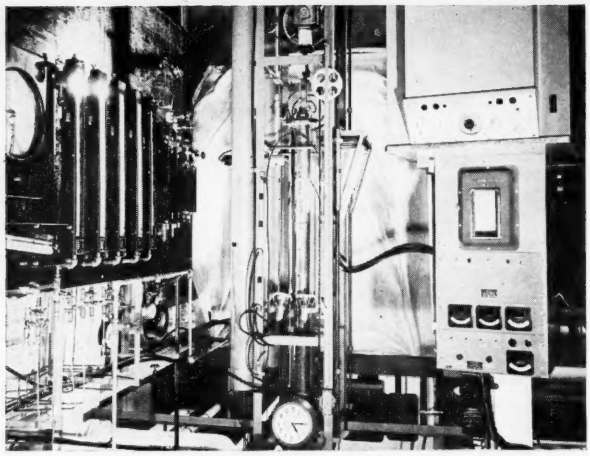

Fig. 2. Over-all view of fluidization apparatus including *X*-ray photometer.

Equation (4*a*) is the basic equation employed in this study for the determination of local bed densities. For this purpose, l_C becomes the thickness of calibration standard (aluminum) which will produce identical attenuation of the incident beam as produced by a localized volume of bed of bulk density, ρ_B. The quantity l_B becomes the inside diameter of the column.

When, as in the present study, polychromatic radiation is employed, and comparisons between the absorption of X rays by the "unknown" and standard materials, respectively, cannot be made under geometrically identical conditions, it is preferable to determine K empirically, by the use of Equation (4*c*), on standard densities of the actual materials contained in the actual vessel to be employed in the investigation proper (silicon in the Pyrex fluidization column in the present case). In this case standard densities must be known or measurable by means other than X-ray absorption. The application of Equation (4*a*), including the determination of K values, is discussed later.

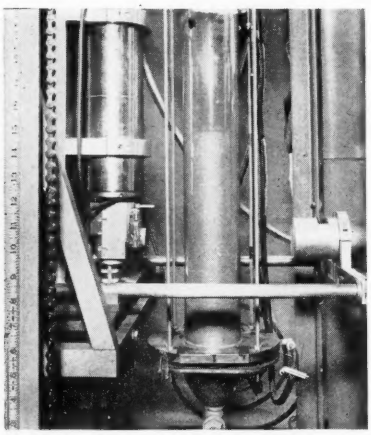

Fig. 3. Close-up of fluidization column showing *X*-ray source and detection probe.

When absorption comparisons can be made under geometrically identical conditions, it is frequently possible to avoid empirical calibrations through the use of published values of mass absorption coefficients of the elements involved (*1* and *16*).

APPARATUS

An over-all view of the experimental setup is given in Figure 2. The fluidization apparatus proper is relatively conventional, although designed for maximum versatility. The column proper is Pyrex glass, 3.33 in. I.D. This diameter was considered to be about the minimum required in order to avoid excessive "wall effects" and about the maximum with which precise density measurements could be made with relatively low-energy X rays. A bank of five Flowrators provides a 30,000-fold range of gas rates, which adequately covers the ranges of fluidized- as well as fixed-bed operation. Five Meriam well-type manometers measure various pressure differentials, including those produced by the gas distributor, the entire bed, 6-in. sections of the bed, and the cyclone-filter system employed for the collection of entrained fines. A multiple flange arrangement at the bottom of the column permits easy changeover of the gas distributor as well as of the charge of solids. With the flange and pressure-tap arrangement employed, the bottom ¼ in. of the bed is excluded in the measurement of bed pressure differentials and included in the measurement of distributor pressure differentials.

Carryover of solids into manometer lines is effectively prevented by the use of short lengths of ordinary pipe cleaners and/or glass wool inserted in the pressure taps. This proved much more satisfactory than the use of "blow-back" devices, which were initially tried.

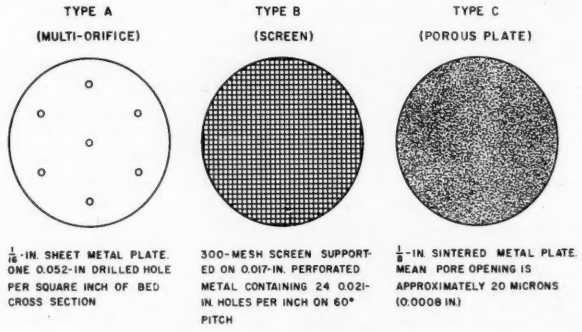
TYPE A
(MULTI-ORIFICE)
TYPE B
(SCREEN)
TYPE C
(POROUS PLATE)
1/16-IN. SHEET METAL PLATE. ONE 0.052-IN DRILLED HOLE PER SQUARE INCH OF BED CROSS SECTION
300-MESH SCREEN SUPPORTED ON 0.017-IN. PERFORATED METAL CONTAINING 24 0.021-IN. HOLES PER INCH ON 60° PITCH
1/8-IN. SINTERED METAL PLATE. MEAN PORE OPENING IS APPROXIMATELY 20 MICRONS (0.0008 IN.)

Fig. 4. Gas distributors.

The unique feature of the present study is the use of the X-ray absorption techniques already discussed. Although believed to be widely applicable to other problems, components of the X-ray photometer employed were specifically designed or selected for the study of fluidization. By means of this photometer, therefore, the action within a fluidized bed can be interpreted in a semiquantitative manner, at least, almost instantly. This is an important advantage in exploratory experimentation. Also, because of the special design features incorporated into the photometer, thorough interpretation of experimental data can be effected much more rapidly than would be otherwise possible.

The X-ray source consists of standard components of the General Electric XRD-3D X-ray diffraction unit with a Machlett AEG-50T tungsten target X-ray tube. The detection equipment consists of a modification of the rate meter in a standard General Electric SPG X-ray detector, fed by a General Electric scintillation probe. The rate-meter response is logarithmic over most of its range

of sensitivity; hence, in accordance with Equation (1*a*), the recorder reading varies approximately linearly with the local bed density being measured. For the purpose of determining instantaneous as well as time-averaged local bed densities, rate-meter time constants ranging from 0.01 to 30 sec. may be employed (*cf.* Figure 8). X-ray intensities are recorded on a General Electric fast-response photoelectric recorder. Details and further discussion of this equipment are given in the Appendix.*

The X-ray tube and radiation probe are mounted on a crank-operated, counterweighted carriage, which can be moved up and down the fluidization column. In this way vertical density traverses of the bed can be made very quickly. The X-ray tube and radiation probe can also be rotated about a vertical axis, by means of which horizontal traverses can be made. Figure 3 shows a close-up of the movable X-ray assembly.

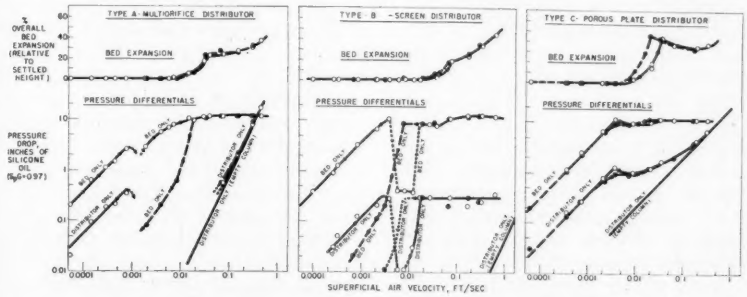
TYPE A - MULTIORIFICE DISTRIBUTOR
TYPE B - SCREEN DISTRIBUTOR
TYPE C - POROUS PLATE DISTRIBUTOR
% OVERALL BED EXPANSION (RELATIVE TO SETTLED HEIGHT)
BED EXPANSION
PRESSURE DIFFERENTIALS
PRESSURE DROP, INCHES OF SILICONE OIL (sp. gr. 0.97)
SUPERFICIAL AIR VELOCITY, FT/SEC

Fig. 5. Bed expansion and pressure differentials: ○, data obtained in order of increasing velocity; ● data obtained in order of decreasing velocity; 3.33 in. I.D. column, 4.0-lb. charge of silicon (all through 200 mesh).

Roller-particle-size Analysis

Micron range	% in range
0—10	2
10—20	8
20—40	34
40—57	50
57—74	4
74	2

BED-EXPANSION AND PRESSURE-DROP STUDIES

Preliminary to the X-ray studies of fluidization, conventional data on bed expansion and pressure drops were obtained in the following manner: 4.00 lb. of commercial silicon powder (all through 200 mesh; *see* Figure 5) was charged through the top flange of the column while a small flow of air was passed through the distributor in cases where the design of the distributor permitted powder to fall through it, i.e., types *A* and *B* of Figure 4. The vent of the column was temporarily closed and the column pressurized with air to about 20 in. of water while a check for gas tightness was made. The bed was expanded and vigorously fluidized for several minutes, then allowed to settle by gradual shutoff of the air flow over a period of at least several minutes. At this point a run was begun.

The lowest practical air velocity obtainable was then applied to the column and maintained for a 3-min. period, following which the total bed expansion and pressure differentials were measured. The flow rate was then increased to a new value and the foregoing procedure repeated. After reaching the maximum velocity for the given run, the entire sequence was repeated in order of decreasing velocity. Figure 5 summarizes the pertinent results for three distinctly different types of gas distributors described in Figure 4.

A of Figure 4 simulates the type of gas distributor frequently employed in commercial fluidization columns. It is designed to produce a reasonably high pressure drop, which ordinarily is required for stable operation of a fluidized column. *B* characterizes the type of distributor frequently employed in laboratory investigations of fluidization (e.g., reference *2*), which offers negligible resistance to gas flow, but tends to produce unstable fluidization. *C* combines the opportunity for uniform gas distribution inherent in the design of *B* with the high pressure drop for operational stability incorporated in the design of *A*.

The distinct superiority of the porous-plate distributor, at least for the single powder composition reported here, appears obvious from Figure 5. Superior bed expansion, for example, is obtained with the porous-plate distributor over the practical range of operating velocities, which is limited by entrainment considerations. Serious gas channeling, visibly obvious during operation with the multiorifice and screen distributors, is graphically indicated by the discontinuities in the pressure-drop curves for these distributors.

The foregoing differences in fluidized-bed performance are even more dramatically brought out by X-ray absorption measurements, as discussed in the following sections.

In Figure 5 pressure differentials across the distributors are shown to be considerably higher when the column is filled with powder than when it is empty, except at the higher gas velocities corresponding to vigorous or violent fluidization. These discrepancies are due partly to the inclusion of the bottom ¼ in. of the bed in the measurement of distributor pressure differentials under filled column conditions (*cf.* p360). From experiments with coarser powders, however, these discrepancies are indicated to be due mainly to obstructions within the gas passages in a distributor caused by the finer particles present in a charge of powder. At sufficiently high velocities these obstructions become largely dispersed.

X-RAY ABSORPTION STUDIES

Preliminary Calibrations

Local bed densities were determined by application of Equation (4*a*) in the following manner:

1. With an incident X-ray beam of the quality* and intensity* employed in the fluidization experiments, the empty column is "calibrated" against a range of standard thicknesses of pure aluminum,† which produces the same range of transmitted intensities as produced by silicon beds in the fluidized as well as unfluidized states. Figure 6 shows a plot of typical results so obtained. Over the thickness range of major interest the plot is essentially a straight line, in accordance with Equation (1*a*). Slight curvatures in Figure 6 are due to (*a*) the use of polychromatic instead of monochromatic X rays, (*b*) deviations from logarithmic amplification at counting rates below around 50 counts/sec. (*cf.* Figure 7), and (*c*) appreciable coincidence counting errors at counting rates exceeding about 1,000 counts/sec. (*E.g.*, at a rate of 2,400 counts/sec. intercepted by the phosphor, the estimated coincidence counting error is approximately 10%.)

2. Detector readings obtained during density-profile determinations were translated into local bed densities by means of Equation (4*a*) as follows: When Equation (4*a*) is ap-

*Copies of the Appendix will be gladly supplied by the author upon request.

*Functions only of the target voltage and emission current for a given X-ray tube.

†Aluminum is particularly suitable as a calibration standard in the present study, since aluminum and silicon differ by only one in atomic number and hence have closely similar X-ray-absorption characteristics.

plied, l_B becomes the inside diameter of the fluidization column and l_C the thickness of calibration standard which will produce identical attenuation of the X-ray beam as produced by a volume of solids of bulk density, ρ_B. The ratio of the mass absorption coefficients $\mu_m{}^C/\mu_m{}^B$ can be expected to be approximately constant over the range of wave lengths involved, since aluminum and silicon are adjacent in atomic number, and the critical absorption wave lengths for these elements are sufficiently removed from the range of "effective wave lengths" of the polychromatic X-ray beams employed (*1* and *5*). Hence it is to be expected that variations of K under the conditions of the present study would be small, and the local bed densities, therefore, would be approximately proportional to the equivalent thickness of aluminum, l_C.

Values of K as a function of ρ_B were determined in the identical column employed in the fluidization investigation. The column, equipped with the porous-plate distributor, was charged with 4.00 lb. of silicon powder. (*See* Figure 5 for particle-size analysis.) After a brief initial period of fluidization to homogenize the bed, the gas velocity was reduced to produce bed conditions at which total bed heights could be accurately measured and, hence, average bed densities accurately calculated. Average bed densities were so determined from the charge weight, column cross-sectional area, and total bed height for bed conditions ranging from those for a densely packed bed, through increasing states of expansion, to conditions approximating those for incipient fluidization, (*2* and *14*). As noted in Figure 5, when the porous-plate distributor is employed bed expansion under conditions of incipient fluidization is actually greater than for conditions for active fluidization, within the range of practical air velocities. Hence this technique permitted the determination of K values corresponding to actual densities which may be encountered in a fluidized bed, ranging from the densities of static or stagnant zones to the densities of vigorously fluidized zones.

At each condition of bed expansion transmitted X-ray intensities were measured over the entire bed height. The value of l_C employed in Equation (4*c*) was selected to correspond to the average recorder reading, obtained by integration of a plot of the recorder readings as a function of the bed level. Since over the range of conditions involved, bed density

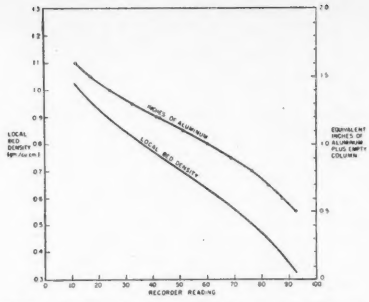

Fig. 6. Typical calibration of X-ray photometer: target voltage, 27,000; emission current, 3 ma.; phototube voltage, 850.

varies essentially linearly with recorder reading, this procedure permitted rigorous evaluation of K values. The eight K values so determined (0.622 to 0.635) varied over a range of only 2%. It is of interest to observe this almost exact agreement with the range of K values (0.620 to 0.635) calculated from literature values of the mass absorption coefficients for pure aluminum and silicon for the energy range of 10 to 30 kv. (*16*). However, this remarkable agreement must be considered at best a coincidence, since significant differences would be expected owing to the small concentrations of elements of higher atomic number present in commercial silicon, such as iron, which have much higher mass absorption coefficients than pure silicon. [*Cf.* Equation (2).]

The density curve in Figure 6 follows directly from Equation (4*a*) upon substitution of the experimentally determined K values.

Probable Error of Density Measurement

In the determination of average local bed densities (Figures 10 and 11) recorder readings taken with a rate-meter time constant of 10 sec. (*cf.* Appendix and Figure 8) and a chart speed of 36 in./hr. were averaged over a period of 1 or 2 min. Maximum and minimum instantaneous local bed densities (Figure 11) were determined by averaging the minimum and maximum recorder readings, respectively, over a period of 5 sec., corresponding on the average to about 25 to 30 cycles of fluctuation of the recorder readings. (*cf.* Figure 8.) For these measurements a time constant of 0.01 sec. and a chart speed of 36 in./min. were employed.

Sample chart records, obtained under typical conditions of vigorous fluidization, are shown in Figure 8 for the entire range of time constants incorporated into the design of the rate meter (*Cf.* Appendix.) The "fast" and "slow" chart speeds correspond, respectively, to 36 in./min. and 36 in./hr.

In X- or gamma-ray absorption some fluctuations in the measurement of transmitted intensities—and hence apparent fluctuations in bed densities—are inherent, even in the measurement of static systems, owing to the random nature of X or gamma radiation.* These random fluctuations, which must be taken into account in the rigorous analysis of radiation measurements made under conditions of fluidization, in order to distinguish between actual and apparent density fluctuations, depend upon the total number of photons, or "counts," recorded by the detector. This number is equal to the product of three factors: transmitted intensity, duration of the intensity measurement, and detection efficiency. In the present study the transmitted intensity is determined by the incident intensity and energy level and the bed density being measured. Duration of intensity measurement is determined by the rate-meter time constant. The detection efficiency is essentially 100%. By proper combination of these factors, random

*Under the conditions employed in this study the random nature of X rays arises chiefly from the randomness of the electron emission from the X-ray tube filament as well as from the random nature of the atomic excitation process which results in the emission of the X rays.

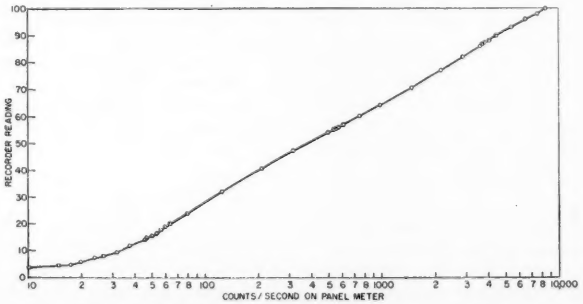

Fig. 7. Relationship between recorder reading and counting rate.

fluctuations in transmitted intensities—and, hence, in bed densities—can be made negligible.

For the X-ray conditions generally employed in this study, random fluctuations in bed density, as a function of actual bed density being measured and rate-meter time constant, are given in Figure 9 by the vertical distances between pairs of curves labeled with the same time constant. For example, if at a given moment the true density of a zone of the bed were 0.75 g./cc., the probable instantaneous density measurement, employing a time constant of 0.01 sec., would range from approximately 0.72 g./cc. minimum to 0.79 g./cc. maximum. Figure 9 was constructed from X-ray measurements taken with various time constants on thicknesses of aluminum equivalent to the bed densities given by the data points. The ranges of fluctuation given in Figure 9 were obtained by averaging the maximum and minimum recorder readings over a suitable time interval (e.g., 1 or 2 min. for the 10-sec. time constant and about 5 sec. for the 0.01-sec. time constant).

Under conditions of the present study random fluctuations in the measurement of average local bed densities, determined with the 10-sec. time constant, were negligible. On the other hand, instantaneous local bed densities, which were determined with the 0.01-sec. time constant, were subject to the following probable errors of measurement due to random fluctuations (approximated from Figure 9):

True instantaneous bed density, g./cc.	Approximate probable Error of measurement, % Positive	Negative
0.70	3	3
0.75*	5	4
0.8	8	6
0.9†	20	7
1.0	30	10

*Approximate density corresponding to "incipient fluidization."

†Approximate settled bed density with porous-plate distributor.

Under most conditions of active fluidization encountered in this study, therefore, the probable errors of measurement of instantaneous bed densities were not excessive.

Increased precision of measurement of higher bed densities for a given time constant is readily attained by the use of an increased target voltage, hence, an increased transmitted intensity.

Bed-Density Profiles

In Figure 10 profiles of time-averaged local bed densities, as functions of gas velocity, are given for the three gas distributors previously discussed. All the results apply to the single powder composition given in Figure 5. The corresponding instantaneous bed density profiles, along with the time-averaged density profiles for comparison, are given in Figure 11.

As a check of the reliability of the time-averaged density profiles, these were integrated over the entire bed height in order to obtain length-average bed densities which could be compared with the corresponding values calculated from the weight of powder charged and the total bed height. Under settled bed conditions and at an air velocity of 0.05 ft./sec., corresponding values of length-average bed density agreed within 3% or better. At velocities of 0.15 and 0.25 ft./sec. it was difficult to measure total bed heights accurately, because of excessive turbulence of the menisci, and discrepancies as great as 9% (and in one case 15% with the multiorifice distributor at 0.25 ft./sec.) were noted.

Before any further discussion of Figures 10 and 11, it is of interest to report the results of an auxiliary series of experiments. In this

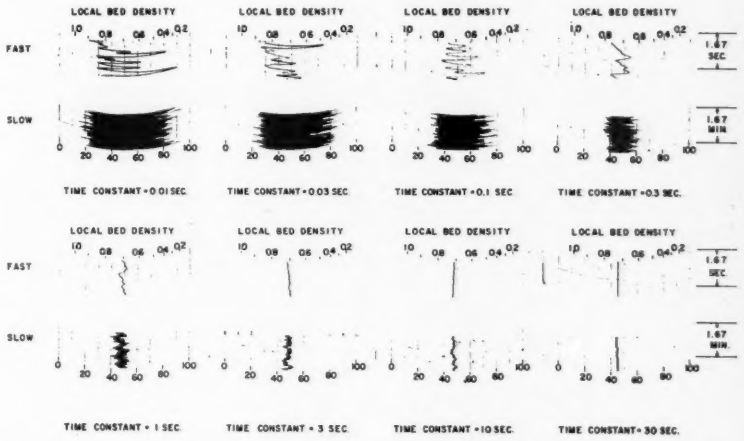

Fig. 8. Sample of *X*-ray absorption measurements of fluid-bed performance.

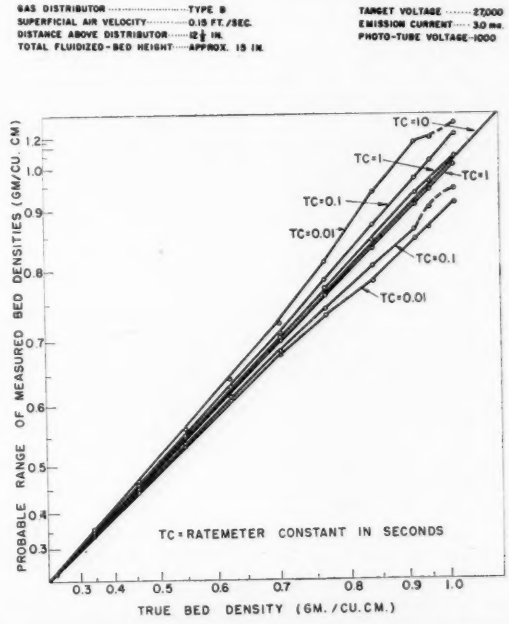

Fig. 9. Apparent fluctuations in bed density due to random fluctuations in the measurement of transmitted radiation intensities.

series the air flow (0.15 ft./sec.) to a vigorously fluidized bed,* employing the porous-plate distributor, was abruptly terminated, and the resulting settling of the bed, with corresponding increased bed densities, was followed by X-ray absorption. A time constant of 0.01 sec. and chart speed of 36 in./min. were employed. The procedure was repeated at various levels of the bed up to the 12-in. level. After an initial rapid increase in bed density immediately following gas shutoff, a distinct leveling off, or "plateau," in the density-time curve was observed, before final settling of the bed began. The duration of these plateaus, ranging from 1 to 15 sec., varied roughly linearly with bed level. The "plateau bed densities" so obtained were essentially constant at 0.74 ± 0.01 g./cc.

The foregoing results follow logically from the fact that upon termination of gas flow to a fluidized bed, collapse or settling of the bed obviously must progress upward from the distributor, and partial expansion of the upper zones of the bed is therefore maintained by the gas liberated from the lower zones of the bed for periods of time roughly proportional to the bed level under consideration.

As postulated by a number of investigators, the general gas-fluidized system includes two "phases": a continuous phase, consisting of uniformly distributed particles in a supporting gas stream, and a discontinuous phase, consisting of essentially solids-free gas, which may pass through the bed in the form of bubbles, channels, or slugs. This is "two-phase" or "aggregative" fluidization. A bed of solids fluidizes when the superficial gas velocity is sufficient to support the particles; this is the point of "incipient" fluidization. At appreciably higher gas velocities, a discontinuous phase appears and imparts convective motion to the continuous phase to produce "aggregative" fluidization. For certain gas-solid systems it may be possible for "single-phase" or "particulate" fluidization to exist over a short range of velocities exceeding that required for incipient fluidization, without the appearance of a second, discontinuous phase. Toomey and Johnstone (*13*) postulate that the appearance of the discontinuous phase imposes no significant changes upon the physical character of the continuous phase; e.g., the voidage or density of the continuous phase and the interstitial velocity remain essentially constant, independent of increasing superficial velocities. The latter is doubtless an oversimplified concept, although very useful for promoting clearer understanding of the mechanism of gas fluidization.

The essentially constant plateau bed density reported above is believed to correspond closely to the condition of incipient fluidization.

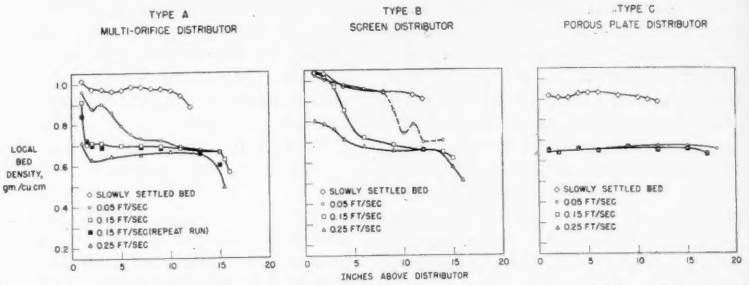

Fig. 10. Average bed-density profiles. 3.33 in. I.D. column; 4.0-lb. charge of silicon (see Figure 5 for particle-size analysis); target voltage: settled-bed data, 31,000, all other data, 27,000; emission current, 3.0 ma.; phototube voltage, 850; time constant, 10 sec.

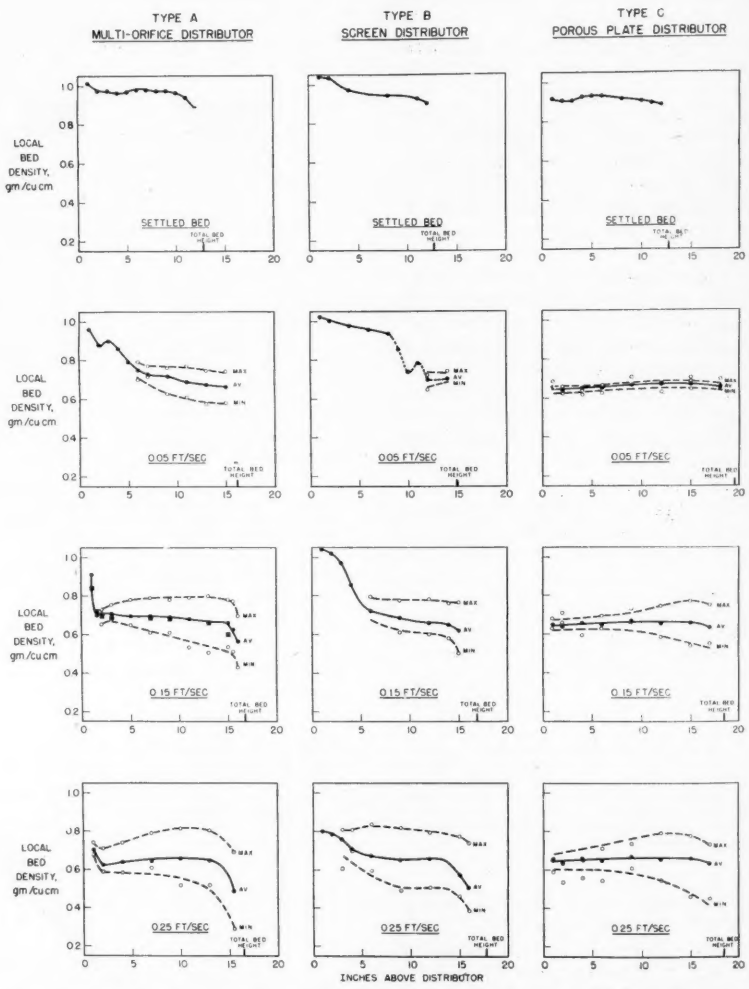

Fig. 11. Instantaneous bed-density profiles (same data as in Figure 10 except for time constant, which is 0.01 sec. for instantaneous densities and 10 sec. for average densities).

Applying the value 0.74 g./cc. for the incipient fluidization density to the total bed-expansion data given for the porous-plate distributor in Figure 5 enables the incipient fluidization air velocity to be estimated at approximately 0.030 ft./sec. if arrived at from a lower velocity and 0.017 ft./sec. if arrived at from a higher velocity. Also, from the porous-plate-bed-expansion data, along with visual observations, the transition between particulate and aggregative fluidization (i.e., the condition of maximum bed expansion without more than intermittent appearance of appreciable gas bubbling) was estimated to occur at a length-average bed density of 0.64 g./cc. and a superficial air velocity of 0.035 ft./sec. if arrived at from a lower velocity and 0.020 ft./sec. if arrived at from a higher velocity. Hence 0.030 to 0.035 ft./sec. and 0.017 to 0.020 ft./sec., arrived at from a lower and higher velocity, respectively, represent the approximate velocity ranges at which particulate fluidization occurs for the given combination of powder and gas properties, column design, and gas distributor design. There was no evidence that particulate fluidization could even be approximated with either the multiorifice or screen distributors.

Local bed densities (Figures 10 and 11) greater than 0.74 g./cc. (i.e., greater than the incipient fluidization density) are indicative of completely or periodically stagnant zones within the bed. In a fluidized reactor stagnant bed conditions would give opportunity for hot spots, tar formation, deactivation of catalyst, powder caking and gas channeling to occur. On the other hand, densities appreciably less than 0.64 g./cc. indicate zones in which an appreciable, and frequently a major, proportion of the incoming gas flow is short-circuiting the bed. Actually it is possible for short-circuiting of the gas flow to occur within zones of the bed possessing densities exceeding 0.64 g./cc., or even within stagnant beds, when gas channeling or intermittent compression of the continuous phase takes place.

The distinct superiority and inferiority, respectively, of the porous-plate and screen* distributors, previously indicated by the bed-expansion and pressure-drop experiments, are emphasized by the X-ray absorption studies. Over the entire range of bed levels possible to probe accurately with the X-ray photometer (to within about an inch from the bottom or from the top of the bed), extremely uniform average bed-density profiles are shown for the porous-plate distributor, even at the lowest gas velocity reported (0.05 ft./sec.). On the other hand, results for the screen distributor exhibit appreciable nonuniformities of the bed at the highest velocity reported (above which entrainment losses become objectionably high) and extremely nonuniform, incomplete, and erratic fluidization at the lower velocities. Performance data for the multiorifice distributor again fall intermediate in quality, compared with those for the porous-plate and screen distributors.

It is of interest to note that the screen distributor employed in the present study, described in Figure 4, is essentially identical in design to that employed by Lewis, Gilliland, and Bauer for the fluidization of Scotchlite glass beads (*3*). Whereas particularly poor performance was obtained with the screen distributor in the present study of the fluidization of silicon, no mention of similar performance deficiencies was made by Lewis et al. The apparent differences in performance are believed likely attributable to inherently different fluidizing characteristics of Scotchlite beads, which are quite round and smooth, and silicon powders, which are of a sharp, gritty nature. It is planned to investigate this apparent anomaly by fluidization of Scotchlite beads in the present apparatus.

Stagnant zones of powder were clearly visible in the operations with the screen and multiorifice distributors. Even with the porous-plate distributor, a small amount of powder inactivity could be observed immediately adjacent to the distributor. In the latter case, however, this is believed likely to have been simply a small "wall" or "corner" effect, extending for only a very short distance above the distributor.

Powder-packing tendencies, which give rise to stagnant zones in fluidized beds, are further indicated by the settled bed-density profiles for the screen and multiorifice distributors. They are less uniform and include appreciably higher densities than in the case of the porous-plate distributor.

Operation of the porous-plate distributor at 0.05 ft./sec. is shown in Figure 11 to be the only case in which the instantaneous bed densities all fell closely within the range corresponding to particulate fluidization, 0.64 to 0.74 g./cc., and, indeed, from visual observations fluidization appeared most uniform under these conditions.

*Same charge and particle-size analysis as employed in the density-profile determinations.

CONCLUSION

Reported above is a preliminary interpretation of the results of the X-ray absorption studies of fluidization. More thorough analysis of such results can be shown to lead to an improved understanding of the mechanism of gas fluidization. Such an analysis, based upon additional experimentation, including the use of high-speed movies, is currently in progress.

LITERATURE CITED

1. Compton, A. H., and S. K. Allison, "X-Rays in Theory and Experiment," 2 ed., D. Van Nostrand Co., Inc., New York (1935).
2. Leva, M. et al., *U.S. Bur. Mines, Bull.* 504 (1951).
3. Lewis, W. K., E. R. Gilliland, and W. C. Bauer, *Ind. Eng. Chem.*, 41, 1104 (1949).
4. Liebhafsky, H. A., and E. H. Winslow, *Gen. Elec. Rev.*, 48, 36 (April, 1945).
5. Liebhafsky, H. A., H. M. Smith, H. E. Tanis, and E. H. Winslow, *Anal. Chem.*, 19, 861 (1947).
6. Liebhafsky, H. A., Ann. N. Y. Acad. Sci., 53, 997 (1951).
7. Morgan, R. H., *Am. J. Roentgenol. Radium Therapy, Nuclear Med.*, 48, 88 (1942).
8. Morse, R. D., and C. O. Ballou, *Chem. Eng. Progr.*, 47, 199 (1951).
9. Rich, T. A., and P. C. Michel, *Gen. Elec. Rev.*, 50, 45 (February, 1947).
10. Shuster, W. W., and P. Kisliak, *Chem. Eng. Progr.*, 48, 455 (1952).
11. Smith, H. M., *Gen. Elec. Rev.*, 48, 13 (March, 1945).

11a. Sproull, W. T., "X-Rays in Practice," McGraw-Hill Book Company, Inc., New York (1946).

12. Titus, A. C., paper presented at A.I.E.E. meeting (1954).
13. Toomey, R. D., and H. F. Johnstone, *Chem. Eng. Progr.*, 48, 220 (1952).
14. ——— *Chem. Eng. Progr. Symposium Series* No. 5, 51, (1953).
15. Weltmann, R. N., and P. W. Kuhns, *Natl. Advisory Comm. Aeronaut. Tech. Note* 2580 (1951).
16. White, G. R., *Natl. Bur. Standards Rept.* 1003 (1952).
17. Winslow, E. H., H. M. Smith, H. E. Tanis, and H. A. Liebhafsky, *Anal. Chem.*, 19, 866 (1947).
18. Zemany, P. D., E. H. Winslow, G. S. Poellmitz, and H. A. Liebhafsky, *loc. cit.*, 21, 493 (1949).

Rate of Fall of Single Liquid Droplets

William Licht and G. S. R. Narasimhamurty, University of Cincinnati, Cincinnati, Ohio

A study was made of the terminal velocities of fall of liquid droplets in another phase liquid under stationary conditions. The studies include dimensional analysis, experimental work for collection of fall-velocity data, and photographic studies of the drop behavior. Six systems were studied for organic liquids insoluble in and heavier than water. The experimental conditions and procedure have been standardized.

For any given system, as the drop size was increased the fall velocities of the droplets increased gradually, reached a maximum, and then fell off asymptotically. Two mechanisms have been postulated, (1) for the range where the fall velocities increased with an increase of drop size and (2) for the range where the fall velocities decreased with an increase of drop size, with the maximum velocity region corresponding to the transition from region 1 and 2.

Although there is considerable information available on the fall velocities of rigid spheres in fluids, information on the motion of liquid droplets in liquids is limited, despite the fact that it is an integral part of liquid-liquid extractions in spray towers. The present problem, which has been simplified so as to lead to a basic knowledge of the hydrodynamics of liquid droplets in liquids, is specifically, terminal velocities of fall of single liquid droplets inside a stationary and infinite medium of another liquid without mass transfer between the phases.

Ailor(*1*), Conway(*3*), Farmer (*4*), Katz(*9*), and Smirnov and Ruban(*13*), observed the fall velocities of liquid droplets in liquids. Ailor used a 1-in.-diam. glass column, and Katz used 2- and 3-in. diam. glass columns and reported wall effect in the 2-in. glass column. The data of Conway and Farmer on fall velocities are more qualitative than quantitative and are also complicated by the presence of mass transfer. It was found in the course of the present work that Tygon tubing, which Katz used for connecting the burrette to the drop-forming tip, lowered the interfacial tension value of the liquids. It will later be shown that a lower interfacial tension lowers the fall velocity of the drop. Only a part of Smirnov and Ruban's work is strictly applicable to the present problem, as for most runs they used a continuous medium in motion. Also an observation of apparatus figures of all the aforementioned workers shows that they used some connecting tubes to join the glass tubes, though they did not clearly state of what materials those tubes were composed. In any case none of them reported any special precautions to prevent the lowering of the interfacial tension values due to contamination with foreign materials.

Spilhaus(*14*) proposed certain general correlations which took into account the air-liquid interfacial tension for the case of rain drops and tested his correlations against the data of Laws(*10*). Hughes and Gilliland(*7*) using a quasithermodynamic approach for drops falling in a gas arrived at results similar to those of Spilhaus (*14*) and tested their correlations against the data of Laws and Watson(*15*) for liquid drops in air. They presented their correlations in the form of a terminal velocity group Tv vs. a gravity group Wt with a surface-tension-size group Sd as parameter, where

$$Tv = V\left[\frac{3\ \rho_o^{\,2}}{4\ g\ \mu_o\ (\rho_i-\rho_o)}\right]^{\frac{1}{3}} \quad (1)$$

$$Wt = D\left[\frac{4\ g\ \rho_o\ (\rho_i-\rho_o)}{3\ \mu_o^{\,2}}\right]^{\frac{1}{3}} \quad (2)$$

$$Sd = \frac{g_c\sigma}{\mu_o}\left[\frac{3\ \rho_o^{\,2}}{4\ g\ \mu_o\ (\rho_i-\rho_o)}\right]^{\frac{1}{3}} \quad (3)$$

The present results were checked against the correlations of Hughes and Gilliland to indicate the difference in behavior between gas-liquid and liquid-liquid systems. Tentative correlations for liquid-liquid systems were developed by the authors.

DIMENSIONAL ANALYSIS

The drag coefficient of a drop is assumed to depend upon

$$C_D = \varphi\ (\sigma, g, D, \rho_i, \rho_o, \mu_i, \mu_o) \quad (4)$$

where the drag coefficient for steady state motion is

$$C_D = \frac{4\ g\ (\rho_i-\rho_o)\ D}{3\ \rho_o\ v^2} \quad (5)$$

By means of dimensional analysis a variety of possible dimen-

G. S. R. Narasimhamurty is at Andhra University, Waltair, India.

TABLE 1.—PROPERTIES OF LIQUIDS USED

		Carbon tetra chloride	Tetra chloro ethane	*O*-Nitro toluene	Tetra bromo ethane	Ethyl chloro acetate	Chloro benzene
Density, g/ml.	(Exper.)	$1.5842^{25\cdot0}$	$1.5813^{25\cdot0}$	$1.1578^{25\cdot0}$	$2.9539^{25\cdot0}$	$1.1451^{25\cdot0}$	$1.1008^{25\cdot0}$
	(Lit.)	$1.5843^{25\cdot0}$	1.5869^{25}	1.1626^{20}	2.9529^{25}	1.159	1.10085^{25}
Viscosity, centipoises	(Exper.)	$0.9296^{25\cdot0}$	$1.502^{25\cdot0}$	$2.093^{25\cdot0}$	$9.464^{25\cdot0}$	$1.101^{25\cdot0}$	$0.7625^{25\cdot0}$
	(Lit.)	$0.912^{24\cdot6}$	1.456^{20}	2.37^{20}	.....	.....	0.7585^{25}
Surface tension, dynes/cm.	(Exper.)	$26.9^{24\cdot4}$	$35.0^{24\cdot4}$	$40.8^{25\cdot0}$	$49.6^{25\cdot2}$	$31.1^{27\cdot9}$	$32.5^{25\cdot6}$
	(Lit.)	26.76^{20}	36.04^{20}	41.67^{20}	49.67^{20}	.....	33.19^{20}
Interfacial tension, dynes/cm.	(Exper.)	$41.6^{24.0}$	$31.3^{24\cdot9}$	$26.6^{24\cdot2}$	$36.2^{23\cdot2}$	$14.6^{25\cdot0}$	$35.4^{25\cdot4}$
	(Lit.)	45.0 ± 1.0^{20}	.....	27.19^{20}	38.82^{20}	$15.8^{25\cdot0}$	37.41^{20}
Solubility, % W/W (lit.)	(Liq. in water)	0.077^{25}	0.288^{25}	0.0652	0.0651^{30}	Insoluble	$0.0488^{\cdot0}$
	(Water in liquid)	0.010^{24}	.....	.....	.....	.....	4.4
μ_i/μ_o		1.040	1.681	2.342	10.59	1.232	0.8533
Sd		2,445	1,843	2,408	1,424	1.359	3,710

sionless correlations may be obtained among these variables. Two which were tested in this work are

$$We = f_1(Re, \mu_r) \tag{6}$$

and

$$\frac{c_D}{c_D^s} = f_2(\beta, Re, \mu_r) \tag{7}$$

Here We represents the Weber number, Re the Reynolds number, and c_D^s the drag coefficient of a rigid sphere of equivalent volume. The two other dimensionless groups used are defined as

$$\beta = \frac{g D^2 (\rho_i - \rho_o)}{4\sigma} \tag{8}$$

and

$$\mu_r = \frac{\mu_i}{\mu_o} \tag{9}$$

SHAPE OF THE DROP

Much interest has been evinced in the shape of the drop in motion by Hughes and Gilliland(*7*), Imai (*8*), McDonald(*11*), Saito(*12*), and Spilhaus(*14*). For drops and bubbles one can write

$$\frac{1}{R_1} + \frac{1}{R_2} = \frac{P_i - P_o}{\sigma} \tag{10}$$

This leads to the fundamental differential equation which, when solved and the boundary conditions substituted, should be expected to give the equation for the shape of the drop.

In order to get a reasonable solution of the foregoing equation, the following simplifying assumptions have been made: The drop (1) can attain an equilibrium shape; (2) has no oscillations or rotations; (3) falls vertically in a straight line; and (4) has axial symmetry about the vertical axis. Photographs taken during the present work indicate the extent to which these assumptions were met. In some instances they are reasonably valid, but there are outstanding exceptions which would seem to defy mathematical treatment of this question.

EXPERIMENTAL WORK

The experimental work consisted of (*a*) the preliminary work done to standardize the experimental conditions with a view to getting reproducible and reliable data as well as ascertaining the accuracy of the results obtained, and (*b*) the main experimental work done to collect data on the terminal velocities of fall of liquid droplets as well as photographic studies of the drop behavior.

Preliminary Work The preliminary work comprised the following:

1. Choice of systems.
2. Determination of the physical properties of the liquids.
3. Production of drops of constant volume.
4. Determination of the initial height of fall of drops required to attain terminal velocities.
5. Elimination of wall effect and end effects.
6. Temperature control.

1. Six organic liquids insoluble in and heavier than water were chosen for the discontinuous phase; whereas laboratory-distilled water was selected for the continuous phase. Only

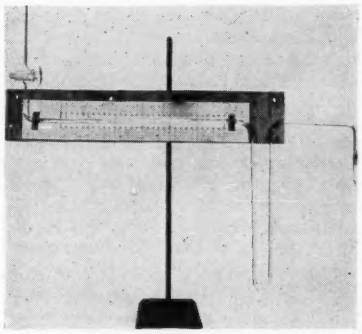

Fig. 1. Capillary *U*-tube microburette.

research-grade organic liquids were used. The physical properties of the six organic liquids chosen are given in Table 1. The properties of distilled water were taken from literature and used as $\rho = 0.99707$ g./ml. at 25.0°C. and $\mu = 0.8937$ centipoise at 25.0°C. The properties of the organic liquids were determined experimentally, distilled water being used as a reference liquid. The solubility data were taken from literature.

Carbon tetrachloride was selected first in order that comparisons might be made with previous work on this material. It has a viscosity near that of water. Tetrachloroethane was selected as its density is very near that of carbon tetrachloride, but its interfacial tension with water is different. *O*-Nitrotoluene was selected as it has almost the same *Sd* value as carbon tetrachloride. This was done in order to facilitate comparison with the correlations of Hughes and Gilliland. *S*-Tetrabromoethane was selected because it has a high viscosity and high density, ethyl chloroacetate because it has a very low interfacial tension with water, and chlorobenzene because it has a low viscosity and density.

2. The densities of the organic liquids were determined with a pycnometer at 25.0° ± 0.1°C., with distilled water as a reference liquid. Viscosities were measured at 25.0° ± 0.1°C., with an Ostwald viscometer, distilled water being used as a reference liquid. A Du Noüy tensiometer, by means of the ring method, was used for the measurement of surface tension of the liquids in air and the interfacial tension of the liquids to water. The surface and interfacial tension values read with the instrument were corrected with a factor obtained from the graph of Zuidema and Waters(*16*), and the corrected values were taken as true values.

3. The production of drops of constant volume consisted of developing (*a*) nozzles and (*b*) burettes which would obviate the necessity of using any materials that may dissolve in and change the properties of the organic liquids used.

Nozzles were used to form the liquid droplets at their tips. To start with, hypodermic needles were used. The oblique cut on the end of the needle was removed and the tip rounded off with a file to give a sharp-edged circular tip. Later the range of drop sizes was extended to smaller values by joining glass tips to the metal bases of hypodermic needles with Corroseal solder. By this procedure all the nozzles produced had the same standard Luer grinding of the hypodermic needles.

Burettes were used for measuring the volume of the droplets. Apart from the question of accuracy of measurement, the other important considerations were (*a*) to avoid any lubricants coming in contact with the organic solvents at any time, (*b*) to regulate the rate of flow of liquids to extremely small flow rates, maintaining, if possible, a steady flow rate for any particular setting, and (*c*) to have a tip to which the nozzles could be attached directly without any other connecting tubes. The following two burettes were developed for the purpose.

One burette was a 5- by 1/100-ml. microburette. It was provided with an adjustable-flow stopcock, precision ground so that it might be worked without grease. A standard Luer grinding was provided at the tip of the burette to take the nozzles at the bottom. In order to minimize the effect of liquid-level variation on the drop formation time, experiments were run with the burette filled to zero mark before each run.

The second burette consisted of a 4-ft. Pyrex-glass capillary tube bent to the shape shown in Figure 1. At the upper end of the tube was fused an adjustable-flow stopcock and at the lower end a 1-cc. tuberculin syringe. The stopcock was open to the air, and hence a small amount of grease might be used, thus obviating precision grinding. The horizontal length of the capillary was 40cm., giving 30 cm. for the graduated section. In this burette the 1-mm. length of the capillary tube corresponded to an average volume of 7.23×10^{-4} ml. Because of the horizontal portion of the capillary, this burette gave more uniform drop-formation times than the previous one.

4. Preliminary work showed that drops attained terminal velocities of

fall after an initial height of fall of 30 cm. in water. However, some data were collected on drops after they fell initially through a height of 60 cm., to serve as check points.

5. Data were collected on carbon tetrachloride drops in water in a 3-in.-diam. glass column up to $D = 0.448$ cm. and compared with the data on the same system in a 6-in.-diam. Lucite column, as shown in Figure 3. It can be seen that there is no noticeable difference in the fall-velocity data in the 3- and 6-in.-diam. columns. However for additional confidence and convenience, the 6-in.-diam. column was used for later work.

To avoid end effects, the lowest mark on the column for collecting the fall-velocity data was kept higher than 15 cm. from the bottom of the column.

6. In the early stages of the work the temperatures in the column were maintained at 25.0° ± 0.5°C., but they were later maintained at 25.0° ± 0.1°C. by a thermostatic water jacket in order to give added confidence to the results obtained.

Main Experimental Work

Apparatus. An oblique view of the apparatus is shown in Figure 2. It consisted of a 6-in.-diam. by 6-ft.-long Lucite column with the top end open and the bottom closed with ½-in.-thick Lucite sheet. One end of a ¼-in. brass pipe was screwed into the Lucite sheet and the other end connected to a petcock to serve as a drain.

One mark was placed on the column 3 cm. from the top, which corresponded to the position of the drop-forming tip. Three more marks were placed on the column at 30, 60, and 160 cm. below the drop-formation point. The last mark was 19.9 cm., from the base of the column. In the photograph these marks are indicated by the upper edge of the white bands around the outside.

Mirrors were placed at the 160-cm. mark so that it might be viewed at the 30-cm. level. This not only served as a convenience but also helped in avoiding any vibrations in the column arising from the operator's moving his position to take the readings. The 160-cm. mark at the bottom was generally illuminated by an electric light placed about 1 meter away.

As Lucite was affected by the organic solvents used in the present work, an 800-ml. beaker of glass was placed at the bottom of the column to collect the organic liquid droplets as they fell. At the end of the day's work the beaker could be removed with the help of copper wires tied to it. The fall-velocity data were checked with and without the beaker and the copper wires, but no difference could be found.

The column proper was surrounded by a square jacket (made of sheets of Lucite) in which water circulated for temperature control. The rest of the apparatus consisted of standard equipment for this control by which the temperature could be maintained at 25.0° ± 0.1°C.

Procedure. The following procedure was adopted as the one giving the most consistent and reliable results.

As will become evident in a later part of the present work, interfacial tension is a very important factor controlling the rate of fall of liquid droplets. Hence absolute cleanliness is of great importance in the work.

After all the apparatus had been cleaned, an 800-ml. beaker was lowered into the 6-in.-diam. Lucite column with the help of copper wires tied to it. The drain cock at the bottom of the column was closed and the column was then filled with distilled water of temperature 25.0° ± 0.1°C. The thermoregulator was turned on and the temperature of water circulating in the jacket outside the 6-in. column was adjusted to 25.0° ± 0.1°C.

The cleaned hypodermic or glass nozzles were attached to tips of the burettes provided with the standard Luer grinding. The capillary U-tube burette was used invariably for the small-sized drops, and the 5 × 1/100 ml. burette was used for the larger sized drops. As a check a certain number of medium-sized drops were obtained with both the burettes. The appropriate burette, filled with the organic liquid, was mounted on top of the column with the tip of the nozzle submerged in water at the 3-cm. mark. Care was taken to center the tip in the column. Also, the column was maintained in the vertical position by being checked occasionally with a plumb bob and the necessary adjustments made.

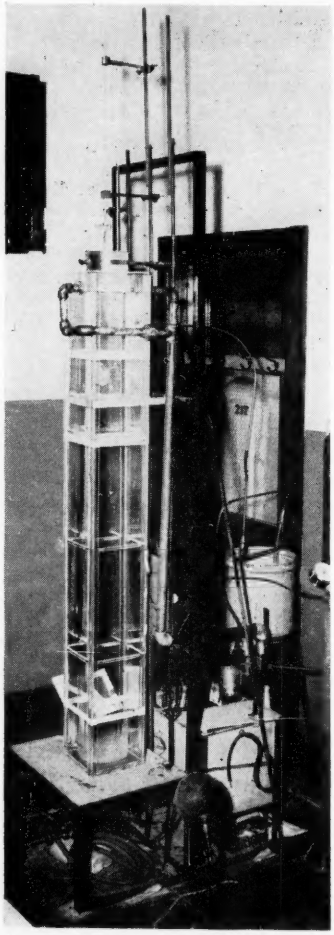

Fig. 2. Apparatus for study of fall of liquid droplets.

The top and bottom temperatures of the water in the column were taken. Generally about 1 hr. after the column was first filled with water, or ½ hr. after the column reached the equilibrium temperature of 25.0° ± 0.1°C., the data were collected.

The burette stopcock was opened slightly and the rate of flow of the liquid adjusted to give approximately the desired drop-formation time. Drop-formation times were chosen to be greater than 30 sec. with greater times for the larger sized drops. The frequency of the drops used in the present work was such that enough time was given for the turbulence in the wake of the previous drop to die down before the next drop fell, so that distortion of the motion of the next drop was avoided. Also, the rate of flow from the burette should be slow enough so that the readings of the liquid levels in the burette might be taken with negligible error. After the rate of flow was adjusted, the volume of liquid run down for a known number of drops was noted. Simultaneously the times of fall of as many drops as possible from 30- to 160-cm. marks were noted. From these values the average drop volume and the average time of fall of the drops were obtained and the fall velocity calculated. During each run the time of formation of every fifth drop was generally noted. In the tables of data* only the lowest and highest drop-formation times were noted. For each run the initial and final temperatures of water at top of the column were recorded.

All timing was done with stop watches manually operated and calibrated against standard time signals to an agreement within less than 1/10 sec. in 10 min. The error in timing would at most amount to ± 1/10 sec. in 5. sec., but in most runs was much less.

The two phases used were not saturated with one another before the runs. As the mutual solubilities were in all cases very low and as no difference in results were noted either with variation in drop-formation time or with the use of the same body of water for an entire day it was assumed that no appreciable error was introduced.

*For tables of complete velocity vs. diameter data order document 4655 from the Photo duplication Service, American Documentation Institute, Library of Congress, Washington 25, D.C., remitting $1.75 for microfilm or $2.50 for photoprints.

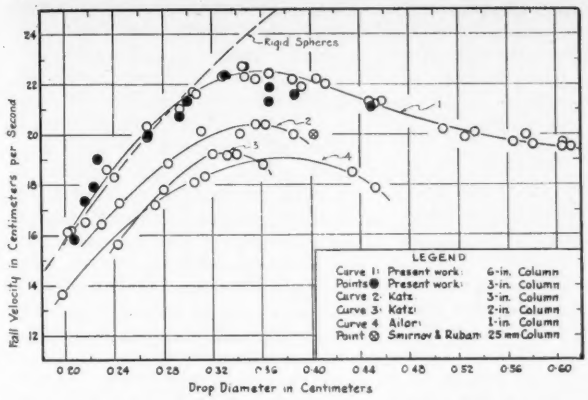
Rigid Spheres
Fall Velocity in Centimeters per Second
Drop Diameter in Centimeters
LEGEND
Curve 1: Present work: 6-in. Column
Points ● Present work: 3-in. Column
Curve 2: Katz 3-in. Column
Curve 3: Katz 2-in. Column
Curve 4 Ailor 1-in. Column
Point ⊗ Smirnov & Ruban 25 mm Column

Fig. 3 Fall velocities of carbon tetrachloride drops in water.

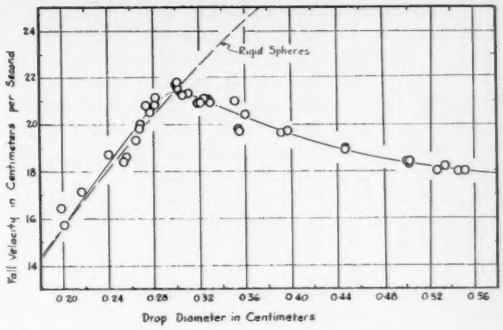

Fig. 4. Fall velocities of tetrachloroethane drops in water.

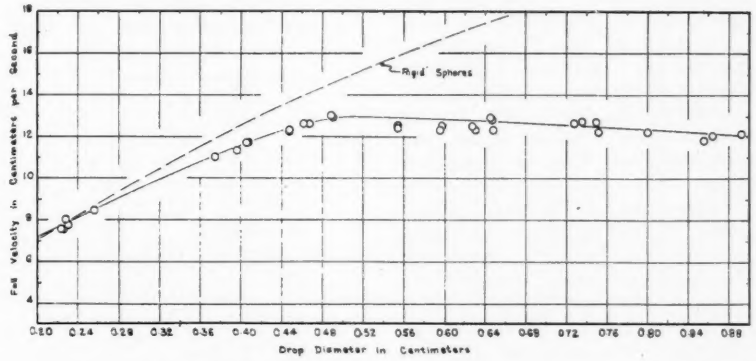

Fig. 5. Fall velocities of *O*-nitrotoluene drops in water.

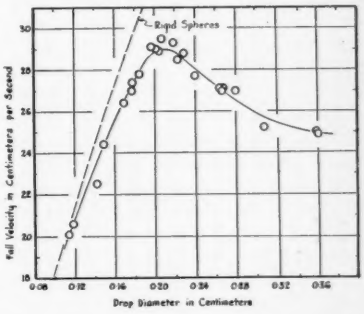

Fig. 6. Fall velocities of *s*-tetrabromoethane drops in water.

RESULTS

The data obtained on the terminal velocities of fall of the different liquid droplets in water are shown on Figures 3 to 8 as experimental points with solid smoothed curves drawn through them. In addition calculated fall-velocity curves for rigid spheres of the same density and volume are shown as dashed lines. Figures 3, for carbon tetrachloride, shows data obtained in both the 3- and 6-in. columns, the smooth curve being only for the 6-in. column. The data of Ailor(*1*), Katz(*9*), and Smirnov and Ruban(*13*) for carbon tetrachloride are also shown for comparison.

The range of drop sizes used for the different liquids was limited by the following considerations. (1) The nozzles used for producing very small drops were very fragile. Therefore the lower limit of drop sizes was fixed when the drops fell with almost the same velocity as rigid spheres. In the case of chlorobenzene drops, data could not be collected on the smaller size drops produced, as they drifted greatly and bumped as many as three to

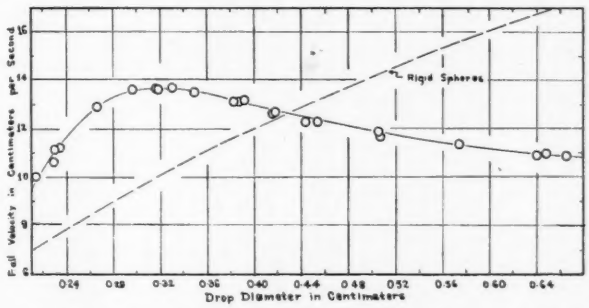

Fig. 7. Fall velocities of ethyl chloroacetate drops in water.

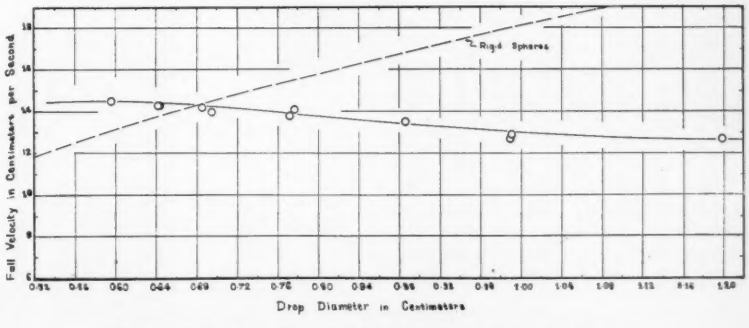

Fig. 8. Fall velocities of chlorobenzene drops in water.

four times on the walls of the 6-in. column in a travel of about 1 meter.* (2) There is a maximum limit to the size of a stable drop. Whether that upper limit was reached in the present work may be questioned, but the maximum drop sizes obtained in the present work can be claimed to be near the upper size limits for stable drops.

The range of variables studied in this work are

$(\rho_i - \rho_o) = 0.1037$ to 1.9568 g./ml.
$D = 0.114$ to 1.119 cm.
$\mu_i/\mu_o = 0.8533$ to 10.59
$\sigma = 14.6$ to 41.6 dynes/cm.

PHOTOGRAPHIC STUDIES

During the course of the work it was felt advisable to record photographically certain observations made visually with a view to explaining the nature of the fall-velocity curves.

Since the drop had to be photographed in motion, a very short exposure time was necessary. As there was also the question of drop vibrations, it was felt that multiple images of the same drop should be taken at small intervals of time. A Strobolux working in conjunction with a Strobotac, producing high-intensity flashes of a duration of 15 to 50 μsec. at frequencies adjustable from 1 to 6,000/min. was used for the work. A 4- by 5-in. Crown graphic camera with a 135-mm. lens was used for taking the picture. A suitable emulsion was found to be Eastman Kodak Super XX.

In order to take the pictures of drops, the same procedure as for the determination of fall velocities was followed, and the drops falling in the center of the column were photographed. A Strobolux frequency of 10 flashes/sec. was found to give satisfactory results with a camera lens opening of $f/11$. A ½-sec. exposure resulting in four or five images of the same drop on the plate was usually found to give good results. Dichlorofluorescein was added to some of the liquids used for producing the drops in order to increase the reflectivity of the drops. Since this addition changes the properties of the drop, the photographic data should be considered as qualitative rather than quantitative. Drop sizes and velocities were generally noted for each of the drops photographed. Finally the pictures of the drops thus obtained were enlarged and are shown in Figures 9 through 13.

*This may have been due to the effect of convection currents, as the density difference $(\rho_i - \rho_o)$—is very small for this system.

The poor contrast in some of these photographs makes it difficult to see the drop behavior. Accordingly tracings were made from the prints of Figures 9, 11, and 12 and are reproduced here.

DISCUSSION OF RESULTS

Figure 3 shows that the fall-velocity data obtained in the present work on carbon tetrachloride drops in water are definitely higher than those reported by the previous workers. This is no doubt due partially to wall effects present in the data obtained with 1- and 2-in. columns. But the lower values reported by Katz(*9*) for a 3-in. column cannot be so explained as the technique was generally the same as in the present work. The disagreement is attributed to contamination of the carbon tetrachloride by stopcock lubricants which lowered the interfacial tension in Katz's experiment. In the authors' work special care was taken to avoid this, as explained above.

Comparison of Figures 3 and 4 shows the fall velocities of tetrachloroethane drops to be lower than those of carbon tetrachloride drops, especially in the larger drop sizes, though their densities are very nearly the same, being 1.5813 and 1.5842 g./ml., respectively, at 25.0°C. The difference in $(\rho_i - \rho_o)$ is only 0.5% and rigid-sphere fall-velocity curves are virtually the same in both figures, and so the difference in fall-velocity curves cannot be thereby explained. The viscosity ratio $(\mu_i/\mu_o) = 1.681$ for tetrachloroethane and 1.040 for carbon tetrachloride. The influence of viscosity, if any, should be to make the drop behave more like a rigid sphere with an increase of viscosity of the drop. Hence the viscosity increase cannot explain the lowering of the fall velocities of tetrachcloroethane drops. The interfacial tension of tetrachloroethane is only 31.3 dynes/cm., compared with 41.6 dynes/cm. for carbon tetrachloride drops. It seems appropriate to assign the responsibility for the lower fall velocities on the lower interfacial tension. It is also consistent, since the rigid spheres with infinite interfacial tension fall faster than the drops in the same region.

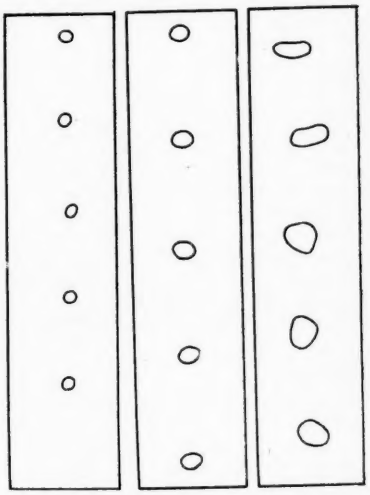

0.241 cm
18.9 cm/sec

0.384 cm
20.9 cm/sec

0.563 cm
18.6 cm/sec

Fig. 9. Carbon tetrachloride and dichlorofluorescein drops in water.

Fig. 10. *O*-Nitrotoluene drops in water.

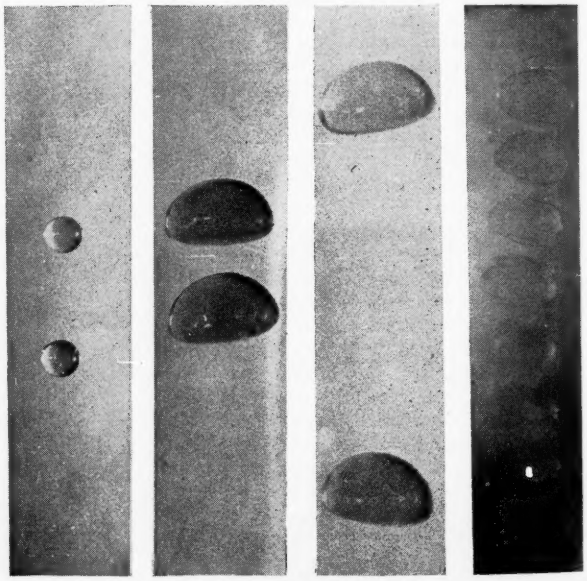

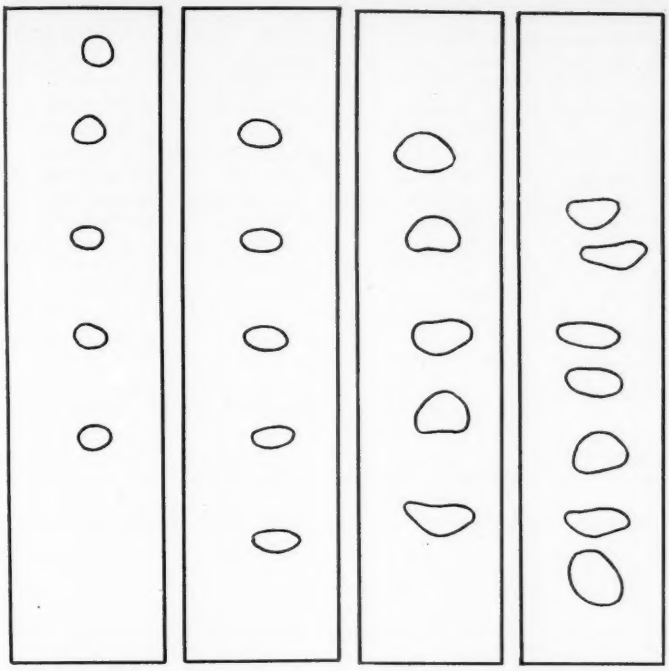

Fig. 11. Ethyl chloroacetate drops in water.

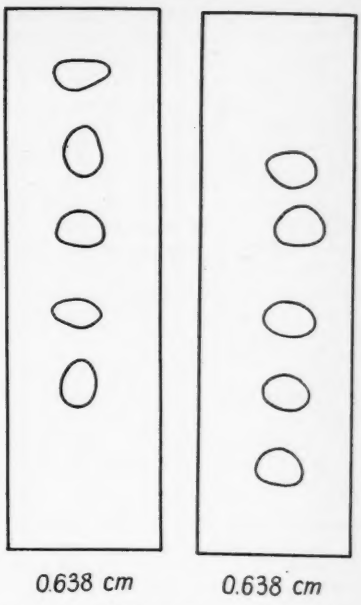

Fig. 12. Ethyl chloroacetate and dichlorofluorescein drops in water.

Figures 3 to 8 show that the fall velocities of liquid drops increase first, reach a maximum, and then fall off asymptotically as the drop size is continuously increased. This behavior of liquid drops contradicts that of rigid spheres. Hence it will be discussed in detail in the light of both the experimental and photographic results.

In the smaller range of drop sizes, the fall velocities of some liquid droplets are greater than those of rigid spheres over a certain range of drop sizes. This criss crossing of the fall-velocity curves of drops and rigid spheres is significant in the case of ethyl chloroacetate and chlorobenzene, which are both characterized by a combination of low values for $(\rho_i - \rho_o)$ and (μ_i/μ_o), but not in the case of the other systems. It has been proposed by various workers that internal circulation with the drop will cause the fall velocity to become greater than for rigid spheres.

In the larger sizes all drops fell with velocities lower than those of rigid spheres. Since drops are deformable, they deviate from the shape of a rigid sphere, and the total surface area of the drop increases and naturally gives rise to a higher drag coefficient. The different shapes of drops given in Figures 9 to 13 will bring out this point clearly.

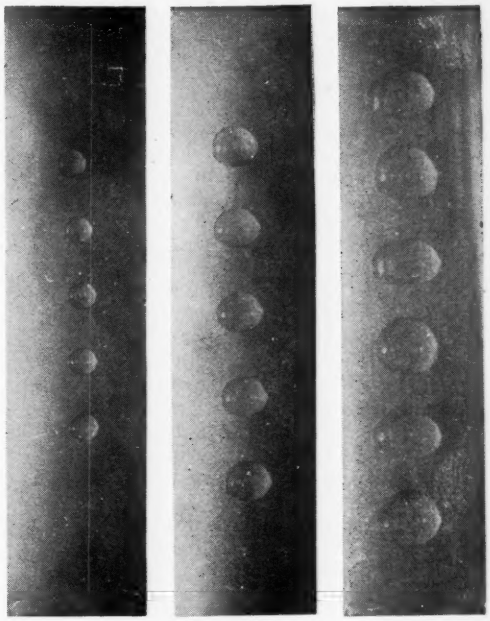

Fig. 13. Chlorobenzene and dichlorofluorescein drops in water.

From a study of the photographs the following observations can be made:

1. The smaller size drops are less deformed than the larger ones and are more nearly spherical.

2. Some of the deformed drops in the larger sizes show vibrations in shape, which were also observed by Blanchard(2) in the case of water drops in air.

3. The drops with an equilibrium shape fall with a uniform velocity even when the time intervals taken for the determination of the fall velocity are small.

4. The drops with vibrations show unequal velocities of fall when the time intervals are reduced, as in the

present work, to say 1/10 sec. This can clearly be seen from the unequal distances between consecutive images in the photographs where the drops showed vibrations in shape.

5. Several drops fall in a path which is neither strictly vertical nor even a straight line. In fact, visual observation shows them to fall in a zig-zag path. It was visually observed that as the drop sizes were gradually increased the smallest drops fell nearly vertically, and for the larger sizes the deviation from the vertical path increased to a maximum (when it was even impossible to collect data as the drops fell on the walls of the container), and then the deviation decreased with further increase of drop sizes, though the deviation did not die down completely. The maximum drifting of the drops as noted above may correspond to the case where the natural frequency of the drop coincides with the frequency of the eddies formed in the wake, as referred to by Gunn(*6*) in the case of water drops in air.

6. In the case of several drops there is no axial symmetry in the shape of the drop.

With the experimental and photographic results combined, the fall-velocity curve for each of the systems studied can be divided into two regions: (*a*) for drop sizes smaller than those corresponding to the maximum fall-velocity and (*b*) for the larger drop sizes. Region (*a*) is characterized by (1) an increase of fall velocity with an increase of drop size and (2) the existence of an equilibrium shape of the drop, though the drop may be vibrating as a whole. Region (*b*) is characterized by (1) a decrease of fall velocity with an increase of drop size and (2) the nonexistence of an equilibrium shape. The range of maximum fall velocities seems to correspond to the transition from region (*a*) to (*b*).

The fall velocity values taken from the smooth curves for drops in Figures 3 to 8, and the experimentally determined properties of liquids as given in Table 1, are used for further calculations.

In Figure 14 the drag coefficients of liquid drops were plotted against Reynolds number. For purposes of comparison, the drag coefficients of rigid spheres were shown in the figure with a broken line. It can be seen that the drag coefficients of liquid drops reach a minimum and then climb up steeply with increasing Reynolds number. An attempt was made to see whether the C_D vs. R_e plot could not be redrawn with Weber number as parameter, but it did not prove to be successful.

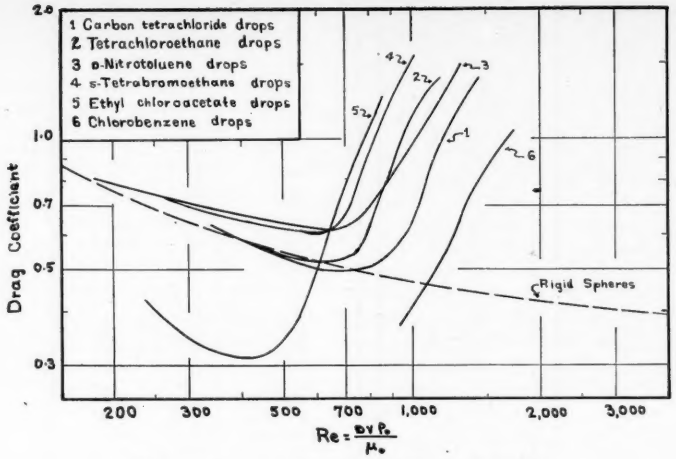

Fig. 14. Drag coefficients of liquid droplets.

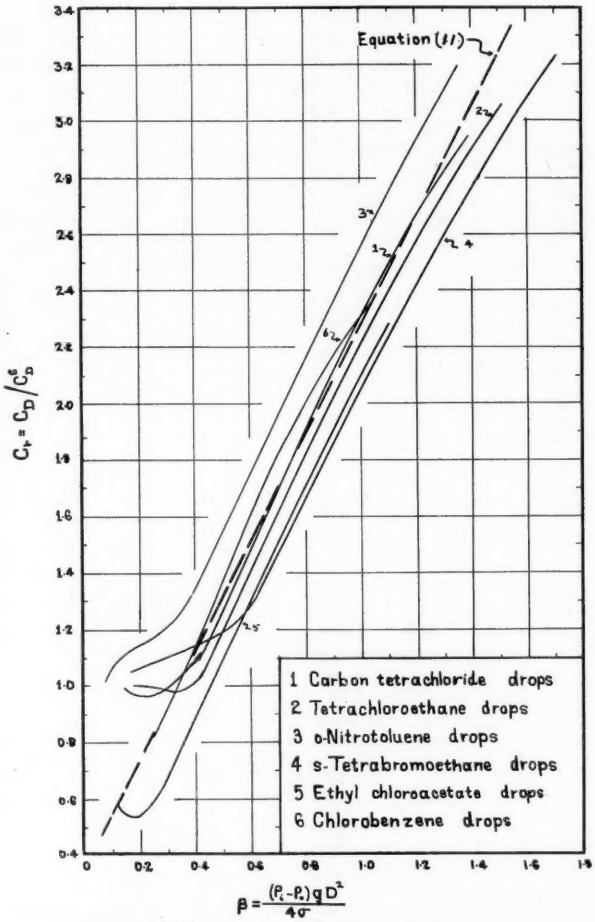

Fig. 15. Correlation of C_r with β group.

The data were also checked against the correlations of Hughes and Gilliland(*7*) in terms of the groups *Tv*, *Wt*, and *Sd* as given by Equations (1), (2), and (3). Poor agreement was obtained, which ought not to have been unexpected. In developing their correlations Hughes and Gilliland had to assume that the density ratio and viscosity ratio were unimportant. This is reasonably true for liquid drops falling through gases but not through liquids.

The Weber numbers of falling drops were plotted against Reyn-

olds number on logarithmic coordinates in an effort to check the correlation suggested by Equation (6). A family of parallel straight lines was obtained below Reynolds number of 700, but they did not correlate with the viscosity ratio. This type of plot is unreliable in any case because both the major variables, diameter and velocity, appear in both groups.

In Figure 15 the ratio of the drag coefficient of a liquid drop to that of a rigid sphere of the same volume and density properties and the same fall velocity as the droplet is plotted vs. the dimensionless group β. In the larger drop sizes, as represented by higher values of β, the curves are nearly linear on a rectangular coordinate plot. The dotted line represents the mean of all the six curves, thus giving a relationship of

$$C_r = \left(\frac{C_D}{C_D^s}\right)_{Re} = 1.87\,\beta + 0.425 \quad (11)$$

Equation (11) may be used with reasonable confidence for the case of liquid drops in water for the range of $\beta \geqq 0.4$.

In this correlation the influence of μ_r seems to be negligible. It may need further refinement and accuracy as well as a more extensive range of experimental conditions to determine exactly the role played by the viscosity of the discontinuous phase.

CONCLUSIONS

1. In addition to the four properties of diameter and density of the discontinuous phase as well as the density and viscosity of the continuous medium, which are important in the case of motion of rigid spheres in fluids, the liquid drops falling in liquids are also influenced by the interfacial tension property. A lower interfacial tension lowers the fall velocities of the drops.

2. For any given system the liquid drops falling in another liquid are nearly spherical in smaller sizes, and their deformation increases with an increase of drop size.

3. Large-sized drops show vibrations in their shape and do not have any equilibrium shape.

4. Drops showing an equilibrium shape fall with a uniform velocity irrespective of the time interval chosen for the measurement of terminal velocity. Drops exhibiting vibrations in their shape do not fall with a uniform velocity if the time interval chosen for the measurement of velocity is small, but they fall with a uniform average terminal velocity if the time interval chosen is large enough.

5. For any given system as the drop size is increased the fall velocity of the drop first increases to a maximum and then falls off asymptotically.

6. The foregoing behavior of drops has been divided into two regions, (*a*) for drop sizes smaller than those corresponding to the maximum fall velocity and (*b*) for drop sizes larger than those corresponding to the maximum fall velocity, with the maximum-fall-velocity region corresponding to the transition from region (*a*) to (*b*).

In region (*b*), above $\beta = 0.4$ the behavior of all liquid droplets insoluble in and falling through water can be represented by $(C_D/C_D^s)_{Re} = 1.87\,\beta + 0.425$.

OTHER WORK

As this manuscript was being prepared, a similar piece of work by Hu and Kintner was reported (*17*). Four of the liquids used were the same in both studies: carbon tetrachloride. *O*-nitrotoluene, tetrabromoethane, and chlorobenzene. A comparison of data indicates that in the present work higher fall velocities were found in each of these four cases. The difference amounts to roughly 10% and may be due to a difference either in the methods of timing employed or in properties of the materials used.

ACKNOWLEDGMENT

The authors wish to acknowledge the help given by William P. Koster in the photographic work.

This is an abstract of the dissertation submitted by G. S. R. Narasimhamurty to the Graduate School of Arts and Sciences of the University of Cincinnati in partial fulfilment of the requirements for the degree of Ph.D (June, 1954).

NOTATION

C_D = drag coefficient, Equation (5), dimensionless
C_D^s = drag coefficient of a rigid sphere, dimensionless
C_r = (C_D/C_D^s), dimensionless
D = equivalent spherical diameter = $(6v/\pi)^{\frac{1}{3}}$, cm.
g = acceleration due to gravity, cm./(sec.)^2
g_c = conversion factor, —980 dynes/g.
P = pressure, force/area, dyne/cm.^{2}
R_1, R_2 = principal radii, length units cm.
Re = Reynolds number, dimensionless
Sd = surface-tension size group, Equation (3), dimensionless
Tv = terminal-velocity group, Equation (1), dimensionless
v = volume cc.
V = velocity, cm./sec.
We = Weber number, dimensionless
Wt = gravity group, Equation (2), dimensionless
β = drop property group, Equation (8), dimensionless
μ = viscosity, poises
$\mu_r = \mu_i/\mu_o$, dimensionless
ρ = density, g./cc.
σ = interfacial tension, dynes/cm.
ϕ = function of

Subscripts

i = discontinuous-phase property
o = continuous-phase property

LITERATURE CITED

1. Ailor, R. M., B. S. thesis, Univ. Tennessee (1950).
2. Blanchard, D. C., *Trans. Amer. Geophys. Union*, **31**, 836 (1950).
3. Conway, J. B., Ph.D thesis, Univ. Cincinnati (1949).
4. Farmer, W. S., M. S. thesis, Univ. Tennessee (1949).
5. Goldstein, S., "Modern Developments in Fluid Dynamics," II, 504, Oxford University Press, London (1938).
6. Gunn, R., *J. Geophys. Research*, **54**, 383 (1949).
7. Hughes, R. R., and E. R. Gilliland, *Chem. Eng. Progr.*, **48**, 497 (1952).
8. Imai. I., *J. Meteorol. Soc. (Japan)*, Series 2, **28**, (4), **113** (April 1950).
9. Katz. H. M., M. S. thesis, Univ. Cincinnati (1950).
10. Laws, J. O., *Trans. Am. Geophys. Union*, 22, part III, 709 (1941).
11. McDonald, J. E., "Theoretical Cloud Physics Studies" (Final Report), Project NR082 093, Office of Naval Research, U. S. Navy Dept.
12. Saito, S., *Science Repts., Tôhoku Imp.* Univ. Series I, 2, 179 (1913).
13. Smirnov. N. I., and V. L. Ruban, *Zhur. Priklad. Khim.* (*J. Appl. Chem.*), 22, 1068 (1949).
14. Spilhaus, A. F., *J. Meteorol.*, 5, 108 (1948).
15. Watson in Ref. 7, page 500.
16. Zuideman, H. H., and G. W. Waters, *Ind. Eng. Chem., Anal. Ed.*, **13**, 312 (1941).
17. Hu, S., and R. C. Kintner, *A.I. Ch.E. Journal*, **1**, 42 (1955).

(Presented at A.I.Ch.E. Louisville meeting)

Mechanism of Heat Transfer to Fluidized Beds

H. S. Mickley and D. F. Fairbanks

Massachusetts Institute of Technology, Cambridge, Massachusetts

In order to determine the nature of the resistance controlling heat transfer between fluidized beds and surfaces in contact with them, heat transfer measurements were made on the same solid constituents with several different fluidizing gases. The heat transfer coefficients obtained with fluidized beds are found to be proportional to the square root of the thermal conductivity of the quiescent beds. This result indicates that the process controlling fluidized heat transfer may be considered to be an unsteady-state diffusion of heat into mobile elements of quiescent bed material.

This picture is analyzed mathematically to yield an equation for the heat transfer coefficient $h = \sqrt{\kappa_m \rho_m c S}$ wherein the effects of the bed thermal properties are separated from the effects of the stirring factor S, which accounts for bed motion and geometry. The mass transfer analogue is also derived and shown to correlate existing mass and heat transfer data reasonably well.

It is concluded that the proposed mechanism yields a satisfactory picture of the fluidized heat transfer process and may provide the beginnings of a rational approach to the correlation and prediction of fluidized heat transfer in engineering work.

Heat transfer coefficients of up to 300 B.t.u./(hr.)(sq.ft.)(°F.) have been reported(*8*) for fluidized beds and surfaces in contact with them; values in the range of 40 to 120 B.t.u./(hr.)(sq.ft.)(°F.) are common. Such coefficients are many times higher than those normally encountered with packed beds or with flowing gases, and the resulting ease of heat transfer is one of the factors favoring the incorporation of fluidization into industrial processes. Despite the many successful commercial applications of fluidization, the nature of the heat-transfer process has remained obscure. The present investigation represents an attempt to delineate the mechanism of heat transfer in "bubbling" beds, i.e., dense-phase, aggregative beds in the absence of slugging or severe channeling. Such beds are a type commonly desired for industrial applications and may be qualitatively described as inhomogeneous tumbling mixtures of solids and upward-moving gas-filled spaces. Knowledge of the heat-transfer mechanism should be of considerable aid in the development of trustworthy design procedures for these beds.

DEVELOPMENT OF A MODEL

As a first step in developing a picture of the mechanism of fluidized heat transfer, it is to be noted that at any time in a fluidized system which is in contact with a surface hotter or colder than the bed, transitory solid-solid, solid-surface, gas-solid, and gas-surface contacts are all occurring, with interconduction of heat to be expected from each such contact. The complicated, irregular motions of solids and gas are constantly making and destroying the individual contacts, and these motions create the means for a convective transfer of heat via both media. By the simultaneous and successive operations of all these individual conductive and convective mechanisms, heat is transferred from the surface and into the core of the bed.

The difficulty with this mode of depicting the heat transfer process is that while the picture is almost certainly correct, it is so complicated as to be quantitatively unmanageable. The need for the creation of a manageable model is the justification for the following discussion.

Bauer(*2*) found evidence that the dense phase of bubbling beds retained a constant void fraction independent of superficial gas velocity and that this void fraction was essentially that of quiescence. Furthermore, his data for uniform glass spheres indicate that the void fraction of quiescence was 0.41. This value may be compared with the theoretical void fractions for spheres packed in cubic and hexagonal prism lattices: 0.475 and 0.395, respectively. In these two

theoretical lattice structures there are, respectively, six and eight neighbors in direct contact with each sphere. It may be concluded, therefore, that at least for uniform spheres the quiescent packing is close enough to allow each particle to be in direct contact with nearly eight neighbors. Each particle in the dense phase of a fluidized bed may be expected to be in contact with several neighbors most of the time, and with this the case it does not seem unreasonable to assume that the particles are locked loosely together and do not usually move in relation to one another. Of course, if the motion of the bed

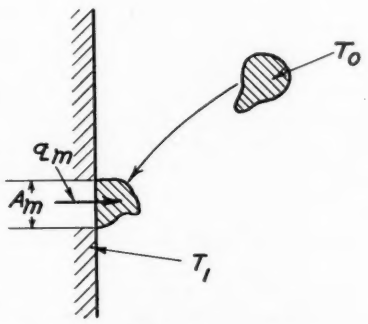

Fig. 1. Transfer of a packet to a heated surface.

creates localized temporary shear forces, separation or relative motion of neighboring particles will result. However, if a small group of neighboring particles is considered, it would appear that it will be a fairly rare occurrence for this group to be so ruptured. It seems reasonable, therefore, to create a picture of fluidization in which small groups of particles are imagined to move as individual units through the bed as the dense phase is stirred. Such a small group or assembly of particles will be here termed a *packet*. Packets are not permanent, but they may be accorded some finite persistence in time. Their void fraction, density, and heat capacity are those of the quiescent bed. The packet thermal conductivity is that of the bed when measured at quiescent packing density in the absence of any solid motion.

In Figure 1 a packet is represented in the main body of the bed. It is here at bed temperature T_o. Suppose that the stirring of the dense phase sweeps this particular packet into contact with a flat surface of temperature T_1. Unsteady-state diffusion of heat into the packet will commence upon contact, and, if it is assumed for analytical purposes that the packet may be considered homogeneous, it can be shown (4) that after being in contact for a time τ, the rate of diffusion of heat into the packet is

$$q_m = \frac{A_m}{\sqrt{\pi}} \sqrt{\kappa_m \rho_m c}\, \tau^{-1/2} (T_1 - T_o) \tag{1}$$

where

q_m is the instantaneous rate of heat flow into the packet, B.t.u./hr.

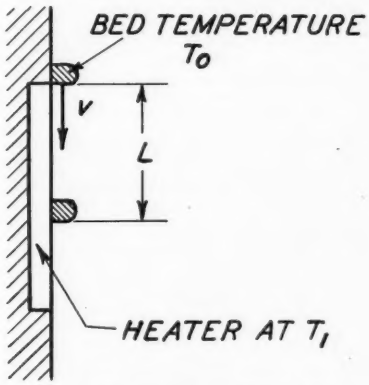

Fig. 2. Downflow of packets past a heated surface.

A_m is the area of contact of the packet with the surface, sq.ft.

κ_m is the thermal conductivity of the packet B.t.u./(hr.)(ft.)(°F.)

ρ_m is the density of the packet, lb./cu.ft.

c is the heat capacity of the packet, B.t.u./(lb.)(°F.)

If the local instantaneous heat transfer coefficient is represented by h_i, then

$$h_i = \frac{q_m}{A_m (T_1 - T_o)} = \frac{1}{\sqrt{\pi}} \sqrt{\kappa_m \rho_m c}\, \tau^{-1/2} \tag{2}$$

The observed local heat transfer coefficient will be the time average of all the local, instantaneous coefficients occurring during a period of time at a particular locality on the heater surface. At this location, let $\psi(\tau)$ represent the frequency of occurrence in time of packets having age τ; that is, over a long period of time, the fraction of the total time during which the surface is in contact with packets of ages ranging between τ and $\tau + d\tau$ is $\psi(\tau)d\tau$. The observed local average coefficient will be due to heat transfer to packets of all ages plus that due to direct contact of gas bubbles at the surface. Neglecting the latter effect, which should generally be small, results in the local coefficient expressed mathematically as the summation of the individual contributions of packets of all ages:

$$h_L = \int_o^\infty h_i(\tau)\, \psi(\tau)\, d\tau = \frac{1}{\sqrt{\pi}} \sqrt{\kappa_m \rho_m c} \int_o^\infty \tau^{-1/2} \psi(\tau)\, d\tau \tag{3}$$

If the term S_L is defined as

$$S_L = \frac{1}{\pi} \left[\int_o^\infty \tau^{-1/2} \psi(\tau)\, d\tau \right]^2 \tag{4}$$

Equation (3) may be succinctly written as

$$h_L = \sqrt{\kappa_m \rho_m c\, S_L} \tag{5}$$

Two important assumptions have entered into this derivation, viz., (1) that relative motion of neighboring particles is rare, at least near heater surfaces, and (2) that the dense phase of the fluidized bed may for the present purpose be considered homogeneous. Some justification has already been given for the first assumption. The second assumption will probably be good if the average residence time of the solid in contact with the surface is long enough for a fair portion of the heat transferred to diffuse into layers of particles lying beyond the layer touching the surface. Justification of the latter assumption requires experimental evidence, which will be offered at a later point.

AVERAGE COEFFICIENTS

Generally one is more interested in the average coefficient for an entire surface than in the local coefficient at a particular point on that surface. The average coefficient for an isothermal surface will be the area mean of the local coefficients. Thus,

$$h = \frac{1}{A} \int_A h_L\, dA \tag{6}$$

where A represents the area of the heat transfer surface. Combining Equations (5) and (6) gives

$$h = \frac{1}{A}\sqrt{\kappa_m\,\rho_m\,c}\int_A S_L^{1/2}\,dA \quad (7)$$

By defining an area mean stirring factor S as

$$S^{1/2} = \frac{1}{A}\int_A S_L^{1/2}\,dA \quad (8)$$

one may write the mean coefficient in a form analogous to Equation (5),

$$h = \sqrt{\kappa_m\,\rho_m\,c\,S} \quad (9)$$

VALUE OF THE MODEL

If Equations (3) and (5) are examined, it will be noted that they relate the heat transfer coefficient to the product of two terms. One of these terms, $\sqrt{\kappa_m \rho_m c}$, is a function only of the thermal properties of the quiescent bed and is readily evaluated. The other term, S_L, offers more difficulty, for it is a function of the packet-age distribution, $\psi(\tau)$, and little is known about how this distribution may be affected by the gross operating variables of the system: gas velocity, particle diameter, heater size, etc. The relation between the two terms S_L and $\psi(\tau)$ is as follows. If solid is exchanged very rapidly at the surface, $\psi(\tau)$ will be very high for low values of τ and negligible for higher ones. This will cause S_L to be large. If solid is exchanged at a slower rate, the average age of solid at the surface will increase, $\psi(\tau)$ will be greater for large values of τ and consequently smaller for small values, and S_L will be decreased. $\psi(\tau)$ represents the distribution of ages among the packets at the surface and is determined only by the processes causing movement of solid across and to and from the surface. $\psi(\tau)$ thus depends on the dynamics of the bed alone. S_L depends on $\psi(\tau)$ and in addition, as will be shown below, on the nature of the temperature or heat-flux distribution on the heater surface.

At present it is impossible to evaluate the stirring term S_L from the dynamic factors which determine it. However, the equations developed are still useful, for, granting the correctness of the assumptions underlying the analysis, the effect of the intrinsic thermal properties of the bed has been identified and isolated from dynamic effects. In this fact there lies an opportunity to test these assumptions experimentally; for beds that are dynamically equivalent, the observed coefficient should vary as $\sqrt{\kappa_m \rho_m c}$. If, contrary to the assumptions made, the real situation involves a gas film next to the wall as the controlling factor, changes of fluidizing gas would cause variations of the coefficient directly proportional to gas conductivity. Other possible controlling mechanisms will give other characteristic behaviors, and from the experimental evidence the admissibility of the various mechanisms may be tested.

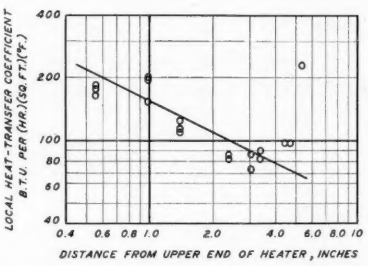

Fig. 3. Variation of the heat transfer coefficient along the vertical length of a heater. Data of Marchetti and Turner (*6*); wall heater; bed diameter: 2.75 in.; No. 11 glass beads, D_p=0.0061 in.; superficial air velocity: 0.25 ft./sec.

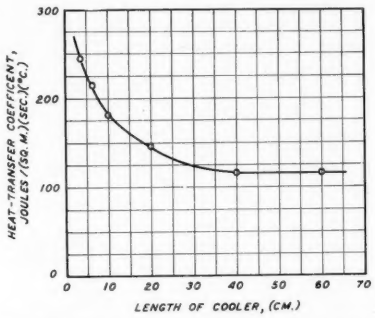

Fig. 4. Effect of cooler length on the heat transfer coefficient. Data of Van Heerden, Nobel, and Van Krevelen (*11*); wall cooler; coke fluidized with air at $V_g = 0.42$ ft./sec.

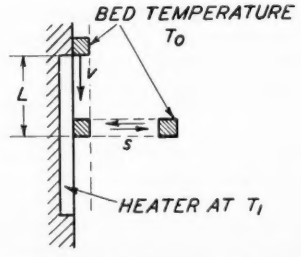

Fig. 5. Downflow of packets past a heater with superimposed side mixing from main body of the bed.

IDEALIZED BED DYNAMICS

Before the experimental checks of the effects of thermal properties are discussed, it is useful to indicate the manner in which some possible forms of bed motion might be expected to affect heat transfer. The motions which will be postulated are undoubtedly too simple to apply generally to actual fluidized beds. It is believed however that the idealized cases approximate actual conditions under special circumstances and that their study may aid in the development of qualitative ideas about the events underlying observed heat transfer phenomena.

Slug Flow of Solid Past the Surface

In a bed which is operating at very low gas rates, just above quiescence, there is not very much turbulence. The solids move up in the center and down at the walls (down also near other surfaces such as those of vertical internal heaters). The flow is not smooth but is spasmodic owing to the intermittent passage of ascending gas bubbles near by in the core of the bed. However, as one possible model of this near-quiescent system, the flow of solid downward past the wall might be assumed to be at some uniform speed v. In Figure 2, then, at a distance L from the leading edge of the heater, the age of all packets is always $\tau = L/v$, and at this position $\psi(\tau) = 0$ except for $\psi(L/v)$ which, assuming the heater to be always in contact with solid, is infinite to such an order that $\psi(L/v)\,d\tau = 1$. The stirring term S_L is then simple to evaluate; viz.

$$S_L^{1/2} = \frac{1}{\sqrt{\pi}}\int_o^\infty \tau^{-1/2}\,\psi(\tau)\,d\tau = \frac{1}{\sqrt{\pi}}(v/L)^{1/2} \quad (10)$$

and

$$h_L = \frac{1}{\sqrt{\pi}}\sqrt{\kappa_m\,\rho_m\,c}\,(v/L)^{1/2} \quad (11)$$

Equation (11) indicates that a heater in contact with such a near quiescent bed will have a heat transfer coefficient which decreases in the direction of the flow of solid along it. If there is a contributing film or surface resistance, the rate of decrease will be lessened, but if there is any degree of decrease in the local coefficient at progressively removed positions from the leading edge, this is an indication that unsteady state diffusion of heat into the flowing solids is an appreciable factor in determining the fluidized heat transfer coefficient.

Baerg, Klassen, and Gishler(*1*) made a qualitative observation of such an effect occurring with an internal heater at the center of a fluidized bed, and they concluded that there was at low gas rates a downflow of solids past the heater.

Marchetti and Turner(*6*) made rough quantitative observations of the leading-edge effect. Some of their results are shown in Figure 3, where a line of slope —0.5 fits their data fairly well. From their data, and from the known thermal properties of the solid, it is possible to estimate that the rate of solid flow v past the wall was about 1 ft./sec. This estimate is based on a modification of Equation (7) which is derived for constant-flux rather than constant-temperature heaters.

Equation (11) gives the heat-transfer coefficient at a point. The mean coefficient for the heater will be the average of the local coefficients:

$$h = \frac{1}{L}\int_{o}^{L} h_L\, dL =$$

$$\frac{2}{\sqrt{\pi}}\sqrt{k_m \rho_m c}\,(v/L)^{1/2} \quad (12)$$

where h is the length-mean coefficient for a surface of height L.

Dow and Jakob(*3*) have reported coefficients between bed walls and fluidized beds operated at low gas rates where an unbroken flow of solid occurred downward at the wall. They found that the observed coefficients varied as the —0.65 power of the depths of these beds. Van Heerden, Nobel and Van Krevelen(*11*) observed similar behavior when the length of cooled wall was varied and the bed depth kept constant. They concluded that the effect determined by Dow and Jakob was due to heater length, not bed depth. This is believed to be a more nearly correct interpretation.

Van Heerden et al. proposed a mechanism involving not only unsteady state transfer but also steady state conduction through a gas layer next to the heater and through a packed solid layer passing the wall. Each of these mechanisms controlled the heat transfer in turn as the solid progressed downward. Their data are shown in Figure 4. They proposed that with short heaters the solid adjacent to the wall was not heated significantly during its short contact time and that the gas layer intervening between wall and solid controlled. For longer heaters the solid began to warm significantly and the combination of gas layer resistance and heat-diffusion resistance in the solid controlled. For very long heaters, the coefficient

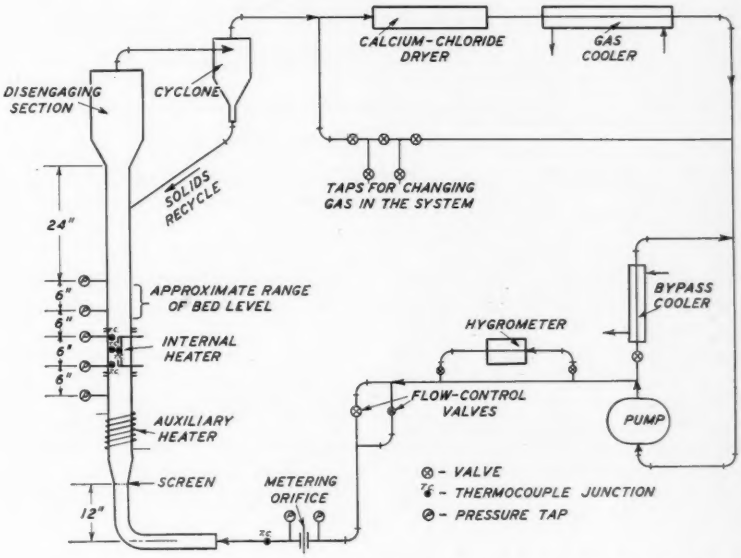

Fig. 6. Experimental fluidized system used in determining effects of gas properties on heat transfer.

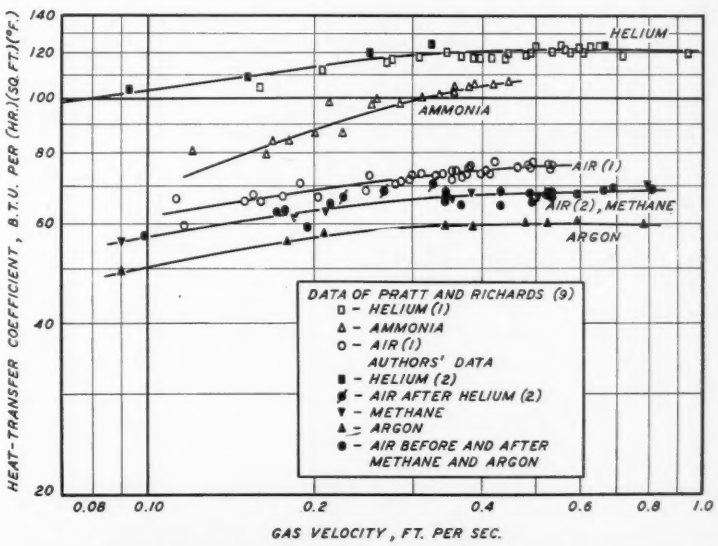

Fig. 7. Heat transfer to microspheres. Bed dimensions: Figure 6; solid properties: Table 1.

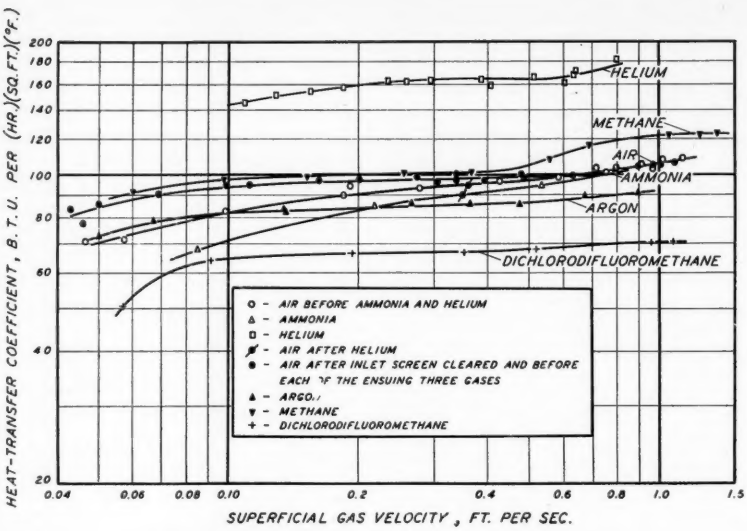

Fig. 8. Heat transfer to glass beads. Bed dimensions: Figure 6; solid properties: Table 1.

became controlled by the conduction of heat from the wall across the laminar layer of solid (now the principal resistance) to the turbulent core of the bed. Although this picture can certainly account for the heater-length effects found by these investigators, it will be shown that the data to be presented here cannot be explained by it.

From these latter data it will be seen that the principal resistance exists in the unsteady state diffusion of heat into the massed solid; independent effects of gas- and solid-layer conduction are negligible. It is believed that the length effects found by Van Heerden et al. are due mainly to variations attributable to the stirring factor S. For very short heaters of the same order of size as the length of the average pulse movement of the solid flow, S should become constant, giving a coefficient independent of length. The effect found with long heaters may be due to the fact that experimentally the heater extended into the poorly stirred solid which exists at the bottom wall of most beds, or it might be due to side mixing of solid.

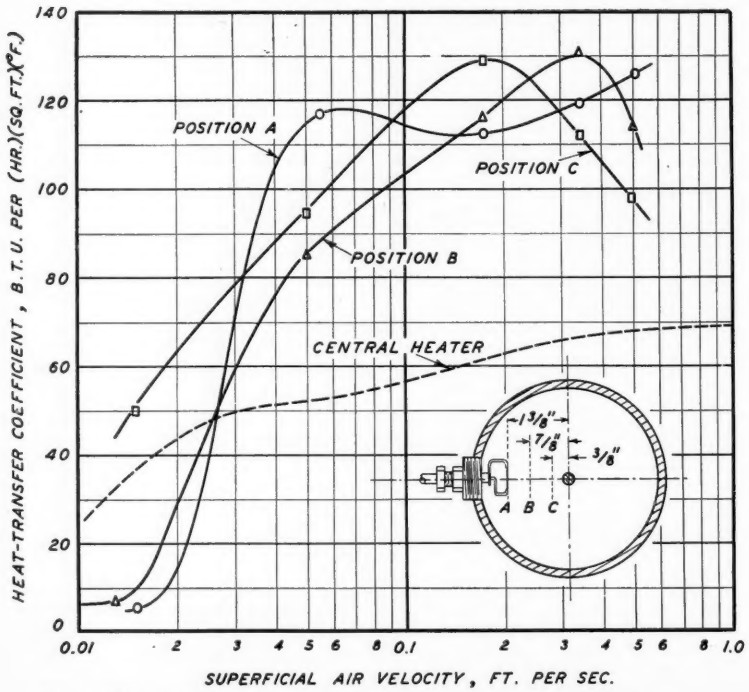

Fig. 9. Heat transfer from the heater probe to a bed of microspheres. Probe dimensions: Figure 10; solid properties: Table 1.

Side Mixing

Although slug flow of solid past the surface may in some circumstances be the primary means by which fresh solid is brought into contact with a surface, there is some evidence to indicate that with large surfaces and highly turbulent beds, sidewise transfer of solid packets to the surfaces will have an important effect on the stirring factor S.

This situation is pictured in Figure 5. Here, as before, the solid mass is flowing down past the surface, but as it passes downward some of the solid at the surface is exchanged with solid brought in sideways from the core of the bed. If s represents the average replacement of packets at the wall per unit time by means of side mixing (i.e., if $s = 0.01$ sec.$^{-1}$, during 1 sec. solid covering one hundreth of the heater area will, on the average, be exchanged by side mixing with fresh core solid), it can be shown (4) that the stirring factor S_L is

$$S_L = \left[s^{1/2} \operatorname{erf}\left(\frac{sL}{v}\right)^{\frac{1}{2}} + \left(\frac{v}{\pi L}\right)^{\frac{1}{2}} \exp\left(-\frac{sL}{v}\right)\right]^2 \qquad (13)$$

When side mixing predominates ($sL/v >> 1$), Equation (9) reduces to

$$S_L = s \qquad (14)$$

and from Equation (5)

$$h_L = \sqrt{\kappa_m \rho_m c s} \qquad (15)$$

Equation (15) is believed to represent the usual condition where transfer surfaces are large and the beds are turbulent. Values of S_L (assumed to be s) obtained in the

TABLE 1.—PROPERTIES OF SOLID MATERIALS

	No. 15 glass beads	Microspheres (as used)	Microspheres (as received) Not Dried	Dried*
Packed-bed density, lb./cu. ft.)				
Loose packed†	91.6	29.0	32.8	29.6
Dense packed‡	99.0	35.0	37.3	34.9
Quiescent packing**	84.3	25.0		
Particle density, by water displacement, lb/cu. ft.	153	137.7	120.3	136
Total void fraction (including internal voids)				
Loose packed	0.401	0.789	0.726	0.782
Dense packed	0.353	0.749	0.690	0.743
Quiescent packing	0.449	0.818		
Extra-particle void fraction¶				
Dense packed	0.35	0.29		
Quiescent packing	0.45	0.49_3		
True particle density, lb./cu. ft.	153	49.3¶		
Average particle diameter, in.	0.0032_8	0.0027		

*Oven-dried at 220°F.
†After being gently poured into container.
‡After prolonged tapping of container.
**From pressure gradient in fluidized condition, extrapolated to quiescence.
¶From analysis of thermal conductivity data. Assumed to include internal voids of individual particles as parts of the particles.

present experiments and believed to represent a typical order of magnitude were about 4 and 10 sec.$^{-1}$ for fluidization of the glass beads and the microspheres respectively.

It should be noted that all equations developed here are for constant-temperature surfaces. If constant-flux (electrically heated) surfaces are used, the constant $1/\sqrt{\pi}$, in Equation (2) becomes $\sqrt{\pi}/2$ and a different definition of the average coefficient is required. The constant-flux analogue of Equation (13) is

$$S_L = \left[\frac{s^{1/2}}{\operatorname{erf}\left(\frac{sL}{v}\right)^{\frac{1}{2}}}\right]^2 \quad (16)$$

and for $s \to 0$ Equation (16) can be shown to yield the analogue of Equation (10), viz.,

$$S_L^{1/2} = \frac{\sqrt{\pi}}{2}(v/L)^{1/2} = \frac{1.571}{\sqrt{\pi}}(v/L)^{1/2} \quad (17)$$

It can be seen that when laminar flow past the surface predominates, an electrical heater will give local coefficients 57% greater than would an isothermal heater. Equations (14) and (15), however, apply to both types of heaters when side mixing predominates.

It is not expected that the equations developed above can be used at present to predict heat transfer with assurance. For this purpose dependable means of predicting solid motion are needed. Experimentally the equations may serve this end by allowing determination of solid motion by means of heat transfer measurements. The above-mentioned development was carried out chiefly to allow a qualitative understanding of the mechanism here proposed.

TABLE 2.—MEASURED CONDUCTIVITIES OF BEDS

Interstitial gas	Gas conductivity B.t.u./(hr.)(ft.)(°F.)	Conductivity of dense bed, B.t.u./(hr.)(ft.)(°F.)	Estimated quiescent conductivity, B.t.u./(hr.)(ft.)(°F.)
Solid: glass beads; bed density: 99.0 lb./cu. ft.			
Air	0.0149	0.0895	0.0620
	0.0148	0.0938	0.0650
	0.0149	0.0893	0.0619
	0.0149	0.0930	0.0645
	0.0149	0.0923	0.0639
Helium	0.0823	0.2188	0.1760
	0.0823	0.2295	0.1850
Methane	0.0188	0.1109	0.0783
Ammonia	0.0140	0.0867	0.0597
Argon	0.0101	0.0687	0.0462
Freon-12	0.00597	0.0484	0.0314
	0.00594	0.0506	0.0328
Solid: microspheres; bed density: 35.0 lb./cu. ft.			
Air	0.0155	0.0505	0.0328
	0.0155	0.0515	0.0335
Helium	0.0839	0.0989	0.0928
	0.0840	0.0980	0.0921
Methane	0.0201	0.0570	0.0390
Ammonia	0.0132	0.0476	0.0300
Argon	0.0104	0.0422	0.0254

The estimated conductivities of the solid particles used in fitting the data to the Schumann-Voss relation (Figure 12) were glass beads, 0.7 B.t.u./(hr.)(ft.)(°F.); microspheres, 0.106 B.t.u./(hr.)(ft.)(°F.). These two conductivities were not measured directly and should be regarded as approximate.

TEST OF THE MECHANISM

Because solids motion cannot be independently determined, it might appear impossible to test the proposed mechanism. However, this is only partly true. The tests that will be presented are based on the assumption that if the heater-bed configuration is the same, the bed motions characterizing S will be nearly the same for a given solid when fluidized at the same gas rate, independent of the physical properties (i.e., viscosity and density) of the gas. This assumption cannot be catagorically proved; nevertheless, on the basis of it a remarkable consistency can be shown to exist among the heat transfer measurements made, a consistency that would be very unusual if the assumption were not a reasonable one.

Granting that bed motion is nearly independent of gas viscosity and density, consideration of the equations developed in the last section shows that the heat transfer coefficient should vary as the square root of the packet conductivity (i.e., the conductivity of the quiescent bed) so long as packet density and heat capacity remain constant. Mechanisms depending on a gas- or solid-film model would, on the other hand, yield variations of the coefficient directly with gas or packet conductivities. For this reason, experiments were carried out in which heat transfer coefficients were measured in beds of solids fluidized with several different gases. The conductivities of beds of these solids were also measured.

EXPERIMENTAL PROCEDURE

The bed in which heat transfer coefficients were measured is shown in Figure 6. The fluidization section was a 4-in. I.D. tube and the heater was a 6-in. section of ¼-in. stainless steel tubing. The heater was supported coaxially in the bed by copper rods at either end. Heat was supplied by passing current through the length of the tube wall, the heat output being obtained from the measured cur-

TABLE 3.—SUMMARY OF EFFECTS OF VARIABLES ON THE STIRRING FACTOR, S

Variable	Exponent in Eq. (20)	Experimental values of exponents	Reference
Particle diameter, D_p	a_1	$-0.6, -1.2$	1, 7
Quiescent density, ρ_m	a_2	-1.1	Present
Gas viscosity, μ_g	a_3	Small	Present
Gas velocity, V_g	a_4	Widely different effects noted, power function inadequate	
Gas density, ρ_g	a_5	$-0.2 < a_5 < 0.2$	Present
Heater length, L	a_6	$-1.0\left(\frac{sL}{v}\text{ small}\right)$ to $0\left(\frac{sL}{v}\text{ large}\right)$	Present
Solids concentration, α_s	a_7	0(low V_g), -1.0($V_g > 1.0$ ft./sec.)	7

Other factors include: 1. Size and geometry of bed and heater
2. Type of heater, constant-temperarure, constant flux, or other
3. Particle roughness
4. Adso ption of vapors on particle surfaces

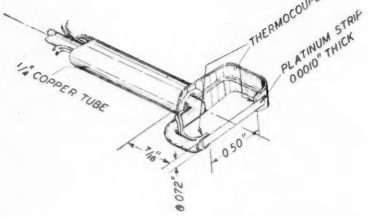

Fig. 10. Isometric sketch of the heater probe.

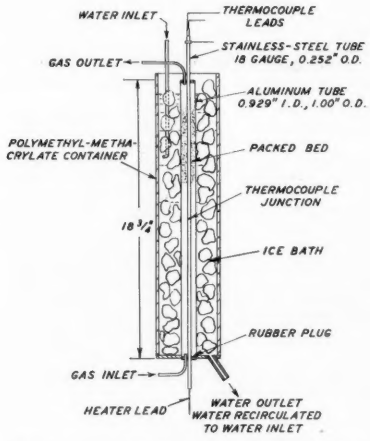

Fig. 11. Apparatus for determination of thermal conductivities of packed solids.

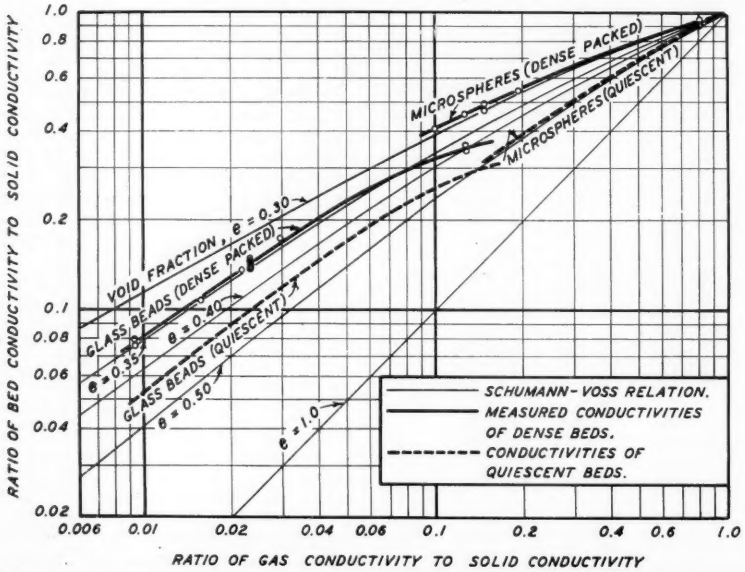

Fig. 12. Conductivities of beds of packed solids. Measured conductivities are shown correlated with Schumann-Voss relation. Quiescent conductivities were obtained from plot by allowing for change of void fraction.

rent and known resistance of the tube. Bed and heater temperatures were measured thermoelectrically, the heater thermocouple being inside the tube at the middle but electrically insulated from it.

During operation, gas was recycled to the bed through a totally closed system which included a cooling section and calcium chloride drier. Table 1 gives properties of the two solid types. The quiescent velocities for these solids, as detected by the onset of bed manometer fluctuation, were small compared with the fluidizing velocities used. Quiescent densities of the fluidizing solids were estimated from the solids concentrations obtained at very low gas velocities. These densities, which are given in Table 1, were, within experimental precision, independent of the gas used.

The heat transfer coefficients obtained are shown in Figures 7 and 8. In the obtaining of these coefficients the temperature difference between heater and bed was given by bucking thermocouples. Fluctuations of the temperature difference of up to $\pm 10\%$ were observed over short intervals of time even though the heating current was constant. Each of the coefficients given is based on the average of about thirty readings of the temperature difference taken over a period of 10 to 15 min.

Some supplementary data obtained with a very small heater probe inserted various distances into the air-microsphere bed are shown in Figure 9. The probe (Figure 10) was a strip of platinum ribbon ½-in. long, 0.072 in. wide, 0.0010 in. thick, its major surface being used in a vertical plane with the long dimension horizontal. The ribbon was heated by direct current, and from its resistance the average temperature was obtained. From this temperature and the current, coefficients were calculated, allowance being made for conduction losses at the ends and the variation of temperature along the length of the ribbon.

The conductivities of the packed solids in the presence of the various gases were measured in a cylindrical apparatus shown in Figure 11. Although the conductivities of quiescent packing were desired under the measurement conditions, the solids were dense packed. The correlations of Schumann and Voss(*10*) were used to adjust the measured values for the difference between these two packings. Both the measured and the adjusted values are given in Table 2, and these data are shown in Figure 12, superimposed on the Schumann-Voss correlation.

RESULTS

1. Probably the most significant result appears when the heat transfer coefficients obtained with the various gases are compared with

the quiescent conductivities of the beds. This has been done in Figures 13 and 14, and it can be seen that for the most part the heat transfer coefficient appears to vary as the 0.52-0.55 power of the quiescent conductivity for a given solid and given gas velocity. The major deviation from this rule occurs in the case of the coefficients obtained with the ammonia-microsphere system, for which the coefficients are 30 to 40% too high. This discrepancy has a reasonable and revealing explanation, which will be discussed below. Except for this one case, the data are consistent, the deviations being easily attributable to experimental error or to small systematic effects of gas viscosity and density on the bed dynamics.

The consistency of the data in these two figures constitutes major evidence for the correctness of the proposed heat transfer mechanism. The effect of quiescent conductivity is very closely the square-root variation expected. If, on the other hand, heat transfer had been controlled by conduction through a laminar layer of solid, the expected variation would have been as the first power of quiescent conductivity. If a gas film had been the controlling factor, the variation should have been as the first power of gas conductivity, and, since, with the gas-solid systems employed, quiescent bed conductivity varied as about the 2/3 power of gas conductivity (*see* Figure 12), the slopes in Figures 13 and 14 would have been approximately $1 \div 2/3 = 1.5$.

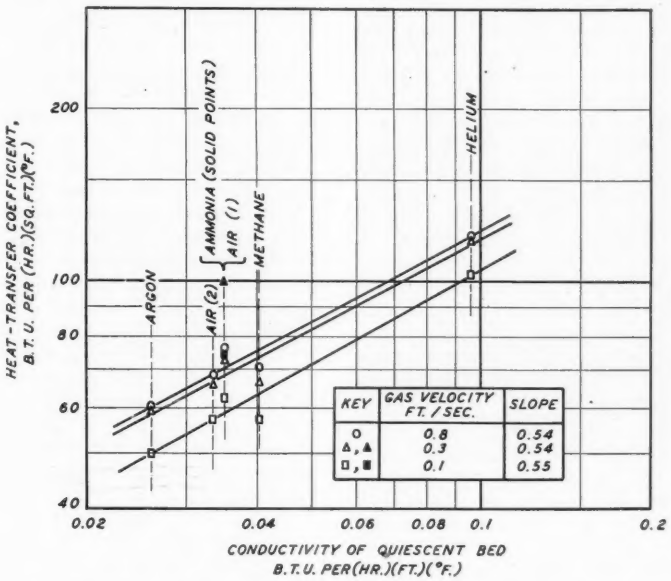

Fig. 13. Microspheres: the heat transfer coefficient as a function of quiescent-bed conductivity.

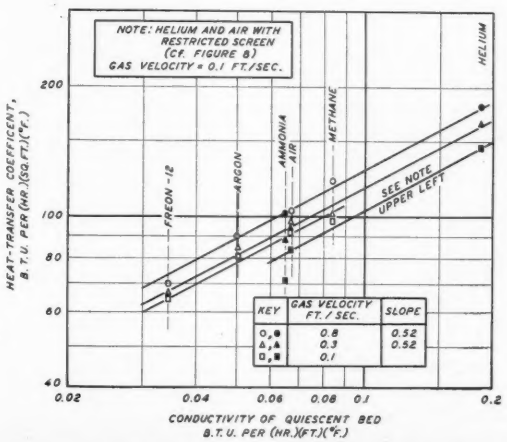

Fig. 14. Glass beads: the heat transfer coefficient as a function of quiescent-bed conductivity.

It is concluded that the packet mechanism is a reasonable picture of the heat-transfer process in fluidized beds.

2. The measured coefficients varied only slightly with gas velocity. Such a lack of important influence of gas velocity has been previously reported by some investigators. Others have found variations ranging from nearly direct to inverse. The reason for this variety of results is not clear and is certainly deserving of further attention.

In this respect it should be noted that the heat transfer coefficients obtained with the small heater probe (Figure 9) display a variety of effects of gas velocity. The interpretation of these probe data is somewhat speculative, but they seem to indicate that fluidization at the lowest velocities occurred only at the center of the bed, i.e., that there was "bubble channeling." As the gas velocity was increased, fluidization quickly extended to the rest of the bed. It is believed that the drop-off of the coefficients near the center of the bed at the higher velocities resulted from the tendency of gas bubbles to congregate there, leaving the small probe frequently out of contact with solid material. Apparently in the vicinity of vertical surfaces (the wall and the central heater) the solid concentration remained high. It can be concluded that the bed was not, in general, homogeneous, that solid preferentially sought the vicinity of large surfaces while the gas bubbles crowded into the spaces between and away from such surfaces.

That much higher coefficients were obtained with the heater probe is believed attributable to the small size of the probe compared with the central heater.

3. There was no noticeable independent effect of solids concentration on heat transfer. In some cases different gases gave significantly different solids concentrations at the same gas rate. These differences had no noticeable correlation with heat transfer nor did they correlate systematically with

the viscosities and densities of the gases.

4. Increasing the gas pressure from 1.0 to 1.3 atm. had no noticeable effect on heat transfer when the superficial velocity was maintained constant.

5. Comparison of the coefficients obtained with microspheres with those obtained with glass beads indicated that density, as characterized by quiescent density, had almost no effect on the heat transfer coefficient, i.e., that S varied as the —1.1 power of quiescent density, thereby nearly canceling the effect of quiescent density indicated by ρ_m in Equations (1) to (15). This result would seem to indicate that lighter particles move faster at equal fluidization velocities.

6. The ammonia - microsphere system behaved paradoxically. It has already been noted that with this system the heat transfer coefficients were higher than expected. When ammonia was first introduced into the microsphere bed, a large heat evolution was noted, and it was concluded that adsorption of ammonia was occurring on the porous microspheres. This conclusion was substantiated by the fact that the microspheres, which displayed a quiescent density with other gases before and after their fluidization with ammonia of 25.0 lb./cu.ft., had a quiescent density of about 29.8 lb./cu.ft. in the presence of ammonia. Because, as stated in section 5 above, heat transfer is nearly independent of quiescent density, the increased weight of the particles could not be the main source of the 30 to 40% excess in the ammonia-microsphere coefficients.

However, the heat capacity of liquid ammonia is high, viz., 1.163 B.t.u./(lb.)(°F.). The microspheres themselves have a heat capacity of about 0.16 B.t.u./(lb.)(°F.). Assuming that the adsorbed ammonia behaves as the liquid, the saturated microspheres would have a heat capacity of

$$[(0.16)\ (25.0) + 1.163\ (4.8)]/29.8 = 0.32 \text{ B.t.u./(lb.)(°F.)}$$

From Equation (15) it would be expected that the saturated microspheres would display coefficients higher by an amount equal to the ratio of the square roots of the heat capacities. Since the ratio of the heat capacities is 0.32/0.16 = 2, and since $\sqrt{2} = 1.41$, a 40% increase can be adequately explained. This only explains in part the misbehavior of the ammonia-microsphere system, for at lower gas velocities, below 0.2 ft./sec., the coefficients obtained were only about 30% too high. In Figure 8 it will be noted that for the ammonia –glass bead system there is a similar drop-off of the coefficients at low gas velocity. The glass beads were nonporous and gave no gravimetric evidence of ammonia adsorption; however, it appears likely that some of the gas condensed on the glass surfaces. Such condensation has been found by other investigators to cause bed particles to stick together and to increase the probability of channeling.

DISCUSSION

Effect of Particle Size

The present investigation included no direct determination of the independent effect of particle size. Other investigators have universally found that with a given bed and heater and the same gas and solid type the heat transfer coefficient increases as the average particle size diminishes. Mickley and Trilling (*7*) found that $h \propto D_p^{-0.6}$, and Baerg et al. (*1*) found that $h \propto D_p^{-0.3}$. The usual interpretation has been that the effect is due to the reduction in thickness of a gas film which offers appreciable resistance to the conduction of heat between heater and solid particles. But the present work shows that no such appreciable gas-film resistance is present.

Here the alternative proposal is made that the particle-size effect is one of bed motion, that beds of smaller particles circulate fresh solid to contacting walls more rapidly at a given gas velocity. In terms of Equations (1) to (16), this means that the stirring factor S is a decreasing function of particle diameter.

Effects of Solids Concentration

As has been mentioned, no independent effect of solids concentration (the ratio of apparent bed density to quiescent density) was noted in the present investigation. However, Mickley and Trilling, employing a higher range of gas velocities (1 to 6 ft./sec.), found that the heat transfer coefficient varied as the 0.48 power of solids concentration. This effect implies that S, the stirring factor, varies as the 0.96 power of solids concentration at high gas velocities.

One possible (but not a unique) interpretation of this relationship is that, when it applies, the heated surface is only partially covered with solid and that, more precisely, the average fraction of the heated surface in contact with dense-phase material is directly proportional to the solids concentration. Meanwhile the rate of formation of fresh area of contact is independent of solids concentration.

Actually, this seems to be a reasonable picture of a slugging bed, but it is to be recognized that, at the higher gas velocities, mechanisms other than the one here proposed may be important in determining the total resistance of the bed to heat transfer.

Mass Transfer to Fluidized Beds

Recently Van Heerden, Nobel, and Van Krevelen (*11*) investigated the transfer of naphthalene to fluidized beds of coke and Devarda's alloy. A ring of naphthalene 6 cm. high was coated on the inner wall of the bed, and with air blowing through the bed at a superficial velocity of 0.42 ft./sec. the mass-transfer coefficients were determined. It was noted that with both types of solid the value of the coefficient declined rapidly with increasing temperature. The coke bed, for instance, yielded a coefficient, k_g, of 9.3 cm./sec. at 5.1°C., whereas at 33.0°C. k_g was 1.45 cm./sec. Heat transfer coefficients were also determined to a heat transfer ring, also 6 cm. high, placed in the beds in the same place as the naphthalene surface. The air rate was the same as before (0.42 ft./sec.). It is illuminating to study these data in the light of the picture of the fluidization mechanism that has been developed here and, especially, to determine what relalationship may exist between the processes of mass and heat transfer.

It will be assumed that mass transfer occurs in a manner completely analogous to the mechanism already developed for heat transfer. On the basis of this assumption, it is easily shown that the mass transfer analogue of Equation (1) is

$$N_m = \frac{A_m}{\sqrt{\pi}} \sqrt{\mathbf{D}_m \rho_m \left(\frac{C_M}{y_s}\right)}\ \tau^{-1/2}\,(y_s - y_e) \qquad (18)$$

where

N_m = rate of mass transfer, g./sec.
A_m = area of transfer surface, sq. cm.

$\mathbf{D}_m$ = diffusion coefficient of the transferring component through the dense phase, sq. cm./sec.

ρ_m = density of the dense phase, g./cc.

C_M = mass-capacity coefficient of the adsorbent (*see* below for full definition), dimensionless

τ = age or time of contact of the adsorbent packet with the surface, sec.

y_s = saturation concentration of the diffusing component in the vapor phase when in equilibrium with the solid, g./cc.

y_e = concentration of the volatile material in the gas phase of the main body of the bed, g./cc.

The mass-capacity coefficient C_M needs fuller explanation. The "mass capacity," C_M/y_s, is the analogue of the heat capacity and represents the mass of additional adsorbate which will be retained by unit mass of the adsorbent following a unit increase in the concentration, y_e, of adsorbate in the vapor phase; that is, if at constant, temperature N_A represents the grams of adsorbate retained on 1 g. of adsorbent, then

$$dN_A = \left(\frac{C_M}{y_e}\right) dy_e \qquad (19)$$

The value of C_M can be determined from the adsorption isotherms of the components involved. It should be noted that C_M is not independent of the vapor concentration, y_e. For the present purpose some value typical of the range of concentration from y_e to y_s is to be selected. Referring to Figure 15, which shows two adsorption isotherms for naphthalene and coke(*11*), the value of C_M is estimated from the slope of the dashed line as 0.000245 at 3.5°C. and as 0.000274 at 17.7°C. From Figure 15 the value of C_M for Devarda's alloy and naphthalene will be taken as 0.0000202 at 0.7°C. It is also to be noted that although C_M, the mass-capacity coefficient, is relatively insensitive to temperature in the present case of physical adsorption, the mass-capacity C_M/y_s decreases markedly with increasing values of the saturation concentration, y_s, and thus with increasing temperature.

From Equation (18), by direct analogy to the development of Equation (9) from Equation (1), it may be shown that

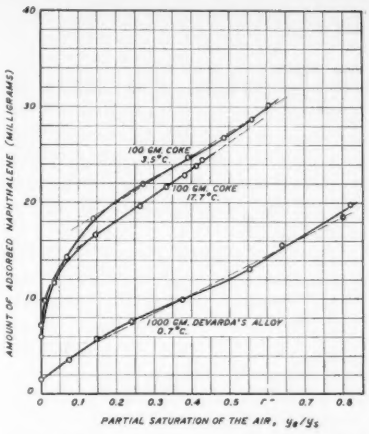
AMOUNT OF ADSORBED NAPHTHALENE (MILLIGRAMS)
100 GM. COKE 3.5°C.
100 GM. COKE 17.7°C.
1000 GM. DEVARDA'S ALLOY 0.7°C.
PARTIAL SATURATION OF THE AIR, y_e/y_s

Fig. 15. Adsorption isotherms for naphthalene on coke and Devarda's alloy. Data of Van Heerden, Nobel, and Van Krevelen(*11*).

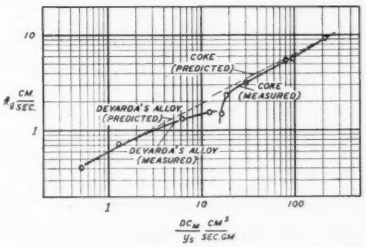

Fig. 16. Comparison of experimental mass transfer coefficients with values predicted from heat transfer coefficients. Data of Van Heerden, Nobel, and Van Krevelen(*11*).

$$k_g = \sqrt{\mathbf{D}_m \rho_m \left(\frac{C_M}{y_s}\right) S} \qquad (20)$$

where k_g is the average mass transfer coefficient between bed and wall (cm./sec.)

If reasonable values can be estimated for the mass transfer and thermal properties of the beds, it should be possible to evaluate the "stirring term," S, from the measured heat transfer coefficient and to use this value in Equation (20) to obtain the mass transfer coefficient. The estimated mass transfer coefficients may then be compared with those obtained experimentally by Van Heerden, Nobel and Van Krevelen.

Exact data are not available for the properties of quiescent coke or Devarda's alloy, and some approximation is necessary.

By use of the data of Dow and Jakob(*3*) for fluidized coke, the quiescent void fraction is estimated as, $\varepsilon_m = 0.634$. Since coke is a relatively high-conductivity solid, it is estimated, with the aid of reference *10*, that $\kappa_m = 2.7$ $\kappa_g = 2.7 \times 0.016 = 0.043$ B.t.u./(hr.)(ft.)(°F.). The heat capacity of coke is taken as $c = 0.223$ B.t.u./(lb.)(°F.). The quiescent density is taken as 44.4 lb./cu.ft. or 0.713 g./cc.

From Equation (9)

$$S = \frac{h^2}{\kappa_m \rho_m \tau c} \qquad (21)$$

Van Heerden et al. obtained a heat transfer coefficient with coke of 230 Joules/(sq.meter)(°C.)(sec.) or 40.25 B.t.u./(hr.)(sq. ft.)(°F.). By means of Equation (21) a value of $S = 1.056$ sec.$^{-1}$ is calculated.

Data are available for the diffusion coefficient of naphthalene in air, and if it is assumed that there is relatively little diffusion through the coke particles, a relation developed by Maxwell(*5*) allows the estimation of the over-all diffusion coefficient of napthalene through a bed of void fraction, $\varepsilon_m = 0.634$. This gives $\mathbf{D}_m = 0.535$ **D** where **D** is the diffusivity of naphthalene into air with no obstruction present in the diffusion path. Substituting the necessary values into Equation (20) (shifting to c.g.s. system of units) gives

$$k_g = \sqrt{(0.535)\,\mathbf{D}\,(0.713)\frac{C_M}{y_s}\,(1.056)}$$

$$= 0.635\sqrt{\frac{\mathbf{D}C_M}{y_s}}$$

Figure 16 shows this relationship plotted as a dashed line with the data of Van Heerden et al. superimposed. The data for Devarda's alloy were treated similarly and are also plotted.

It is to be noted that notwithstanding the possible imprecision of some of the estimated bed properties used in the calculations, the magnitude of the experimental mass-transfer coefficients is fairly well predicted. Perhaps even more significant is that a decrease in the coefficient obtained with increasing temperature is predicted in fair accordance with the observed behavior. It is concluded that this decrease in coefficient with increasing temperature is due to the increase in vapor pressure of the adsorbate and consequent reduction in the "mass capacity" of the adsorbent.

The ability to correlate mass and heat transfer seems to offer

further confirmation for the proposed transfer mechanism.

CONCLUSION

The results of the present investigation indicate that the principal resistance to the transfer of heat or mass from surfaces to dense fluidized beds exists in the layers of solid particles nearest the surface. The rate of transfer appears to be controlled by the unsteady state diffusion of heat or mass into this layer and by the rate of replacement of parts of this layer with solid from the bed core. There is no evidence of a steady state film of gas or solid offering significant resistance.

The functional relationship of the heat-transfer coefficient to other bed properties is adequately comprehended by equations of the form

$$h = \sqrt{\kappa_m \rho_m c S} \qquad (9)$$

where S, the stirring factor, accounts for the type and degree of bed motion and also may be affected by the type, size, and position of the heat source. At the present time too little is known about bed motion in the vicinity of surfaces to relate S analytically to the parameters suspected of determining bed motion. It is believed to be a function of many variables; thus

$$S = \phi_1(D_p, \rho_m, \mu_g, V_g, \rho_g, L, \alpha_s, \text{ and others}) \qquad (22)$$

Some of the functional variations have been determined both here and by other investigators. Thus if the foregoing equation could be represented as a product of powers of the factors, i.e.,

$$S = D_p^{a_1} \cdot \rho_m^{a_2} \cdot \mu_g^{a_3} \cdot V_g^{a_4} \cdot \rho_g^{a_5} \cdot L_g^{a_6} \cdot \alpha_s^{a_7} \cdot \phi_2 \text{ (other factors)} \qquad (23)$$

the values for the exponents that have been mentioned in the present paper are summarized in Table 3.

More work on the mechanics of fluidized beds is needed if it is to be possible to predict heat transfer coefficients adequately. It is recommended that data be reduced to the form

$$S = \frac{h^2}{\kappa_m \rho_m c} \qquad (21)$$

and that the correlation of S with operating variables and the characteristics of the solids be made.

It should be noted that if trustworthy data are available for a bed-heater system fluidized with one gas, the present findings make possible the prediction with fair reliability of coefficients with another gas.

However, until heat transfer data more comprehensive than those presently available appear, the use of stirring-factor correlations based on such data must be treated with caution when applied to uninvestigated ranges of the many variables.

NOTATION

A = area of heat transfer surface, sq.ft.

A_m = area of packet in contact with heat transfer surface, sq.ft.

a_1-a_7 = exponents in Equation (23)

C_M = mass-capacity coefficient of solid adsorbent, dimensionless

c = heat capacity of fluidized solid, B.t.u./(lb.)(°F.)

$\mathbf{D}$ = diffusion coefficient of transferring component through fluidizing gas, sq.cm./sec.

$\mathbf{D}_m$ = diffusion coefficient of transferring component through fluidized solid-gas mixture, sq.cm./sec.

D_p = average diameter of the fluidized particles, ft.

erf = error function

exp = exponential function

h = coefficient of heat transfer from surface to bed (time and local-area average), B.t.u./(hr.)(sq.ft.)(°F.)

h_i = instantaneous heat transfer coefficient, B.t.u./(hr.)(sq.ft.)(°F.)

h_L = local time-average heat transfer coefficient, B.t.u./(hr.)(sq.ft.)(°F.)

k_g = coefficient of mass transfer from surface to bed (time and local-area average), cm./sec.

L = length of heater from upper edge, ft.

N_A = amount of component adsorbed per unit of adsorbent, g./g.

N_m = instantaneous mass transfer rate between bed and surface, g./sec.

q_m = instantaneous heat transfer rate between bed and surface, B.t.u./hr.

S = area-mean stirring factor, hr.$^{-1}$

S_L = local stirring factor $= 1/\pi (\int_0^\infty \tau^{-\frac{1}{2}} \psi(\tau)\, d\tau)^2$ (hr.$^{-1}$)

s = fraction of heater-surface area contacted by fresh packets from the main body of the bed per unit time, sq.ft./(hr.)sq.ft.

T = temperature, °F.

t = time, hr.

V_g = superficial fluidizing-gas velocity, ft./sec.

v = average downward velocity of solid past a vertical surface, ft./hr.

y_e = concentration of component in gas-phase, g./cc.

y_s = concentration of component in gas phase in equilibrium with adsorbent, g./cc.

α_s = solids concentration, ratio of bed density to quiescent density

ε_m = void fraction of quiescent bed

κ_g = thermal conductivity of fluidizing gas, B.t.u./(hr.)(°F.)(ft.)

κ_m = thermal conductivity of quiescent bed, B.t.u./(hr.)(°F.)(ft.)

μ_g = viscosity of fluidizing gas, centipoises

ϱ_g = density of fluidizing gas, lb./cu.ft.

ϱ_m = density of quiescent solid, lb./cu.ft.

τ = packet age, i.e., time during which packet has been in contact with surface, hr.

$\psi(\tau)$ = frequency of occurrence, at a point on the heater surface, of packets of age τ, hr.$^{-1}$

$\pi = 3.14159$

$\phi(x)$ = function of x

LITERATURE CITED

1. Baerg, A., J. Klassen, and P. E. Gishler, *Can. J. Research*, 28F, 287 (1950).
2. Bauer, W. C., Sc.D. thesis, Mass. Inst. Technol. (1949).
3. Dow, W. M., and M. Jakob, *Chem. Eng. Progr.*, 47, 637 (1951).
4. Fairbanks, D. F., Sc.D. thesis, Mass. Inst. Technol. (1953).
5. Jakob, M, "Heat Transfer," p. 85, John Wiley and Sons, Inc., New York (1949).
6. Marchetti, E. J., and R. A. Turner, S.B. thesis, Mass. Inst. Technol. (1951).
7. Mickley, H. S., and C. A. Trilling, *Ind. Eng. Chem.*, 41, 1135 (1949).
8. Nicholson, E. W., J. E. Moise, and R. L. Hardy, *Ind. Eng. Chem.*, 40, 2033 (1948).
9. Pratt, S. L., Jr., and R. L. Richards, Jr., S. M. thesis, Mass. Inst. Technol. (1951).
10. Schumann, T. E. W., and V. Voss, *Fuel*, 13, 249 (1934).
11. Van Heerden, C., P. Nobel, and D. W. Van Krevelen, *Ind. Eng. Chem.*, 45, 1237 (1953).

Diffusion Coefficients in Hydrocarbon Systems: *n*-Hexane in the Gas Phase of the Methane—, Ethane—, and Propane—*n*-Hexane Systems

L. T. Carmichael, B. H. Sage, and W. N. Lacey
California Institute of Technology, Pasadena, California

Experimental information concerning the molecular transport of the lighter hydrocarbons in the gas phase is limited. For this reason a study was made of the Maxwell diffusion coefficients of *n*-hexane in the gas phase of the methane–*n*-hexane, and propane–*n*-hexane systems.

Maxwell diffusion coefficients were determined at steady state for pressures up to 70 lb./sq. in. at temperatures between 70° and 220°F. The effects of interfacial resistance were considered and uncertainties as to the behavior at the end of the transport path were eliminated. Coefficients were reported with partial pressure and with fugacity as the potential. Fick diffusion coefficients were calculated for each component on the assumption that the gas phase was an ideal solution.

These data indicated that the Maxwell hypothesis with fugacity as the potential in an ideal solution is a fair description of the transport characteristics of the lighter hydrocarbons in the gas phase at relatively low pressures. A regular decrease in the Maxwell diffusion coefficient with an increase in the molecular weight of the stagnant component was observed.

The molecular transport of components in the gas phase has been the subject of many investigations. The work of Maxwell(*12*) and Stefan(*25, 26, 27*) laid a satisfactory foundation for the treatment of such processes in situations where the kinetic theory may be applied. Chapman and Cowling(*7*) extended the analysis to include the effects of changes in composition, and Enskog(*8*) contributed materially to an understanding of such phenomena in gases at elevated pressures. Recently a review of experimental work in this field was presented(*21, 22*), and summaries of the basic equations of transport are available(*10*). It does not therefore appear necessary to review the literature of gas-phase diffusion or to consider in detail the derivation of the basic equations of transport.

Drickamer's(*16, 29*) active program is an example of the current interest in the field of molecular diffusion* in the gas phase. Little experimental work is available concerning the diffusion coefficients of the lighter hydrocarbons in the gas phase even for low pressures. Schlinger(*21*) measured the Maxwell diffusion coefficients of *n*-heptane and *n*-hexane in air at atmospheric pressure for temperatures from 100° to 220°F. Recently Carmichael(*4*) reported the coefficients of methane and *n*-heptane in the gas phase of the methane–*n*-heptane system. The work was carried out at pressures up to 70 lb./sq.in. in the temperature interval between 100° and 220°F., and the results indicated good agreement of the experimental data with the Maxwell hypothesis.

Drickamer recently reported experimental evidence(*24, 30, 31*) of a resistance at an interface associated with a transport process. Schrage(*23*) predicted that such resistances are of primary importance at low pressures where the mean free path of the molecules becomes large. Schlinger(*21*) and Carmichael(*4*) found the resistance at the gas-liquid interface of the *n*-heptane–air, the *n*-hexane–air, and the *n*-heptane–methane systems to be small.

The present work involved the measurement of the diffusion coefficients of *n*-hexane in the gas phase of the methane–, ethane–, and propane–*n*-hexane systems for pressures up to 70 lb./sq. in. in the temperature interval between 70° and 220°F. The experimental measurements were made under steady conditions and regard was taken of the resistance at the interface and of possible variations in the effective transport length as a result of nonuniform conditions at each end of the transfer path. In addition, the Fick diffusion coefficients of each of the components were calculated as a function of pressure, temperature, and composition. Throughout this discussion and in the associated figures the pressures are reported in pounds per square inch absolute or pounds per square foot absolute.

METHODS AND APPARATUS

The details of the methods and the apparatus employed have been described(*5*). Figure 1 depicts schematically the steady state equipment used for the present measurements. The *n*-hexane in the liquid phase was introduced at a known rate into the chamber *A* and flowed upward through the porous disk *B*. After evaporation at the upper surface of the porous disk it diffused through the gas phase in the working section *C* and was withdrawn from the apparatus at *D* by circulating the stagnant component, which was brought to equilibrium with *n*-hexane liquid

*Molecular diffusion here refers to that component of material transport which is not due to turbulence and does not imply the very low-pressure phenomena to which this term is also applied.

at 32°F. in the condenser. The rate of introduction of the n-hexane into the diffusion cell as a liquid at B was measured with a probable error of 0.1% and was maintained by the use of a modulated electric drive for a mechanical injector. The speed of the drive was controlled by means of a quartz oscillator and a suitable electronic circuit(*15*). Supplemental electrical heaters were provided at A of Figure 1 in order to permit the temperature of the liquid evaporating at B to be controlled within small limits. Multijunction platinum-constantan thermocouples were employed to establish the temperature of the evaporating liquid with a probable error of less than 0.03°F. Attainment of steady state was indicated by the constancy of the level of the meniscus in the capillary manometer E, which also indicated constancy of the exposed surface of liquid in the porous disk. Most of the measurements were made with a capillary depression of approximately 1 in. of n-hexane at the evaporationg surface B.

The mole fraction of n-hexane at D, the upper end of the transport path, was maintained at a steady small value by the circulation of the stagnant component across the upper end of the diffusion cell. The gaseous mixture of the stagnant component and n-hexane being circulated was in equilibrium with a liquid phase of this system at 32°F. at the pressure of measurement. To avoid large effects from convection at the upper end of the diffusion cell, the circulating gas was introduced through the interstices of a tube bundle located in the upper part of the cell. The gas was returned through the interior of the tubes of the bundle to the condenser. Circulation was maintained by means of a small centrifugal blower in the external circuit. Details of the condenser have been described(*5*).

The temperature of the diffusion path was known with a probable error of 0.05°F. from the international platinum scale, and variations with time and position were less than 0.02°F. The temperature of the surrounding oil bath was controlled by means of a platinum resistance thermometer which actuated a modulating circuit(*15*) through a galvanometer and photoelectric cell combination. The temperature was related to the international platinum scale by means of a resistance thermometer of the strain-free type(*14*), which was compared with the indications of a similar instrument which had been calibrated at the National Bureau of Standards.

The pressure of the system was determined by means of a multiple mercury-and-butyl phthalate manometer. The relative elevations of the six phthalate-mercury interfaces were determined by means of a cathetometer, the probable error in the difference in elevation of the interfaces being less than 0.003 in. Corrections were made for local gravity and for the temperature of the phthalate-and-mercury column as well as for irregularities in the pitch of the screw of the cathetometer. The probable error in the measurement of pressure was less than 0.01 lb./sq.in. However, during the investigation of the ethane–n-hexane and the propane–n-hexane systems measurable decreases in pressure were observed as a result of the large negative partial volume of n-hexane in these systems.

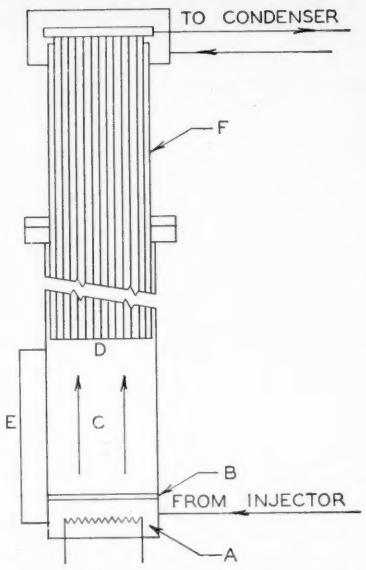

Fig. 1. Schematic arrangement of steady state equipment.

The change in length of the transfer path from one set of measurements to another was determined by means of a cathetometer and was known within 0.002 in. after suitable corrections for the effect of temperature upon the dimensions of the equipment(*4*). An additional correction to the actual length of the transfer path was made in order to take into account the end effects associated with the evaporation of the liquid at the porous plate B of Figure 1 and of the disturbance associated with the circulation of the gaseous mixture at D(*5*). The composition of the gas circulated at D was determined from the equilibrium behavior of the particular binary system at 32°F. for the pressure in question. This equilibrium information is based upon the data of Boomer and Johnson(*3*) for the methane–n-hexane system and upon ideal solutions(*11*) for the ethane– and propane–n-hexane systems. The measurements of Michels and Nederbragt (*13*) together with recent compilations(*17, 19*) were used to establish the volumetric behavior of methane, ethane, and propane; whereas the Benedict equation of state with the constants recently suggested by the originator(*1*) was used to determine the volumetric behavior of n-hexane in the gas phase. The fugacities of the components were also determined from the Benedict equation of state.

The diffusion coefficients and the resistance at the interface were established by solution of each of the following equations(*21*) simultaneously for at least two different transport lengths:

$$D_{M,\,k} = \frac{\mathring{m}_k\, b_k\, T\,(l_G - l_c)}{\ln\left(\dfrac{p_{j,\,t}}{p_{j,\,i} + b_k\, T r_{i,\,k}\, \mathring{m}_k}\right)} \qquad (1)$$

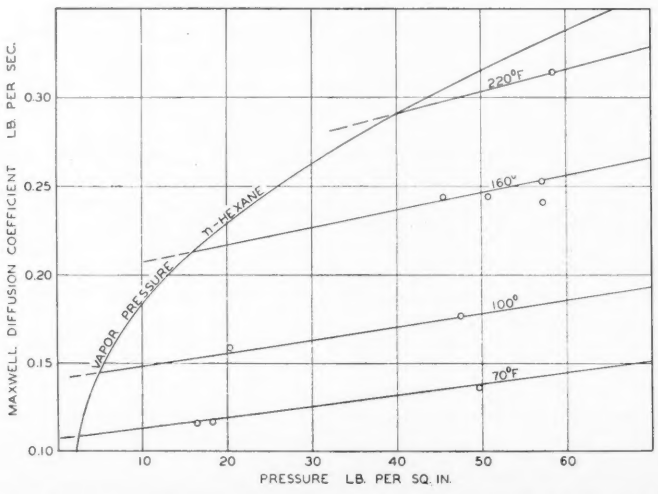

Fig. 2. Diffusion coefficients for n-hexane in the methane–n-hexane system.

TABLE 1.—MAXWELL DIFFUSION COEFFICIENTS FOR *n*-HEXANE AND PROPERTIES IN THE GAS PHASE

Pressure, lb./sq. ft.	Temperature, transport path, °F.	Compressibility factor: Stagnant component	Compressibility factor: *n*-Hexane	Vapor pressure *n*-hexane, lb./sq. ft.	Fugacity of pure *n*-hexane, lb./sq. ft.	Diffusion coefficient: Perfect gas, lb./sec.	Diffusion coefficient: Ideal solution, lb./sec.
			Methane–*n*-hexane				
2,361	69.95	0.9976	0.9279	354.38	2,197	0.1149	0.1161
7,141	69.74	0.9936	0.7360	354.24	5,445	0.1345	0.1358
2,627	69.97	0.9974	0.9197	354.10	2,423	0.1164	0.1164
2,929	100.00	0.9978	0.9300	711.36	2,727	0.1557	0.1584
6,836	99.98	0.9950	0.8227	717.40	5,668	0.1730	0.1764
6,545	159.99	0.9967	0.9001	2,279.52	5,877	0.2357	0.2439
8,223	160.02	0.9960	0.8719	2,282.40	7,147	0.2438	0.2527
7,366	159.98	0.9964	0.8875	2,268.00	6,556	0.2354	0.2439
8,250	160.00	0.9960	0.8700	2,276.64	7,168	0.2323	0.2400
8,403	220.00	0.9972	0.9180	5,748.48	7,679	0.2943	0.3130
			Ethane–*n*-hexane				
2,265	70.27	0.9920	0.9300	357.26	2,115	0.0902	0.0917
3,061	100.54	0.9907	0.9265	720.00	2,842	0.1080	0.1107
4,353	100.00	0.9867	0.8959	712.80	3,862	0.1145	0.1171
7,276	99.94	0.9777	0.8091	711.36	6,006	0.1132	0.1167
4,473	160.60	0.9899	0.9325	2,299.70	4,190	0.1536	0.1607
8,275	160.32	0.9813	0.8705	2,289.60	7,183	0.1461	0.1534
4,250	160.59	0.9904	0.9363	2,278.10	3,995	0.1525	0.1593
7,537	219.95	0.9873	0.9265	5,739.80	6,957	0.1856	0.1988
			Propane–*n*-hexane				
2,245	70.00	0.9829	0.9342	354.38	2,093	0.0443	0.0453
2,919	100.00	0.9814	0.9308	712.80	2,694	0.0742	0.0765
3,349	100.00	0.9785	0.9195	713.52	3,089	0.0697	0.0721
4,320	160.00	0.9793	0.9353	2,278.10	4,037	0.1074	0.1128
8,887	159.68	0.9565	0.8592	2,263.70	7,614	0.0976	0.1050
4,859	160.30	0.9767	0.9270	2,288.20	4,499	0.1095	0.1148
8,773	160.23	0.9570	0.8613	2,291.00	7,531	0.0938	0.1007
8,718	220.32	0.9679	0.9149	5,771.50	7,847	0.1428	0.1532

$$D_{M,\,k} = \frac{\mathring{m}_k\, b_k\, T\,(l_G - l_c)}{Z\left(\frac{\mathring{f}_k}{P}\right) \ln\left(\frac{\mathring{f}_k - f_{k,\,t}}{\mathring{f}_k - f_{k,\,i} + b_k\, T r_{i,\,k}\, \mathring{m}_k}\right)} \qquad (2)$$

Equation (1) assumes perfect gas behavior and employs partial pressure as the potential, whereas Equation (2) is based upon an ideal solution with fugacity as the potential. By proper choice of path lengths and transport rates it was possible to isolate to a large extent the effect upon the diffusion coefficient of uncertainties in transport length and of resistance at the interface. As was indicated earlier(*5*), the corrections to the transport length were found to be a single-valued function of the Reynolds number of the flow in the tube bundle *F* of Figure 1, which brought the circulating gas to the upper end of the transport path.

Throughout all this work the weight rate of flow of the gaseous mixtures to the upper end of the transport path was maintained at known values between 4×10^{-6} and 8×10^{-6} lb./sec. The Reynolds number was taken as a linear function of the weight rate of flow at a given state, as indicated in the following expression:

$$\frac{Re}{Re^+} = a\left(\frac{\eta}{\eta^+}\right)(\mathring{m}'_j + \mathring{m}'_k) \qquad (3)$$

In estimating the Reynolds number of the flow in the tubes at the upper end of the diffusion path, suitable small corrections were made for the effect of temperature and pressure upon the viscosity of methane, ethane, and propane when mixed with *n*-hexane(*2, 18, 20*). Available calibrations(*5*) were employed to establish quantitatively the influence of the Reynolds number upon the effective length of the diffusion path.

MATERIALS

The sample of deaerated *n*-hexane, obtained from the Phillips Petroleum Company, had a specific weight of 40.8817 lb./cu.ft. at 77°F. and atmospheric pressure, as compared with a value of 40.87932 reported by Rossini (*17*) for an air-saturated sample. The index of refraction at 77°F. relative to the *D* lines of sodium was 1.3737, as compared with the value for an air-saturated sample of 1.37226 reported by Rossini(*17*) for the same temperature. It is believed that the sample employed contained only traces of air and less than 0.002 mole fraction of material other than *n*-hexane.

Methane was obtained from the San Joaquin Valley through the courtesy of The Texas Company and as received contained less than 0.002 mole fraction of impurities. Before use it was passed over calcium chloride, activated charcoal, and anhydrous calcium sulfate at a pressure in excess of 200 lb./sq.in. A spectroscopic analysis indicated that methane obtained from this source and subjected to the above-described treatment contained less than 0.001 mole fraction of heavier hydrocarbons, nitrogen or argon.

Ethane and propane were obtained from the Phillips Petroleum Company. The ethane was reported to contain less than 0.0006 mole fraction of impurities and was employed without further purification. There was no indication upon freezing in liquid air that the sample contained any quantities of volatile components. A spectroscopic analysis of the sample indicated that it contained less than 0.0019 mole fraction of material other than ethane. The impurity was predominantly ethene. The propane, reported to contain less than 0.002 mole fraction of impurities, was subjected to a fractionation similar to that described for *n*-hexane. The sample employed contained less than 0.0001 mole fraction of material other than propane, as indicated by spectroscopic analysis.

RESULTS

A total of twenty-six measurements of the rate of transport of *n*-hexane was made in the gas phase of the methane–*n*-hexane, ethane–*n*-hexane, and propane–*n*-hexane systems; the data therefrom are available(*6*). The results of the calculation of the diffusion

coefficients from these experimental data are recorded in Table 1, which includes the pressure, temperature, compressibility factor, vapor pressure, fugacity, and diffusion coefficients for each of the states investigated. The vapor pressure of *n*-hexane was based upon the critical review of Rossini(*17*). The fugacities were calculated from the Benedict equation of state utilizing the coefficients proposed by the originator(*1*). The equation of state was employed to predict the fugacity and volumetric behavior for *n*-hexane at pressures in excess of vapor pressure. In the application of Equation (1) it was assumed that the phases were perfect gases and in the use of Equation (2) that they were ideal solutions.

The Maxwell diffusion coefficients were calculated from Equations (1) and (2) by means of available information(*5*) concerning the small influence of Reynolds number, described in Equation (*3*), upon the effective length of the diffusion path. For these relatively low pressures there is little to choose between the diffusion coefficients calculated on the basis of a perfect gas and those derived from the behavior ascribed to an ideal solution. Throughout the remainder of the discussion the Maxwell diffusion coefficients based upon fugacity as a potential in an ideal solution were employed.

Maxwell diffusion coefficients for *n*-hexane in the gas phase of the methane–*n*-hexane system are shown in Figure 2. The curves were drawn to indicate a substantial increase in the coefficients with an increase in pressure, as was found in the methane–*n*-heptane system(*4*). A firm evaluation of such trends with pressure must await measurements over a wider range of this variable than was covered in the present study. The data shown in Figure 2 yielded a standard deviation of 0.00475 lb./sec. for the experimental data from the straight lines drawn through the points for each of the four temperatures. Smoothed values of this coefficient for *n*-hexane are recorded in Table 2. It should be realized that the apparent effect of pressure found in the methane–*n*-hexane system at the lower temperatures is an indication that the Maxwell hypothesis(*12*) does not describe the transport process with precision.

Experimental data for the Maxwell diffusion coefficients for *n*-hexane in the ethane– and in the propane–*n*-hexane systems are shown in Figures 3 and 4 respectively. In these instances there was no marked tendency for the coefficients to change with pressure; however, in the case of the propane–*n*-hexane system the data indicated a possible tendency for the Maxwell diffusion coefficient to decrease with an increase in pressure. Some difficulty was experienced in the experimental work for the propane–*n*-hexane system as a result of the diffusion of propane through the liquid *n*-hexane in the porous-glass disk *B* of Figure 1. It was necessary to eliminate some of the measurements involving the longer transfer paths since the rate of diffusion of propane through the disk under steady conditions was significant. With shorter transfer paths the gross motion of the *n*-hexane liquid in the pores of the disk more than compensated for the molecular diffusion of the propane into the *n*-hexane liquid. The standard deviation of the measurements for the ethane–*n*-hexane system was 0.003 and in the propane–*n*-hexane system 0.005 lb./sec. from the smoothed data. Table 3 records smoothed values of the Maxwell diffusion coefficient for *n*-hexane in the ethane– and propane–*n*-hexane systems. Since the data of Figures 3 and 4 indicated no significant influence of pressure upon the Maxwell diffusion coefficient, there was no need to include the latter variable in the tabulation, as was done in Table 2 for the methane–*n*-hexane system.

The influence of temperature upon the Maxwell diffusion coefficient is shown in Figure 5. The behavior of *n*-hexane in the methane–*n*-hexane system was compared at a pressure of 40 lb./sq.in. with the behavior in the ethane– and propane–*n*-hexane systems, which were found not to be influenced by pressure. The diffusion coefficient for *n*-hexane in-

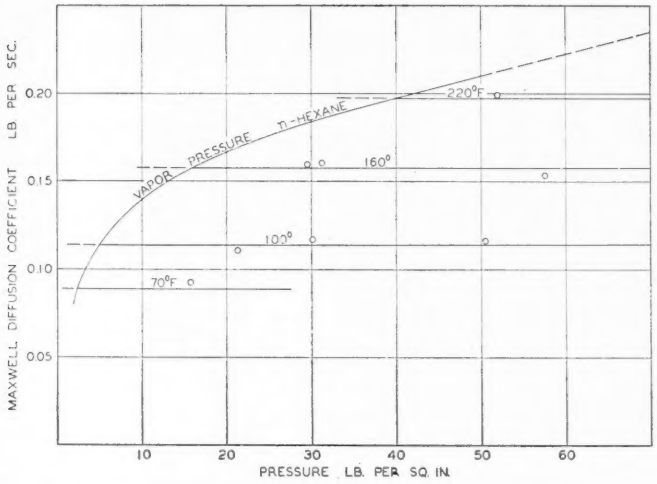

Fig. 3 Diffusion coefficients for *n*-hexane in the ethane–*n*-hexane system.

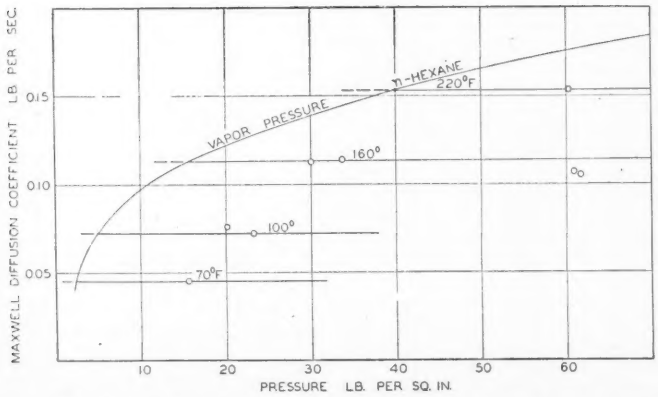

Fig. 4. Diffusion coefficients for *n*-hexane in the propane–*n*-hexane system.

TABLE 2.—MAXWELL DIFFUSION COEFFICIENTS FOR *n*-HEXANE IN THE METHANE-*n*-HEXANE SYSTEM

Temperature, °F.	Pressure, lb./sq. in. 14.696	20	30	40	50	60
70	0.1160*	0.1190	0.1255	0.1320	0.1380	0.1443
100	0.1520	0.1560	0.1634	0.1710	0.1765	0.1855
130	0.1811	0.1876	0.1962	0.2049	0.2128	0.2211
160	.....	0.2168	0.2262	0.2368	0.2458	0.2555
190	.....	.....	0.2545	0.2645	0.2762	0.2863
220	.....	.....	.....	0.2909	0.3031	0.3155

*Maxwell diffusion coefficients are expressed in pounds per second.

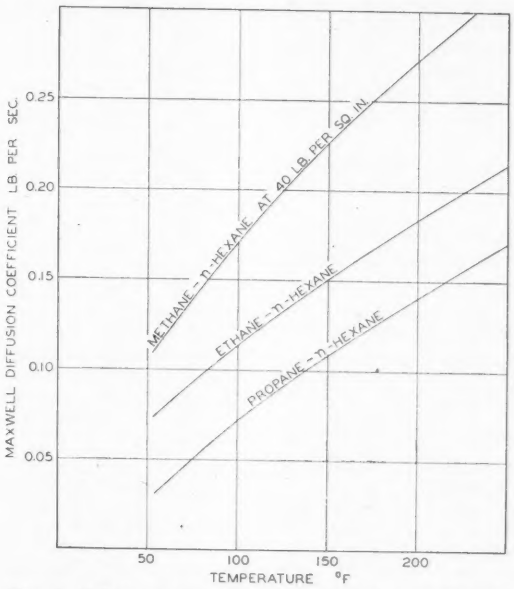

Fig. 5. Effect of temperature on diffusion coefficients for *n*-hexane.

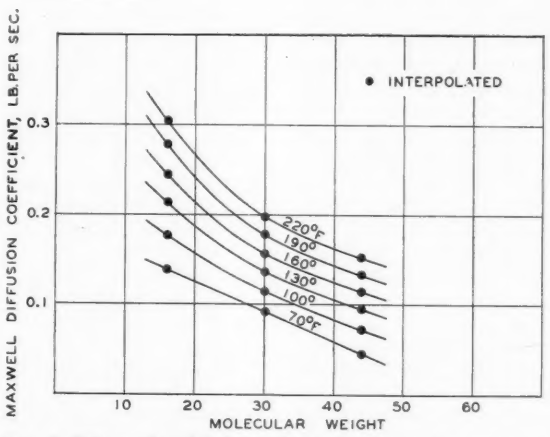

Fig. 6. Effect of molecular weight of stagnant component on diffusion coefficient for *n*-hexane.

creases more rapidly with an increase in temperature for the methane–*n*-hexane system than it does for either the ethane– or the propane–*n*-hexane systems. A pressure of 40 lb./sq. in. was chosen for the methane data in order to permit comparison throughout the temperature range investigated and still involve as low a value as feasible.

Figure 6 depicts the effect of the molecular weight of the stagnant component upon the Maxwell diffusion coefficients for *n*-hexane at several temperatures. Again the data for methane at a pressure of 40 lb./sq.in. were compared with

TABLE 3.—MAXWELL DIFFUSION COEFFICIENTS FOR *n*-HEXANE IN THE ETHANE-*n*-HEXANE AND PROPANE-*n*-HEXANE SYSTEMS

Temperature, °F.	Ethane–*n*-hexane	Propane–*n*-hexane
70	0.0890*	0.0450
100	0.1136	0.0720
130	0.1361	0.0948
160	0.1571	0.1133
190	0.1778	0.1336
220	0.1980	0.1525

*Maxwell diffusion coefficients are expressed in pounds per second and are considered to be independent of pressure.

the diffusion coefficients in the other systems, which were independent of pressure. The experimental points correspond to those recorded in Tables 2 and 3. There is a rapid decrease in the diffusion coefficient with an increase in molecular weight, as would be predicted from the Sutherland equation(*28*). The regularity of decrease in the diffusion coefficient with an increase in molecular weight offers encouragement in regard to predictions of the transport behavior of hydrocarbon gases.

FICK DIFFUSION COEFFICIENTS

The Fick diffusion coefficient (*9*) may be defined by

$$D_{F,k} = -\frac{\dot{m}_{k,d}}{\left(\frac{\partial \sigma_k}{\partial x}\right)} \qquad (4)$$

Equation (4) applies only to one dimensional transport, and the component flux is that resulting from molecular diffusion and does not include the transport associated with any gross motion of the fluid. It may be shown that the Fick coefficients are related to the Maxwell coefficients for a perfect gas in the following way:

$$D_{F,k} = \left(\frac{n_j}{n_j}\right) \frac{D_{M,k}}{P} \qquad (5)$$

In case the gas phase follows the behavior of an ideal solution but may deviate from perfect gas behavior, Equation (5) assumes the form

$$D_{F,k} = \frac{\left(\frac{n_j}{n_j}\right)\left(\frac{\mathring{f}_k}{P}\right)\left(\frac{Z^2}{P}\right) D_{M,k}}{[1 + \sigma_k(\mathring{V}_j - \mathring{V}_k)]} \qquad (6)$$

By utilization of Equation (6) the Fick diffusion coefficients for *n*-hexane were computed from the Maxwell coefficients as a function of pressure, temperature, and composition and are available(*6*) for the methane–*n*-hexane, ethane–*n*-hexane, and propane–*n*-hexane systems.

The Fick diffusion coefficients for the two components are related by the following expression:

$$D_{F,\,j}\frac{\partial \sigma_j}{\partial x} = -D_{F,\,k}\frac{\partial \sigma_k}{\partial x} \qquad (7)$$

Equation (7) may be simplified to

$$D_{F,\,j} = \frac{\overset{\circ}{\sigma_k}}{\overset{\circ}{\sigma_j}} D_{F,\,k} \qquad (8)$$

Equation (8) and the information, already discussed, concerning the volumetric behavior of each of the components were utilized to compute the Fick diffusion coefficients for methane, ethane, and propane, which are available(*6*). The Fick diffusion coefficients are markedly functions of pressure, temperature, and composition. They are discussed here because it is often more convenient to employ such coefficients in the analysis of transport processes involving hydrodynamic velocities than the Maxwell coefficients.

The results obtained in this investigation indicate that the Maxwell hypothesis(*12*) is a reasonable description of the transport phenomena in the gas phase of the binary systems of methane, ethane, and propane with *n*-hexane at low pressures. The differences in composition within the experimental transport path were significant, particularly at pressures approaching the vapor pressure of *n*-hexane. However, there was only a small change in the coefficient for the methane–*n*-hexane system with pressure and none for the other systems. Such behavior indicates that the Maxwell hypothesis took into account the effect of composition upon the transport to at least a first degree of approximation.

ACKNOWLEDGMENT

This paper is a contribution from American Petroleum Institute Research Project 37 located at the California Institute of Technology. Betty Kendall carried out the computations and Elizabeth McLaughlin aided in the preparation of the manuscript. The cooperation of The Texas Company in making the supply of methane available is acknowledged.

NOTATION

a = dimensional constant
b = specific gas constant of phase (R/M), ft./°R.
b_k = specific gas constant of component k, (R/M), ft./°R.
$D_{F,\,k}$ = Fick diffusion coefficient of component k, sq.ft./sec.
$D_{M,\,k}$ = Maxwell diffusion coefficient of component k, lb./sec.
f_k = fugacity of component k in the phase, lb./sq.ft.
f_k° = fugacity of component k in the pure state, lb./sq.ft.
l_c = effective correction to gross transfer distance, ft.
l_G = gross transfer distance, ft.
M = average molecular weight of phase
$\overset{\circ}{m}_k$ = weight rate of transport of component k, lb./(sec.)(sq. ft.)
$\overset{\circ}{m}_k'$ = total weight rate of circulation of component k, lb./sec.
n_k = weight fraction of component k
n_k = mole fraction of component k
P = pressure, lb./sq.ft.
p_j = partial pressure of component j, (Pn_j), lb./sq. ft.
R = universal gas constant, ft./°R.
r_i = resistance at interface, sec./ft.
Re = Reynolds number
T = thermodynamic temperature, °R.
V_k = molal volume of component k, cu.ft./lb.mole
x = distance in direction of diffusion path, ft.
Z = compressibility factor, PV/bT
η = absbolute viscosity, (lb.)(sec.)/sq.ft.
σ_k = concentration of component k, lb./cu.ft.
$\overset{\circ}{\sigma}_k$ = molal concentration of component k, lb.mole/cu.ft.
∂ = partial differential operator

Superscripts

° = pure state
+ = reference state

Subscripts

d = diffusion
i = conditions at interface
j = component j, the stagnant component
k = component k, the diffusing component
t = conditions at exit of transfer tube

LITERATURE CITED

1. Benedict, M., *Chem. Eng. Progr.*, **47**, 419, 449, 571, 609 (1951).
2. Bicher, L. B., Jr., and D. L. Katz, *Trans. Am. Inst. Mining Met. Engrs.*, **155**, 246 (1944).
3. Boomer, E. H., and C. A. Johnson, *Can. J. Research*, **B16**, 328 (1938).
4. Carmichael, L. T., H. H. Reamer, and B. H. Sage, *Ind. Eng. Chem.* (in press).
5. ———, Am. Doc. Inst., Washington, D. C. (1955).
6. Carmichael, L. T., B. H. Sage, and W. N. Lacey, Am. Doc. Inst., Washington, D. C., Doc. No. 4661.
7. Chapman, S., and T. G. Cowling, "The Mathematical Theory of Nonuniform Gases," Cambridge University Press, Cambridge (1939).
8. Enskog, D., *Kungl. Svenska Vetenskaps. Akad. Handl.*, **63**, No. 4 (1922).
9. Fick, A., *Ann. Phys.*, **94**, [2], 59 (1855).
10. Kirkwood, J. G., and B. L. Crawford, *J. Phys. Chem.*, **56**, 1048 (1952).
11. Lewis, G. N., *J. Am. Chem. Soc.*, **30**, 668 (1908).
12. Maxwell, J. C., "Scientific Papers," **2**, 625 Cambridge University Press, Cambridge (1899).
13. Michels, A., and G. W. Nederbragt, *Physica*, **3**, 569 (1936).
14. Myers, C. H., *Bur. Standards J. of Research*, **9**, 807 (1932).
15. Reamer, H. H., and B. H. Sage, *Rev. Sci. Instr.*, **24**, 362 (1953).
16. Robb, W. L., and H. G. Drickamer, *J. Chem. Phys.*, **19**, 1504 (1951).
17. Rossini, F. D., "Selected Values of Properties of Hydrocarbons," Natl. Bur. Standards (November, 1947).
18. Sage, B. H., and W. N. Lacey, *Ind. Eng. Chem.*, **30**, 829 (1938).
19. Sage, B. H., and W. N. Lacey, "Thermodynamic Properties of the Lighter Paraffin Hydrocarbons and Nitrogen," Am. Petroleum Inst., New York (1950).
20. Sage, B. H., and W. N. Lacey, *Trans. Am. Inst. Mining Met. Engrs.*, **127**, 118 (1938).
21. Schlinger, W. G., H. H. Reamer, B. H. Sage, and W. N. Lacey, API Biennial Volume, 70-106 (1952-53).
22. Schlinger, W. G., H. H. Reamer, and B. H. Sage, Am. Doc. Inst., Washington, D. C., Doc. No. 4071 (1953).
23. Schrage, R. W., "A Theoretical Study of Interphase Mass Transfer," Columbia University Press, New York (1953).
24. Scott, E. J., L. H. Tung, and H. G. Drickamer, *J. Chem. Phys.*, **19**, 1075 (1951).
25. Stefan, J., *Ann. Physik*, **41**, 725 (1890).
26. ———, *Sitz. Akad. Wiss. Wien. Math. Naturw. Klasse*, **63**, Abt. II, 63 (1871).
27. *Ibid.*, **65**, Abt. II, 323 (1872).
28. Sutherland, W., *Phil. Mag.*, **38** [5], 1 (1894).
29. Timmerhaus, K. D., and H. G. Drickamer, *J. Chem. Phys.*, **20**, 981 (1952).
30. Tung, L. H., and H. G. Drickamer, *loc. cit.*, p. 6.
31. *Ibid.*, p. 10.

Chemical Factors in Propellant Ignition

Melvin A. Cook and Ferron A. Olson
University of Utah, Salt Lake City

A method of studying solid propellant ignition is described which utilizes detonating gas igniters. This article describes (1) conditions required for obtaining reproducible igniter systems and (2) results of application of the method to four well-known rocket propellants in which various "chemical" and "thermal" effects were brought out by suitable variations in the initial pressure and composition of the detonating gas igniter. Successful application of the detonating-gas-igniter method requires the use of steady state detonation waves, i.e., waves in which the detonation head has attained a steady "size" and momentum. Experimental data are presented which show that detonation (following the initial predetonation buildup) must travel 40 to 50 cm. in a 1-in. diam. steel tube before these steady state conditions are established in the systems studied.

Results of studies by the detonating gas ignition method show that, besides the important purely physical effects of temperature and pressure, free oxygen and solid carbon in the igniter system are very effective in lowering the threshold ignition pressure. Moreover, increasing oxygen in the igniter markedly lowers the ignition time lag (τ_p) for appearance of an observable flame although it increases the time lag (τ_i) for appearance of reaction sufficient to cause the first measurable ionization in the reaction zone ($\tau_p >> \tau_i$). Although true flame-ignition time lags were observed to be of the order of several milliseconds, reaction of the propellant was observed to start within 1 msec. (possibly immediately) after collision of the detonation wave with the propellant.

The detonating gas method is shown to provide a reliable measure of the relative ignition sensitivities of various rocket propellants.

Chemical effects on propellant ignition may be defined as the effects exerted by various chemical species by virtue of specific chemical reactions, aside from the physical or "thermal" factors of temperature and pressure. It is important, however, to realize that the chemical effects described in this article require high temperature. Most investigations in propellant ignition have been concerned with the influence of temperature (*12, 24, 32*); pressure (*12*); and heat transfer by radiation (*1, 2, 20, 29*), convection (*13, 27*), and conduction (*18, 28*). The results of the few studies on chemical effects reported (*4, 13, 5, 27*) thus far have been inadequate to show conclusively that chemical effects are actually involved to an appreciable extent in propellant ignition, most investigators having attributed ignition primarily to the physical factors, temperature and pressure. One reason for uncertainty in this regard is that chemical factors have been studied at temperatures much lower than those encountered in practical ignition system. Also in many investigations, especially those with conditions comparing favorably with practical igniters, it was difficult to ascertain the composition of the gases actually contacting the propellant during the time interval between the initial application of energy and subsequent decomposition or burning of the propellant.

In an attempt to evaluate the specific or chemical influence of various chemical species on propellant ignition at realistic temperatures and pressures, a detonating-gas-ignition technique was developed. Detonating gases develop pressures and temperatures of the magnitude found in practical igniter systems, and these conditions may be varied reproducibly over relatively wide ranges by proper selection of the initial pressure and composition of the igniter system (*19*). Furthermore, the thermohydrodynamic theory of detonation, solved by use of the ideal gas equation of state, $pv = nRT$, known to be reasonably valid for gases (*26*), provides, in addition to the temperature, pressure, and other thermodynamic data for conditions existing in the detonation front (*15, 19*), the chemical composition of the products of detonation. Unfortunately detonation conditions prevail for only a few microseconds (*17*), whereas true ignition requires in general a much longer induction period. On the other hand, calculations show that the Chapman-Jouguet concentrations of the molecular species (i.e., the composition existing in the detonation wave) for the various igniters used here should maintain at least approximately during the entire ignition induction period. The detonation-head model, described in Appendix I, suggests that once the detonation wave has

This study was supported by U. S. Naval Ordnance Test Station Contract N123-60530S-1980. It comprises part of a thesis to be presented by Ferron A. Olson in partial fulfillment of the requirement for the degree of doctor of philosophy at the University of Utah.

propagated a length L_m, a steady state detonation head of constant size, momentum, pressure, and average particle velocity is attained. Consequently, according to this model thermodynamic conditions existing in the igniter gas from the wave front rearward should be relatively constant for a distance which should be equal to the distance covered by the wave front in about 10 to 20 μsec. Even though the ignition time lag is much greater than this, however, the most profound thermal effect on subsequent ignition should be that exerted during the time interval of application of detonation conditions owing to relatively sharp rarefactions and cooling outside the detonation head. Chemical effects on the other hand exert themselves over the entire induction period and are probably most important in the later stages.

The complete heat-balance equation of the propellant being ignited may be written as follows:

$$\alpha + \beta = \delta \qquad (1)$$

where the first term on the left ($\alpha = -K\nabla^2 T$) accounts for the heat conduction, the second term ($\beta = C\rho dT/dt$) for the heat content of the propellant, and the term on the right ($\delta = \rho Qk'f$) expresses the heat generated by chemical reaction of the propellant. (Here K is the thermal conductivity, ρ the density, C the specific heat, Q the specific heat of reaction, and f a dimensionless function expressing the order of reaction.) Thus when ignition of propellants is accomplished with a detonating gas igniter, it is reasonable to assume that a relatively constant temperature corresponding to T_2 (the detonation temperature) persists at the propellant surface for the short period of application of detonation conditions (10 to 20 μsec.), during which term α is strongly positive, term β increases rapidly in time, but term δ reaches importance probably only toward the end of this stage. The depth of penetration of heat into the propellant may be very small, possibly a few microns or less, but the surface should be raised essentially to gas-phase temperature. The increase in β when α is positive starts reaction at the surface, and term δ increases exponentially in T, reaching a certain magnitude while α is still positive. During this phase both α and δ thus contribute to β but α is of far greater importance. From considerations of the mechanism of burning of propellants (*12*) the first reaction involves only partial decomposition and is in general much less energetic than complete reaction. After the detonation head has passed beyond the propellant, the temperature of the surrounding medium drops rapidly; term α then becomes negative and heat flows outward from the now reacting propellant surface into the surrounding medium. (Sporadic positive thermal effects of the igniter after passage of the detonation wave exist owing to recurrent shock effects which are ever present, especially in short shot tubes, but may be reduced to negligible proportions by use of long shot tubes and careful control of the method of collision of the detonation wave with the propellant.)

The chemical effects described in this report are probably of very little, if any, significance during the part of the process where term α is positive. As soon as reaction has become appreciable, however, these chemical effects become important (1) by their influence on Q in term δ and (2) by specific influences on the rate of reaction. While the surrounding medium will thus exert an adverse thermal influence on ignition after the detonation head has passed, or as soon as term α becomes negative, it may have a very pronounced positive chemical effect if it contains chemical substances which upon contacting the reacting surface can contribute to the heat and/or rate of reaction. Ignition or nonignition of the propellant will thus depend (1) on the magnitude of the energy input by the term α while the detonation head is in contact with the propellant and (2) on the later influence of specific chemical reactions between the gas phase and the propellant in the propellant reaction zone.

The detonating gas igniter method was for the reasons given above considered to offer promise as a means for studying propellant ignition.

EXPERIMENTAL METHOD

Ignition Threshold and Time Lag.

Quantitative data observable in the detonating gas ignition method for the study of propellant ignition include (1) ignition or nonignition and (2) ignition time lag. The most satisfactory index for ignition-nonignition is the minimum, or "threshold," pressure for ignition, where threshold pressure, designated $p_1°$, is here defined as the minimum initial pressure required to produce consistent ignitions of a given propellant by a particular detonating gas of given composition. A more fundamental index is, of course, the threshold detonation pressure $p_2°$. However, since p_2 may be computed from p_1 and ρ_1 through the hydrodynamic theory, $p_1°$ is quite as reliable an index as $p_2°$. It has the advantage of being a directly observable quantity where $p_2°$ is not. From numerous calculations made at this laboratory it was observed that for most of the igniter compositions used, many of the detonation properties were a linear function of log p_1(*7*). For example, in comparing a detonation property calculated at two different values of p_1, the following equation was found to hold satisfactorily. (*See* Figure 1.)

$$\psi_i''/\psi_i' = 1 + \beta_1 \log_{10} p_1''/p_1' \qquad (2)$$

where ψ_i refers to any of the following thermodynamic variables: Q_2 (heat of explosion), D (detonation velocity, n_2 (moles of detonation products/kg.), T_2 (detonation temperature), and some others not used in this study. Also β_1 is a different constant for each of the variables in question, and p_1''/p_1' is the ratio of initial pressures.

The ignition time lag τ is defined as the interval between the initial application of energy to the propellant, i.e., impact of the propellant by the detonation front, and the time of ignition of burning of the propellant. The latter requires careful definition; it depends on the particular initial stage of burning one observes. Depending on how this "ignition" is observed, it may be identified with various stages of burning; for example, it may correspond to the first observable partial decomposition of the propellant, the initial observation of evolution of gas, or the initial appearance of a high-temperature, luminous flame. The literature describes three zones of propellant burning, namely foam, fizz, and flame zones(*30*). Each of these zones makes its appearance at a somewhat different time, and as a result observations involving different zones of burning would be described by different ignition time lags. One must, of course, exercise care to ascertain that the stage one is observing actually provides an adequate criterion of ignition, i.e., that a stable flame always appears at the particular stage observed.

One time-lag index employed in this study involved measurement of the induction period of initial decomposition sufficient to produce enough ionization for discharge of an ionization gap. This was determined by a technique(*7*) in which the time τ_i' to start decomposition and erode a given thickness d of propellant from the surface of the exposed propellant face was measured. The real time lag τ_i corresponding to this index was then calculated from the equation

$$\tau_i = \tau_i' - d/k \qquad (3)$$

where τ_i' is the measured time and k is the (pressure dependent) burning rate of the given propellant (*30*). Unfortunately d could be determined only to within an accuracy of about 20 μ, and the pressure was known only for the relatively short period of contact by the detonation head. Consequently the third term in Equation (3) was not known precisely. Since it turned out that under operating conditions $\tau_i << \tau_i'$, this criterion involved appreciable error. Moreover, there is some question whether τ_i may be considered as a true ignition index since true flame always appeared considerably later. However, it provides a means for detecting reaction in its early stages.

A relatively unambiguous definition of time lag is that based on the initial appearance of a stable flame τ_p. This time lag, designated τ_p, was determined by direct photography of the propellant face by use of either a streak or a Fastax camera. However, at p_1 values above 300 to 600 lb./sq.in. abs., depending on the igniter composition, the light from the detonation and recurring shock waves persisted a sufficient time to mask the initial appearance of the stable flame. Hence this method was applicable only at fairly low initial igniter pressures.

Equipment and Techniques

The results presented in this paper were obtained in three different heavy-walled, steel shot tubes all of 1-in. I.D. Initiation of the gas was effected in each case by the discharge of a 1-μf capacitor at 4,400 volts through a high-pressure (airplane) spark plug. Detonation and predetonation flame velocities were measured by means of the pin-oscillograph technique(*7*). Ionization gap pins were connected to separate capacitors charged to voltages of 250 to 1,700 volts (as desired). The capacitors were discharged in turn through the pin gaps by the highly conducting ionized wave front of the detonation or predetonation flame. This discharge was fed through suitable pulse-forming circuits to an oscilloscope, where it was recorded photographically as a "pip" on the calibrated sweep of an oscilloscope.

Shot tube I was 92 cm. long and was designed for pressures up to 30,000 lb./sq.in.abs. It contained ionization gap stages 50, 25, and 0 cm. ahead of the propellant to ascertain that a constant velocity was obtained at least 50 cm. before contact with the propellant. The propellant in this case was a smooth-surfaced 2.5-cm.-diam., 3-mm.-thick wafer and was mounted on the end of a plug that was threaded into the end of the tube opposite the point of initiation of the gas. Consequently the face of the wafer was perpendicular to the axis of the tube, and the detonation wave struck it broadside. Ignition was viewed in tube I through a plastic window sealed into the tube with O rings.

Shot tube I incurred difficulties associated with broadside collision of the detonation wave with the propellant, including excessive shock-wave interactions and complete interruption of the detonation wave. Despite these difficulties, results of threshold ignition measurement proved surprisingly reproducible, but the measurements of time lag were less satisfactory. Tube I served admirably in the preliminary evaluation of the detonating-gas-igniter method.

Shot tube II was designed to eliminate the undesirable features of shot tube I. It was a 1-in. I.D. tube 302 cm. long, capable of withstanding pressures up to 30,000 lb./sq.in.abs. The propellant was machined in the shape of truncated cones 7 mm. thick and 11 mm. in diameter at the apex. The propellant sample was forced into a conical hole in the side of the tube 107 cm. downstream from the igniter plug. In ignition threshold measurements the propellant face was allowed to crown out slightly into the bore as long as the edges of the pellet were not exposed. In measurements of τ_i the pellet face was machined flush with the tube walls by use of a spiral reamer. In either case the detonation wave could pass over the propellant without being appreciably disturbed, and consequently shock reflections back to the propellant occurred only later, at relatively long intervals. A 12.5-mm.-diam. window was located directly opposite the propellant pellet, allowing a direct view of the face of the propellant for photographing and manipulation. Also with tube II propellant wafers could be placed at one end of the tube just as in shot tube I, by means of which one could study the effect of the length of the column of igniting gas by comparison with results obtained in shot tube I.

In the measurement of τ_i' an ionization "pin" was located directly opposite the propellant to provide the time reference. The pellet pin, insulated except for a pointed end, was inserted through the plug holding the pellet in the tube wall into the back side of the pellet until the point was the desired distance d under the pellet face. Adjusting the circuitry permitted the pips from each pin to be identified by variation in the voltages on the pins.

Shot tube III was designed for pressure up to 5,000 lb./sq.in.abs. primarily to study conditions required for the development of a steady state detonation head. It was 1.83 meters long and contained twenty-seven ionization gap stages, each of which could be interchanged with the igniter plug to enable one to ignite the gas at any desired position in the tube. Eighteen of these stages were spaced at 10-cm. intervals, and the remaining nine at 1-cm. intervals (spiraled around the tube) between the second and third 10-cm.-interval ionization-gap stages. Variable pip amplitudes were again used to enable one reliably to identify each pip with its respective ionization gap. This arrangement made possible the determination of the length L' between the points of ignition and creation of the detonation wave and the variation of L' with p_1 and composition. It also made possible the determination of the velocity of the flame front and its variation with distance L (the total length of flame propagation from point of igniter gas ignition) in both the predetonation and detonation stages.

Pressures and total end impulse or momentum were measured by use of a dynamic condenser-type pressure gauge having a flat response between 0 and 10 kc., a resonant frequency of about 20 kc., and a 100% rise time of less than 50 μsec. It was located in the end of the tube opposite the igniter plug and thus received the full impact of the detonation head. The output of the pressure gauge was coupled to the vertical input of an oscilloscope, and the resulting sweep recorded a pressure-time curve.

The initial temperature of the igniter gas systems varied less than 15C.° in determination of p_1° for any particular propellant. Variations in the initial temperature of this magnitude have very little effect on the actual detonation conditions(*26*). Moreover, variation in the ambient temperatures seemed to have very little effect on ignition if held within this limit. The gases were used as received from the suppliers without further purification but were of about 99.5% purity.

Four homogeneous double-base rocket propellants, designated for security reasons as propellants *A*, *B*, C, and *D*, were studied. Each propellant

had about 50% nitrocellulose, approximately 30 to 40% nitroglycerine, and varying percentages of the usual plasticizers, stabilizers, and other additives. The propellant *C* had the highest nitroglycerine, and propellant *D* had slightly more nitroglycerine than *A* and *B*, which had equal amounts. Because propellant ignition seems to be dependent somewhat on the physical characteristics of the propellant, such as size, shape, and degree of roughness of the exposed surface, each of these factors was held constant in any particular series.

Composition of the igniter system was determined by the partial pressures admitting the gases into the mixing tubes separately. The gases were allowed to mix usually 10 min. or more in a mixing tank. All the shot tubes were thoroughly dried with an air nozzle, brushed with a wire brush, and then blown out with dry air after each shot. After evacuation of the shot tube the mixed gases were introduced from the mixing tank into the tube and allowed to remain there for 2 min. before firing.

Thermohydrodynamic Calculations

By means of the thermohydrodynamic theory of detonation (*19, 26, 15*) the thermodynamic properties and the chemical composition at the Chapman-Jonguet plane were calculated for each of the igniter systems used. Calculations were made for each composition at three fugacities, corresponding approximately to the initial pressure p_1 of 1, 10, and 100 atm. Any desired thermohydrodynamic values in the range of 1 to 100 atm. could then be obtained very accurately by interpolation through Equation (2). These calculations are too extensive for presentation completely in this report but are available upon request. Some of the most important results for the H_2-O_2 system are given in Figure 1.

EXPERIMENTAL RESULTS AND INTERPRETATIONS

Detonating Gas System

Figure 2 shows comparisons of measured and calculated detonation velocities for the H_2-O_2 and C_2H_2-O_2 systems. The agreement between calculated and observed velocities was in general satisfactory, except in the C_2H_2-O_2 system for C_2H_2/O_2 mole ratios greater than 0.90, where the calculated velocities were higher than experimental. The experimental values agreed fairly well with those obtained by Breton (*26*) and Kistiakowsky and coworkers (*21, 23*). The discrepancy for high C_2H_2/O_2 ratios is attributed to failure to take into account all the important products of detonation. This problem has been discussed adequately by Kistiakowsky, et al., who computed detonation velocities in fair agreement with experiment for acetylene-rich C_2H_2-O_2 systems by making some further assumptions as to the detonation products and the mechanism of the reaction.

TABLE 1.—DISTANCE L' FROM IGNITER TO POINT OF DETONATION FORMATION FOR THE H_2–O_2–A IGNITER

Igniter composition (H_2-O_2-A) (Parts by volume)	p_1, lb./sq. in. abs. 12.5	25	50	75	100	150
1 3-0	—	127	121	112	107	101
1-2-0	75	65	56	—	52	45
1-1-0	—	40	29	27	20	20
2-1-0	31	20	13	16	15	10
3-1-0	42	23	22	15	17	12
4-1-0	64	58	48	41	39	37
6-1-0	—	116	112	94	108	99
2-1-½	25	15	17	—	—	15
2-1-1	24					

The L' vs. p_1 and composition results for the H_2-O_2 and a portion of the H_2-O_2-A system are shown in Table 1.

L' was determined with tube III from measurements of the average velocity of the flame front between

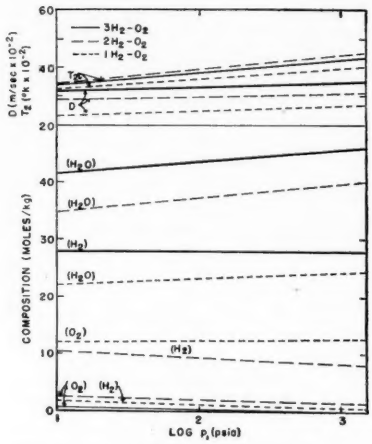

Fig. 1. Variations of theoretical detonation composition, temperature T_2 and velocity D with initial pressure p_1 and initial composition for the H_2-O_2 igniter system.

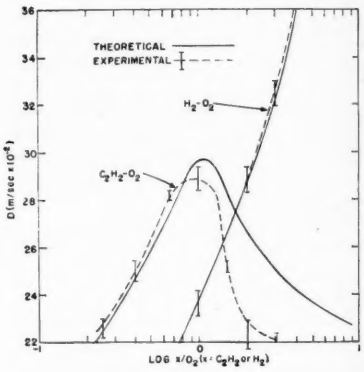

Fig. 2. Variations of theoretical and experimental detonation velocity with initial composition for the igniters C_2H_2-O_2 ($p_1 = 2$ atm.) and H_2-O_2 ($p_1 = 1$ atm.).

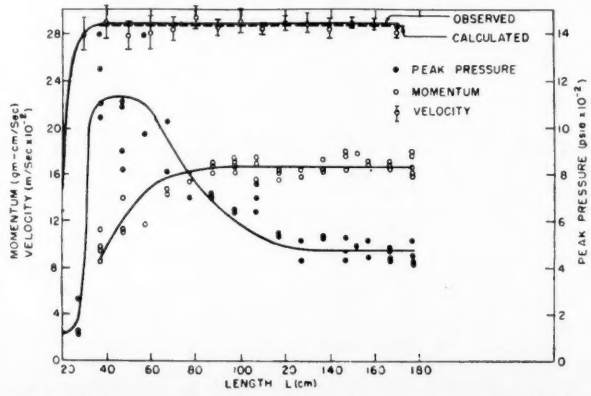

Fig. 3. Momentum, velocity, and peak pressure vs. length for the system $2H_2$-O_2 at 12.5 lb./sq. in. abs. (tube III).

ionization-gap stations. The data given are subject to a possible error of about ± 2 to 10 cm., being greater for large values of L'. L', like the thermohydrodynamic variable mentioned above, seemed to show a linear relationship with log p_1. As was expected, the most energetic compositions in the region of $2H_2$-O_2 (2-1) (compositions being expressed throughout in parts by volume) showed the minimum value of L', although 3-1 and 1-1 exhibited only slightly larger values of L'.

Velocity-distance (D-L), peak-pressure–distance (p-L), and end-impulse - or - momentum–distance (M-L) relations obtained in shot tube III with $2H_2$-O_2 are shown in Figure 3.* It will be observed that steady state momentum was established at about 80 cm. from the point of ignition of the gases, although 120 cm. of propagation was required for the attainment of a steady state peak pressure. L' was about 30 cm.

As mentioned, solid explosives show a steady state detonation head of constant size and momentum for $L_m > 3.5d$. Also L_m is dependent primarily only on the geometry of the charge and not on the initial density and composition. The momentum vs. L results for the mixture $H_2/O_2 = 2$ given in Figure 3 show that a steady state detonation head is also established in gaseous detonations in this case for $L_m \sim 50$ cm. Studies are in progress for the other systems but are as yet incomplete. It is expected that they will confirm the suggestion of the detonation-head model that L_m should be relatively insensitive to composition and density. In such a case steady state detonation should have been attained at the position of the propellant in both tubes I and II for all H_2-O_2 compositions in the range $1 < H_2/O_2 < 4$. In all cases L' was less than 42 cm. for these igniters. These conclusions seem to be substantiated by curves (2) and (3) (Figure 8), which are comparisons of plots of $p_1°$ vs. H_2/O_2 data obtained in shot tubes I and II. (*See* below.)

For the C_2H_2-O igniter systems (Figure 2) detonation occurred after a flame propagation of less than 42 cm. ($L' < 42$ cm.) for all compositions in the range $0.2 < C_2H_2/O_2 < 1.5$. The upper limit, however, is somewhat uncertain owing to the formation of excessive free carbon in this range which caused erratic behavior of the pin-oscillograph equipment. Detonation should thus have been steady in this system at the position of the propellant in both shot tubes.

Although not a great deal is known concerning the limits of detonation of the H_2-O_2-N_2 and the H_2-O_2-A igniter systems, it appears unlikely that steady state detonation was established in shot tube I for the 2-3-X (N_2 or A) systems, although steady state detonation was probably developed in the 4-1-X (N_2 or A) systems for small values of X. With the 2-1-X (N_2 or A) igniters the steady state occurred possibly for X as high as 40%.

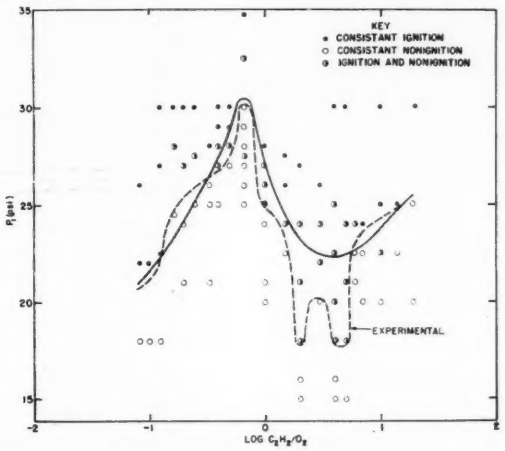

Fig. 4. Threshold ignition pressures $p_1°$ vs. igniter composition for propellant A in shot tube I.

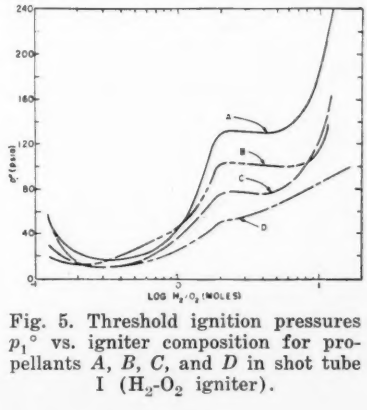

Fig. 5. Threshold ignition pressures $p_1°$ vs. igniter composition for propellants A, B, C, and D in shot tube I (H_2-O_2 igniter).

*Experimental velocities of 2,819 and 2,821 meters/sec. were obtained by Lewis (*25*) and Bone (*3*) respectively.

Ignition-threshold Pressures

Figure 4 is a plot of the logarithm of the mole ratio C_2H_2/O_2 vs. $p_1°$ for propellant A. The broken line gives the ignition-threshold curve as a function of composition. However, it is doubtful that the results were sufficiently consistent to justify the detailed broken curve; the solid curve is considered to be the best smooth curve through the observed data. The threshold pressure curve showed a maximum for the 2-3 (C_2H_2-O_2) igniter and decreased sharply on both sides. Powdered carbon was found in minute quantities with the igniter 1-1 (C_2H_2-O_2); it increased rapidly to copious amounts as the proportion of the acetylene in the igniter was increased. These results show that both oxygen and solid carbon are effective in enhancing ignition of propellants.

The $p_1°$-vs.-composition curves for the propellants A, B, C, and D, achieved by means of H_2-O_2 igniters, given in Figure 5 were obtained from 300 tests at eight different H_2/O_2 ratios between 0.125 and 12.0. The data were too extensive for each point to be shown, but they were quite consistent, and the curves may thus be considered as a reliable representation of the experimental data. They show in general large $p_1°$ values for the hydrogen-rich igniter and quite small $p_1°$ values for the oxygen-rich igniters. While all propellants showed marked sensitivity to excess oxygen in the products of detonation, propellant A appeared somewhat more sensitive to oxygen than propellant D. From Table 1 and Figure 5 it may be seen that detonation was produced in shot tube I only in the igniter composition range H_2/O_2 from 0.4 to 5.0, and the failure of $p_1°$ to increase sharply with H_2/O_2 from 5 to 7, even though these igniters did not detonate, indicates that the deflagaration flame, although cooler and less intense than the detonation flame, is at least as effective as the detonating gases in igniting the propellant. With the extremely hydrogen-deficient and hydrogen-rich igniters the curves were very steep, except for propellant D at $H_2/O_2 = 12.0$. This steep rise may be due to the re-

duced temperature of the flames as the limits of inflammability were approached (*26*).

The ignition-threshold method used with igniters with little or no oxygen or solid carbon clearly differentiated the relative sensitivities of the propellants. On the oxygen-rich side the sensitivities differed very little, owing to the large oxygen effect. Hence the measurement of relative ignition sensitivity should be confined to a particular composition in which (O_2) is small or absent, for example, $2H_2$-O_2.

Ignition-threshold pressures of propellant *B* in shot tube I resulting from use of igniter systems 2-3-XN_2 and 4-1-XN_2 (H_2-O_2-N_2), 2-3-*X*A, 2-1-*X*A, and 4-1-*X*A, where XN_2 and *X*A refer to the mole ratio of nitrogen and argon in the igniter system, are summarized in Figures 6 and 7. The percentage of nitrogen and argon was varied from 0 to 70 mole %. It was thought that the initial decrease in $p_1°$ with N_2 might be associated with oxides of nitrogen and that therefore the substitution of argon for N_2 would change the shape of the curves considerably. Instead the comparable sets of curves proved to be surprisingly alike. It is possible that the reduced heat capacity of the argon systems produced approximately the same trend as oxides of nitrogen in the nitrogen systems. In nearly all cases the curves exhibited more than one minimum. The maximum percentage of nitrogen at which detonation was obtained in shot tube I is not known accurately but was limited to less than 40% as judged from the disappearance of the characteristic "ping" at this percentage of nitrogen. Hence the minima observed at about 50% may be associated with the change from detonation to deflagration and finally to simple quiescent burning. Incomplete studies of the ignition thresholds of propellants *A* and *C* were also made with the igniters $2H_2$-O_2-XN_2 and H_2-O_2-XN_2. They too exhibited the characteristic minima which seems to be associated with change in the burning mechanism.

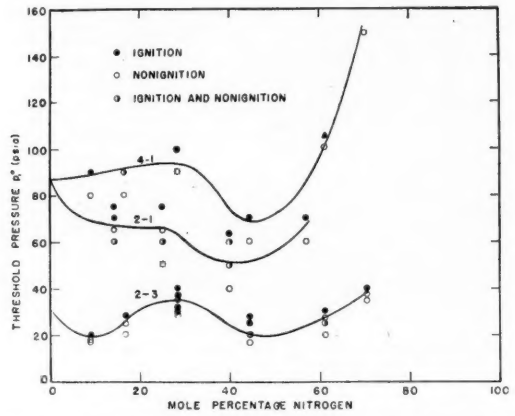

Fig. 6. Threshold ignition pressure $p_1°$ vs. percentage of nitrogen for propellant *B* at $H_2/O_2 = 4$, 2, and 0.67 (shot tube I).

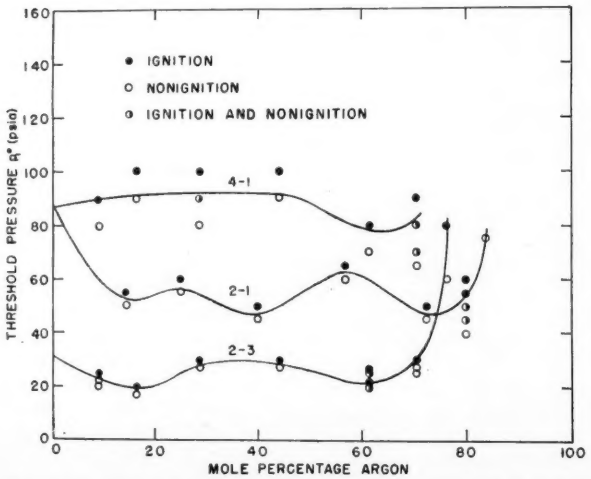

Fig. 7. Threshold ignition pressure $p_1°$ vs. percentage of argon for propellant *B* at $H_2/O_2 = 4$, 2, and 0.67 (shot tube I).

Figure 8 gives a comparison of $p_1°$-vs.-composition curves of propellant *C* obtained in shot tubes I and II with the H_2-O_2 igniter system. Curve (1) was obtained in tube. I. For this curve the gases were mixed in the tube for at least 10 min. Curve (2) was also drawn from data obtained in tube I, but the gases were premixed at least 30 min. in the mixing tank. The two curves agree fairly well except for a decrease in $p_1°$ for H_2/O_2 above 2. The data for curve (3) were obtained under exactly the same conditions as (2) but in shot tube II. It is believed that all compositions in the range $3.0 > H_2/O_2 > 1.0$ should have attained a steady detonation head at $L << 302$ cm. It may be noted that the curves are similar in shape but differ by a fairly constant value of about 60 to 70 lb./sq.in.abs., indicating that the same steady state detonation conditions existed in the 92-cm. tube as in the 302-cm. tube for this system. These results illustrate the importance of recurrent shocks in shot tube I. Data for curve (4) were also obtained in tube II, but in this case the propellant pellet was placed in the side of the tube 107 cm. from the point of igniter ignition. Here $p_1°$ for $H_2/O_2 = 2$ was about double that of curve (3), where the propellant wafer was at the end of the tube and interrupted the detonation wave directly, but at $H_2/O_2 = 1$ for glancing incidence $p_1°$ was much less than was obtained for broadside collision with the detonation wave.

The most significant result of the ignition threshold studies with H_2-O_2 mixtures is the marked influence of oxygen on threshold pressure $p_1°$.

Figure 9 shows plots of all the pertinent (calculated) detonation properties at the threshold pressure $p_1°$ against the H_2/O_2 ratio together with the experimental $p_1°$-vs.-H_2/O_2 plot itself. This figure brings out clearly this oxygen effect. (O_2) refers to the concentration of free uncombined oxygen, in

mole per cent, in the detonation head.) The threshold pressure was eight times greater for the maximum temperature composition $2H_2$-O_2 than for one of 20% lower temperature but about ten times higher $(O_2)+(O)$ content. Figure 10, in which the index $1/p_1°$ (instead of $p_1°$) is plotted against C_2H_2/O_2, shows in a striking manner the influence of (O_2) and (c_s), concentrations which considerably outweighed even the temperature involved. (It is $1/p_1°$, not $p_1°$ which should parallel relative ignition sensitivity.)

Ignition Time Lag

Table 2 gives values of τ_i' obtained with propellant *C* and various H_2-O_2 systems. Negative values of *d* denote results in which the pellet pin protruded completely through the propellant pellet face into the chamber of the tube. In these cases pips were observed on arrival of both the detonation wave and the first reflected shock, the time being sufficient for the pins to recharge. Even though the pellet pin was exposed directly to the gases in the tube, the ionization gap did not break down a second time until the first reflected shock wave crossed the pellet face. The recurrent shock did not cause breakdown of the pellet gap when the pellet pin was not exposed, i.e., for a pin still buried in the pellet. It was possible to ascertain this from the fact that the pip furnished by the pellet gap was much larger than that from the reference pin. Also at $d \geqslant 75, \geqslant 10$, and $\geqslant 10$ μ, respectively, for the igniters 1-1, 1-2, and 1-4, the first shock failed to cause pellet-pin breakdown, as shown by the τ_i' values obtained for these values of *d*.

From the data in Table 2, with p_2 as the upper limit of *p* during reaction and the known burning-rate law of propellant *C*, the upper

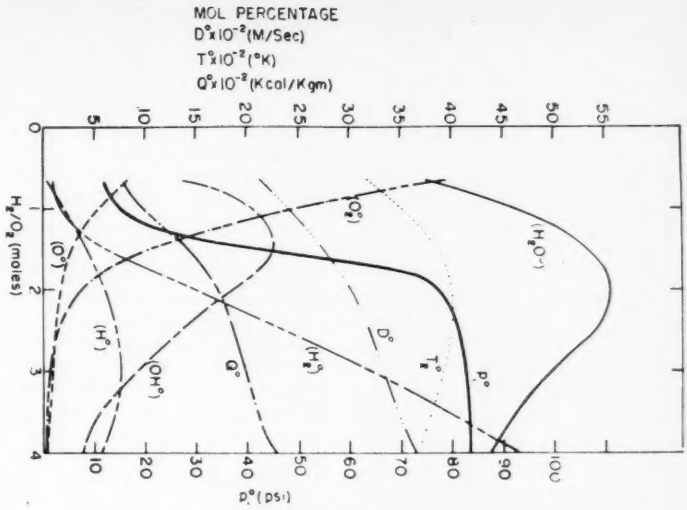

Fig. 9. Comparison of threshold detonation conditions ($D°$, $T_2°$, $O_2°$, etc.) for propellant *C*.

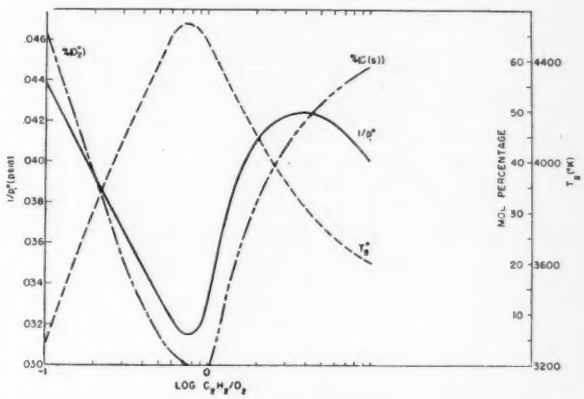

Fig. 10. Comparison of threshold detonation conditions ($T_2°$), ($O_2°$), and ($C_s°$) with $1/p_1°$ for propellant *A*.

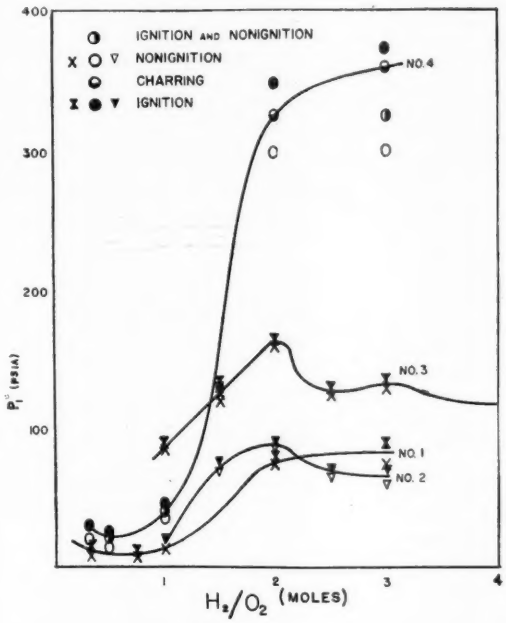

Fig. 8. Comparison of threshold pressures in shot tube I (curves 1 and 2) and shot tube II (curves 3 and 4) for propellant *C* (H_2-O_2 system).

TABLE 2.—DATA ON τ_i' FOR PROPELLANT *C* WITH THE H_2–O_2 IGNITER AT 300 LB./SQ. IN. INITIAL PRESSURE

H_2–O_2		H_2–2 O_2		H_2–4 O_2	
d, μ	τ_i', msec.	*d*, μ	τ_i', msec.	*d*, μ	τ_i', msec
750	59.40	10	4.65	95	13.27
400	18.20	0	2.52	90	16.40
200	8.80	0	2.52	60	3.98
85	6.25	0	2.50	50	4.11
75	6.80	−5	2.50	10	5.03
50	2.02			0	2.70
30	2.11			−40	2.70
10	2.13				
10	2.05				
0	2.13				
−30	2.11				

limit of τ_i' was computed to be 1.1 msec. Since the pressure was much lower than p_2, τ_i must have been much less than 1.1 msec. Similarly, τ_i was much less than 2.5 msec. for propellant *C* when the 1-2 and 1-4 igniters were used.

The meager data obtained so far for τ_p are given in Table 3. They indicate that the true ignition time lag is directly dependent on the initial pressure and inversely dependent on the percentage of oxygen in the igniter; i.e., τ_p varied linearly with the mole ratio H_2/O_2, extrapolating to 260 msec. for τ_p at $H_2/O_2 = 2.0$. As expected, τ_p was much larger (seventeen times as large for the igniter 2-1) for glancing than for broadside collisions of the detonation wave with the propellant.

From tables 2 and 3 and observed τ_i and τ_p data it appears that (1) reaction is initiated within about 1 msec. and possibly within a few microseconds if not immediately after the detonation front strikes the propellant, (2) the time to start the initial reaction apparently is highly temperature dependent and not appreciably dependent on the chemical effects, (3) stable ignition occurs several milliseconds later, and (4) stable burning is initiated more rapidly in the presence of oxygen. Presumably (4) would be true also of solid carbon but no measurements of time lag have yet been made to determine this. In normal burning of propellants three stages of reaction have been observed, namely foam, fizz, and flame(*30*). The ordinarily slightly exothermic (or perhaps even endothermic) foam stage consists of partial decomposition of the large polymers in the propellant to large molecules which remain on the surface. The fizz stage consists evidently of the initial formation of gaseous products. This stage is exothermic nearly to the extent of the very hot flame stage, where the propellant reactions go to completion. Application of this burning theory to the time-lag results indicates that the foam stage may occur within a very few microseconds after the very intensive energy source, the detonation head, is applied and that τ_i may measure a stage in the initial formation of the fizz zone. In the formation of the foam zone one requires a strong supply of heat. The reaction becomes strongly exothermic only after the fizz zone has developed sufficiently. Apparently collision of the detonation head with the propellant produces the foam zone and early stages of the fizz zone. Only after a time τ_i has the fizz zone developed sufficiently to produce enough ions for discharge of the pins of the pin oscillograph. During this stage thermal effects are much more pronounced than the chemical effects discussed in this report. This is in accord with the observation that τ_i increases with the oxygen content (or more fundamentally with decreased temperature) for H_2-O_2 igniter systems of positive oxygen balance.

Chemical effects on ignition are limited to the fizz zone and possible even to the later stages of development of this zone. This would account for the strong inverse oxygen dependance of true flame ignition time lag τ_p. It would also account for the decreasing threshold pressures found for igniters with increasing oxygen content, since the magnitude of exothermicity in the fizz zone would increase sharply with increased oxygen in this zone. Further evidence for this mechanism was found in observing the character of the propellant following ignition failure at p_1 values below $p_1°$; partial burning was observed to have occurred for the oxygen-deficient igniter systems but never for the oxygen-rich ones, where the propellant was either completely burned or showed no evidence of reaction.

TABLE 3.—DATA ON τ_p, THE IGNITION TIME LAG AS BASED ON A STABLE FLAME OF PROPELLANT *C*, SHOT TUBE I USED WITH THE DETONATION WAVE INTERRUPTED AND SHOT TUBE II USED WITH THE PROPELLANT NONINTERRUPTING

Shot Tube I, $2H_2$–O_2 Igniter		Shot Tube II, H_2–O_2 Igniter at $p_1 = 300$	
p_1, lb./sq. in. abs.	τ_p, msec.	Igniter H_2–O_2, parts by vol.	τ_p, msec.
90	170	1–1	140
150	100	3–2	200
150	84	7–4	225
150	66	7–4	230
300	15		
450	12*		
600	8*		

*Possibly less than given owing to masking of propellant ignition by the detonation shock waves.

ACKNOWLEDGMENT

Appreciation is expressed to A. S. Filler and W. N. Bryan for assistance in the calculations and some of the experimental work in this paper.

NOTATION

p_1 = initial pressure of the detonating gas igniter
T_1 = initial (ambient) temperature of the ignition system
p_2 = detonation pressure (hydrodynamic theory)
T_2 = detonation temperature
D = detonation velocity
Q_2 = heat of explosion
n = number of moles per kilogram of the products of detonation
p = peak pressure measured at the end of the shot tube (approximately twice p_2)
L = length
M = momentum or end impulse
L_m = length of propagation of detonation necessary to establish a staeady state detonation
L' = length of propagation from the point of initiation to the point of formation of detonation
$p_1°$ = minimum or threshold (initial) pressure for ignition of the propellant
τ_i = time lag of initial propellant decomposition
τ_p = time lag of stable propellant ignition
d = thickness of propellant between pellet ionization pin and surface of propellant pellet
k = burning rate of propellant
$\psi_i°$ = ignition threshold value of the variable ψ_i where ψ_i may be (O_2), D_2, Q_2, T_2, and other detonation functions
( ) indicates that the chemical species enclosed in the brackets was a product of detonation for conditions in the wave front computed thermohydrodynamically.

LITERATURE CITED

1. Avery, W. H., *J. Phys. & Coll. Chem.*, 54, 917 (1950).
2. Berthelot, D., and H. Gaudechon, *Compt. rend.*, 153, 1220 (1911).
3. Bone, W. A., and D. T. A. Townend, "Flames and Combustion in Gases," p. 163, Longmans, Greene and Co., London and New York (1927).
4. Brian, R. C., and C. A. McDowell, *Trans, Faraday Soc.*, 197, 212 (1949).
5. Chase, C. T., W. H. Smith, Rept. F 2338, Contract DA-36-034-ORD-1105 RD, Franklin Institute, Philadelphia (Oct. 31, 1953).
6. Cook, M. A., *J. Chem. Phys.*, 16, 1081 (1948).

7. Cook, M. A., and F. A. Olson, Tech. Rept. IV, Contract N-123S-80062, Task Order I, Explosives Research Group, Utah University, Salt Lake City (Sept. 15, 1954).
8. Cook, M. A., G. S. Horsley, W. S. Partridge, and W. O. Ursenbach, *J. Chem. Phys.* (to be published).
9. Cook, M. A., and R. T. Keyes, *J. Chem. Phys.* (to be published).
10. Cook, M. A., E. B. Mayfield, and W. S. Partridge, *J. Phys. Chem.* (in press).
11. Cook, M. A., *J. Phys. Chem.* (in press).
12. Crawford, B. L., C. Huggett, and J. J. McBrady, *J. Phys. & Coll. Chem.*, **54**, 854 (1950).
13. Crawford, B. L., and R. G. Parr, *Univ. Minnesota Inst. Technol., Rept.*, **20** (Oct. 10, 1944).
14. Dixon, H. B., *J. Chem. Soc.*, **97**, 662 (1910).
15. Eyring, H., R. E. Powell, G. H. Duffy, and R. B. Parlin, *Chem. Revs.*, **45**, 69 (1948).
16. Gibson, R. E., *J. Phys. & Coll. Chem.*, **54**, 847 (1950).
17. Gordon, W. E., "Third Symposium on Combustion Flame and Explosion Phenomena," p. 579, Williams and Wilkins Co., Baltimore (1949).
18. Jones, E. *Proc. Roy. Soc.* (*London*), **A198**, 523-39 (1949).
19. Jost, W., and H. O. Croft, "Explosion and Combustion Processes in Gases," Chap. V, McGraw-Hill Book Company, Inc. (New York and London) (1946).
20. Kent, R. H., Aberdeen Proving Ground, BRL No. 9 (May, 1935).
21. Kistiakowsky, G. B., H. T. Knight, and M. E. Malin, *J. Chem. Phys.*, **20**, 884 (1952).
22. ———, and P. H. Kydd, *J. Chem. Phys.*, **23**, 271 (1955).
23. ———, and W. G. Zinan, Second ONR Symposium on Detonation, p. 80, Office of Naval Research, Washington, D. C. (February, 1955).
24. Klein, R., M. Menster, G. von Elbe, and B. Lewis, *J. Phys. & Coll. Chem.*, **54**, 877 (1950).
25. Lewis, B., and J. B. Friauf, *J. Am. Chem. Soc.*, **52**, 3905 (1930).
26. Lewis, B., and G. von Elbe, "Combustion Flames and Explosion of Gases," Chap. XI, Academic Press, Inc., New York (1951).
27. Univ. Michigan, Report No. 1 (1951).
28. Naval Ordnance Laboratory, NOLM 10808, White Oak, Md. (July, 1950).
29. Penner, S. S., *J. App. Phys.*, **19**, 278, 392 and 511 (1948).
30. Rice, O. K., and R. Ginnell, *J. Phys. & Coll. Chem.*, **54**, 885 (1950).
31. Rinehart, J. S., and J. Pearson, "Behavior of Metals Under Impulsive Loads," p. 49, American Society for Metals, Cleveland (1954).
32. Wilfong, R. E., S. S. Penner, and F. Daniels, *J. Phys. & Coll. Chem.*, **54**, 863 (1950).

APPENDIX

The detonation-head model was proposed initially in 1943 in classified reports by one of the authors to account for the observations pertaining to shaped charges with solid explosives. More recently it has been applied to explain various other observations, important among which are velocity-diameter curves (*8* to *11*). It is entirely phenomenalistic in character and, though lacking a fundamental basis, it has proved highly successful as an empirical model for correlating observations, developing new experimental approaches, and solving problems in the design of devices. An important reason for presenting it here is that in reality it is the only model yet available to handle many of the important problems in the technology of detonating explosives. Moreover experience has shown that it provides an intuitive picture of detonation which may be relied upon in predictions of the influence of various geometrical factors, including conditions required for the development of steady state detonations. Here briefly outlined are some of the experimental observations considered most pertinent to the development of the detonation-head model and its essential features.

The total end effect (i.e., the impulse and kinetic energy generated at the end of the charge) applicable, for example, in the formation of jets from shaped charges is adequately described by the following semi-empirical equations:

$$I = F(L)\frac{\pi}{9}\rho_1 (d')^3 W = F(L)\,\pi\,(d')\,p_2/D \qquad \text{(i)}$$

$$T = F(L)\,\pi\,(d')^3\,p_2/12 \qquad \text{(ii)}$$

$$F(L) = 1 - \left(1 - \frac{L}{3.5\,d'}\right)^3;\ \text{for } L < L_m = 1;\ \text{for } L \geqslant L_m \qquad \text{(iii)}$$

where I is the end impulse or momentum, T the effective kinetic energy, ρ_1 the charge density, d' the effective diameter (or $d' = (d - d_e)$ where d_e, a constant edge effect shown equal to about 0.6 cm. in most solid explosives, is the actual charge diameter), W is the particle velocity calculated for conditions at the Chapman-Jouguet plane, p_2 is the "detonation" pressure, and L is the charge length.

Equation (i) to (iii) express the following facts:

1. End effect as measured, for example, by the total hole volume and/or depth of penetration in a homogeneous target of the jet from a shaped charge liner of total mass approximately M increases with charge length, as shown by Equation (ii). That is, end effect increases in proportion to the height of hypothetical truncated cones of constant base diameter d and a height proportional to $L/3.5\ d'$ reaching a maximum (corresponding to a fully developed detonation-head cone) at about 3.5 charge diameters. For L greater than $3.5\ d$ the penetration is independent of L.

2. The end impulse varies as the product $\rho_1\ W$ of the explosive, other factors being constant.

3. The total end effect varies as the cube of the effective diameter with other factors constant.

4. Finally, the optimum liner mass for a liner of any angle, shape, and composition is that given approximately by the equation

$$M = F(L)\frac{\pi}{9}\rho_1 (d')^3 \qquad \text{(iv)}$$

That is, the liner should have the same mass as the detonation head.

Equations (i) to (iv) suggest that there exists behind the wave front a detonation head which when fully developed has a mass given approximately by Equation (iv) and a shape resembling approximately a cone of mixmum height d'. Before it is completely developed, the detonation head appears to resemble truncated cones of height $h = d'(L/3.5d')$ and base diameter d'. The outline of this cone,

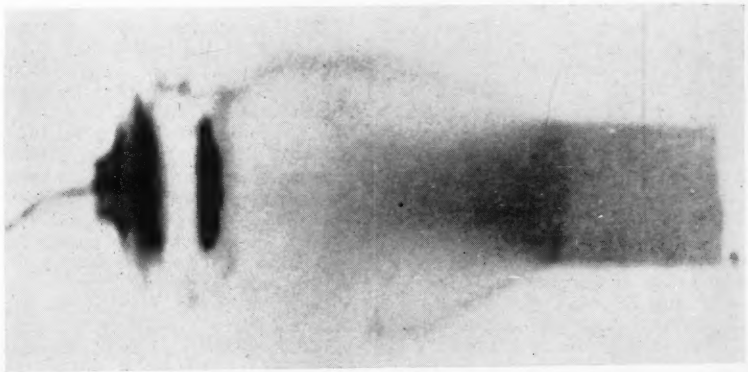

Fig. i. Flash radiograph of unconfined solid explosive charge (square rather than circular in cross section) showing curved front and "triangular region."

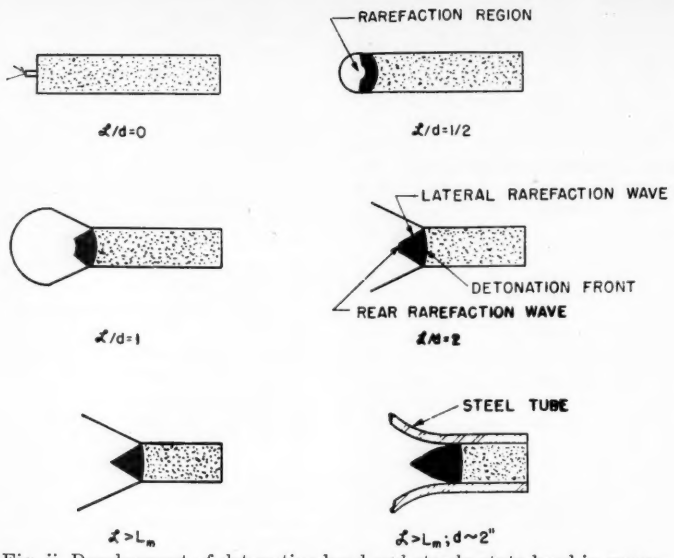

Fig. ii. Development of detonation head and steady state head in unconfined and confined solid explosive charges.

although not yet completely developed, may be seen vaguely in the flash radiograph of a square cross-sectional charge kindly furnished by Ballistics Research Laboratory, Aberdeen, Maryland, shown in Figure i. A charge of square cross section was used in order to eliminate all variations in X-ray density not associated directly with initial compression as the gases entered the detonation head and with expansion as they left the detonation-head region. This theory is described very briefly, in terms of the essentially equivalent release wave theory of Pugh and associates, by Rinehart and Pearson (*31*).

The detonation-head model proposed to account for these results simply assumes that for many purposes the high-density conical region, sometimes called the "triangular region," in the front of a detonation wave may be regarded as a slug of gas of fairly uniform density and pressure. This region is largely uninfluenced inside its boundaries by rarefactions that move in toward the center from the side of the charge. The fronts of these rarefactions form the boundaries of the detonation head, except for the front boundary, which is the detonation front. According to this model, following initiation of a detonation wave at least the main part of the rarefaction wave moving forward from the rear is assumed to lag somewhat behind and moves at a lower velocity than the wave front. Between the wave front and the front of the main part of the rarefaction region (which is assumed to appear near the stagnation plane, i.e., the region behind the shock front where the particle velocity has finally reached zero), the wave is considered to be approximately a constant density region. For unconfined charges rarefactions moving toward the charge axis from the sides of the charge also are assumed to move forward at speeds lower than the detonation velocity. Figure ii illustrates the apparent development of the head as a function of the charge length, first as a spherical expansion region and later as truncated cones (the base and top being spherical) when the rarefactions start in from the sides; finally, after L becomes equal to or greater than 3.5 d, the head is completely formed as a conical region. In order to account for the apparent shape of the detonation head in condensed explosives, one would assign a velocity of about 0.6 D for the front of the main portion of the rarefaction waves from the rear and sides.

One may take into account the hydrodynamic arguments that rarefactions should extend right up to the wave front and still retain the essential features of the detonation-head model by assuming, in accord with conventional hydrodynamics, density gradients (represented in Figure iii by a series of constant density contours equally spaced in density space), small in the region of the detonation head and becoming large only at the boundaries of the detonation head. It is important to realize that experimental evidence argues strongly against very large density gradients in the region designated as the detonation head. Likewise the gradient must be very steep at the boundary of the head (heavy solid line of Figure iii in order to produce the radiographic image. Inside these characteristic boundaries (the lateral rarefaction front or release wave front) rarefactions are thus considered relatively unimportant, but outside they are sufficiently important that momentum and energy cannot be contributed in the direction of propagation by material outside this detonation head. This model should not therefore be regarded as inconsistent with the hydrodynamic concepts that an isentropically spreading rarefaction wave should not have a discontinuous front and that limited rarefactions should extend right up to the wave front; but it merely emphasizes the relative unimportance of these effects within the conical region corresponding to the detonation head determined primarily by the release waves.

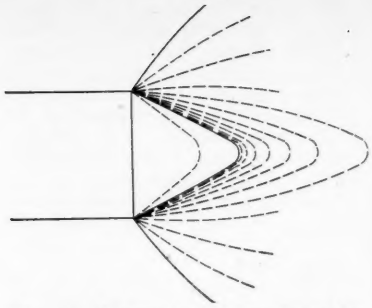

Fig. iii. Schematic representation by constant density contours of pressure gradient in detonation front. (Large distance between contours suggests small gradients, small distance large gradients.)

This concept has been applied only to a limited extent to gaseous detonations, and experimental evidence showing that it may be applicable to gases confined in heavy walled tubes is limited to the following two observations.

1. After detonation propagates a certain critical distance L_m, a steady state momentum is attained in gases just as with solids, except that in solids L_m is only about 3.5d, whereas in gases L_m is considerably larger.

2. Direct measurements of the density contours (*22*) of the detonation front in gases appear to show that the density is relatively constant for a distance of about one diameter after the wave has propagated about seven charge diameters from the point of creation of the detonation wave. Facts 1 and 2 are found consistent when one realizes that, owing to a much higher compression ratio, ρ_2/ρ_1, in gaseous than in condensed explosives, the stagnation plane should have a velocity in the neighborhood of 0.8D compartd with 0.6D in solids. The reason that the maximum effective length L_m is not infinite or not even excessively large in gaseous detonations in heavy walled tubing is simply that lateral rarefactions or lateral release waves still exist in such gaseous detonations. Instead of being associated with free expansion as in condensed explosives, these lateral release waves result from rapid quenching at the walls of the tube. The important fact shown in this article is that steady state heads are established in gases as well as in condensed explosives.

Presented at A.I.Ch.E. Louisville meeting

Estimation of Ternary Vapor-liquid Equilibrium

W. H. Severns, Jr., Alexander Sesonske, R. H. Perry, and R. L. Pigford
University of Delaware, Newark

Isothermal vapor-liquid equilibrium measurements were made at 50°C. for the ternary systems acetone-methanol-chloroform, acetone–methanol–carbon tetrachloride, and acetone–methanol–methyl acetate, by means of an improved vapor-recirculation type of apparatus. The complete range of concentrations was investigated, including six of the seven constituent binary systems. Chemical methods, supplemented by density and refractive-index measurements, were used for analysis.

Results are presented in the form of activity coefficients γ as a function of various concentrations. Binary and ternary constants for the three-suffix Margules equations were determined by plots of $(\log \gamma)/(1-x)^2$ as a function of the mole fraction x. Such equations have been found to represent both the binary and the ternary data adequately except in the system containing both methanol and carbon tetrachloride. For these mixtures a simplified four-suffix equation, including a single ternary constant, correlates binary and ternary equilibrium data.

The data indicate that reliable estimates of ternary equilibria can be based on the assumption that the ternary constant C^* is zero for mixtures in which all deviations from Raoult's Law are positive. This is interpreted as indicating that the probability of existence of trimolecular aggregates, two- or three-component, in ternary solutions is no greater than the average of probabilities of existence of trimolecular aggregates in the constituent binary systems.

Based on equations of the Margules type, a procedure is outlined for determining binary constants rapidly and for planning experiments whereby a ternary system may be completely investigated with the aid of very few measurements.

The composition changes that the accompany differential distillation of the three ternary mixtures are described qualitatively in terms of the shape of the vapor-pressure-composition surfaces.

In the design of azeotropic and extractive distillation equipment, reliable multicomponent vapor-liquid equilibria are necessary for the estimation of heat requirements and separation efficiencies. It would be most helpful to be able to predict equilibrium relationships from the properties of the pure compounds or, failing this, from a minimum of experimental data. Such information would be useful, for example, for the selection of a suitable third component to facilitate the separation of two close-boiling or azeotropic liquids by distillation. The use of empirical equations for extension or prediction of multicomponent vapor-liquid equilibria is useful for this purpose but is tedious even for the case of ternary mixtures.

A method for treating equilibria in ternary mixtures which would reduce the required experimentation and simplify the fitting of existing empirical equations to isothermal ternary data would appear to be of value. A method for predicting the constants in these empirical equations, preferably from the properties of the pure compounds or, alternatively, from data on the binary systems involved, would simplify calculations. Methods have been proposed for extending basic data and estimating values of constants in the equations for prediction of activity coefficients, but the literature does not presently contain sufficient thermodynamically reliable data to test these methods thoroughly. Experimental data have been published for several ternary and quarternary systems, but a complete test of equations for activity coefficients has usually not been possible because the whole range of compositions was not covered, because the experimental errors were too great, or because one of the pairs was ideal, leading to a degenerate case.

During this investigation isothermal data were determined for the systems acetone-methanol-chloroform, acetone-mtehanol–methyl acetate, and acetone-methanol–carbon tetrachloride at 50°C. The first system has both positive and negative deviations from Raoult's Law and none of its binary mixtures are ideal. The other two systems are of the type most frequently encountered: mixtures of organic liquids which exhibit only positive deviations from ideality. Again none of the binary mixtures are ideal. Wohl's Margules-type equations (*12* and *13*) were compared

W. H. Severns, Jr., is with E. I. duPont de Nemours and Company, Newport, Delaware; Alexander Sesonske is at Purdue University, Lafayette, Indiana; and R. H. Perry is with Shell Development Company, Emeryville, California.

with the data. A systematic approach to experimentation and techniques facilitating the use of the equations were developed.

MATHEMATICAL REPRESENTATION OF ACTIVITY COEFFICIENTS

The equation describing the distribution of a component, i, at equilibrium between liquid and vapor phases and defining its activity coefficient, γ_i, is

$$\pi\, y_i z_i = \gamma_i P_i x_i \qquad (1)$$

Generally either π or the temperature is fixed; P_i and z_i are characteristic of the pure component. The liquid-phase mole fraction, x_i, may be chosen arbitrarily, and the activity coefficient, γ_i, is related to it by solutions of the equations

$$\ln \gamma_i = (1/RT)\,(\partial/\partial n_i) \sum_1^j n_j G^E \qquad (2a)$$

$$\sum_1^j x_i\, d(\ln \gamma_i) = 0 \qquad (2b)$$

Equation (2b) indicates a simple test for thermodynamic consistency of isothermal vapor-liquid equilibrium data.

Carlson and Colburn(*2*) gave methods of extending and predicting binary vapor-liquid equilibria. They pointed out the utility of end values of log γ_i at infinite dilution of component i as constants in the development of empirical equations applicable to binary mixtures. Wohl(*12* and *13*) presented a series of equations of varying complexity to describe activity coefficients as functions of concentration in binary, ternary, and quarternary mixtures using as constants the end values of log γ_i for the component binary pairs. The simplest of Wohl's equations to fit a wide variety of binary mixtures is the three-suffix Margules type expressed in mole fractions. In this case the excess free energy of mixing is assumed to be given by

$$G^E/2.3\,RT = x_1 x_2\,(A_{21}\,x_1 + A_{12}\,x_2)$$

$$A_{12} = \lim_{x_1 \to 0} (\log_{10} \gamma_1) \qquad (3)$$

From Equation (3), by application of Equation (2), the equations for logarithms of activity coefficients are

$$\log_{10} \gamma_1 = x_2^2 [A_{12} + 2\,(A_{21} - A_{12})\,x_1] \qquad (4)$$

$$\log_{10} \gamma_2 = x_1^2 [A_{21} + 2\,(A_{12} - A_{21})\,x_2] \qquad (5)$$

These equations fitted each of the binary systems investigated in this study with the exception of mixtures of methanol and carbon tetrachloride, in which the deviations from ideal behavior were extremely large. The function (log γ)/(1-x)^2, hereafter called J, was used for evaluation of the data. From Equations (4) and (5)

$$J_1 = A_{12} + 2\,(A_{21} - A_{12})\,x_1 \qquad (6)$$

$$J_2 = A_{21} + 2\,(A_{12} - A_{21})\,x_2 \qquad (7)$$

At $x_1 = 0$, $J_1 = A_{12}$; at $x_2 = 0$, $J_2 = A_{21}$. Similarly, at $x_1 = 0.5$, $J_1 = A_{21}$ and $J_2 = A_{12}$. J is a linear function of x. The linearity of this function for binary systems described by Margules-type equations is also noted elsewhere(*8*).

In Equation (1) the quantities π, z_i, P_i, and temperature may be measured or calculated accurately. J is very sensitive to errors in measurement of concentrations and consequently is a good function with which to check adequacy of equilibrium experiments and accuracy of analyses. However, in the region $0.5 < x_i < 1.0$, J becomes very erratic even for good data. The most significant values of J_i are those observed in the region $0 < x_i < 0.5$.

For more complex binary mixtures, particularly those involving very large deviations from ideality, the four-suffix Margules binary equation of Wohl(*12*) may be useful. These equations, when plotted as J vs. x, result in curved lines, as for carbon-tetrachloride-methanol, as shoyn in Figures 19 and 20.

In Wohl's nomenclature, recently revised(*13*), the three-suffix Margules ternary equation, written in mole fractions, is derived from

$$G^E/2.3\,RT = x_1 x_2\,(x_1 A_{21} + x_2 A_{12}) + x_1 x_3\,(x_1 A_{31} + x_3 A_{13}) + x_2 x_3\,(x_2 A_{32} + x_3 A_{23}) + x_1 x_2 x_3\,[\tfrac{1}{2}\,(A_{12} + A_{21} + A_{13} + A_{31} + A_{23} + A_{32}) - C^*] \qquad (8)$$

In this new method of representation Wohl has used a new ternary constant, C^*, that is independent of the numbering of components. It is related to the older definition of C(*12*) by the equation

$$C^* - C = \tfrac{1}{2}\,(A_{12} - A_{21} + A_{23} - A_{32} + A_{31} - A_{13}) \qquad (8a)$$

By use of Equation (2), it follows that

$$\log_{10}\gamma_1 = x_2^2[A_{12} + 2x_1\,(A_{21} - A_{12})] + x_3^2[A_{13} + 2x_1\,(A_{31} - A_{13})] + x_2 x_3\,[\tfrac{1}{2}\,(A_{21} + A_{12} + A_{31} + A_{13} - A_{23} - A_{32}) + x_1\,(A_{21} - A_{12} + A_{31} - A_{13}) + (x_2 - x_3)\,(A_{23} - A_{32}) - (1 - 2x_1)\,C^*] \qquad (9)$$

Log γ_2 and log γ_3 may be determined from Equation (14) by cyclic permutation of subscripts according to the scheme

Let R_2 be defined as $x_2/(x_2 + x_3)$, the mole fraction of component 2 on a one-free basis; then J_1 may be expressed as

$$J_1 \equiv (\log_{10}\gamma_1)/(1 - x_1)^2 = R_2^2[A_{12} + 2x_1\,(A_{21} - A_{12})] + (1 - R_2)^2[A_{13} + 2x_1\,(A_{31} - A_{13})] + R_2\,(1 - R_2)\,[\tfrac{1}{2}\,(A_{21} + A_{12} + A_{31} + A_{13} - A_{23} - A_{32}) + x_1\,(A_{21} - A_{12} + A_{31} - A_{13}) + (1 - x_1)\,(2R_2 - 1)\,(A_{23} - A_{32}) - (1 - 2x_1)\,C^*] \qquad (10)$$

As in binary systems, J_1 is a linear function of x_1 for R_2 constant. At $R_2 = 1$, Equations (4) and (9) as well as (6) and (10) are equivalent and describe the activity coefficient of component 1 in binary mixtures with component 2. At $R_2 = 0$ the activity coefficient of component 1 in binary mixtures with component 3 is obtained.

Equations (8), (9), and (10) fit the data of the first two ternary systems investigated with sufficient accuracy that use of more complicated equations was not required. The experimental data for the third ternary system were also fitted satisfactorily but the slightly more complicated four-suffix equations of Wohl(*13*) showed a statistically significant improvement, owing to the fact that the binary system methanol–carbon tetrachloride required the use of the four-suffix binary equations.

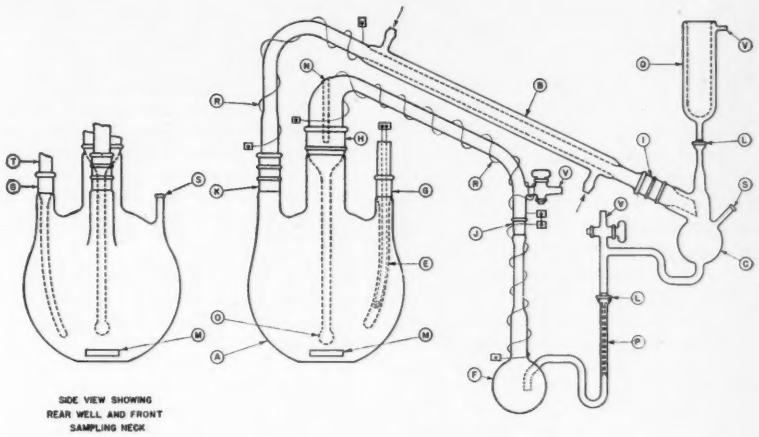

Fig. 2. Isothermal equilibrium apparatus.

PLANNING OF EXPERIMENTS

Use of J as a correlating function, as shown in Equations (6) and (7), suggests a procedure for taking ternary vapor-liquid equilibrium data which will reduce appreciably the number of experiments required to investigate a system adequately. All compositions at constant R lie on a straight line on a ternary diagram such as Figure 1. From Equation (9) the ternary constant contributes most to the value of log γ_i in the region $x_i \doteq 0$, $x_j \doteq x_k \doteq 0.5$. One such region is found in Figure 1 for each of three components; these are the regions in which experimental ternary measurements should be concentrated once the binary data are fully known.

Chemical analysis for the dilute component should be accurate if the J value is to be significant; analytical accuracy need not be so great for the other compounds, although greater accuracy is required if these other compounds have very different molecular weights. Ternary equilibrium determinations in each of the regions 1, 2, and 3 of Figure 1, plus data on the three binary systems, are sufficient to evaluate all the constants in the equations. In their most general form the four-suffix equations contain three different ternary constants; consequently, three independent ternary determinations are required. A single ternary determinmination may be sufficient, however, if the binary systems are satisfied by the simpler three-suffix equations; even when the more involved equations are needed, the three C^* values may often be equal.

For rapid comparison of data with calculated J values based on Equation (10), it is useful to know particular values of J_i at strategically chosen compositions. For example, at $x_1 = 0$ and $R_2 = \frac{1}{2}$, J_1 becomes

$$J_1 = \tfrac{1}{8}\left[3\,(A_{12} + A_{13}) + (A_{21} + A_{31}) - (A_{23} + A_{32}) - 2C^*\right] \quad (11)$$

for the three-suffix ternary Margules equation. The equivalent function for the other components are obtained by cyclic permutation of subscripts. Moreover, at $R_2 = \frac{1}{2}$, $x_1 = 0.5$, Equation (11) is altered to

$$J_1 = \tfrac{1}{4}\left[2\,(A_{21} + A_{31}) - \tfrac{1}{2}\,(A_{23} + A_{32})\right] \quad (12)$$

This latter equation does not include a term containing C^* and consequently the value of J is independent of C^* at $x = 0.5$. Thus it is clear that data taken at nearly equal mole fractions of the mole components give little information regarding ternary contributions to nonideality. Data plotted as J vs. x may be easily and sensitively checked for self-consistency and those taken at $R =$ constant rapidly compared with the three- and four-suffix Margules equations. By use of Equations (11) and (12) from those data taken with x dilute and $R \doteq \frac{1}{2}$, C^* may be accurately

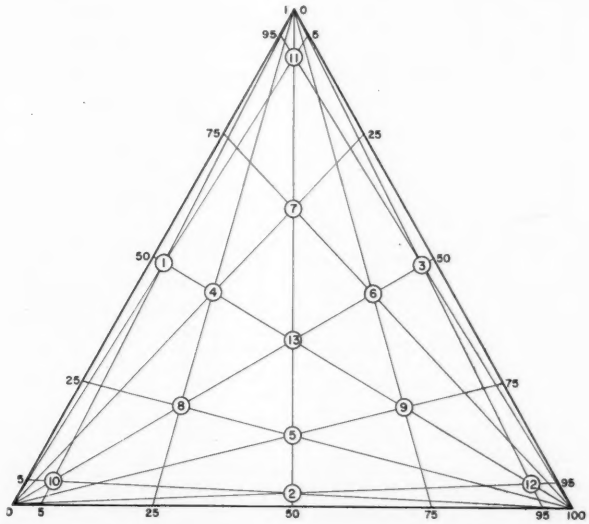

Fig. 1. Ternary compositions experimentally investigated for vapor-liquid equilibria.

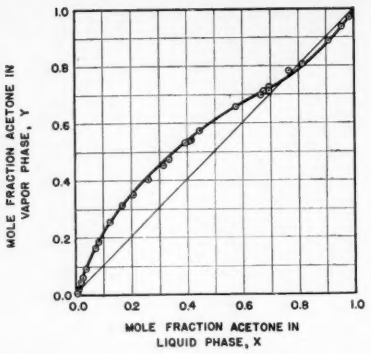

Fig. 3. Vapor-liquid equilibria for system acetone-methanol at 50°C.

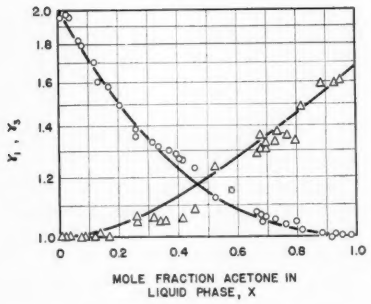

Fig. 4. Activity coefficients for binary system acetone-methanol at 50°C.

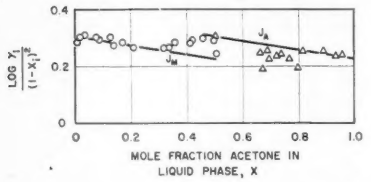

Fig. 5. Comparative plot of activity coefficients for acetone-methanol at 50°C. with three-suffix Margules equation.

and rapidly determined from the plot. Equations (11) and (12) give values of J calculated from ternary equations at the liquid-phase concentrations which are at the limits of the practical significance of the function. The J-plot procedure is equally applicable to three- and four-suffix equations of Wohl(*13*) in q or volume fractions. These modified equations, however, were not required to fit any of the systems investigated here.

EXPERIMENTAL PROCEDURE

A modification of the vapor-recirculation equilibrium still described by Jones, Schoenborn, and Colburn (*5*) was used for the equilibrium determinations. The present apparatus, shown in Figure 2, differs from the original model in two essentials. To provide better temperature control, the equilibrium chamber was surrounded by a water bath. Increasing the liquid-chamber volume to 3 liters increased the condensate volume and yet greatly reduced the condensate-to-liquid volume ratio. This permitted larger condensate samples to be taken for analysis and yet kept small the required time for attainment of equilibrium. In addition, several runs could be made at or very near the same composition with a given charge of components. The reprodicibility of successive samples provided an estimate of the accuracy of the experimental technique. Further, by starting with a binary charge and adding only the third component to change the composition between ternary determinations, successive experiments could be made at constant R.

A magnetic stirrer was used for agitation in the liquid chamber. This improved the rate of response to adjustments in total pressure. Both the liquid and condensate were sampled with a hypodermic syringe provided with a special long needle. The temperature of the liquid was compared with that of the water bath by means of a double-junction copper-constantan thermocouple. A small internal heater was useful for adjusting the vapor circulation rate to begin an experiment but was turned off after circulation had commenced. If the pressure became too high during operation, circulation promptly ceased; if the pressure was reduced below the equilibrium value, the circulation rate increased until the flash boiler flooded. The range of pressures over which steady circulation occurred was about 1 mm. Hg.

The pressure in the system was adjusted by introducing nitrogen into the condenser and was measured by means of a temperature-compensated mercury barometer. The temperature of the water bath was controlled and measured by standard apparatus.

For analysis of ternary mixtures, measurement of at least two independent properties is necessary. Chemical methods specific for acetone and methanol were supplemented by densities sensitive to the amount of chloroform, methyl acetate, or carbon tetrachloride present. A modification of the hydroxylamine hydrochloride method of Huckabay, Newton, and Metler(*4*) was used for acetone, and the acetyl chloride method proposed by Smith and Bryant(*10*) was used to determine methanol. Density was determined by the pycnometric method described by Langdon and Keyes (*6*). Refractive indexes were measured with a Bausch and Lomb dipping-type refractometer and were used instead of density for analyses of the acetone-chloroform and chloroform-methanol binary systems. In acetone analyses, results were reproducible to about 0.5 mole % of the acetone present in the sample and the methanol results were reproducible to about 1.0 mole % of the methanol present. Density and refractive-index measurement were reproducible to a precision equivalent to 0.1 mole % chloroform or carbon tetrachloride or 0.2 mole % methyl acetate. This high precision was possible because the two physical properties were found to be almost a linear function of the volume fraction of chloroform, carbon tetrachloride, or methyl acetate present. A calibration curve of deviations from additivity of density or refractive index when plotted vs. ideal volume fraction permitted precise determination of composition. To obtain complete analyses of ternary sample, check measurements were made by use of both chemical methods and density in practically all cases.

Large quantities of the pure components were required both for the vapor-liquid measurements and for the establishment of analytical methods. Baker and Adamson technical-grade chloroform was dried over phosphoric acid anhydride, then distilled batchwise at an 8-to-1 reflux ratio through a large-capacity, 24-theoretical-plate packed column. A heart fraction was collected having a boiling range of 0.2°C. Reagent-grade acetone and methanol were distilled in a similar manner. Technical-grade methyl acetate was dried over silica gel for 48 hrs. and a heart cut with a boiling range of 0.2°C. was collected. Technical-grade carbon tetrachloride was distilled batchwise in the fractionating column. The middle 60% of a batch was collected; the distillate temperature did not vary more than 0.1°C. during collection of the heart cut.

EXPERIMENTAL RESULTS

Vapor-liquid equilibrium determinations were made on the three ternary systems acetone-methanol-chloroform, acetone-methanol–carbon tetrachloride, acetone-methanol–methyl acetate and on six of the seven constituent binary systems. All activity coefficients were corrected slightly for nonideality of the vapor phase by the method described by Mertes and Colburn (*7*).*

The acetone (1)-methanol (3) binary system is common to all the ternary groups. Figures 3 to 5 show, in order, the x-y diagram, curves of $\log_{10}\gamma$ vs. x, and J plots for this system. End values were computed from the J plots by the method of least squares. The values compare favorably with the results of Uchida et al.(*11*).

*Experimental data may be obtained as document 4510 from the Photoduplication Service, American Documentation Institute, Library of Congress, Washington 25, D.C., for $1.75 for microfilm or $2.50 for photoprints.

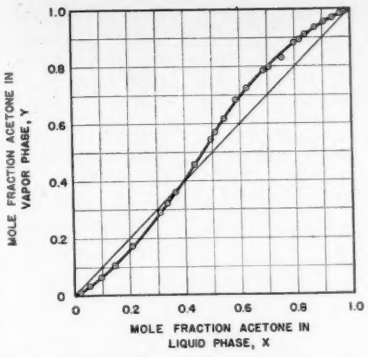

Fig. 6. Vapor-liquid equilibria for acetone-chloroform at 50°C.

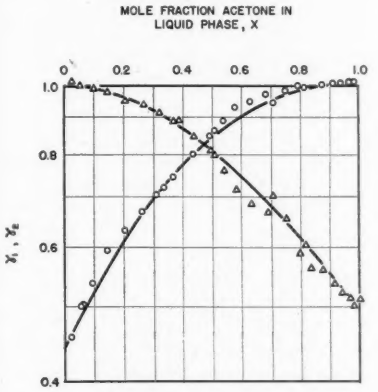

Fig. 7. Activity coefficients for system acetone-chloroform at 50°C.

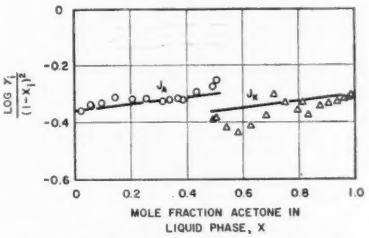

Fig. 8. Comparative plot of activity coefficients for acetone-chloroform at 50°C. with three-suffix Margules equation.

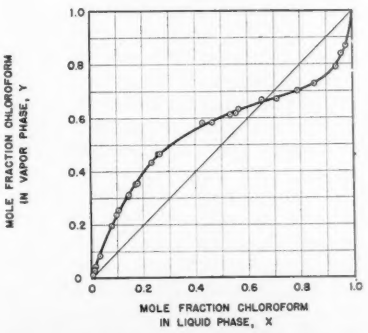

Fig. 9. Vapor-liquid equilibria for chloroform-methanol at 50°C.

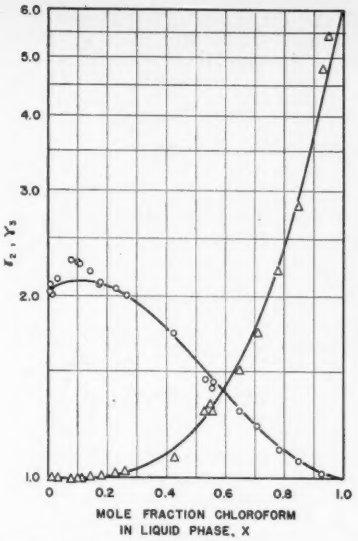

Fig. 10. Activity coefficients for chloroform-methanol at 50°C.

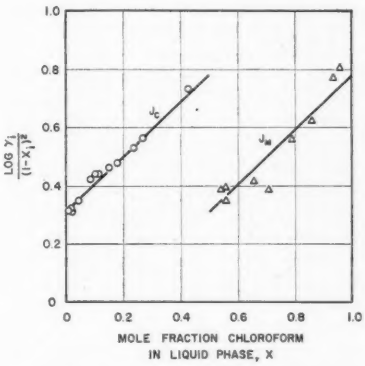

Fig. 11. Comparative plot of activity coefficients for chloroform-methanol at 50°C. with three-suffix Margules equation.

The system acetone (1)-chloroform (2) shows negative deviations from ideality; Figures 6 to 8 represent the results.

Figures 9 to 11 show the characteristics of the system chloroform (2)-methanol (3), which is interesting because of the great asymmetry of the log γ–x curves.

The data used for the carbon tetrachloride–methanol system are those of Scatchard, Wood, and Mochel(*9*), who recommended a four-suffix equation for representing the excess free energy.

Table 1 lists the Margules constants for each of the systems.

Observed vapor-liquid equilibrium compositions for the ternary systems acetone-methanol-chloroform (A-M-C or 1-3-2), acetone-

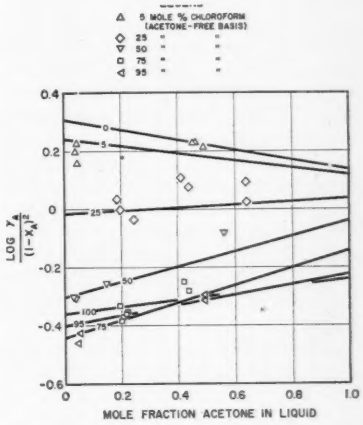

Fig. 12. Comparative plots of activity coefficients for acetone in the ternary system acetone–methanol–chloroform at 50°C. with three-suffix Margules ternary equation.

TABLE 1—MARGULES CONSTANTS FOR CONSTITUENT BINARY SYSTEMS

System	End values, A_{ij} Three-suffix Margules	Four-suffix Margules	Azeotropic composition
Acetone (1) Chloroform (2)	$A_{12} = -0.36$ $A_{21} = -0.30$		$x_1 = 0.38$
Acetone (1) Methanol (3)	$A_{13} = 0.305$ $A_{31} = 0.225$		$x_1 = 0.81$
Chloroform (2) Methanol (3)	$A_{23} = 0.31$ $A_{32} = 0.78$		$x_2 = 0.66$
Acetone (1) Methyl acetate (2′)	$A_{12'} = 0.065$ $A_{2'1} = 0.050$		$x_1 = 0.78$
Methyl acetate (2′) Methanol (3)	$A_{2'3} = 0.465$ $A_{32'} = 0.445$		$x_3 = 0.32$
Acetone (1) Carbon tetrachloride (2″)	$A_{12''} = 0.41$ $A_{2''1} = 0.31$		$x = y$ in range $0.89 < x_1 < 1.0$
Methanol (3) Carbon tetrachloride (2″)	$A_{2''3} = 0.765$ $A_{32''} = 1.10$	$A_{2''3} = 0.891$(9) $A_{32''} = 1.132$(9) $D_{2''3} = 0.483$(9)	$x_3 = 0.45$(9)

TABLE 2—EXPERIMENTALLY OBSERVED TERNARY CONSTANTS FOR THE SYSTEM ACETONE-CHLOROFORM-METHANOL

Run	Dilute Component	C^*
145	Acetone (1)	0.61
121		0.63
122		0.59
141	Chloroform (2)	0.37
142		0.53
117		0.53
120		0.43
132	Methanol (3)	0.37
133		0.34
144		0.52
	Mean:	0.49
	Standard deviation of mean:	0.10

TABLE 3—EXPERIMENTALLY OBSERVED TERNARY CONSTANTS FOR THE SYSTEM ACETONE—METHYL ACETATE—METHANOL

Run	Dilute Component	C^*
52	Acetone (1)	−0.16
53		−0.16
69		−0.02
70		0.00
59	Methyl acetate (2′)	−0.05
60		0.00
61		+0.04
62		+0.11
57	Methanol (3)	+0.14
58		+0.12
82		**+0.04**
	Mean:	0.00
	Standard deviation of mean:	0.09

TABLE 4—EXPERIMENTALLY OBSERVED TERNARY CONSTANTS† FOR THE SYSTEM ACETONE-CARBON TETRACHLORIDE-METHANOL

Run	Dilute component	C^* Three-suffix	C^* Four-suffix
1	Carbon	−0.13	+0.07
2	tetrachloride (2″)	−0.28	−0.09
3	Acetone (1)	+0.26‡	+0.38‡
4		−0.17	+0.05
5	Methanol (3)	−0.07	+0.17
6		−0.13	+0.06
	Mean:	−0.16	+0.05
	Standard deviation of mean:	0.04	0.04

†Assuming $C^*_1 = C^*_2 = C^*_3 = C^*$ in the four-suffix equation of Wohl (*13*).
‡This value omitted from average, based on statistical rules.

methanol–carbon tetrachloride (A-M-CT or 1-3-2″), and acetone-methanol–methyl acetate (A-M-MA or 1-3-2′) are also on file.* Multiple equilibrium determinations were made at each of the points 1 to 13 of Figure 1 for the systems A-M-C and A-M-MA. About a third of the data on each system were taken near regions 1 to 3 of Figure 1. For the system A-M-CT, determinations were made only at points 1 to 3.

J plots for each component of the A-M-C system are presented in Figures 12 to 14. Curves for the three-suffix Margules equations with $C^* = 0.5$ are plotted. Values of C^* were calculated from the three-suffix Margules equations by use of data from individual runs in the region $R = \frac{1}{2}$ *x* dilute. The results are shown in Table 2. Calculation of three different ternary constants, C^*_1, C^*_2, C^*_3, for use in the four-suffix Margules equation of Wohl was also carried out, but the resulting values did not differ significantly from each other or from the single C^* average listed in the table.

For the system A-M-MA, *J* plots are shown as Figures 15 to 17. The lines correspond to the three-suffix Margules equation with $C^* = 0$. Values of C^* were calculated from individual runs as indicated in Table 3. Again a single ternary constant was found adequate to describe the system.

J plots for the system A-M-CT are presented in Figures 18 to 20. The lines are calculated from the four-suffix Margules equation with $C^* = 0$. Calculations of C^* from each of the six experiments are summarized in Table 3. The two sets of C^* values correspond to the three- and the four-suffix equations. Based on the latter, the average value of C^* is not significantly different from zero. This is in agreement with data from other ternary systems and the slightly more complicated equations are therefore preferred. Whenever one or more of the binary systems require the use of four-suffix equations, the multicomponent equations should also be of the four-suffix variety, but the ternary effects may be no more complicated in these cases than they are for systems with simpler binary component systems.

This is in accord with a recent study by Carlson (*1*), who examined published data for twelve different ternary systems and concluded that $C^* = 0$ is satisfactory for all systems of which the deviations from ideal behavior are either zero or uniformly positive.

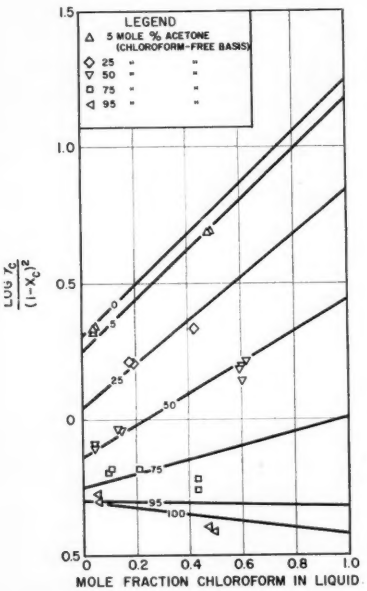

Fig. 13. Comparative plots of activity coefficients for chloroform in the ternary system acetone–methanol–chloroform at 50°C. with three-suffix Margules ternary equation.

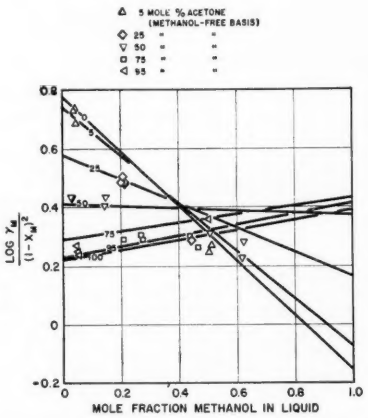

Fig. 14. Comparative plots of activity coefficients for methanol in the ternary system acetone–methanol–methyl acetate at 50°C. with three-suffix Margules ternary equation.

DISCUSSIONS OF RESULTS

Figures 21 to 23 are isothermal plots for the three ternary systems. In each case the isobars were calculated by use of the appropriate Margules equations.

In each system a steep gradient of vapor pressure is evident in the region of high methanol concentrations. The cause of this positive deviation from ideality probably is the decomposition of methanol aggregates brought about by dilution with either one of the other components. The methanol–carbon tetrachloride binary system is very strongly nonideal and causes very large vapor pressures over the whole range of compositions in the A-M-CT system. Figure 23 shows that the isobars for this system are nearly symmetrical about a line representing equal amounts of methanol and carbon tetrachloride. The A-M-MA system is dominated to a lesser degree by the methanol–methyl

*See footnote on page 404.

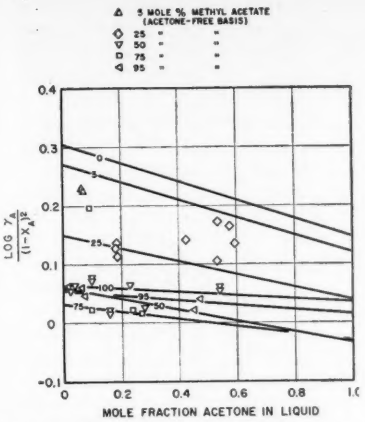

Fig. 15. Comparative plots of activity coefficients for acetone in the ternary system acetone–methanol–methyl acetate at 50°C. with three-suffix Margules ternary equation.

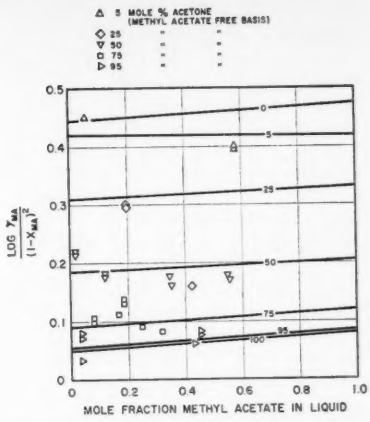

Fig. 16. Comparative plots of activity coefficients for methyl acetate in the ternary system acetone–methanol–methyl acetate at 50°C. with three-suffix Margules equation.

acetate binary system; the mixtures of methanol and acetone show only moderate positive deviations from ideality.

The extent of positive deviations from ideality of binary mixtures of acetone, methyl acetate, and carbon tetrachloride, respectively, with methanol is in inverse relation to their ability to accept protons in the formation of hydrogen bonds. In the order listed, they show decreasing ability to form aggregates with methanol and, consequently, are decreasingly compatible with it in mixtures.

The replacement of one chlorine of carbon tetrachloride by hydrogen, resulting in chloroform, makes a very large change in the deviations from ideal behavior in ternary systems with acetone and methanol. Chloroform and acetone have a strong tendency to form hydrogen-bonded aggregates in their binary mixtures. This results in negative deviations from Raoult's Law. Methanol, on the other hand, shows moderate positive deviations from ideality when mixed with either acetone or chloroform. Hydrogen bonds are formed also in these cases, but positive deviations result from the decomposition of methanol aggregates. This is particularly noticeable (Figure 9) in the activity of dilute methanol in chloroform.

In spite of positive deviations in the A-M and M-C binary systems, ternary mixtures nearly equimolar in acetone and chloroform, regardless of methanol concentration, exhibit a vapor-pressure depression relative to the methanol-containing binary systems that may be partially attributed to the formation of ternary aggregates (Figure 21). The excess free energy of the A-M-C- system is successfully represented by an equation in the third powers of mole fraction, suggesting that aggregates no more complex than trimolecular are responsible for the deviations observed. In addition, the value and the positive sign of C^* observed experimentally for this system enter Equation (13) in such a way as to lower the excess free energy. From this it seems likely that ternary aggregate of acetone, chloroform, and methanol exist in the molar ratio 1:1:1. It appears unlikely that significant negative values of C^* in Equation (13) will occur in any ternary system.

The Margules equations successfully predict that, owing to the strongly positive deviations in the methanol–carbon tetrachloride system, the activity coefficients of acetone in ternary solutions should fall outside the region between the two binary lines on Figure 18. Slightly negative deviations are predicted for a limited range of compositions. Apparently, even though acetone is "repelled" or made abnormally active by the presence of either methanol or carbon tetrachloride molecules alone, when these latter substances are present together they repel each other so strongly that a few molecules of acetone find ample free space in the solutions. Probably the partial entropy of acetone is therefore abnormally large, owing to this greater degree of freedom to occupy free volume in the liquid, resulting in a decreased free energy without necessarily involving energy effects.

The distillation characteristics of the three ternary systems are of interest because of their extremely nonideal behavior. The triangular plots of total vapor pressure can be used to bring out some general features of this behavior. With reference to Figure 22, for the A-M-MA system, for example, the location of the calculated ternary azeotropic composition is shown by the small circle inside the diagram. The binary azeotropes are located on each of the three sides of the triangle. The dashed lines (called "path lines") on the figure show the predicted gradual change of the liquid residue away from the azeotropes in a differential batch distillation. These lines were constructed by drawing straight tie lines on the triangle, each joining a pair of compositions representing liquid and vapor phases in equilibrium. If a liquid mixture is differentially distilled in apparatus having an

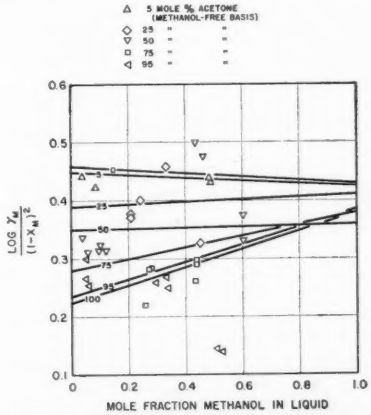

Fig. 17. Comparative plots of activity coefficients for methanol in the ternary system acetone–methanol–methyl acetate at 50°C. with three-suffix Margules equation.

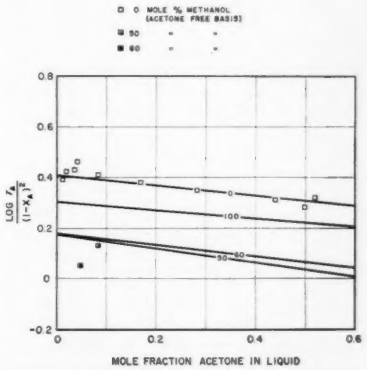

Fig. 18. Activity coefficients for acetone in the system acetone–methanol–carbon tetrachloride at 50°C.; lines are four-suffix ternary Margules equation.

efficiency equivalent to one theoretical plate, the residue will move for a short distance along the tie line through its original composition but in a direction away from the vapor end of the tie line. The path lines on Figure 22 therefore are constructed so that the tie lines are their tangents.

When the path lines are nearly straight, as they are near the bottom of the triangle or in the corners, the liquid and the equilibrium vapor are greatly different in composition, and vice versa. The path lines form a family of curves radiating from the dotted lines that join the three binary azeotropes to the ternary azeotrope. These dotted lines are called "characteristic lines" of the system because they cannot be crossed by any path line. A liquid whose initial composition falls on a dotted line at any point other than the azeotropic point will move along the dotted line to the nearest binary azeotrope. When it reaches this limiting composition, the residue will not change, but if a trace amount of one pure component is added to this residue it will move in a direction toward one of the pure-component vertices of the triangle, provided the azetrope has a minimum boiling point. The characteristic lines and the sides of the triangle are therefore path lines of singular characteristics.

In a ternary system with two binary azeotropes a characteristic line will join the two corresponding points on the sides of the triangle. Any possible ternary azeotrope will lie on this characteristic line. If the third binary pair is nonideal but does not have an azeotrope, owing to a large difference in the vapor pressures of the pure components, a ternary azeotrope still may exist. This may be the situation of the A-M-CT system, shown by Figure 23, in which it is not clear from the data whether a binary azeotrope exists or not. (Along the acetone–carbon tetrachloride side binary mixture containing more than about 90% acetone have very nearly equal liquid and vapor compositions. It does not appear to be essential that three binary azeotropes be present in a ternary system in order to have a multicomponent azeotrope; two binary azeotropes would appear to be sufficient if the third system is sufficiently nonideal.

The A-M-C system has mixed deviations from ideal behavior, owing to negative deviations in the A-C binary system (a maximum-boiling azeotrope) and positive deviations in the A-M and M-C binary pairs(minimum-boiling azeotropes). This results in an inflection point of invariant composition called by Ewell and Welch (*3*) a "saddle point," which is neither maximum- nor minimum-boiling with respect to other possible ternary compositions. Figure 21 shows the location of this saddle. The residue in a differential batch distillation tends to move across this saddle-shaped surface in a general down-hill direction, as indicated by the path lines on Figure 21.

CONCLUSIONS

Ternary vapor-liquid equilibria of nonideal liquid mixtures exhibiting only positive deviations from ideality can be predicted in many cases from data on the binary pairs alone by use of the appropriate Margules equation. Selection of the three- or four-suffix forms of the Margules equation is determined by the most complicated binary system involved, usually the one with the highest activity coefficients. Mixtures having uniformly positive deviations from ideality in the binary pairs may frequently be represented by $C^* = 0$, as indicated by two ternary systems described here and confirmed by an extensive evaluation of literature data by Carlson(*1*). Only one ternary system including both positive and negative deviations has apparently been investigated to date: the system A-M-C investigated here. This system ap-

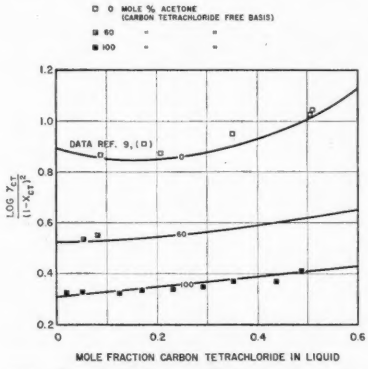

Fig. 19. Activity coefficients for carbon tetrachloride in the system acetone–methanol–carbon tetrachloride at 50°C.; lines are four-suffix ternary Margules equation.

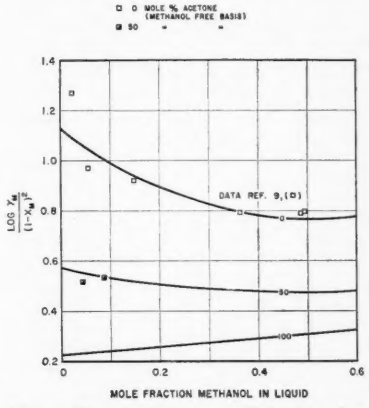

Fig. 20. Activity coefficients for methanol in the system acetone–methanol–carbon tetrachloride at 50°C.; lines are four-suffix ternary Margules equation.

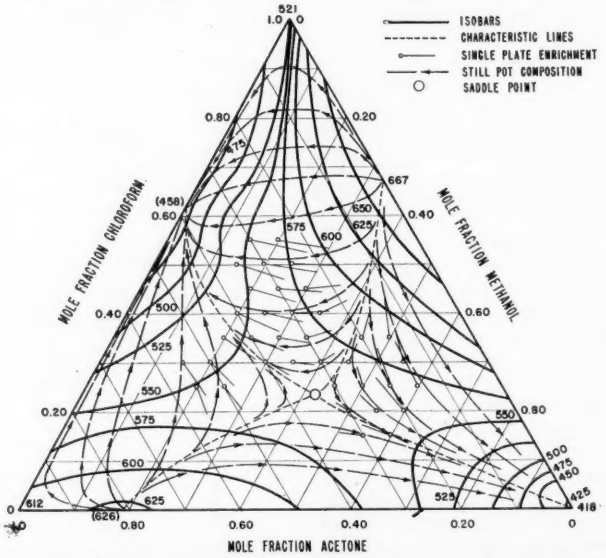

Fig. 21. Vapor pressures at 50°C. for system acetone–methanol–chloroform. Tie lines showing single-plate enrichment are drawn with small circle at the end representing the equilibrium liquid composition.

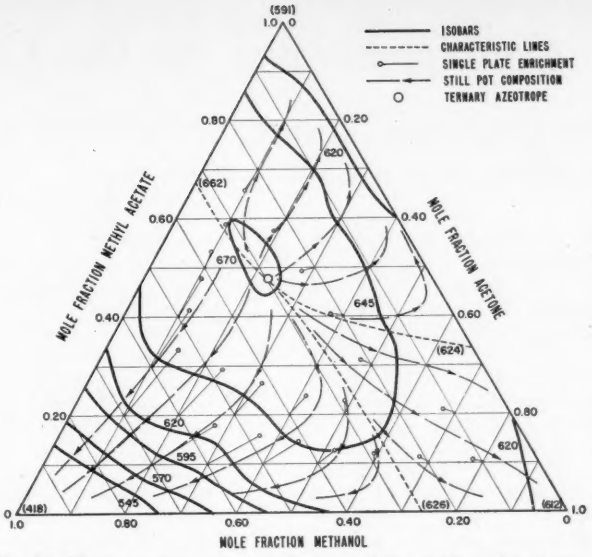

Fig. 22. Vapor pressures at 50°C. for system methanol–acetone–methyl acetate. Tie lines showing single-plate enrichment are drawn with small circle at the end representing the equilibrium vapor composition.

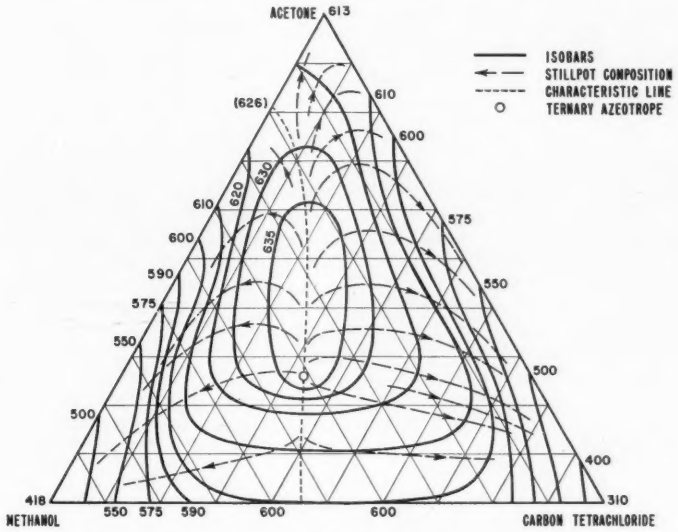

Fig. 23. Vapor pressures at 50°C. for system methanol–acetone–carbon tetrachloride.

pears to require a value of C^* that is significantly different from zero in order to be accurately described by the three-suffix Margules equation, but whether this behavior will also be found in other mixtures having both negative and positive deviations simultaneously is not yet known.

ACKNOWLEDGMENT

The aid of E. Bagnoli, J. C. Reynolds, and J. M. Witheford in certain phases of the experimental work is gratefully acknowledged. The authors also express their appreciation to H. C. Carlson and John Mitchell, Jr., for helpful advice.

This investigation was made possible by the financial assistance of the Engineering Department, E. I. duPont de Nemours and Company, Wilmington, Delaware.

NOTATION

A_{ij} = logarithm to base ten of activity coefficient of component i at infinite dilution in binary mixtures with j

C^* = ternary constant in three- or four-suffix modified ternary Margules equation. Also, coefficient of term in equation for excess free energy of mixing expressing effect of triple aggregates of unlike compounds

D = constant in four-suffix Margules equation for description of complex binary mixtures

G^E = Gibbs's free energy per mole of mixture in excess of that of an ideal mixture of the same composition

$J_i = \log \gamma_i/(1-x_i)^2$

P_i = vapor pressure of pure component i

q = arbitrary multiplier to x, originally molecular volume in liquid phase

R = gas constant

$R_2 = x_2/(x_2+x_3)$; $R_3 = x_3/(x_3+x_1)$; $R_1 = x_1/(x_1+x_2)$

T = absolute temperature, °K.

x = mole fraction in liquid phase

y = mole fraction in vapor phase

z = correction factor for nonideality of vapor phase, ratio of fugacity to partial pressure of component in vapor mixture

γ = activity coefficient, ratio of thermodynamic activity to mole fraction in the liquid phase

π = total pressure

Subscripts

1 refers to component 1, the most volatile in the pure state

2 refers to component 2

3 refers to component 3, the least volatile

i refers to any component

j refers to any component including i

k refers to any component except i or j

LITERATURE CITED

1. Carlson, H. C., personal communication (March, 1951).
2. Carlson, H. C., and A. P. Colburn, *Ind. Eng. Chem.*, 34, 581 (1942).
3. Ewell, R. H., and L. M. Welch, *loc. cit.*, 37, 1224 (1945).
4. Huckabay, W. B., C. J. Newton, and A. V. Metler, *loc. cit.*, Anal. Ed., 15, 272 (1943).
5. Jones, C. S., E. M. Schoenborn, and A. P. Colburn, *loc. cit.*, 35, 666 (1943).
6. Langdon, W. M., and D. B. Keyes, *loc. cit.*, 34, 459 (1942).
7. Mertes, T. S., and A. P. Colburn, *loc. cit.*, 37, 787 (1947).
8. Robinson, C. S., and E. R. Gilliland, "Elements of Fractional Distillation," 4th ed., McGraw-Hill Book Company, Inc., New York (1950).
9. Scatchard, G., S. E. Wood, and J. M. Mochel, *J. Am. Chem. Soc.*, 68, 1957 (1946).
10. Smith, D. M., and W. M. D. Bryant, *J. Am. Chem. Soc.*, 57, 61 (1935).
11. Uchida, S., S. Ogawa, and M. Yamaguchi, *Japan Sci. Rev., Ser.* I, No. 2, 41 (1950).
12. Wohl, K., *Trans. Am. Inst. Chem. Engrs.*, 41, 539 (1946).
13. ———, *Chem. Eng. Progr.*, 49, 218 (1953).

(Presented at A.I.Ch.E. Washington meeting)

Communications to the Editor

A NOTE ON EQUATIONS OF TIME

E. G. Scheibel, York Process Equipment Corporation, West Orange, New Jersey

I should like to call attention to a serious limitation in Equation (5) of the paper entitled "Approximate Equations for Time of Batch Fractionations" by A. I. Johnson, Chen-Juang Huang, and F. D. F. Talbot(*1*), which contains several relationships which were derived for my course in distillation calculations at the Polytechnic Institute of Brooklyn. I had advised the students that I had no intention of publishing the work, which was distributed in mimeographed form, and that they were free to use the equations wherever they could be applied. This aforementioned limitation was not given in my original notes but was discussed and illustrated by problems in the accompanying lecture.

Equation (5) does not recognize the fact that at large values of x a large number of trays are squeezed into the upper right-hand corner of the xy diagram to produce substantially pure distillate. For example, an impossible result is obtained if the equation is used to calculate the amount of distillate produced at a reflux ratio of 3 from a feed consisting of equal moles of two components having a relative volatility of 4.0, up to the time when the instantaneous distillate is 90% of the light component. At this point the concentration x in the residue is obtained by solving the quadratic relationship derived by Smoker(*2*) for the intersection of the operating line and the equilibrium curve.

$$\frac{R}{R+1}(\alpha-1)\,x^2+\left[\frac{R}{R+1}+\frac{(\alpha-1)\,x_D}{R+1}-\alpha\right]x-\frac{x_D}{R+1}=0 \qquad (1)$$

The value of x is 0.0945, and substituting in Equation (6) of reference *1* gives 71.5% of the initial batch remaining as residue. Since 90.55% of this is the less volatile component it contains 64.8% based on the original charge. This is 14.8% more than the 50% initially charged to the still.

The error lies in the initial product obtained from the still, which according to Johnson, Huang, and Talbot's Equation (3) is 170% light component (illustrated in Figure 1). Equation (5) in the previous paper(*1*) holds only when the concentration of light component in the initial charge is equal to $1/[(\alpha-1)R]$ or less. However, the equation can be used for other feed compositions if it is recognized that the distillate composition up to this point is substantially pure light component.

Thus in the previously cited problem the over-all material balance on the distillation when the residue concentration is equal to $1/(3\times 3)$, or 0.1111, mole fraction of light component is as follows:

	Charge to still moles	Residue Moles	Residue m%	Distillate Moles	Distillate m%
Light component	50	6.25	11.11	43.75	100
Heavy component	50	50.	88.89		
	100	56.25			

Using $W_i = 56.25$ and $x_i = 0.1111$ in Equation (5) gives a value for W of 55.1 for the final conditions, indicating that 44.9% of the batch will be distilled off when the distillate purity drops to 90%.

In this same course the relationships between residue quantity and composition were also derived from the same concept of a large number of plates in a system in which the equilibrium curve is substantially straight.

The equation is

$$\ln\frac{W_i}{W}=\frac{1}{(R+1)\,(k-1)}\ln\frac{x_i}{x} \qquad (2)$$

where k is the slope of the equilibrium curve.

This equation will hold only in the dilute region and is most useful in the calculation of systems at high reflux ratios, where the lower end of the operating line falls in this region. It also has the limitation that it cannot be applied directly if the initial charge concentration is greater than $1/[k+R(k-1)]$. By making the same assumption that the distillate is pure until the composition of the residue reaches this concentration, one can then apply the equation to the quantity at this time.

Thus in the previous problem the equilibrium curve can be assumed straight in the dilute region with a slope equal to the limiting slope of the constant relative volatility curve at zero concentration, namely $m = 4$. The distillate will be pure until the residue composition

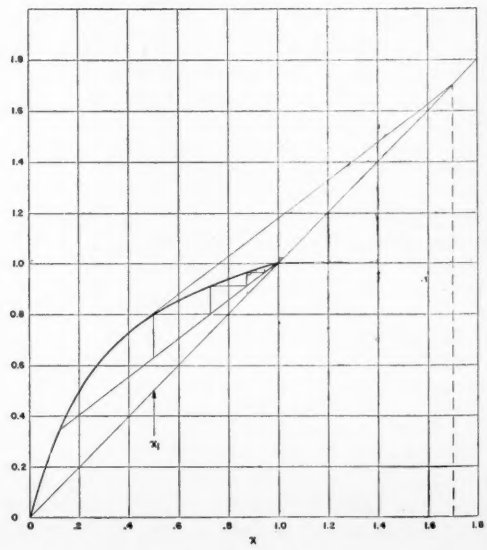

Fig. 1

is 7.7 mole % light component, when 45.8 moles of distillate will be obtained. When the overhead composition is 90%, the residue concentration x given by the equation

$$x = \frac{x_P}{k+R\,(k-1)} \qquad (3)$$

is 0.069 mole fraction, and the total amount of distillate obtained up to this point can be calculated as 100 — 53.7, or 46.3, moles. The agreement between the two equations will be better at higher reflux ratios.

It is also interesting to recognize that when $R=0$ both the authors' equation (5) and Equation (2) of this work reduce to the well-known equations derived from the integration of the Rayleigh equation without reflux for the respective cases of a constant relative volatility and a straight equilibrium curve.

The authors' Equation (34), based on a constant distillate composition, is also derived in my lecture notes for a number of trays sufficiently large so that the value of the residue composition a at total reflux will be substantially zero. In these notes I do not consider the case of a small number of trays. I have, however, also derived an alternate equation for the constant distillate composition operation. This equation can be more readily adapted for a small number of trays than the one selected by the authors of the present article for their development. It does not include the relative volatility of the components and therefore may be used for nonideal systems. The accuracy depends upon the degree to which the actual end of the operating line follows the parabolic curve.

If the slope of the operating line is assumed to vary linearly with the bottoms concentration from the initial feed concentration to a zero concentration at total reflux conditions, it may be shown that at any residue composition x the slope of the operating line is given by

$$\frac{L}{V} = \frac{x_D - y_i}{x_D - x_i} + \frac{x_i - x}{x_i}\left(1 - \frac{x_D - y_i}{x_D - x_i}\right) \qquad (4)$$

where y_i is the vapor in equilibrium with the feed composition. Thus it may also be found that

$$1 - \frac{L}{V} = \frac{y_i - x_i}{x_i\,(x_D - x_i)}\,x \qquad (5)$$

Substituting this value in the Bogart equation gives

$$\theta = \frac{W_i\,(x_D - x_i)^2 x_i}{V\,(y_i - x_i)} \int_x^{x_i} \frac{dx}{x(x_D - x)^2} \qquad (6)$$

which upon integration between the indicated limits gives

$$\theta = \frac{W_i\,(x_D - x_i)^2 x_i}{V\,(y_i - x_i)\,x_D}\left[\frac{x_i - x}{(x_D - x_i)(x_D - x)} - \frac{1}{x_D}\ln\frac{(x_D - x_i)x}{(x_D - x)x_F}\right] \qquad (7)$$

This equation can be rearranged in terms of the rate of product withdrawal from the still. Thus p_M, the maximum rate of product withdrawal, which occurs at zero time, is given as

$$p_M = \frac{V}{R_M + 1} = V\frac{y_i - x_i}{x_D - x_i} \qquad (8)$$

where R_M is the usual minimum reflux ratio for the given feed composition x_i.

At any time θ when the residue composition is x, the instantaneous rate of product withdrawal is given as

$$p = \frac{p_M}{x_i}\,x \qquad (9)$$

Eliminating y_i and x in Equation (7) by the use of relationships (8) and (9) yields the expression for the time required to reach a rate of product draw-off p

$$\theta = \frac{W_i\,x_i^2\,(p_M - p)}{p_M x_D\,(x_D p_M - x_i p)} + \frac{W_i\,x_i\,(x_D - x_i)}{p_M x_D}\ln\frac{x_D p_M - x_i p}{p\,(x_D - x_i)} \qquad (10)$$

If a small number of trays are considered and so the lower end of the operating line does not approach the equilibrium curve, the value of y_i can be determined by a trial-and-error procedure, adjusting the reflux ratio until the given number of trays provide a concentration of x_i. The maximum rate of product withdrawal can thus be calculated from this reflux ratio according to Equation (8), considering this reflux ratio as the minimum for the given column.

The given number of trays can then be stepped off at total reflux on a McCabe-Thiele diagram to determine the value of a. When the equivalent assumption is made that the slope of the operating line varies linearly over the range of x_i and a from the minimum slope $R_M/(R_M+1)$ to unity; Equations (4), (5), (6), (7), (9), and (10) became as follows:

$$\frac{L}{V} = \frac{x_D - y_i}{x_D - x_i} + \frac{x_i - x}{x_i - a}\left(1 - \frac{x_D - y_i}{x_D - x_i}\right) \qquad (4a)$$

$$1 - \frac{L}{V} = \frac{(y_i - x_i)}{(x_D - x_i)}\frac{(x - a)}{(x_i - a)}\,(5a)$$

$$\theta = \frac{W_i\,(x_D - x_i)^2\,(x_i - a)}{V\,(y_i - x_i)} \int_x^{x_i} \frac{dx}{(x - a)\,(x_D - x)^2} \qquad (6a)$$

$$\theta = \frac{W_i\,(x_D - x_i)\,(x_i - a)}{V\,(y_i - x_i)\,(x_D - a)}\left[\frac{x_i - x}{(x_D - x_i)\,(x_D - x)} - \frac{1}{x_D - a}\ln\frac{(x_D - x_i)\,(x - a)}{(x_i - x)\,(x_F - a)}\right] \qquad (7a)$$

$$p = p_M\frac{x - a}{x_i - a} \qquad (9a)$$

$$\theta = \frac{W_i\,(x_i - a)^2\,(p_M - p)}{p_M\,(x_D - a)\,[(x_D - a)\,p_M - (x_i - a)p]} + \frac{W_i\,(x_i - a)\,(x_D - x_i)}{p_M\,(x_D - a)^2}\ln\frac{(x_D - a)\,p_M - (x_i - a)\,p}{p\,(x_D - x_i)} \qquad (10a)$$

These equations are identical to the previous ones except that the origin has been moved to the point (a, a) and so all values of x are replaced by $x - a$.

It can be noted that the final equation includes only terms which are functions of the initial draw-off rate and total reflux conditions. It may thus be applied to nonideal

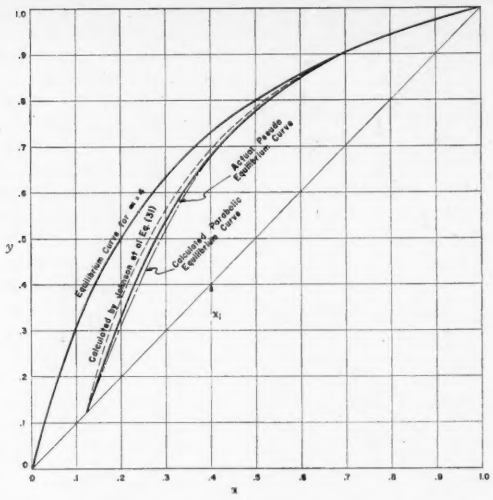

Fig. 2

systems and the agreement with the rigorous graphical technique will depend upon the deviation between the actual variation in the product draw-off rate with residue composition and the assumed linear variation. In all cases the equation can be used as a first approximation and for preliminary studies.

Calculation of the time for the distillation at constant product composition in the problem illustrated in Table 1 of the previous paper(*1*) gives a value of 8.38 by Equation (7) of this work, which compares with 8.10 calculated by Equation (34) of the previous paper. This is consistent with my experience in numerous other cases studied where the agreement was within 5% by the two equations.

In the problem given in Table 2 of the previous paper, involving two theoretical plates, the calculated time is very sensitive to the final reflux ratio. Thus calculating the final reflux ratio from Equation (9*a*) and substituting in Equation (10*a*) give a time of 1.94 hr. The trays at the corresponding reflux ratio of 7.5 were stepped off on a McCabe-Thiele diagram and the residue composition was 0.17; so this time corresponds to a somewhat greater recovery of distillate than anticipated in the authors' statement of the problem, since they specified a bottoms composition of 0.18. On the other hand, the authors' Equation (32) gives a reflux ratio of 4.4 at the final conditions. When the value of p calculated from this reflux ratio is used, the time given by the previous Equation (7) was in perfect agreement with the authors' calculated value of 1.48 hr. However, stepping this off on the McCabe-Thiele diagram gave a final residue composition of 0.20, which indicates poorer recovery than specified in the problem. On interpolation to a reflux ratio of 6.2 a residue composition of 0.18 was obtained, and at the corresponding product draw-off, Equation (7) gives a time of 1.74 hr. This latter value gives the best agreement with the previous authors' graphical integration and indicates that Equation (7) is the more readily adaptable to the problem when the final reflux ratio is properly established.

The relationship between both equations and the true value obtained by graphical integration of the Bogart equation can be readily seen from Figure 2, which has been constructed for the conditions of this problem. The pseudoequilibrium curve calculated by the authors' Equation (31) lies above the actual curve, and consequently the time required for a given change in the composition of the residue will be less than the true value. On the other hand, the parabolic equilibrium curve lies below the actual curve, and therefore a greater time will be calculated from Equations (9*a*) or (10*a*). The same relationship between the two forms of equations has also been found to hold in all the cases involving a large number of trays which I have calculated. No studies have been made, as yet to establish which equation more nearly represents the true condition encountered in practical systems.

LITERATURE CITED

1. Johnson, A. I., C. J. Huang, and F. D. F. Talbot, *A.I.Ch.E. Journal*, 51, No. 1, 111 (1955).
2. Smoker, E. H., *Trans. Am. Inst. Chem. Engrs.*, 34, 165 (1938).

REPLY

A. I. Johnson and C. J. Huang
University of Toronto, Canada

In writing this paper(*1*) the authors were interested primarily in developing analytical expressions for treating constant reflux and constant overhead distillations for a small number of plates. The authors regret possible serious omission of references to previous work with large numbers of plates but believed this information to be generally known. While the integration of Rayleigh's equation leading to Equation (5) was first learned by one of the authors in Dr. Scheibel's excellent course, this work is treated in a very similar manner in Robinson and Gilliland's text(*2*). In this work the limitation discussed by Dr. Scheibel in his correspondence (that the overhead product cannot exceed 100%) is also treated. The authors chose their example of Table 1 so that this difficulty did not need to be considered.

In his correspondence Dr. Scheibel has proposed an alternative procedure for treating constant overhead distillation with a small number of plates. This appears to require some trial and error in its application and is quite different from the method proposed in the present authors' paper. It should be pointed out that the integration of Bogart's equation leading to Equation (34)(*1*) is uniquely different from the integration leading to Equation (10), which Dr. Scheibel covered in his course. The authors suggest that Dr. Scheibel's technique could form much of the material for a paper in this field.

The authors wish also to thank Dr. Scheibel for pointing out the following slide-rule calculation errors in Table 1:

Column 1

22.2 moles should be 19.5 moles
6.10 hr. should be 6.44 hr.

Column 2

7.11 hr. should be 8.10 hr.

There should not be so large a difference between the results by graphical analysis and those by the equations listed in the paper. This difference apparently was due to limitations in the graphical calculation.

LITERATURE CITED

1. Johnson, A. I., C. J. Huang, and F. D. F. Talbot, *A.I.Ch.E. Journal*, 51, No. 1, 111 (1955).
2. Robinson, C. S., and E. R. Gilliland, "Elements of Fractional Distillation," 4 ed., McGraw-Hill Book Company, Inc., New York (1950).